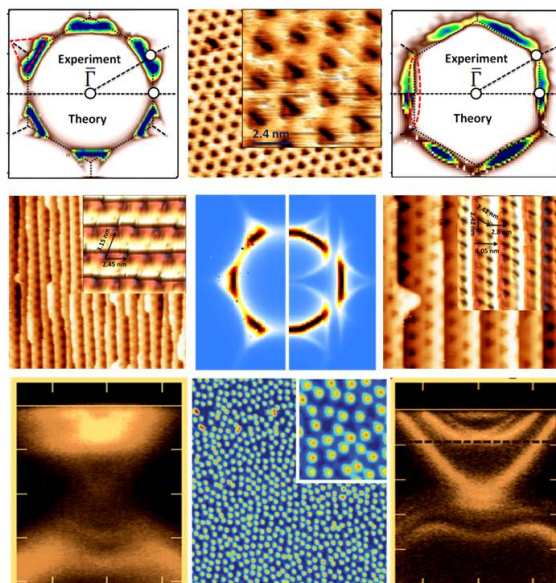


Surface States Manipulation via Surface/Interface Defects and Adsorbates



Zakaria Mohammed Mahmoud Abd El-Fattah

Física Aplicada I

Universidad del País Vasco (UPV/EHU)

Submitted for the degree of PhD in Physics

San Sebastián, 2012 September

Surface States Manipulation via Surface/Interface Defects and Adsorbates

By

Zakaria M. Abd El-Fattah

A thesis submitted in total fulfilment of the requirements for the
degree of Doctor of Philosophy

**Departamento de Física Aplicada I
Universidad del País Vasco (UPV/EHU)**

Donostia-San Sebastián
Spain

Supervisors

**Prof. Dr. Jose Enrique Ortega
Dr. Frederik Michael Schiller**

September 2012

Abstract

WAVE-particle duality firmly established for light in the beginning of the twentieth century and, later, for electrons has set a great analogue between the latter and photons and brought together their corresponding physics. A number of physical properties have, since then, shown to hold for both electrons and photons. The band theory, first, fulfilled for electrons in periodic solids, has been successfully applied to photons and a variety of artificial periodic 1D, 2D and 3D photonic crystals have been extensively studied. For nanophotonics applications, structures with periodicity of the order of the light wavelength (300-1000 nm) are required and the lithographic techniques were commonly used for this purpose. Noble metal surfaces, for example, host Shockley type surface states characterized by a Fermi wavelength of the order of 1-3 nm. Clearly, much smaller periodic structure is required to fabricate surface state based devices. Techniques, such as self-assembly, made the fabrication of these nanostructures possible. A case study in the present thesis is a 2D lateral superlattice made by combination of two noble metal surfaces with large lattice mismatch. Such combinations commonly self-assemble into moiré superstructures. The 1 ML Ag/Cu(111), in particular, exhibits an irreversible transformation from such moiré pattern into hexagonal lattice of dislocation network (periodicity ~ 2.4 nm). In contrast to the ring-like Fermi Surface (FS) characteristics for Ag and Cu apart, the presence of such superstructure has led to a highly featured FS and surface band structure with 25 meV wide gap above the Fermi level. In analogy to photonic crystals, electron guiding and focusing on this system has been theoretically examined and a new technology, namely “*Surface State Nanoelectronics*” (SSNE), has been proposed. Toward experimental realization and potential applications of SSNE the full gap of this system has to be set at the Fermi level and, for

further generalization, tunable and locally controlled nano-periodicities are required.

USING Angle Resolved Photoemission Spectroscopy (ARPES), we will show that interfacial doping of the 1 ML Ag/Cu with Au atoms allowed us to tune the energetic position of the surface state without significant broadening of its electronic features, hence without affecting its lifetime. For certain combination of Au doping and annealing temperature, we observed a complete “*Lifshitz transition*” at such noble metal surfaces. The tunable periodicity required for SSNE generalization has been experimentally examined on the 1 ML Ag grown on vicinal Cu(111) crystal with tunable 1D periodicity. Highly shaped and tunable constant energy surfaces were obtained by tuning the step-step periodicity. Particularly, the situation where the step-step periodicity is the same or twice the dislocation periodicity was examined, and both the dislocation and step induced gaps were coexisting. Fundamentally, we also noticed that the Ag steps are highly transparent to surface defects. In more qualitative view, we will also show that the 1 ML Ag/Cu system, when grown on “*magnetic*” Ni(111) substrate, exhibits significantly different surface electronic structure. In particular, transition from the gapped surface state to an apparent spin-orbit split state was observed for Cu thicknesses less than 4 ML.

SCATTERING of surface states by periodic array of scatterers is what allows us to engineer their full dispersions, in the first place. Recently a new class of materials, namely “*topological insulators*”, was found to host topological surface states that are robust against scattering by surface defects/impurities. We investigate the near surface electronic structure of such a topological insulator crystal, namely Bi₂Se₃. In particular, we noticed that a Rashba-split 2D electron gas and M-shaped surface states coexist with the topological state after exposure to few Rb atoms. Interestingly, we found that -by slight annealing of the sample- Rb atoms initially at the surface, incorporate into the bulk and enhance the stability of the near surface electronic states even under intentional exposure to oxygen, the finding of which clearly points towards environmental applications.

To my parents, my sisters, my brother
& to Ainara Berdonces

To Prof. Dr. Mohammed El-Okr

To my lifetime friends

Acknowledgements

The thesis would not have been possible without the contribution, guidance and help from several people who extended their valuable assistance in the preparation and completion of this study.

I would first like to thank **J. Enrique Ortega** and **Frederik Schiller** for the supervision of my thesis and for the many helpful discussions and suggestions related to my project, from which I learned a great deal. I also want to thank them for the time they took to read and correct the manuscript these last months.

I am grateful to **Manfred Matena**, from whom I learned everything related to the ARPES technique, and the set up of our machine. His continuous help with the data processing and interpretation were very valuable.

My thanks go to **Martina Corso** for providing all the STM data in this thesis, as well as for her supervision during my master's thesis, where one learned to run the STM and its data processing.

The theoretical calculations for the Ag/Cu/Ni were made, and still in progress, by **Elena Cannuccia**. Many thanks go to her, and also to **J. García de Abajo**, who provided us with a user-friendly interface for the EBEM code and showed me to use it. His help and discussions whenever I have problems running the code are really appreciated.

The work on topological insulators was done in Aarhus, in the group of Philip Hofmann in the frame of a short stay in Denmark. Thanks to the whole group · · · **Philip Hofmann**, **Marco Bianchi** and **Richard Hatch** · · · for such an interesting and stimulating three months.

Discussions with **Jorge Lobo** and **Andrew Walter** about the Nickel project are appreciated. Also, thanks to Andrew for providing me with some Igor scripts which allows for a quick analysis of the data.

When writing a thesis in Latex, and using Igor for data analysis one inevitably runs into numerous problems. Thanks to **Rubén González** for his many tips.

Finally, I'd like to thank my friends **Afaf El-Sayed**, **Maidor Ormaza**, and **Eli Goiri** for their help at work... reading the introductory chapters first draft, XPS data acquisition, and introducing me to the magic Find&Replace tip (respectively)... but also for the good times we had together during these years.

Contents

List of Figures	ix
List of Tables	xv
1 General Introduction	1
2 Experimental Techniques	9
Part I: Theoretical Background	11
2.1 Analysis of the Surface Physical Structure:	11
2.1.1 Scanning Tunneling Microscopy (STM):	11
2.1.1.1 Basic Principles:	11
2.1.1.2 Theory of STM:	12
2.1.2 Low Energy Electron Diffraction (LEED):	14
2.2 Analysis of the Surface Electronic Structure:	18
2.2.1 Angle Resolved Photoemission Spectroscopy:	19
2.2.1.1 Photoemission Theory:	21
2.2.1.2 Band Mapping with ARPES:	22
2.2.1.3 Modes of Photoemission Data Acquisition:	24
2.2.1.4 Photoemission Line Width and Life Time:	26
Part II: Experimental Setup	29
2.3 General Aspects of the Experimental Setup:	29
2.4 General Aspects of Samples Preparation:	30
2.4.1 Substrate Preparation:	30
2.4.2 Metal Deposition:	31
2.5 Data Acquisition:	33

CONTENTS

2.5.1	Scanning Tunneling Microscopy:	33
2.5.2	Angle Resolved Photoemission Spectroscopy:	34
2.5.2.1	ARPES at Nanophysics Laboratory:	35
2.5.2.2	ARPES at SRC:	40
2.5.2.3	ARPES at ISA:	42
3	Results and Discussion I	45
Part I:	Tunable Cu(111) Surface States Induced by Au Alloying	47
3.1	Introduction and Literature Survey I:	47
3.2	Sample Preparation and Characterization Tools I:	49
3.3	Results and Discussion I:	50
3.3.1	Au/Cu(111) Surface Alloy:	50
3.3.2	Quantum Well States on Au/Cu(111) Surface Alloy:	66
3.4	Conclusions:	76
Part II:	Lifshitz Transition across the 1 ML Ag/Cu(111) Superlattice	
	Band Gap Tuned by Interface Au alloying	79
3.5	Introduction and Literature Survey II:	79
3.6	Sample Preparation and Characterization Tools II:	82
3.7	Results and Discussion II:	83
3.7.1	1 ML Ag/Cu(111) Gapped Superlattice:	83
3.7.2	Au doped-1ML Ag/Cu(111) Gapped Superlattice:	86
3.7.3	Temperature Dependent Measurements:	96
3.8	Outlook:	105
3.8.1	Au Doped-2ML Ag/Cu(111) Moiré Superlattice:	106
3.8.2	Tunable Periodicity in 1 ML Ag/n-ML Au/Cu(111):	108
3.9	Conclusions:	112
4	Results and Discussion II	115
Coexistence of 1D and 2D Lateral Periodicities on the Surface of 1 ML		
Ag/v-Cu(111)		117
4.1	Introduction and Literature Survey:	117
4.2	Samples Preparation and Experimental Tools:	120

4.3	Results and Discussion:	121
4.3.1	Curved Cu(111) and Ag(111) Crystals:	121
4.3.2	1 ML Ag/Curved-Cu(111):	128
4.4	Conclusions:	144
5	Results and Discussion III	147
Apparent Spin-Orbit Split of the 1 ML Ag/Cu/Ni(111) Surface State:		
	Qualitative View	149
5.1	Introduction and Literature Survey:	149
5.2	Sample Preparation and Experimental Tools:	150
5.3	Results and Discussion:	151
5.3.1	Surface States on Ni(111):	151
5.3.2	Surface States on 1 ML Ag/Ni(111):	154
5.3.3	Surface States on 1 ML Ag/5 ML Cu/Ni(111):	157
5.3.4	Surface States on 1 ML Ag/1-3 ML Cu/Ni(111):	160
5.4	Conclusions:	176
6	Results and Discussion IV	177
Robust Surface Doping of Bi₂Se₃ Topological Insulator by Rb Intercala-		
	tion	179
6.1	General Introduction:	179
6.2	Sample Preparation and Experimental Tools:	183
6.3	Results and Discussion:	185
6.4	Conclusions:	200
7	Summery	203
A	Noble Metals and Surface States	205
I.	Crystallographic Structure of Noble Metals: Bulk and Surface	205
II.	Fermi Surface and Band Structure of Bulk Noble Metals	208
III.	Electronic Structure of Surfaces: Surface States	212
IV.	Shockley Surface states of the (111) Noble Metal Oriented Surfaces . . .	220

CONTENTS

B Fermi Surface Distortion Correction	221
I. Sources of Distortion:	221
II. Distortion Correction: An Example	227
Images Preparation:	229
CCD Camera Misalignment:	230
Energy Calibration	231
SPECS Transformation:	232
Manipulator Tilt and Curved Slit Corrections:	234
III. Data Visualization: Second Derivative Plots	236
C Acronyms	241
Bibliographic Research	243

List of Figures

2.1	STM Operation Principle	12
2.2	Density of States Mapping by STM	13
2.3	Si(111) Reconstruction	14
2.4	LEED Operation Principle	16
2.5	Ewald's Construction	17
2.6	Principle of Photoemission	20
2.7	Three and One-Step Models	22
2.8	Surface vs. Bulk in ARPES	24
2.9	Acquisition Modes in ARPES	25
2.10	The Curved Crystal	31
2.11	The Metal Evaporator and Wedge Preparation	32
2.12	Our STM Setup	33
2.13	STM Calibration	34
2.14	Our ARPES Setup	36
2.15	Electron Analyzer	38
2.16	Synchrotron Radiation	40
2.17	SRC-Synchrotron	42
2.18	ARPES Setup at ISA	43
2.19	ISA-Synchrotron	44
3.1	STM Images: 0.15 ML Au/Cu	51
3.2	STM Images: 0.8 ML Au/Cu	52
3.3	STM Images: 1.3 ML Au/Cu	52
3.4	LEED Patterns: Cu vs. Au/Cu	53
3.5	Core-Levels Spectra: Au/Cu	54

LIST OF FIGURES

3.6	Growth Mechanism: Au/Cu(111)	56
3.7	ARPES Data: Band Minima EDCs: Au/Cu	57
3.8	Band Minima: Data Points: Au/Cu	58
3.9	Summary of the Dispersion Parameters: Au/Cu	60
3.10	Bulk Projected Gap: Cu vs. Au/Cu	61
3.11	Phase Accumulation Model: moiré Corrugation Effect	64
3.12	STM Images: 3 ML Au/Cu	66
3.13	Schematic Drawing of Investigated Samples: Au/Cu Wedge	67
3.14	LEED Patterns across the Au/Cu Wedge	68
3.15	Valence Band: Au/Cu Wedge	70
3.16	Valence Band and Growth Mechanism	71
3.17	ARPES Data: As-Deposited Au/Cu	72
3.18	LEED Pattern vs. Dispersion Plot: 3 ML Au/Cu	73
3.19	ARPES Data: 650 K-700K Annealed Au/Cu	74
3.20	ARPES Data: 800 K Annealed Au/Cu	75
3.21	Phase Accumulation Model: 650 K and 750 K Annealed Au/Cu	76
3.22	Growth Modes	80
3.23	Wedges Preparation: Ag/Au/Cu(111)	83
3.24	Ag Thickness Calibration	84
3.25	ARPES, LEED and STM: 1 ML Ag/Cu	84
3.26	FS and Band Structure: 1 ML Ag/Cu	85
3.27	Band Minima and FWHM: Au Doped 1 ML Ag/Cu	86
3.28	\bar{M} -Point Gap Analysis: Au(Wedge)/1 ML Ag/Cu	88
3.29	STM and LEED: Au doped Ag/Cu	89
3.30	Band Structure and LDOS: EBEM	90
3.31	Experimental CESs: 0.4 ML Au/Ag/Cu	92
3.32	Theoretical CESs: 0.4 ML Au/Ag/Cu	93
3.33	Lifshitz Transition: Ag/Cu vs. Au/Ag/Cu	94
3.34	LT Measurements: Dispersion Plots: Ag/Cu vs. Au/Ag/Cu	97
3.35	EDCs: Band Minima: 0.2 ML Au/Ag/Cu	98
3.36	\bar{M} -point Gap Analysis: 0.2 ML Au/Ag/Cu	99
3.37	The Rate of the Downward Shift: Band Minima	100
3.38	Line Width: Band Minima	102

LIST OF FIGURES

3.39	Experimental Line Width: Electron-Phonon Coupling	104
3.40	Experimental Line Width: Au/Cu(111)	105
3.41	ARPES Data: Band Minima- Au/2 ML Ag/Cu(111)	107
3.42	ARPES Data: Dispersion Plots: Au/2 ML Ag/Cu(111)	108
3.43	ARPES Data: CESs: Au/2 ML Ag/Cu(111)	109
3.44	STM Images: 1 ML Ag/3 ML Au/Cu(111)	110
3.45	Valence Band Spectra: Au/Cu vs. Ag/Au/Cu	111
3.46	ARPES Data: QWSs: Ag/Au/Cu	111
3.47	Line Width vs. Band Minima Shift: Summery	112
4.1	Schematic View: Curved Crystal	118
4.2	Invetsigated Samples: Wedge Preparation	121
4.3	STM Images: Curved Ag(111)	122
4.4	STM Images: Curved Cu(111)	123
4.5	LEED Patterns: Curved Cu(111)	123
4.6	ARPES Data: Curved Ag(111) and Cu(111)	125
4.7	Kronig-Penney Model: Curved Ag(111) and Cu(111)	126
4.8	STM Statistical Analysis: Curved Ag(111) and Cu(111)	128
4.9	ARPES Data: 1 ML Ag/Curved-Cu(111)	129
4.10	Elastic vs. Inelastic Scattering	130
4.11	Surface States Dispersions: Small Miscut Angles	131
4.12	STM Images: Miscut Angle = 5.5° : {111} Step	133
4.13	STM Images: Miscut Angle = 3° : {100} Step	133
4.14	STM Images: Miscut Angle = 5.5° : {100} Step	134
4.15	Surface States Dispersions: Medium Miscut Angles	135
4.16	Surface States Dispersions: Theory vs. Experiment	137
4.17	EBEM Input Geometries	138
4.18	Theoretical CESs: 1 ML Ag/Cu(111)	139
4.19	Theoretical CESs: 1 ML Ag/v-Cu(111): One Triangle/Terrace	141
4.20	Theoretical CESs: 1 ML Ag/v-Cu(111): Two Triangle/Terrace	142
4.21	Experimental CESs: Miscut Angle = 5.5°	143
4.22	Experimental FS: Miscut Angle = 6°	144
5.1	Schematic Diagram of Investigated Samples	151

LIST OF FIGURES

5.2	Bulk Band Structure and Surface States on Nickel	153
5.3	LEED Patterns: Ag/Ni(111)	154
5.4	ARPES Data: 1 ML Ag/Ni(111)	155
5.5	EDC Spectra: Ni(111) vs. 1 ML Ag/Ni(111)	156
5.6	ARPES Data: 1 ML Ag/Ni(111)	157
5.7	ARPES Data: 5 ML Cu/Ni vs. 1 ML Ag/ 5 ML Cu/Ni: Annealed to 600 K	158
5.8	ARPES Data: 5 ML Cu/Ni vs. 1 ML Ag/ 5 ML Cu/Ni: Annealed to 800 K	158
5.9	Valence Band Spectra: 5 ML Cu/Ni vs. 1 ML Ag/ 5 ML Cu/Ni	159
5.10	Valence Band: Ni, Ag/Ni, and Ag/Cu/Ni	160
5.11	ARPES Data: 1 ML Cu/Ni	161
5.12	Valence Band: Cu/Ni vs. Ag/Cu/Ni	162
5.13	ARPES Data: 1 ML Ag/ 1 ML Cu/Ni	162
5.14	Dispersion Plots: 3 ML Cu/Ni	163
5.15	CES Plots: 3 ML Cu/Ni	164
5.16	Dispersion Plots: 1 ML Ag/ 3 ML Cu/Ni	165
5.17	CES Plots: 1 ML Ag/ 3 ML Cu/Ni	166
5.18	Calculated Magnetic Moments	167
5.19	ARPES Data: 1 ML Ag/ 1 ML Cu/Ni	168
5.20	Structure vs. Dispersion Plots: Ag/Cu/Ni	171
5.21	Band Structure: Pt vs. Ni	173
5.22	Hybridization Effect in Ag/Cu/Ni(111)	175
6.1	Trivial vs. Topological Surface States	180
6.2	Real vs. Reciprocal Space of Bi ₂ Se ₃	181
6.3	Parity Inversion in Bi ₂ Se ₃	182
6.4	The Bi ₂ Se ₃ Crystal	184
6.5	ARPES Data: Rb Deposition	186
6.6	ARPES Data: Energy Dependent Plots	187
6.7	ARPES Data: FSMs	188
6.8	ARPES Data: Dispersion Plots	189
6.9	Band Bending vs. Van der Waals Interlayer Relaxation Scenarios	191

LIST OF FIGURES

6.10 ARPES Data: Dispersion Plots	192
6.11 The Bi_2Se_3 Crystal	194
6.12 ARPES Data: Oxygen Exposure Test	195
6.13 STM Topographs	197
A.1 Crystal Structure: <i>fcc</i> Lattice	206
A.2 Brillouin Zone: <i>fcc</i> Lattice	207
A.3 Bulk Band Structure: Noble Metals	209
A.4 Projected Bulk Gap: Cu(111)	209
A.5 Fermi Surface: Copper	210
A.6 Fermi Surface: All Noble Metals	211
A.7 Types of Surface States	214
A.8 Image Surface States	215
A.9 Multiple Reflection Theory	216
A.10 Phase Accumulation Model: Cu(111)	217
A.11 Noble Metals Surface States: Temperature Dependent	218
A.12 Surface States Dispersion: Experimental Data	219
B.1 Iso-Angle Contours: Different Lens Modes	222
B.2 Distortion due to a Curved Slit	223
B.3 SPECS Transformation Applied to Inclined Fermi Edge	225
B.4 Distortion due to a Manipulator Tilt	226
B.5 Manni Tools: Main Panel	228
B.6 ARPES Raw Data	228
B.7 Sub-Menu: Energy to Pixel Transformation	229
B.8 Fermi Edge Fitting: Pixel Units	230
B.9 Sub-Menu: Image Rotation and Energy Scaling	230
B.10 Surface State Fitting: Pixel Units	231
B.11 Fermi Edge Fitting: eV Units	232
B.12 Sub-Menu: SPECS Transformation	233
B.13 Surface State Fitting: eV Units	233
B.14 Distorted CES: Degree (Angle) Units	234
B.15 Normal Emission vs. Manipulator Angle	235
B.16 Sub-Menu: Manipulator Tilt and Curved Slit	236

LIST OF FIGURES

B.17 Normal Emission vs. Manipulator Angle after Curved Slit Correction . .	236
B.18 Elliptically Distorted CES: Degree (Angle) Units	237
B.19 Sub-Menu: Channel Plate Scaling	237
B.20 Spherical CES: Final Result	237
B.21 Second Derivative vs. Curvature Method: EDCs Spectra	239
B.22 Second Derivative vs. Curvature Method: CES Plots	240

List of Tables

3.1	Fitting Parameters: Electron-Phono Coupling	103
3.2	Life Time Contributions: Theory & Experiment	103
4.1	Step-Step Separation in a Curved Crystal	139
5.1	Dispersion parameters of Ni(111) Surface States	153
6.1	Survey on the 2DEG and M-States	199
6.2	Band Bending vs. van der Waals Relaxation	200
A.1	Fitting Parameters: Noble Metals	208
A.2	Dispersion Parameters: Noble Metal Surfaces	220
B.1	ARPES Data: Calibration Files	227

LIST OF TABLES

General Introduction

In his famous talk in 1959, Richard P. Feynman pointed out that there is “*plenty of room at the bottom*”^[1]. He predicted exciting new phenomena that might revolutionize science and technology and affect our everyday life- if only we were to gain precise control over matter, down to the atomic level. Nowadays a field whose basic goal is the control of matter in an atomic scale has arisen, namely “*nanotechnology*”. Nanotechnology deals with structures that have one, two, or three dimensions with 100 nanometers or smaller, and involves developing materials or devices within that size. As a special case, “*surface science*” is concerned with the scale of 0.1-10 nm in the single dimension perpendicular to a given surface or interface^[2]. Surface science thus restricts itself to nanometer scale in one dimension (1D), studying structures that are spatially extended in two dimensions (2D).

In the present thesis we investigate the electronic structure of “2D metallic surfaces”. We further discretize the 2D surface by creating extra lateral 1D or 2D superperiodicities to control and tune the electronic properties of such 2D surfaces, gaining fundamental information and nanotechnology applications.

Surface science has reached its current development due to many inventions and fabrications that took place over a relatively long period of time. Clearly, to ensure a correct measure of the property of a desired surface, it has to be clean for a time long enough to perform an experiment. This has been facilitated by the development of the “*Ultra-High Vacuum*”(UHV) technology^[3-6]. The search for a characterization technique in order to probe the atomic and electronic structure of sur-

1. GENERAL INTRODUCTION

faces has become possible with the development of a vast amount of surface sensitive techniques^[7–10]. The surface structure can, nowadays, be nicely determined with atomic precision, for example, using “*Low Energy Electron Diffraction*” (LEED) and “*Scanning Tunneling Microscopy*” (STM). The electronic structure can be also probed by different spectroscopic techniques based on the detection of electrons (to gain surface sensitivity), e.g. “*Angle Resolved Photoemission Spectroscopy*” (ARPES). *All these techniques will be introduced in chapter two of this thesis.*

Beside the UHV-ensured clean surfaces and the development of surface sensitive techniques, fabrication methods of surfaces and/or nanostructured materials are required. Generally speaking, the fabrication of nanostructured materials can be classified into two main approaches, namely the “*top-down*” and “*bottom-up*” approaches^[11–15]. The top-down approach, which includes lithographic methods, relies either on the removal or division of bulk materials to produce the desired structure and has a number of limitations to the minimum features to be patterned with, however, several efforts have been made to exceed these limits^[16,17]. The need of atomic and molecular scaling to overcome the well known Moor’s law limit -at one hand- and to enhance the quantum size effects -on the other hand- has turn the direction of nanostructures fabrication to the bottom-up approach aiming to achieve smaller and smaller nanostructures^[18]. Within this approach, atoms, molecules, or even nano-sized objects are used as building blocks to fabricate complex nanostructures. The limitation of this method stems from the difficulty of gathering gigantic amounts of atoms into ordered devices^[19]. Two strategies can be envisioned. The first strategy is enabled by the development of “*Scanning Probe Microscopes*” (SPM) that opened up the possibility of not only imaging and studying matter at the atomic scale, but actually interacting with it^[18,20]. The second strategy is the so-called “*self-assembly*” approach. In the self-assembly processes, the building blocks (atoms, molecules, or nano-objects) organize themselves into functional structures as driven by the energetics of the system. The most important driving force for self-assembly are the interaction energies between the subunits itself^[21]. During the growth of these subunits on a flat or patterned surface, the interaction between the substrate and subunits serve as a driving force for the self-organization.

In the present work, self-assembled metallic systems have been prepared by physical vapor deposition of noble metal adlayers (typically, Ag and Au) on top of flat and

vicinal Cu(111) substrates. The evaporation conditions and parameters as well as the subsequent heat treatments of the samples will be detailed in the corresponding chapters for each investigated system.

Since we are interested to map out the electronic properties of such self-assembled metallic systems, the periodicity of the lattice is a fundamental property. In fact, a crystal is different from other materials due to the presence of a discrete translational symmetry. Meaning that, an ideal single crystal is generated by the “*endless*” repetition of single unit cells^[22–24]. This fact reduces the massive many-electron problem of an infinitely extended 3D solid into a simpler one via Bloch theorem. There is also a remarkable interplay between the atomic arrangements within a solid, the type and shape of the constituents of its unit cell (atoms, molecules, group of atoms, etc.) and the electronic structure of the solid. For a 2D system, the translational symmetry is still present (or modified) in the direction parallel to the surface but is completely broken in the perpendicular direction^[25,26]. As a consequence, new states localized at this new boundary (the surface or interface) can emerge. These states are called “*surface states*”^[27–29] and their 2D parallel dispersions on metallic surfaces are the subject of the present thesis.

In spite of the high advance in surface cleaning and the UHV conditions, an ideally ordered surface with complete 2D translational symmetry does not occur in reality^[30,31]. There are always a certain number of different types of defects (e.g. steps, dislocations, vacancies) that coexist on a clean surface. These defects do, in turn, scatter the surface electrons and, for example, reduce the surface conductivity. Depending on the way the surface is cleaned one can reduce the amount of such defects considerably. In contrast, the presence of such defects can be of considerable importance if one was able to assemble one and/or two type of defects and manage to have it periodically distributed over the surface. This will result in the formation of a 1D or 2D “*lateral superlattice*” with a new (larger) discrete translation symmetry. In the mentioned Feynman’s room, the prediction was actually based on the emergence of a quantum size effect when one or more dimensions of the solid are comparable to the interatomic distances in a crystal, and hence to the wavelength of the electron wave function. If the periodicity of the lateral defects is, thus, tuned to the nanoscale regime (hence approaching the Fermi

1. GENERAL INTRODUCTION

wavelength of the surface electrons), the Fermi electrons will be feeling these superlattice periodic potential and interesting quantum phenomena, such as charge density wave^[32–35], Fermi surface nesting^[36–38], quantum confinement of electronic states^[39,40], etc, can emerge. Fortunately, such lateral superlattices are experimentally accessible. For example, 1D periodic array of steps, i.e., “*vicinal surfaces*”, can be created by cutting the bulk crystal with a slight miscut angle to a high symmetry direction^[41–44]. 2D moiré patterns are also common via the deposition of atomic layer(s) on top of a substrate with a certain lattice mismatch between them. As an example for the latter, 1 ML Ag on top of Cu(111) crystal results in the formation of a six-fold rotationally symmetric moiré pattern when deposited at low temperature, followed by a three-fold rotationally symmetric dislocation network upon annealing^[45–47]. The same happens for graphene when grown on different substrates^[48,49]. This is when the symmetry of the building block that constitutes the superstructure becomes significant. A reduction in the rotational symmetry of the superstructure from the moiré to the dislocation network has its signature in the surface electronic structure by opening up a gap at the \bar{K} -point in the surface Brillouin zone^[50–54]. A similar situation happens when the atomic lattice of the graphene is locally disturbed^[55,56]. More conflicting superstructure periodicities on the surface, such as the combination of 1D periodic arrays of steps and 2D Moiré-like patterns, can have a significant influence on the surface electronic structure^[57]. The relative strength of the periodic potential related to each array of scatterers, the periodicity of each sub-superlattice, and the ability of tuning one or simultaneously the two superstructure periodicities represent the difficulty and the state of art within this area.

The above mentioned lateral superstructures of 1D, 2D and combination of both on the (111) oriented noble metal surfaces, Cu(111) in particular, and their interaction with the surface states characteristic of the bare substrate are the main subject of the present thesis.

Recently, a new type of electronic states that does exist on the surfaces of some layered semiconductors has been discovered. Due to their physical origin, which is different compared to the previously mentioned surface states, they are rather classified as “*topological states*”, and the supporting semiconductors (or insulators in the lan-

guage of theoreticians) are called “*topological insulators*”^[58]. One of the most exciting properties of topological surface states is its robustness to defects/impurities.

A separate general introduction to topological insulators will be discussed in the last chapter of the present thesis.

The thesis will then be organized as follow;

Chapter Two, entitled “***Experimental Techniques***”, will detail the basic theory (**Part 1: Theoretical Background**) and the experimental consideration of the techniques and their different setups (**Part 2: Experimental Setup**) employed for the surface and electronic structure determination. These are; STM, LEED, and ARPES.

Chapters Three, Four, Five, and Six contain the results and discussion on the investigated systems. Each of these chapters will start with a brief and more specific introduction as well as a literature survey on the investigated system, followed by the sample preparation and some experimental considerations. Conclusions will be given at the end of each chapter highlighting the main findings.

Chapter Three, will be further divided into two connected parts. In **Part I**, entitled “***Tunable Cu(111) Surface States Induced by Au Alloying***”, the effect of Au deposition with thicknesses from 0 to 1 ML on top of Cu(111) on the dispersion of the later surface state and its connection to the surface structure will be investigated as a function of the annealing temperature. The main finding of this part is the formation of a Au/Cu surface alloy upon annealing and the consequent shift of the Cu(111) surface state toward higher binding energy. We also explore wider Au coverage (multilayers) and the emergent quantum well states due to Au/Cu alloy formation. **Part II**, entitled “***Lifshitz Transition across the 1 ML Ag/Cu(111) Superlattice Band Gap Tuned by Interface Au alloying***”, concerns the possible tuning of the 1 ML Ag/Cu(111) surface state by means of interface Au doping. The main finding of this part is the observation of a “*Lifshitz transition*” by shifting the full surface band structure towards higher binding energy without significant change of the line width of the spectral features. A model calculation based on Boundary Element Method will be given and compared to the experimental data. The line width analysis of the surface state in the Au doped and undoped 1ML Ag/Cu(111) as a function of the measuring

1. GENERAL INTRODUCTION

temperature will be briefly presented. An outlook containing the possible extension of the work, presented on qualitative background will be given by the end of the chapter. These are; the 2 ML Ag/Au/Cu(111) and the 1 ML and 2 ML on top of multilayer Au/Cu(111) system.

Chapter Four, entitled “*Coexistence of 1D and 2D Lateral Periodicities on the Surface of 1 ML Ag/v-Cu(111)*”, reports the surface geometry and electronic structure of the dislocation network of 1ML Ag on top of vicinal Cu(111) with tunable step-step separation. This crystal is called “*curved*” crystal and a brief analysis of its geometric and electronic structure in Ag(111) and Cu(111) are presented at the beginning of the chapter for systematic comparison. The situation at which the step periodicity nearly coincides with one and/or two of the dislocation network will be discussed in more detail. The rest of the chapter will be devoted to some model calculations for better description of the 1 ML Ag/Cu(111) system and the search for possible technological applications.

Chapter Five, entitled “*Apparent Spin-Orbit Splitting of the 1 ML Ag/Cu / Ni(111) Surface State: Qualitative View*”, explores the interaction of the 1 ML Ag/Cu surface state with that of Ni(111) substrate. The apparent spin-orbit split surface state was observed for Cu thickness < 4 ML, above/below which a (1 ML Ag/Cu)/(Ni)-like surface states were obtained.

Chapter Six, entitled “*Robust Surface Doping of Bi_2Se_3 Topological Insulator by Rb Intercalation*”, reports the electronic structure of the newly discovered class of matter, namely topological insulators. In particular, the effect of alkali metal (Rb) doping on the Bi_2Se_3 topological insulator will be detailed and compare to recent studies. The stability of the induced 2D electron gas states will be compared in two distinct cases, when Rb atoms are attached to the surface or intercalated inside the material layers.

In **Chapter Seven**, entitled “*Summary*”, the specific conclusions of each chapter are all collected for an easy access to the thesis main message.

The thesis is further supported by two appendices. **Appendix A** reviews some basic information concerning the geometric and electronic structure of the bulk noble

metal and the corresponding high symmetry surfaces. A basic introduction to the origin of surface states, their different type, etc, will be given. In particular, the surface state on the (111) oriented surfaces experimentally measured by ARPES will be highlighted. The application of the phase accumulation model to surface and quantum well states will be briefly mentioned. “*We encourage readers with no pervious background to surface states to go through this appendix before proceeding to the results and discussion chapters*”. **Appendix B**, on the other hand, is mainly recommended for experimentalists dealing with electron analyzers and ARPES techniques. The appendix deals with some experimental difficulties while initiating our ARPES setup with some possible corrections through mathematical algorithms and/or mechanical changes. A detailed example showing the history of the corrections applied to the data presented throughout the thesis is also given.

1. GENERAL INTRODUCTION

2

Experimental Techniques

The chapter describes the experimental techniques that have been employed to study the electronic/geometric surface structure of the various systems reported in this work. The major part of the thesis is devoted to the measurements conducted using “*Angle Resolved Photoemission Spectroscopy*”(ARPES), which gives the electronic structure information, i.e. the main subject of the thesis. “*Low Energy Electron Diffraction*”(LEED), which gives structural information in the reciprocal space, was used to provide information regarding the cleanliness and the surface structure of the investigated systems, while “*Scanning Tunneling Microscopy*”(STM) was used for structural information in the real space with atomic resolution. Therefore, the basic theory as well as some experimental considerations of these techniques will be discussed in the following sections paying more attention to ARPES.

The chapter is, therefore, divided into two main parts. In part one, the theory behind the experimental techniques will be described. The operation principle of each technique will be briefly mentioned. In part two, only the experimental considerations, i.e. chambers, experimental setup, calibration, and data acquisitions are concerned.

2. EXPERIMENTAL TECHNIQUES

Part I: Theoretical Background

2.1 Analysis of the Surface Physical Structure:

2.1.1 Scanning Tunneling Microscopy (STM):

The first successful tunneling experiment was performed in a metal-oxide-metal junction^[59,60]. STM, which can be thought of as metal-vacuum-metal junction, was then invented by Binnig, Rohrer, and their co-workers at IBM Research Laboratory, Zurich, Switzerland, in the early 1980s^[61–63]. The authors got the Noble prize in physics in 1986. The basic principle and theory of the STM are described briefly in the following subsections.

2.1.1.1 Basic Principles:

STM is based on the quantum mechanical “*tunneling effect*”. When an atomically sharp tip is brought close to a sample surface, at a distance of ~ 1 nm, under a bias voltage, V_t , between the tip and a sample, a small tunneling current, I_t , starts to pass between them. This tunneling current drastically increases with decreasing separation between the tip and the sample^[19]. It is, therefore, possible to precisely evaluate the change in the separation by measuring the tunneling current. The tip is raster-scanned across the surface by using, e.g. a piezoelectric tubes. The atomic corrugation of the surface gives, then, rises to variations in the tunneling current with distance (z) between the sample and the tip. As a rule of thumb, the current reduces an order of magnitude for an increase of the gap distance by ~ 1 Å. This sensitivity leads to a high lateral and vertical resolution: the topmost atom at the tip-apex drags around 90 % of the current (assuming that it protrudes ~ 1 Å further than other tip atoms).

The whole STM operation is usually fully computer-controlled and the scanning parameters like V_t , I_t , and the raster speed are set via an interface, see Fig. 2.1 for

2. EXPERIMENTAL TECHNIQUES

clearness. There are basically two modes of operating the STM^[7,19,64]. In the “*constant-current mode*”, the current I_t is compared to a preset current by a feedback circuit. It provides a correction voltage to the scanner tubes which adjusts the z position of the tip in order to keep I_t constant. The correction feedback signal is recorded together with the $x - y$ position of the tip and hence the STM image is obtained. In the “*constant-height mode*”, the z -position of the tip is kept constant and the tunneling current is recorded as it varies while raster scanning the sample surface. Generally, the constant-current mode yields better resolution whereas constant-height mode allows faster scanning.

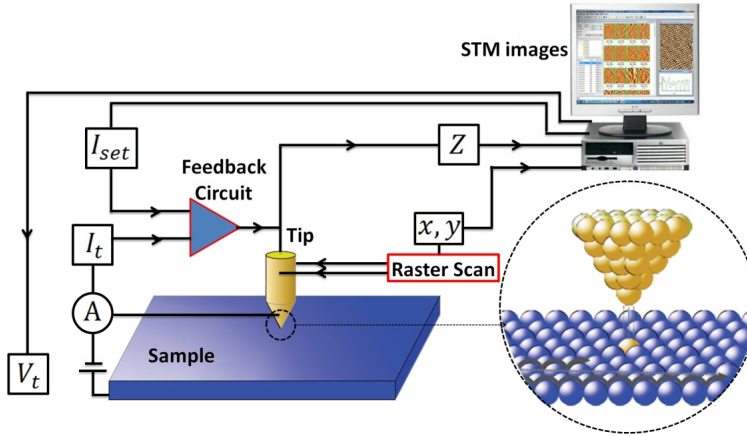


Figure 2.1: STM Operation Principle - Schematic drawing illustrating the operation principle of a fully computer controlled STM. Tip positioning with atomic precision is realized by piezoelectric elements. The current is recorded in a defined number of points while scanning the tip from left to right (gray lines in the zoomed view), but not during the fly-back to the next scan line (dashed line).

2.1.1.2 Theory of STM:

An exact theoretical treatment of the tunneling process in STM is virtually impossible for several reasons. It requires a detailed description of the sample and tip states and their evanescence into the tunnel gap; this is not feasible for a low symmetry object like the tip with mostly unknown shape and exact chemical composition^[19]. Moreover, the tip apex structure can even change in the course of an experiment. In a simple approach, the tunneling process in one dimension serves as an introduction to the concept of STM imaging. Assuming a constant potential barrier U in a region $0 < z < d$, the wavefunction

2.1 Analysis of the Surface Physical Structure:

$\psi(z)$ describing an electron with energy $E < U$ in the positive z direction, in a classically forbidden region is given by^[64]

$$\psi(z) = \psi(0) e^{-kz} \quad (2.1)$$

where $k = \sqrt{\frac{2m(U-E)}{\hbar}}$ is the wavevector, m is the mass of an electron and \hbar is the Planck's constant divided by 2π . Hence, the probability of observing an electron at the end of the potential barrier ($z=d$) is proportional to $|\psi(z)|^2 = |\psi(0)|^2 e^{-2kz}$.

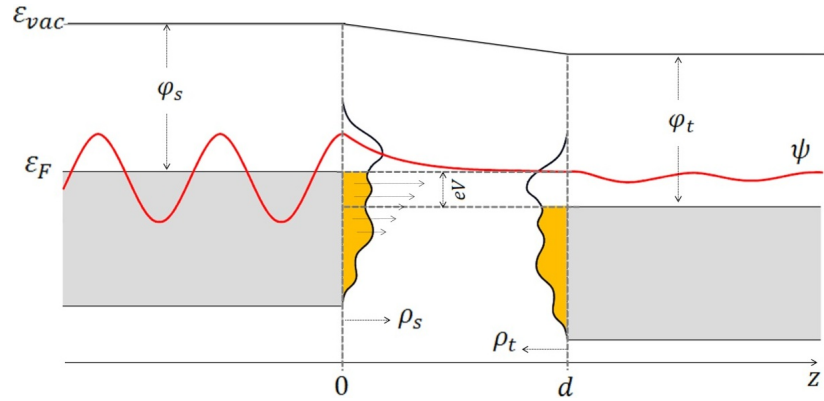


Figure 2.2: Density of States Mapping by STM - Schematic energy diagram for the sample-tip tunnel junction with a width d . A positive bias voltage V is applied to the tip, i.e. tunneling proceeds from occupied sample states to empty tip states (occupied states in the sample/tip are shaded grey). Tunneling is only permitted within the small energy interval eV . φ_s and φ_t are the (local) work function of the sample and the tip, respectively. The density of states ρ of the sample and the tip are sketched. The symbol ψ illustrates a wavefunction at the Fermi energy E_F that decays exponentially in the junction but still has non-zero amplitude at the tip position. The vacuum energy is denoted by E_{vac} . Adapted from Ref. [19]^[19].

This exponential decay in the barrier region is illustrated in Fig. 2.2. The simplistic theory presented above is not enough to explain all phenomena observed by STM. For example, by changing the applied bias from -2 V to +2 V in case of Si(7×7) reconstructed surface^[7,65] a completely different image is obtained, see Fig. 2.3. In this theory the current at a given energy is proportional to the product of the density of states (DOS) of the tip ρ_t and the local DOS (LDOS) of the sample ρ_s . The expression for the current, I , has the following form^[64,66]:

$$I(V, T, x, y, s) \propto \int_{-\infty}^{\infty} \rho_s(E, x, y) \rho_t(E - eV) \tau(E, V, s) \times [f(E - eV, T) - f(E, T)] dE \quad (2.2)$$

2. EXPERIMENTAL TECHNIQUES

where x and y are the lateral coordinates, f is the Fermi-Dirac function, T is the transmission probability, and τ is the transmission factor. The latter in general depends also on the parallel momentum but in a first approach it can be disregarded without losing any qualitative understanding. Then, the following simplified expression is obtained for the current:

$$I(V, T, x, y, s) \propto e^{-2s\sqrt{\frac{m}{\hbar^2\sqrt{2\bar{\phi}}}}} \int_{-\infty}^{\infty} \rho_s(E, x, y) \rho_t(E - eV) \times [f(E - eV, T) f(E, T)] dE \quad (2.3)$$

where $\bar{\phi} = \frac{\varphi_t + \varphi_s}{2}$ is the average work function.

According to this equation, the tunneling current will depend on: the tip-sample distance s (I depends exponentially on s), the applied bias eV , and the energy of the state (the higher the energy of the electron the lower the potential barrier and thus the higher the transmission probability. This is schematically shown in Fig. 2.2 by the length of the horizontal arrows)^[66].

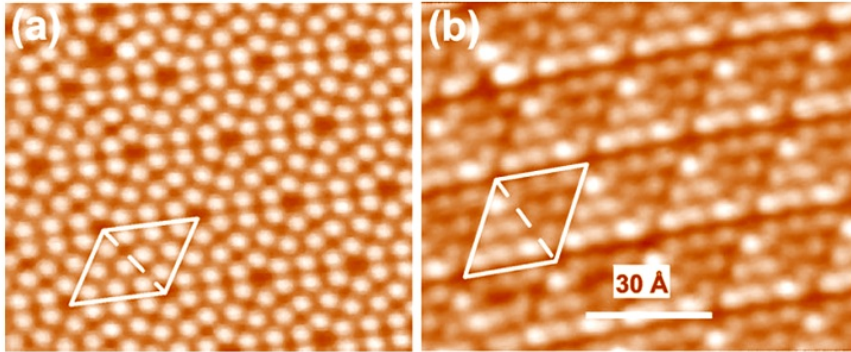


Figure 2.3: Si(111) Reconstruction - STM image of 7×7-reconstructed Si(111) surface taken at -2 V (a) and +2 V (b). Adapted from Ref. [65]^[65].

2.1.2 Low Energy Electron Diffraction (LEED):

Since its invention in 1927^[67], by Davisson and Germer, low energy electron diffraction has become a standard tool for the analysis of surface structure. In a LEED experiment, low energy electrons (10-500 eV) are used as a probe instead of the photons used in the more common x-ray diffraction. The ability to use low energy electrons for diffraction and their surface sensitivity originate from the correspondence between their wavelengths (0.5-1.5 nm) and the typical distances in crystals as well as the very

2.1 Analysis of the Surface Physical Structure:

short mean free path (few nanometers), respectively. There are two major applications for LEED. The first one is to learn something from the pure inspection of the surface diffraction pattern. One short LEED experiment gives immediate and direct information about the surface order and quality. When the surface is reconstructed, stepped or covered with periodically ordered adsorbates, the LEED images can quickly give some information about the surface symmetry and periodicities. The second application of LEED is the quantitative structure determination. In the present work, diffraction patterns were used to give, mostly, qualitative structural information.

The operating principles of a standard LEED setup are schematically illustrated in Fig. 2.4. A narrow beam of low energy electrons is incident on the surface at a given angle (mainly perpendicular) and the elastically backscattered electrons are then detected. The main components are thus, the electron gun to generate the incident electrons, and the detector to monitor the diffracted beams^[68]. Electrons can be generated either by on-axis -indirectly heated- cathodes, or by off-axis tungsten filaments. The effective diameter of the electron beam is ~ 1 mm and the energy spread is typically 0.5 eV. The sample holder should allow precise motion and rotation of the sample. The detector consists of three or four metal grids at different voltages and a fluorescent screen. The first grid (counted from the sample) is on ground potential to ensure a field free region around the sample. The next two grids are set to the so-called retarding voltage. This voltage is slightly lower than the kinetic energy of the electrons produced by the gun. The backscattered electrons pass through a retarding grid (G1) to stop inelastic electrons and later they are accelerated back (G2) to be collected in a fluorescent screen (S) which is set to a high positive voltage. Behind the screen there is a window in the vacuum system so that the diffraction pattern can be observed directly or recorded with a video camera.

The overall recorded picture is called the “*LEED pattern*” and the diffracted beams are referred to as “*LEED spots*” the brightness of which reflects the quality of the surface. A single LEED pattern gives a two-dimensional, $k_{\parallel}^{out} - k_{\parallel}^{in}$, section of the reciprocal space and is determined by a variety of surface properties, such as lattice constant, reconstruction, step arrays, the presence of adsorbates, or surface disorder^[69]. Here k_{\parallel}^{out} and k_{\parallel}^{in} are respectively the outgoing and incoming electron momentum

2. EXPERIMENTAL TECHNIQUES

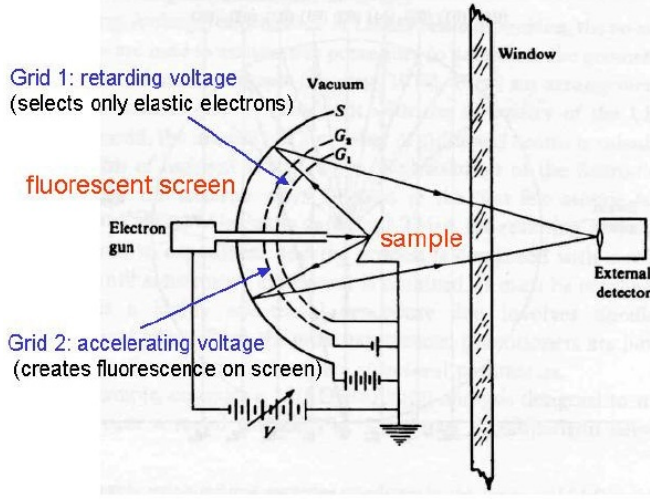


Figure 2.4: LEED Operation Principle. Operation principles of a standard LEED setup, side-view of LEED apparatus. Taken from Ref. [66]^[66].

parallel to the surface. Since the scattering theory is basically the same as for x-ray, the Ewald-construction, Laue's and Bragg's equations can also be applied for LEED.

For an illustrative example, let's consider the case of a surface consisting of a 1D linear monatomic step array (this is the case of the vicinal surfaces studied in chapter four). The surface geometry and the Ewald's construction are shown in Fig. 2.5(a). This diffraction plot of k_{\perp} versus k_{\parallel} is a graphic construction to determine the LEED pattern at different incident electron energies and angles^[66]. The vertical rods correspond to the two-dimensional (2D) reciprocal atomic surface lattice. They appear broadened due to the finite size of the terraces (yellow rods). Actually, the finite penetration of the electrons into the crystal modulates the rods in the vertical direction showing a maximum at the bulk reciprocal lattice points. These lateral and vertical modulations are represented in the figure as a color modulation. In the limit of infinite penetration, the rods should be replaced by the three-dimensional (3D) bulk reciprocal lattice points (white points). The dashed tilted lines form the reciprocal lattice of the step array, and the cigar-shaped rods correspond to the intersection of the latter with the atomic lattice rods, with their width representing the intensity of the intersected part of the rod. These are the zones where constructive interference takes place. Note that the step array defines a periodic lattice in the average surface, not in the terrace plane. For elastic scattering, all scattered momenta will have the same modulus as the incident momentum k^{in} and will therefore be contained in a circle of radius k , which depends on the energy as $\sqrt{\frac{2m^*}{\hbar^2 E_{kin}}}$. In order to match the scattered momenta with

2.1 Analysis of the Surface Physical Structure:

the diffraction pattern the specular reflection k_{00}^{out} must be connected with the (00) diffraction order. Once the Ewald's sphere is fixed, the intersection of this with the cigars will determine the LEED pattern. At the energy shown in the figure, the (00) and $(\bar{1}0)$ orders of the atomic lattice will show up as a single spot, while the (10) order is split into two spots. The distance between the split spots can be used to determine the terrace width^[66].

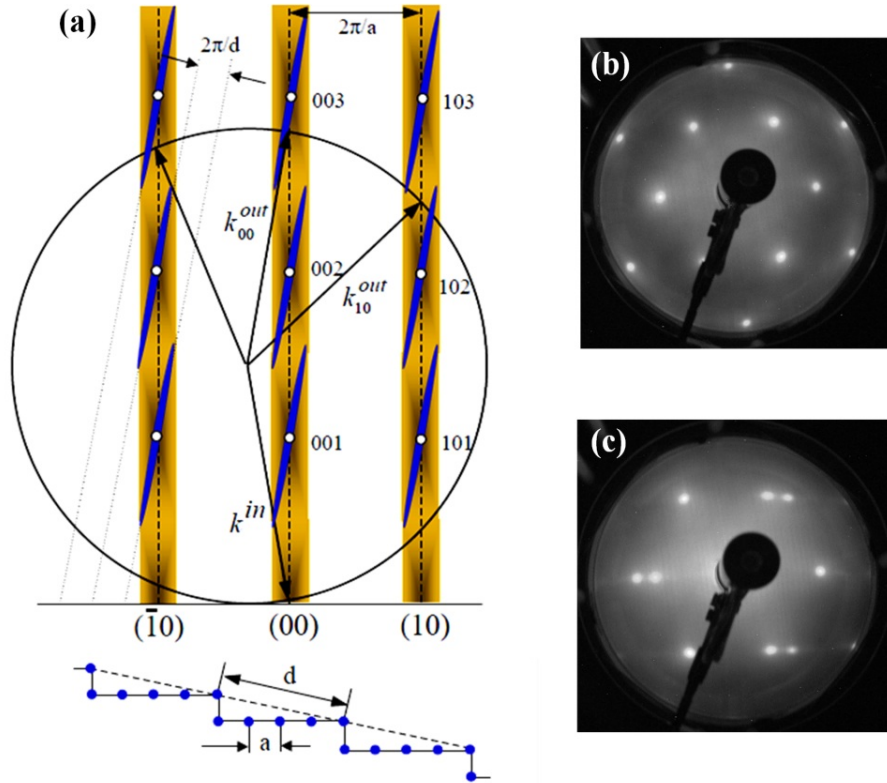


Figure 2.5: Ewald's Construction - (a) Ewald's construction for a LEED pattern of a surface with a regular step array. The vertical rods, broadened by the finite size of the terraces, correspond to the surface atomic lattice. The tilted cigars represent the intersected intensity between the step superlattice and the atomic lattice. The intersection of the cigars with the Ewald's sphere shows a single spot in the (00) and $(\bar{1}0)$ rod and a double (split) spot in the (10) rod. A schematic drawing of the surface geometry is shown at the bottom of (a) and the average surface is marked with a dashed line. Taken from Ref. [66]^[66]. LEED patterns of two points on the curved Ag(111) surface are shown: the point corresponding to the flat and vicinal surfaces are shown, respectively in (b) and (c). Electron energy in (b-c) was 60 eV.

2. EXPERIMENTAL TECHNIQUES

A typical LEED pattern of a curved Ag(111) surface is displayed in Fig. 2.5(b-c). Figure 2.5(b) shows the hexagonal pattern of the (111) planes of a typical *fcc* lattice. This is where the electron beam is sampling the flat part of the Ag(111) curved surface. The quality of the spots reflects the cleanness degree of the surface. As far as we scan the electron beam towards other parts of the sample rather than the flat one, a clear splitting of the spots, indicating the formation of a regular array of steps, takes place as seen in Fig. 2.5(c). The splitting direction can also be used to assign the direction perpendicular to the steps. The separation between the sub-spots is a measure of the step array periodicity, where the splitting is bigger for lower step-step separation. The quality of the sub-spots also is a sign of the regularity of the step array over a large scale. Coexisting 1 D periodicity, as those in faceted surfaces, results in additional spots and can be easily identified. Throughout the present work only vicinal surfaces, with no faceting phases, are mainly concerned.

2.2 Analysis of the Surface Electronic Structure:

Most of the properties that involve the low-energy electron excitations, such as those in metals, depend significantly on the “*electronic structure*” near the Fermi level and on the shape of their “*Fermi surfaces*”. The knowledge of these two properties is, thus, of obvious importance. Likewise, the measurement of such properties contains information about both the electronic structure and the shape of the Fermi surface. In metals, for example, direct information about the geometry of the Fermi surface can be extracted by experimentally following the behavior of some physical properties. Such experiments rely on the ability to construct a physical situation in which there is some interaction between the outside world and a selected group of electrons on the Fermi surface. These properties may be described as microscopic, direct, topological, or topographical properties; they include the various size effects, and the “*quantum oscillations*” in a variety of phenomena as a function of applied magnetic field, of which the best known are the de Haas-van Alphen and the Schubnikow-de Haas effects^[70]. The main difficulties associated with those methods, are the requirement of ultra clean, defect free samples, very low temperature, large sample size, and extremely high magnetic field. Moreover, the requirements of low temperature measurements limit those techniques to study only

2.2 Analysis of the Surface Electronic Structure:

materials that do not have phase transitions close to room temperature. One more disadvantage of those techniques is the ability of measuring only the electronic structure at the Fermi surface, but the rest of the band structure cannot be sampled^[9].

In general, solids can be characterized by two main types of properties, namely their vibrational (elastic) and electronic properties, which are intimately connected. In solids and due to the periodicity of the crystal, the phonon and electron excitations depend on an additional quantum number, namely the wave vector \mathbf{k} . In order to perform wave-vector dependent measurements one needs to work with exciting particles which can transmit or absorb wave vectors of the same magnitude as those present in a solid. Therefore, the optical techniques are no longer sufficient to scan the phonon or electron distributions over the whole Brillouin zone. In this case, the quantum numbers of individual electrons are not sampled and the techniques are integrated over the angle (momentum). Angle-integrated photoemission spectroscopy, even though, can directly measure the electronic density of states (DOS), but it is still integrating in angle and therefore information about the electron momentum is lost. The phonons dispersion curves have been first studied via the neutron diffraction technique. With respect to the electron dispersion curves the situation was different up to ~ 1980 , when the first electron dispersion curves were measured by ARPES^[9]. With ARPES the full set of electronic quantum numbers (except spin) can be obtained. ARPES has been developed further and now is the main tool to study the electronic dispersion curves, Fermi surfaces, and band structures of solids and solid surfaces^[10]. The use of ARPES is not necessarily restricted to low temperature measurements and the technique is not limited to the measurement of the Fermi surface, and hence different constant energy cuts are accessible together with the full band structure mapping.

In the subsequent sections, the basic principle, theory, as well as the capability of mapping the surface state band structure using ARPES will be explained.

2.2.1 Angle Resolved Photoemission Spectroscopy:

The photoelectron spectroscopy is based on the “*photoelectric effect*”, experimentally reported by Hertz in 1887^[71] and later explained by Einstein in 1905^[72] as a quantum phenomenon where the particle nature of light (photons) was proposed. For this reason Einstein was later awarded the Noble price in physics in 1921. In his derivation, the

2. EXPERIMENTAL TECHNIQUES

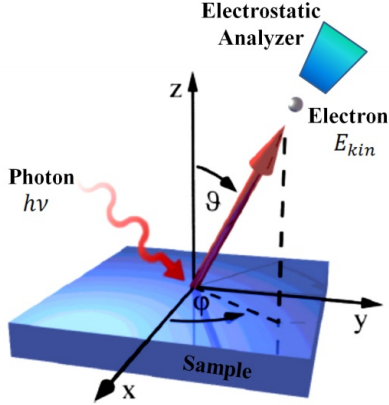


Figure 2.6: Principle of Photoemission. Principle of photoemission. It consists mainly of a photon source, a sample to be investigated and an electrostatic analyzer. Taken from Ref. [74] [74].

relationship between the photon energy $h\nu$ and the maximum kinetic energy E_{kin}^{max} of the photoemitted electrons, i.e. the fundamental photoelectric effect equation, was found to be

$$E_{kin}^{max} = h\nu - \varphi_o \quad (2.4)$$

where φ_o is a characteristic constant of the sample surface which is defined as the work function.

Nowadays, a photoemission experiment for spectroscopic purposes is basically performed in the same way as reported by Hertz. Monochromatized photons, either vacuum ultraviolet (VUV) light, x-ray light, or monochromatized synchrotron radiation, are directed on a sample, and the photoelectrons, liberated by the photoelectric effect, are analyzed with respect to their kinetic energy and/or emission angle using an electrostatic analyzer [73], Fig. 2.6. Depending on the photon energy used in the photoemission experiment, one usually distinguishes two different kinds of spectroscopies, namely x-ray photoemission spectroscopy (XPS) and ultraviolet photoemission spectroscopy (UPS, ARUPS, or ARPES), when x-ray and ultraviolet radiation, respectively, are used. XPS provides the investigation of the core-level states at high binding energies and is, therefore, sensitive to the chemical composition. ARPES, on the other hand, investigates the valence band states and the electronic structure. One major advantage of photoemission spectroscopy is the short escape depth of the photoemitted electrons (few Å for the range of the kinetic energies relevant for photoemission experiments), which renders the technique being surface sensitive and, thus, well suited to map the electronic properties of surfaces, surface alloys, thin films, etc.

2.2.1.1 Photoemission Theory:

The interaction of the electrons with an oscillating electromagnetic wave field $\mathbf{A}(\mathbf{r}, t)$ is described by the canonical replacement of the momentum operator \mathbf{p} by $\mathbf{p} + \mathbf{A}$ [9,73]. Assuming that the spatial variation of the light field is small on an atomic scale, the resulting perturbation to the original Hamiltonian is $H_{int} = \mathbf{A} \cdot \mathbf{p}$. According to Fermi's Golden Rule the transition rate between the initial and final one-electron states $|i\rangle$ and $|f\rangle$ with energies E_i and E_f , respectively, can now be written as

$$\omega_{i \rightarrow f} \propto |\langle f | \mathbf{A} \cdot \mathbf{p} | i \rangle|^2 \delta(E_f - E_i - h\nu) \quad (2.5)$$

The situation is the same for a solid with a lattice-periodic potential, where the quantum numbers i and f are replaced by the Bloch vectors \mathbf{k}_i and \mathbf{k}_f for the initial (occupied) and final (empty) state, respectively. The total photocurrent can therefore be written as

$$I_{abs} \propto \sum_{\mathbf{k}_f, \mathbf{k}_i} |\langle \mathbf{k}_f | \mathbf{A} \cdot \mathbf{p} | \mathbf{k}_i \rangle|^2 \delta(E_f - E_i - h\nu) \quad (2.6)$$

In an ARPES experiment, free photoelectrons of specified energy E and momentum \mathbf{K} (in vacuum) are measured. This means that only absorption into final states with $E = E_f$ is detected. The momentum component parallel to the surface is a conserved quantity (except for a surface reciprocal lattice vector $\mathbf{G}_{||} : \mathbf{K}_{||} = \mathbf{k}_{f||} - \mathbf{G}_{||}$). This is not the case for the perpendicular component k_{\perp} due to the potential barrier at the surface. The photoelectron current can then be expressed as

$$I(\mathbf{K}, E) \propto \sum_{\mathbf{k}_f, \mathbf{k}_i} |\langle \mathbf{k}_f | \mathbf{A} \cdot \mathbf{p} | \mathbf{k}_i \rangle|^2 \delta(E_f - E_i - h\nu) \delta(\mathbf{K}_{||} - \mathbf{k}_{f||} - \mathbf{G}_{||}) \delta(E - E_f) \quad (2.7)$$

Due to the Bloch form of the one-electron wavefunctions the matrix element in the above equation also conserve the momentum (except for a reciprocal lattice vector \mathbf{G}):

$$|\langle \mathbf{k}_f | \mathbf{A} \cdot \mathbf{p} | \mathbf{k}_i \rangle|^2 = |\mathbf{M}_{if}|^2 \delta(\mathbf{k}_f - \mathbf{k}_i - \mathbf{G}) \quad (2.8)$$

where $|\mathbf{M}_{if}|^2$ is the residual matrix element. Hence the expression for the photoemission current can be written as

$$I(\mathbf{K}, E) \propto \sum_{\mathbf{k}_f, \mathbf{k}_i} |\mathbf{M}_{if}|^2 \delta(E_f - E_i - h\nu) \delta(\mathbf{k}_f - \mathbf{k}_i - \mathbf{G}) \delta(\mathbf{K}_{||} - \mathbf{k}_{f||} - \mathbf{G}_{||}) \quad (2.9)$$

2. EXPERIMENTAL TECHNIQUES

This is actually the expression derived from the frequently used three-step model^[74,75], illustrated in Fig. 2.7. The model assumes three discrete steps as follows. A photon is absorbed and excites an electron in the solid from an initially occupied state to an unoccupied temporary state. This excited electron is then scattered by the ions and eventually arrives at the surface of the solid. At the surface the excited state penetrates through the surface into the vacuum^[76]. Those three steps are clearly described in the photoemission current expression, where the first two δ -function takes care of the energy and (parallel) momentum conservation during the photoexcitation deep in the solid, and the last two δ -functions consider the energy and momentum conservation at the solid-vacuum interface. Using this expression, the initial state band dispersions can be mapped out using the energy and momentum of the photoelectrons measured in an ARPES experiment.

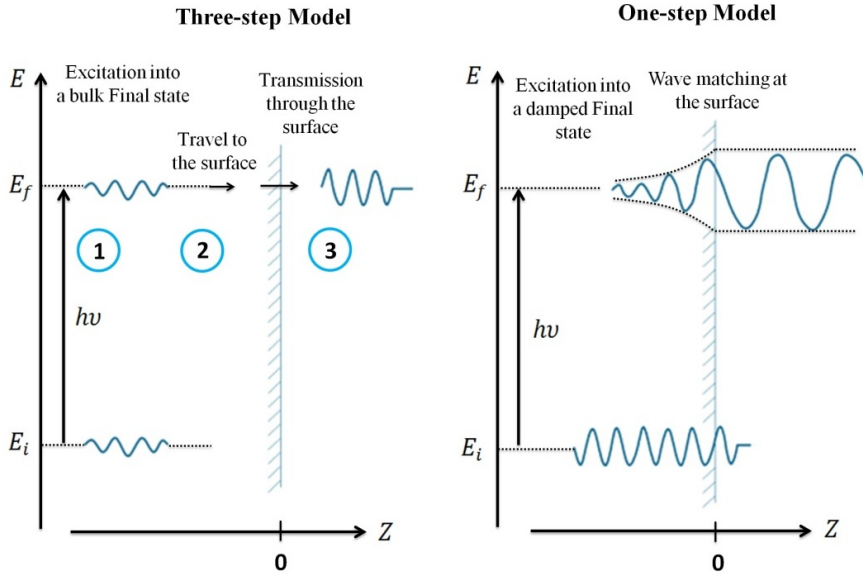


Figure 2.7: Three and One-Step Models - Pictorial representation of three-step and one-step model description of the photoemission process. Adapted from Ref. [77]^[77].

2.2.1.2 Band Mapping with ARPES:

In ARPES experiment, like the one shown in Fig. 2.6, a photon with energy $h\nu$ is shined to the sample and the emitted electrons are analyzed with respect to their kinetic energy (E_{kin}) and emission angle (θ). Rewriting Equ. (2.4), the binding energy

2.2 Analysis of the Surface Electronic Structure:

(E_B) is related to the kinetic energy via the equation.

$$|E_B| = h\nu - \varphi_o - E_{kin} = E_F - E_i = E_{vac} - h\nu - E_i = E_{vac} - E_i \quad (2.10)$$

where E_i, E_f, E_{kin}, E_F , and E_{vac} are respectively, the initial, final, Kinetic, Fermi, and vacuum energy. Throughout the thesis all the energies inside the crystal will be referred to the Fermi level, unless specified. The components of the parallel momentum are related to the emission polar angle (θ) and the azimuthal angle (ϕ) via the equation.

$$(k_{||x}, k_{||y}) = \sqrt{\frac{2mE_{kin}}{\hbar^2}} (\sin(\theta)\cos(\phi), \sin(\theta)\sin(\phi)) \quad (2.11)$$

Usually, in the ARPES experiment, one fixes a surface axis to the emission azimuthal direction to obtain the simplified form;

$$(k_{||x}, k_{||y}) = \sqrt{\frac{2mE_{kin}}{\hbar^2}} \sin(\theta) = 0.512 \sqrt{E_{kin}} \sin(\theta) \text{\AA}^{-1} \quad (2.12)$$

For 2D states, such as the surface states of noble metals explained in appendix A, and by measuring E_{kin} as a function of θ , E_B and $k_{||}$ can easily be calculated and hence the initial state band dispersion comes out^[78]. In order to map the Fermi surface and the initial state full band structure, E_{kin} as a function of θ has to be measured for different ϕ . For 3D bulk states, on the other hand, the measurement of the initial state band structure is more complicated. Due to the presence of a surface, the perpendicular component of the moment is not preserved. Qualitatively, the bulk state can be identified by its dispersion as a function of the photon energy (for the same $k_{||}$, changing the photon energy only changes the k_{\perp} component involved in the photoemission) used for the measurement. This is shown schematically in Fig. 2.8. Clearly, a surface state has to keep its binding energy fix while it disperses in the case of bulk state^[76].

Moreover, the bulk state dispersion can be quantitatively mapped if certain assumptions are made. Even though, the expression for the photocurrent in Equ. (2.9) does not, explicitly, include the perpendicular component of the momentum k_{\perp} of the initial state wave vector, it can be determined from the assumption of free electron-like states that at the surface have to cross a potential barrier of height V_o :

$$E = \frac{\hbar \mathbf{K}^2}{4\pi m} = E_f = \frac{\hbar \mathbf{k}_f^2}{4\pi m} - V_o \quad (2.13)$$

2. EXPERIMENTAL TECHNIQUES

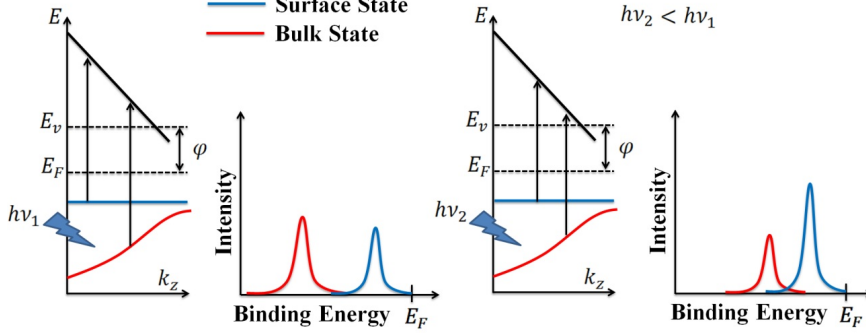


Figure 2.8: Surface vs. Bulk in ARPES - Schematic representation of ARPES ability to identify surface and bulk states. Adapted from Ref. [76]^[76].

where $\mathbf{k}_f = \mathbf{k}_i$ (neglecting \mathbf{G}). Here V_o , or m , is treated like a fit parameter to obtain the expected periodicity of the resulting dispersion in the reciprocal lattice. This model is only valid for isotropic free electron-like materials^[75].

2.2.1.3 Modes of Photoemission Data Acquisition:

The most common type of ARPES data representation is an “*Energy Distribution Curve*” (EDC). In EDC mode, the number of photoemitted electrons is measured as a function of the kinetic energy (at fixed photon energy). Energy conservation implies that different initial energies are sampled, see Fig. 2.9. A family of such EDC curves at closely spaced emission angles (or photon energy) could map out the dispersion of the initial state as well as the life time of the initial and final hole and electron, respectively. As the photon energy is kept constant, conventional UV lamps can be used as the light source. In principle, all the information from the photoemissive properties of a sample for a given geometry is implicit in such EDC data set. However, detailed amplitude differences in adjacent EDC’s are difficult to extract.

Taking advantage of the smooth stable Synchrotron radiation continuum and the possibility of scanning the photon energy continuously, two new modes of experimental procedure for ARPES have been devised^[79]. These are the “*Constant Final State*” (CFS) and “*Constant Initial State*” (CIS) spectra, depicted in Fig. 2.9. In the CFS spectrum, one scans the photon energy, while fixing the energy window of the analyzer (the kinetic energy). Using energy conservation, the CFS spectrum can be re-plotted as, the photoemission intensity as a function of initial state E_i energy for a

2.2 Analysis of the Surface Electronic Structure:

fixed final state E_f . By examining a family of CFS's, the initial energy and photon energy peaks can be distinguished if the peaks has a given E_i or $h\nu$, respectively. Using CFS's mode, one can observe how various different initial states couple to the same final energy and for ARPES, fixing E_f makes $K_{||}$ a constant for the spectrum.

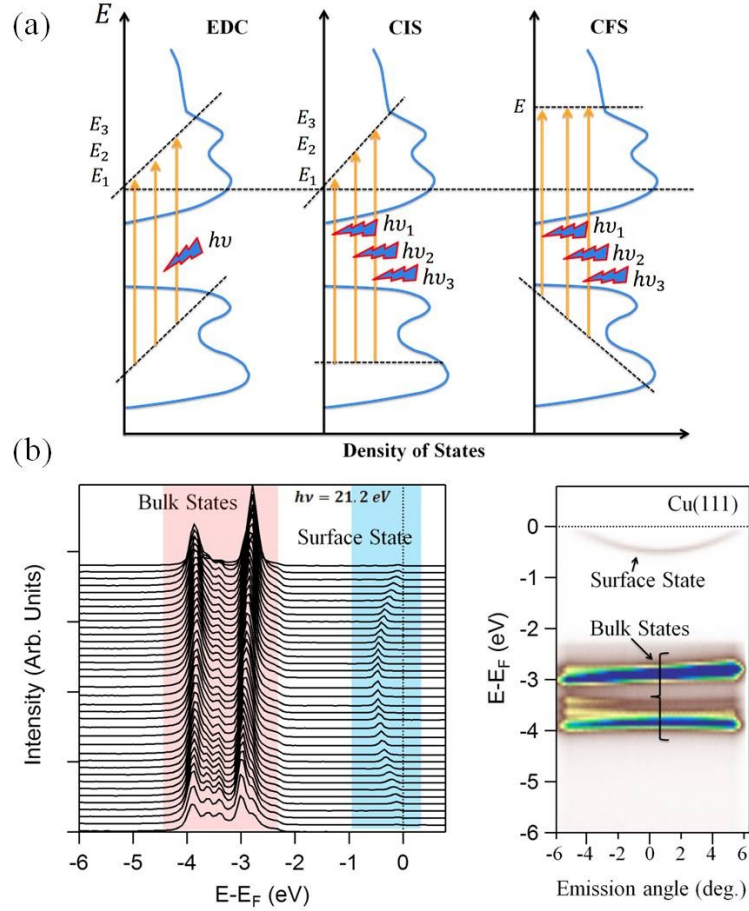


Figure 2.9: Acquisition Modes in ARPES - (a) Photoexcitation process in the three types of photoemission spectra EDC, CIS, and CFS. Adapted from Ref. [80,81]^[80,81]. (b) Right: EDC series of the Cu(111) crystal each of which corresponds to an emission angle. Left: 2D photoemission intensity plot showing the energy vs. emission angle for the Cu(111) crystal. The surface and bulk states are shown in both plots.

In CIS mode, both the photon energy and the energy window of the analyzer are synchronously scanned. Using energy conservation, the CIS spectra can be re-plotted as the photoemission intensity as a function of $h\nu$ for a fixed E_i , and similarly, CIS peaks can be classified as final energy or photon energy peaks. Hence the CIS mode

2. EXPERIMENTAL TECHNIQUES

provides one with a final state spectroscopy. In the present work, unless specified, all data have been collected while the photon energy is fixed and the energy window of the analyzer is scanned, i.e., in the EDC mode. Figure 2.9(b) depicts an example for an EDC series for different emission angles (left) and the corresponding 2D (energy vs. angle) plot (right) for a Cu(111) crystal. The dispersing feature close to the Fermi level is the Shockley surface state, whereas states at higher binding energies all belong to the less dispersive bulk d -bands.

2.2.1.4 Photoemission Line Width and Life Time:

Within the framework of the three-step model, the sudden approximation has been used, where the electron transition step is decoupled from the propagation to the surface ignoring the possible relaxation that might occur during the photoexcitation process^[75]. This approach, thus, ignores the fact that the photoemission process has to be described as one coherent excitation (one-step model) that involves excitation into a damped state in order to match the wavefunction at the interface between the solid and vacuum, as illustrated in Fig. 2.8. Furthermore, the conservation law's delta functions derived in Equ. (2.9), are suitable for non-interacting electrons, and do not include information regarding the interaction between electrons and other elementary excitations within the solid, such as phonons, plasmons, etc. Therefore, photoemission current expression in Equ. (2.9) needs a new treatment to explore such many-body-effects^[77,80]. The photoemission current including the effect of the $(N-1)$ electrons relaxation can be written as

$$I(K, E_{kin}, T) \propto \sum_{k_f, k_i} |M_{if}|^2 A(\hbar\nu - E_{kin} - \phi, k_{||}, T) \quad (2.14)$$

Where A is called the hole spectral function and describe the influence of relaxation of the remaining $(N-1)$ electrons on the current. In case of non-interacting electrons, A is the delta function with infinite hole life time. The many body interactions, however, broaden and shift the energy of A . The shift and broadening effects can be included by defining a complex energy, namely the “*self-energy*” $[\Sigma(k, E, T) = \Sigma' - i\Sigma'']$, where its real part renormalizes the energy compared to the bare dispersion and its imaginary part accounts for the induced broadening to the non-interaction delta-like spectral function. One can, in a similar way, define a complex momentum perpendicular to

2.2 Analysis of the Surface Electronic Structure:

the surface to account for the broadening due to the uncertainty of k_{\perp} . The later is only relevant for 3D states, which are not the subject of the present work. The photoemission intensity from a 2D system can, then, be given by;

$$I(\mathbf{K}, E_{kin}, T) \propto \sum_{k_f, k_i} |\mathbf{M}_{if}|^2 A(h\nu - E_{kin} - \phi, k_{||}, T) f(h\nu - E_{kin} - \phi, T) \quad (2.15)$$

where f is the Fermi distribution. Thus, the photoemission current is given by the shape of the hole-spectral function convoluted with the Fermi function. The spectral function itself is related to the imaginary part of the single-particle Green's function and is given by;

$$A(k, E) = \frac{\Sigma''}{\pi[E - E_o - \Sigma']^2 + [\Sigma'']^2} \quad (2.16)$$

where E_o is the bare particle dispersion (i.e., no many body interactions). Therefore, the spectral function, and hence the photoemission intensity profile, has the form of a 2D Lorentzian function for small variations of the self-energy. The finite energy resolution induces extra broadening to the spectral function and can be accounted for by convoluting the spectral function with a Gaussian. The finite angular resolution together with momentum broadening due to scattering to adsorbates, induce some asymmetry in the otherwise pure Lorentzian spectral shapes. The self-energy components contain the effect of the many-body interaction on the shape of the spectral function and, for a fixed k and T , are given by $\Sigma'' = \frac{FWHM}{2}$ and $\Sigma' = E_0 - E$, where $FWHM$ is the full width at half maximum and E is the peak position of a given EDC. The quasiparticle (i.e. the electron dressed with all possible many-body interactions) life time is related to the $FWHM$ of the photoemission peaks and is given by $\tau = \frac{\hbar}{FWHM}$. The three main contribution to the $FWHM$, and hence τ , are the electron-electron ($FWHM_{e-e}$), electron-phonon ($FWHM_{e-ph}$), and electron-impurity ($FWHM_{imp}$) scattering. The total $FWHM$ is, thus, given by;

$$FWHM = FWHM_{e-e} + FWHM_{e-ph} + FWHM_{imp} \quad (2.17)$$

A detailed description of the contribution and the signature from each of those scattering sources will be given in line with the results and discussion of the low temperature measurements on the undoped and Au doped Ag/Cu(111) system in chapter three.

2. EXPERIMENTAL TECHNIQUES

Part II: Experimental Setup

2.3 General Aspects of the Experimental Setup:

The key-ingredient to surface science experiments is “*ultra-high vacuum*” (UHV). This means pressures in the 10^{-9} mbar range and below. Only such low pressure assures that a surface stays clean for a time long enough to perform some experiments. In order to achieve such UHV a set of vacuum pumps are commonly used, that is a roughing pump ($\sim 10^{-3}$ mbar), a combination of a turbomolecular pump ($\sim 10^{-9}$ mbar), an ionic pump ($\sim 10^{-10}$ mbar), and a titanium sublimation pump ($\sim 10^{-11}$ mbar). In order to reach a low pressure in a short time it is necessary to perform the so-called bakeout of the whole vacuum system. During the bakeout, the system is heated to at least $100 - 200^\circ\text{C}$ for an extended period of time (24 *h* or more). The heating causes a fast removal of the impurities adsorbed on the walls of the vacuum system (mostly water). The need for baking systems renders working with UHV chambers rather time-consuming. It also requires that the system is built only of components which can withstand high temperatures for a long period of time^[31]. The next consideration is how to obtain clean surfaces. There are various ways of doing so, the most common are; cleavage of the bulk crystal, heating, ion bombardment (sputtering) with noble gas ions (Ne^+ or Ar^+), *in-situ* chemical treatment, etc^[31,76]. Therefore, the ARPES and STM apparatus have to be supported by a UHV preparation chamber where the samples can be cleaned. In the present work, repetitive cycles of sputtering followed by annealing were used for this purpose.

2. EXPERIMENTAL TECHNIQUES

2.4 General Aspects of Samples Preparation:¹

The clean noble metal substrates used throughout the full thesis were, mainly, flat and curved Cu(111) single crystals. The metal atoms or layers investigated on top of those substrates were sub-monolayer up to one and/or two monolayers of Ag, sub-monolayer up to multilayers of Au, and a mixture of both Ag and Au on top of the Cu substrates. The description of those metallic systems and the control parameters of deposition will be stated in their corresponding chapters.

2.4.1 Substrate Preparation:

The curved Cu (Mateck GmbH, Germany) were mechanically polished defining $\alpha = \pm 15^\circ$ cylindrical section (11.6 mm radius) around the [111] direction with the ($\alpha = 0^\circ$) line pointing towards the $[1\bar{1}0]$, see Fig. 2.10 for details. Left and right sides of the crystal correspond to A-type ($\{100\}$ oriented microfacets) and B-type steps ($\{111\}$ microfacets), respectively (Fig. 2.10). Each point on the curved crystal should correspond to a vicinal surface, with a terrace width that systematically depends on the miscut angle α . The description of such curved crystals is detailed elsewhere^[43,44,82,83] and will be further discussed in chapter 4. Due to its relatively small size, this substrate is the one used in the STM chamber (due to its local scanning) and in the ARPES setup at the Synchrotron Radiation Center (SRC) (because of the small light spot, $< 100 \mu\text{m}$). A flat Cu(111) ($15 \times 15 \text{ mm}^2$) was used for ARPES measurements in the NanoPhysics Lab. The substrates are cleaned in vacuum following the standard ion (Ne^+ and Ar^+ in ARPES and STM setups, respectively) sputtering/annealing cycles.

The energy of the ions was adjusted to be between 800 eV and 1000 eV depending on the type and quality of the crystals. In case of curved surfaces, ion sputtering is carried out with the incidence plane parallel to the surface steps in order to minimize surface damage. The annealing process for all samples is conducted at a temperature of 700 K - 800 K.

¹The general aspects of sample preparation presented here are completely different for the topological insulator samples discussed in the last chapter. For this reason, the sample preparation for the latter will be stated completely in their corresponding chapter.

2.4 General Aspects of Samples Preparation:

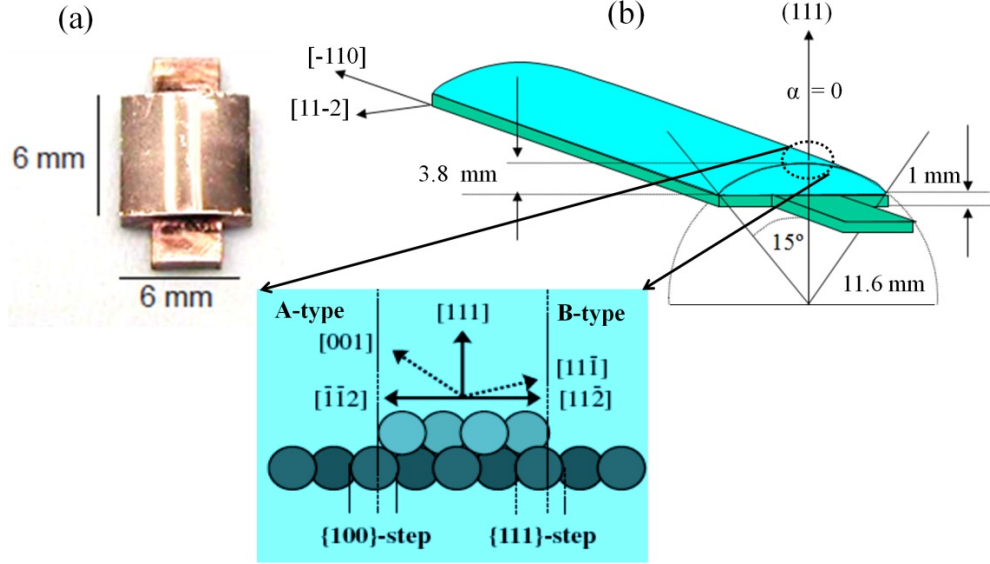


Figure 2.10: The Curved Crystal - A real top view of the curved Cu(111) crystal (a) and the corresponding schematic description of the crystal parameters and orientations (b). The zooming of (b) explains the different step type at different side of the crystal.

2.4.2 Metal Deposition:

The metallic atoms and layers were deposited on top of the previously mentioned clean surfaces by means of simple physical vapor deposition method. For this purpose a homemade evaporator has been constructed, see Fig. 2.11(a).

The metal atoms, namely Au and Ag, in the form of balls or pieces of wires were inserted into a molybdenum crucible and were evaporated by electron bombardment of the crucible. For this purpose the crucible was put to a positive high voltage (typically 800 -1000 V) between the crucibles containing the metal pieces and a resistively heated filament attached in the vicinity of the crucible, Fig. 2.12(b). Once the evaporation conditions are reached (a stable flux for long enough time), the clean metal substrate of interest is rotated to face the evaporator. The coverage rate was controlled by either the evaporation parameters (voltage and filament current) or by the evaporation time. It was also possible to cool the substrate down to the temperature of liquid Nitrogen while evaporating. Both STM and ARPES preparation chambers are supported by a quartz microbalance (QMB) which was used as a first rough estimation for the coverage. Moreover, in STM the average value of the coverage was estimated from large scale

2. EXPERIMENTAL TECHNIQUES

STM images using the floating area algorithm as a feature of the WSXM software^[84]. In ARPES experiments, however, the coverage was determined from the well known ARPES signal of the 1 ML Ag/Cu(111) system. Since all metal crucibles are very close to each other, one can use the calibrated Ag evaporator and the QMB to further calibrate the Au source by changing only the density in the QMB. This issue will be explained later with an example.

In NanoPhysics lab and SRC ARPES chambers, the possibility of growing a wedge of the despite metal is facilitated by the presence of a shutter facing the evaporator. By computerized motors, the sample can be moved in a controlled way in front of the evaporator and wedges from sub- to multilayers of the metals have been grown this way, see Fig. 2.11(c).

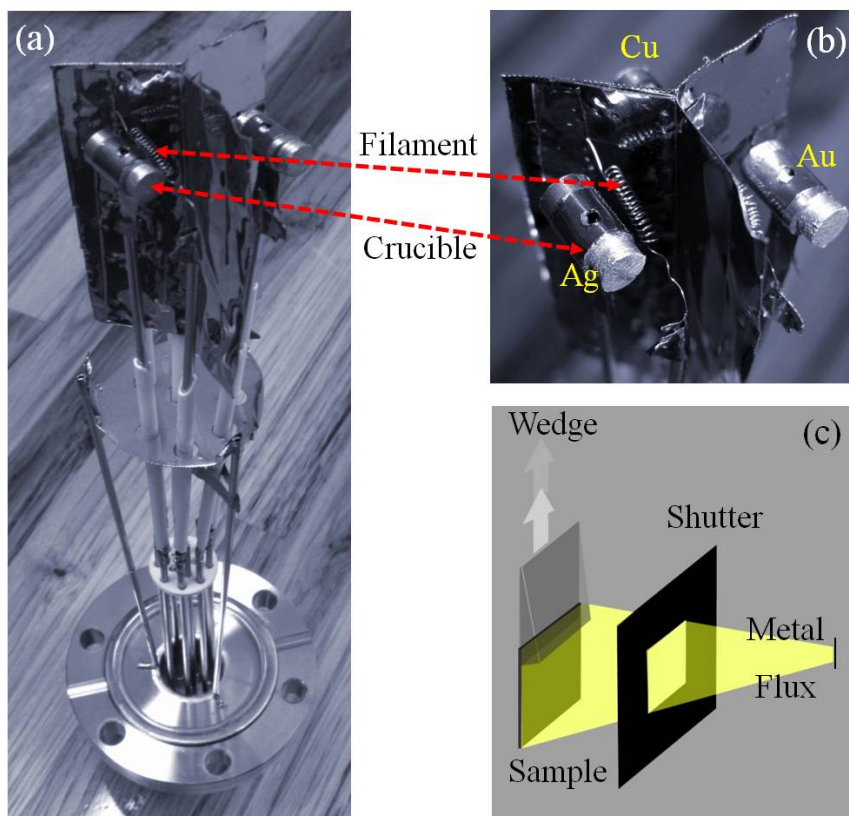


Figure 2.11: The Metal Evaporator and Wedge Preparation - (a) A real view of the home made evaporator used in this work. (b) An enlarged view showing the filaments and crucibles. (c) Schematic representation of the wedge growing process.

2.5 Data Acquisition:

2.5.1 Scanning Tunneling Microscopy:

The local surface structure of the investigated systems is determined using Omicron variable temperature STM, and the cleanliness of the surfaces in macroscale was ensured by LEED. Figure 2.12 shows a real view of our STM setup with its preparation and main chambers. The main chamber contains the STM head and the LEED apparatus, Fig. 2.12(b). The samples are transferred from the preparation chamber to the STM head, shown in Fig. 2.12(c); via a transfer rod and wobble stick. The acquired STM data have been analyzed using the WSXM software^[84]. However, before even acquiring the data and going to any further analysis, the STM has to be calibrated laterally and vertically.

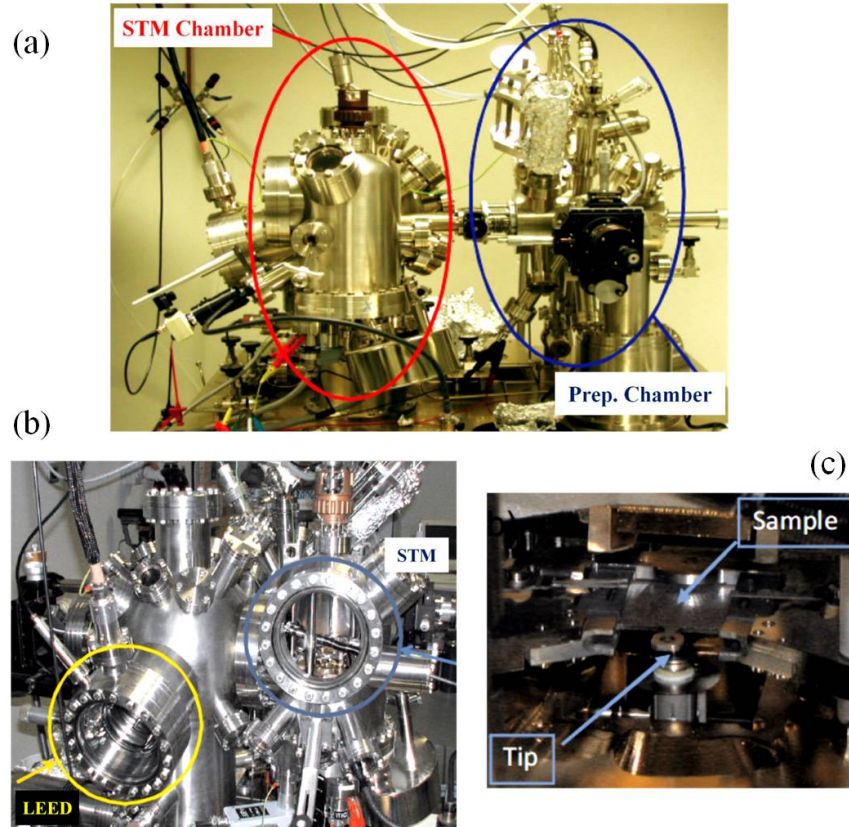


Figure 2.12: Our STM Setup - (a) View of our 10^{-11} mbar UHV VT-STM (Omicron). The main chamber consists of the STM head and the LEED apparatus (b). The position of the sample and the tip inside the STM head are shown in (c).

2. EXPERIMENTAL TECHNIQUES

For this purpose, a Si(111) wafer has been cleaned enough till the 7×7 reconstruction was clearly observed by LEED. Therefore, the periodicity for such well known reconstruction was used to calibrate laterally the STM. In order to calibrate the STM vertically, an image containing a step must be acquired. STM measurements of the clean 7×7 reconstructed Si(111) are shown in Fig. 2.13. The lattice parameter and the step height were found to be 2.688 nm and 0.306 nm, respectively. The very same values are reported in the literatures^[85–87].

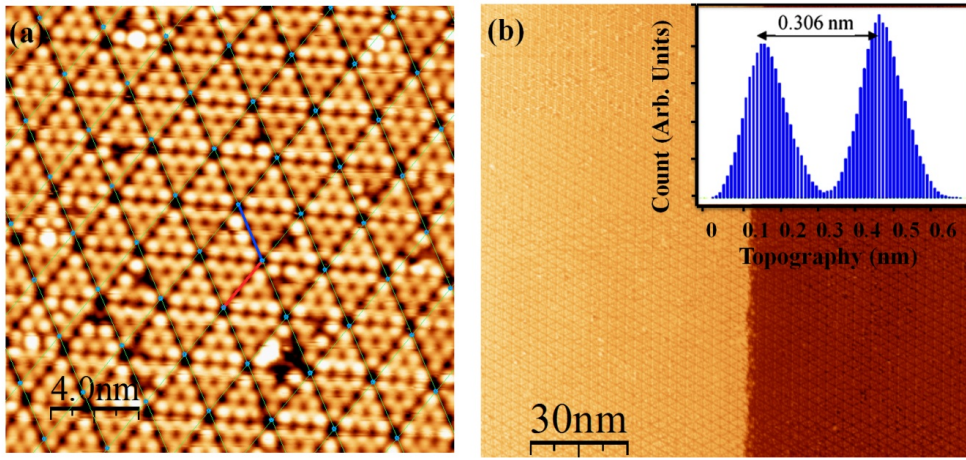


Figure 2.13: STM Calibration - STM images of the 7×7 -Si(111) reconstructed surface taken at flat terrace (a) and near a step (b). The image shown in (a) is used for the lateral calibration of the STM. The inset in (b) shows a histogram of the topography along the step shown in Fig. 2.7(b), where the step height being estimated (peaks separation) and the vertical scan is calibrated accordingly.

2.5.2 Angle Resolved Photoemission Spectroscopy:

Three different ARPES setups are used throughout this work. A more detailed description will be devoted to the ARPES setup at the Nanophysics laboratory. The other two setups are located at the Synchrotron Radiation Center (SRC) in Wisconsin-Madison, USA and at ASTRID, Aarhus, Denmark. The main difference between the three setups lies on the light source being used and the type of the electron analyzer. Therefore, these two aspects will be highlighted in each subsection.

2.5.2.1 ARPES at Nanophysics Laboratory:

The ARPES setup at Nanophysics laboratory (San Sebastian/Donostia, Spain) consists mainly of two connected UHV-chambers: the main chamber, with the electron spectrometer and the light source, and the preparation chamber for sample preparation. A view of our ARPES setup is shown in Fig. 2.14(a-c). The zoom in Fig. 2.14(b) (right) highlights the UV-lamp components and its position with respect to the analyzer. The substrates were mounted on a manipulator with four degrees of freedom; X, Y, Z, and rotation (θ) around the manipulator axis. The movements of the manipulator in the four degrees of freedom are fully motorized. The manipulator contains up to three samples which have to be manually mounted; these are shown in Fig. 2.14(b) (right). Therefore, the replacement of the samples requires a break of the vacuum in the preparation chamber. The transfer of the samples between the two chambers is done by moving the manipulator into the main chamber through a valve separating both chambers. In addition to the electron spectrometer and the light source, the main chamber is equipped with a LEED apparatus. This allows a check of the sample quality and, in some cases, the exact surface structure. Three different cameras are mounted on the main chamber windows, two of them are intended for the safer transfer of the manipulator to the main chamber and the other one is to collect the LEED data. Two diode-lasers are mounted on windows in the main chamber which make it possible to position the sample in the center of the chamber and in the focal point of the electron spectrometer. The manipulator is equipped with a closed cycle He-refrigerator. This allows cooling of the sample down to ~ 25 K. The temperature of the sample is measured via a C-type thermocouple attached to the sample holder plate.

The sample preparation procedure consists of the sputtering and a successive annealing of the sample. The latter process is necessary to “*heal*” the roughness induced by the sputtering. The annealing process was achieved by electron bombardment from a filament mounted behind the sample towards the positively charged sample. In the preparation chamber there is also the ion gun for sputtering the sample with noble gas ions and several flanges available for mounting different equipments like metal or molecular evaporators etc. The preparation chamber is also supported by a quartz microbalance (QMB) for calibrating the rate of evaporation. The QMB and the evaporators are continuously cooled down by water to allow thermal stability. The prepa-

2. EXPERIMENTAL TECHNIQUES

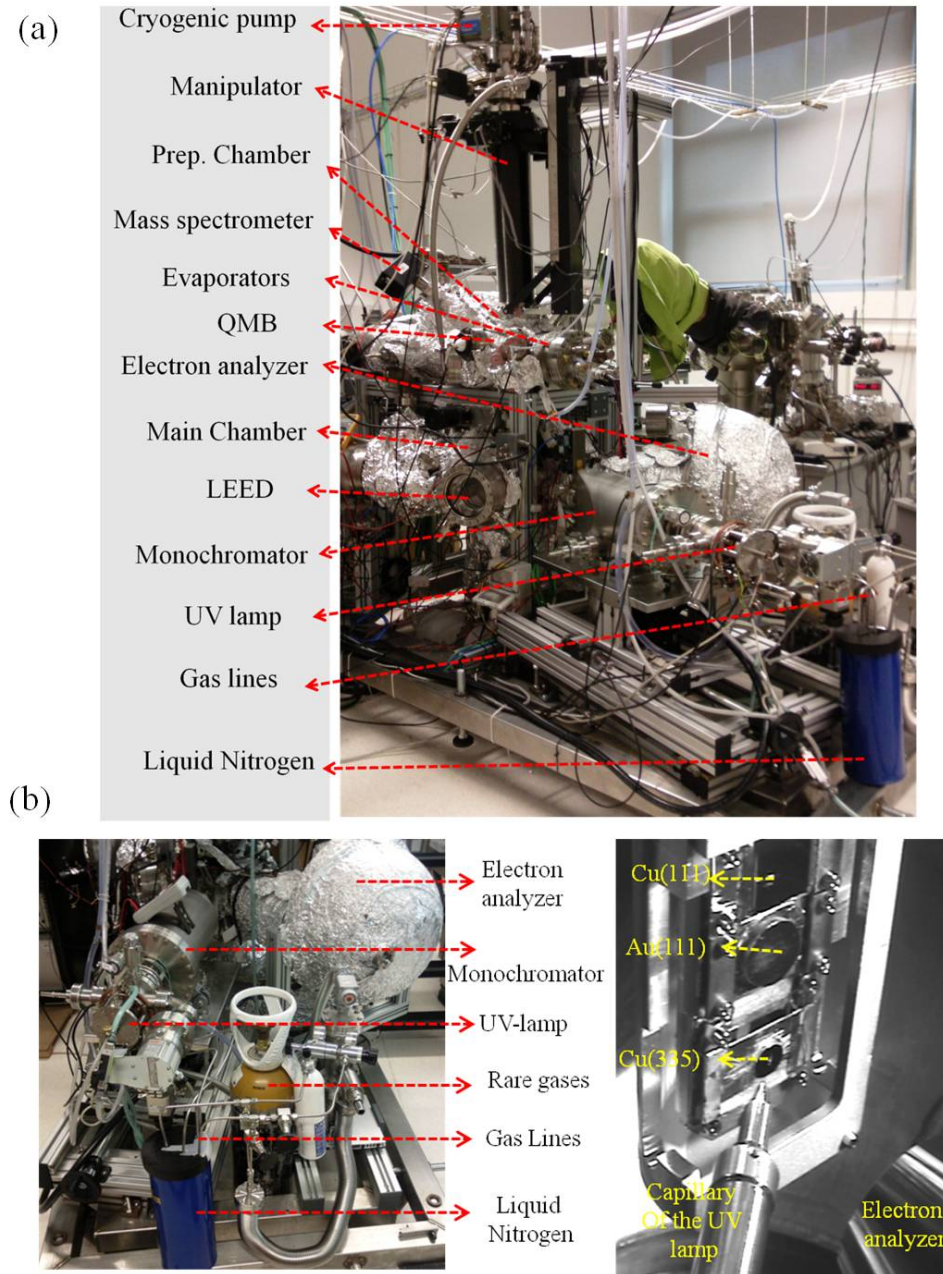


Figure 2.14: Our ARPES Setup - (a) View of the ARPES setup at Nanophysics laboratory. (b) Left: Closer external view showing the main component of the ARPES experiment (the light source and the analyzer), Right: Inner view in the main chamber showing the three available samples at the end of the manipulator and its position with respect to the light capillary and the entrance slit of the analyzer.

ration chamber is equipped with a mass spectrometer to allow detection of possible leak sources and identifying the residual gases inside. The residual gases in the main chamber are similarly analyzed with the same mass spectrometer by opening the valve to both chambers.

The heart of the main chamber is the light source and the electron spectrometer which give the technique its name. The light source used in our ARPES setup was SPECS Vacuum Ultra-violet (VUV) light source, namely UVS300. The UV lamp is attached coaxially with a toroidal mirror monochromator (TMM 302) and the ellipsoidal transfer capillary (ETC). The presence of the monochromator and the capillary allows for a fine selection of the photon energy and a narrow light spot (500 m), respectively. In order to tune the photon energy, different gas lines are installed, these are He, H, Ne, Xe, and Ar. The purity of most of the gases was 99.9999 %. In order to purify the gas lines further, the lines are immersed in a cylinder containing liquid nitrogen. This allows freezing the extra impurities in the gas lines and, as a consequence, increases the life time of the UV lamp filament.

The electron spectrometer at the Nanophysics laboratory is a multichannel Phoibos 150 hemispherical analyzer provided by SPECS. The Phoibos 150 hemispherical analyzer is equipped with a set of different entrance slits. The data acquired in this work is based on the use of a curved entrance slit that has about twice the curvature of the hemisphere, which is a feature that is intended to compromise between energy resolution and electron lens distortion, see appendix B. A schematic view of the hemispherical analyzer and the mechanism of its operation are shown in Fig. 2.15. It consists of electrostatic focusing lenses, hemispherical deflector which is the main heart of the analyzer, and the electron detector. The hemispherical deflector consists of two concentric spheres between which a voltage difference is applied. The photoemitted electrons are accelerated in the electrostatic input lenses, then retarded and focused onto the entrance slit of the hemispherical deflector^[88-92]. The analyzer defines two distinct planes; these are the dispersive and the non-dispersive planes. The dispersive plane is the one where the lenses and the detector lie and define the kinetic energy (E_K) axis, as shown in Fig. 2.15. The Phoibos 150 spectrometer has an acceptant angle, in this plane, smaller than 0.1o and can reach an energy resolution of few meV.

2. EXPERIMENTAL TECHNIQUES

In the dispersive plane the analyzer is working as a pass-band filter, where only photoelectrons with energies in a narrow energy window ($E_p - \Delta E$) to ($E_p + \Delta E$) can reach the detector. Electrons with higher and lower energy are impinging at the walls of the outer and inner hemispheres, respectively. While ΔE and E_p (the pass energy) are defined by the potential set between the hemispheres, a retarding potential set at the entrance of the analyzer will take care of reducing the kinetic energy of the electrons. For better resolution one thus need to go to lower pass energies. The overall resolution is then given by the combined resolution of both the analyzer and the UV light source.

The non-dispersive plane, on the other hand, is orthogonal to the dispersive one and within it the emission angle (θ_X) is concerned, as shown in Fig. 2.15. Only electrons which are emitted in a specific angle range around the dispersive plane can reach the detector. This angular range, and therefore the angular resolution, can be tuned by varying the potential on the electrostatic lenses. Different lenses modes, e.g. Low Angular Dispersion (LAD), Wide Angular Mode (WAM), etc, can be used depending on the preferred angular range and resolution in both angle and energy.

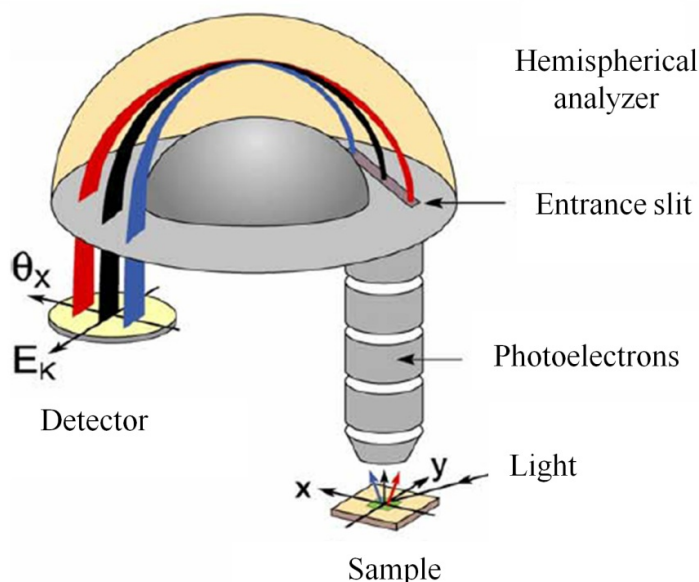


Figure 2.15: Electron Analyzer - A schematic view of the concentric hemispherical analyzer (CHA) type and the mechanism of its operation. The dispersive and non-dispersive planes are the ones that contain the kinetic energy and the emission angle axes, respectively. Adapted from Ref. [89] [89].

A 2D display-type detector will allow for the simultaneous measurements of both the energy and the angle (momentum) of the photoemitted electrons. This kind of detectors facilitates the acquisition of ARPES data, where the full dispersion of the electrons can be obtained as a live-snapshot in few minutes compared to the conventional way that requires a restricted angular acceptance and a movable analyzer^[90–92]. The detector consists of two micro-channel plates that amplify the signal of the photocurrent towards a phosphorus screen, where each electron makes a pulse of light into the phosphor. The data are then acquired as a 2D picture of the screen using a charge-coupled device (CCD) camera. The data is saved in units of (pixel \times pixel) and intensity image, where the rows and columns represent the energy and momentum of the photoemitted electrons, respectively. The transformation from pixel to physical units is then performed and the dispersion relation of the electrons is obtained. To access information about different constant energy surfaces, including the Fermi surface (FS), the 2D image that represents the dispersion of the photoelectrons has to be acquired at different manipulator angles (in off-normal geometry). This can be done by rotating the surface of the sample around an axis orthogonal to the dispersive plane, hence the rotational axis of the manipulator where the samples are mounted. The final result is a 3D data set that maps the energy distribution of the electrons versus the two orthogonal angles (the channel plate and the manipulator angle). The FS can then be extracted by taken a constant energy cut at the Fermi energy, after the transformation to physical units. Such data set also include the full band structure.

The software provided by SPECS to allow for data acquisition are SPECS Lab and CCD acquire. Those, in fact, do not allow for an easy control of the different variable needed to acquire the set of ARPES data. Therefore, Labview based software have been used for the data acquisition. The software is developed in the beamline 7.03 of the ALS light source in Berkeley, mainly by Aaron Bostwick. The software facilitates the communication between the Juggler (the SPECS software that controls the detector and screen voltages, pass energy, etc) and the motors. It also allows for adding many different frames taken at the same and/or different set energies in order to enhance the statistics of the collected data. The transformation from pixel to angle can be done simultaneously with the data acquisition, which in turn renders the sweep mode possible. The fact that, the transformation from pixel to angle is not straightforward,

2. EXPERIMENTAL TECHNIQUES

except in LAD, limits the use of the sweep mode for different lenses modes. For detailed discussion concerning the transformation from pixel to physical units together with the physical and mechanical distortion correction the reader is referred to appendix B.

2.5.2.2 ARPES at SRC:

The ARPES setup at the Synchrotron Radiation Center (SRC, Wisconsin-Madison, USA) is basically the same as the one at Nanophysics lab, hence two connected UHV-chambers: the main chamber and the preparation chamber. The differences, however, lie in the two main ingredient of an ARPES experiment, i.e., the light source and the electron analyzer. The light used in SRC is the synchrotron radiation. Below we give a brief introduction to the synchrotron radiation including its advantages over the conventional light sources.

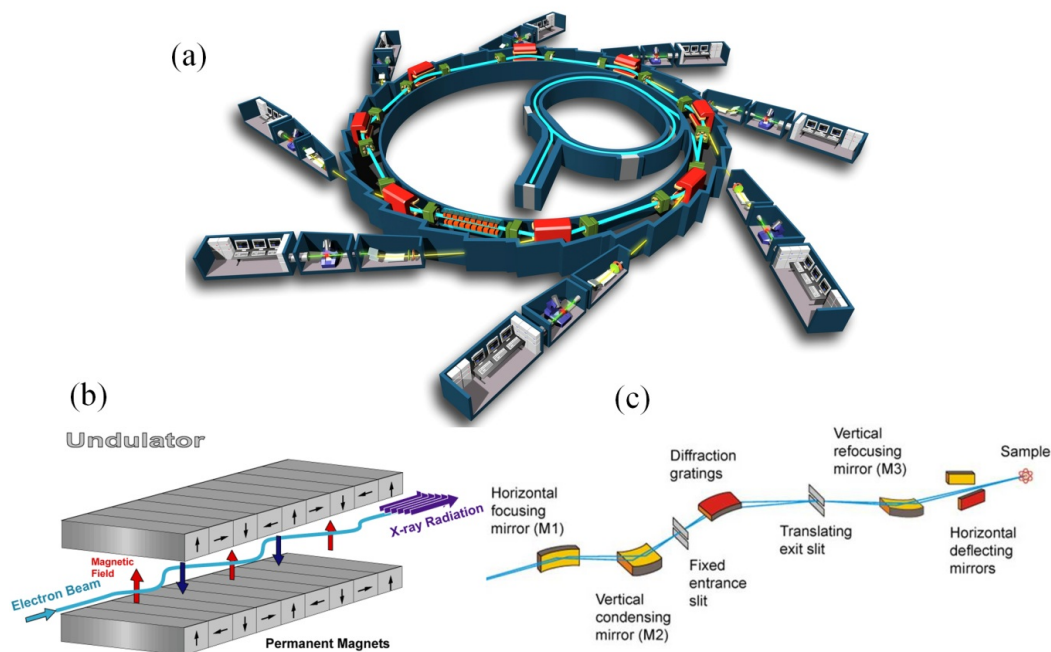


Figure 2.16: Synchrotron Radiation - (a) A schematic view of the synchrotron radiation facility showing the electron source, the storage ring, and the end-station beamline. (b) Undulator, a linear insertion device. Adapted from Wikipedia. (c) The beamline, showing the mirrors, slits and grating used to further monochromatize and direct the light to a sample, located at the end-station. Adapted from Ref. [89]^[89].

Synchrotron radiation is an electromagnetic radiation emitted, tangentially, by charged particles with relativistic velocities as they are accelerated, radially, by a static magnetic field, originally the field of what is called bending magnet in the accelerator^[80]. The charged particles are electrons generated in an electron gun, like the cathode ray tubes, and then accelerated up to a relativistic speed through a series of three particle accelerators; the linear accelerator, the booster synchrotron, and the large storage ring, as schematically shown in Fig. 2.16(a). In a storage ring, a set of bending magnets are installed at the corners in order to steer the electrons around the ring. As the electrons pass through them, they lose energy in the form of light. The third generation synchrotrons, however, use -beside the bending magnets- the advantages of extra linearly inserted devices to tune the brightness and the energy of the light; these are undulator and/or wiggler, Fig. 2.16(b). The undulator, and wiggler, consists of a linear periodic array of permanent magnets alternatively connected. For example, when a magnetic field along the undulator is alternating, electrons have to undergo oscillation and radiate energy. With the aid of such new insertion devices, the generated radiation has the advantage of being collimated, strongly polarized, and with high photon flux as compared to current conventional light sources. The emitted light is later monochromatized and directed to the experimental chamber, mounted at the end-stations, by means of gratings and mirrors, Fig. 2.16(c).

The Alaadin Storage Ring in SRC is relatively small storage ring with 88.9 m circumference and twelve bending magnets^[93], see Fig. 2.17. The electrons are stored at 800 MeV, and the synchrotron radiation is most intense in the low energy x-ray range. The monochromator that was used is a varied line space plane grating monochromator (VLS-PGM). A number of six undulator sources are installed. The ARPES setup belongs to the end station of the U9 1 meter Apple undulator with horizontal/vertical linear and left/right circular polarized light. The vertical spot size in the experimental chamber is generally less than 300 μm . The horizontal spot size is 400 μm over most of the energy range. In any case the vertical spot size is further decreased to less than 100 μm by a reduction of the exit slit. This leads to a better energy resolution and, in our case, to a reduced spot size at the curved crystal aiming a better angular resolution. This, in fact, is considered as a big advantage where wedged and/or vicinal surfaces can be systematically studied with reasonable lateral accuracy. In the other hand, the in-

2. EXPERIMENTAL TECHNIQUES

tensity decreases and the measuring time have to be increased. The analyzer connected to the main chamber in SRC, is a Scienta (SES200) analyzer with energy and angular resolution better than 10 meV and 0.4 degree, respectively. The components and performance of the Scienta-type analyzers are the same for the Phoibos one discussed earlier, however, with some slight technical differences.

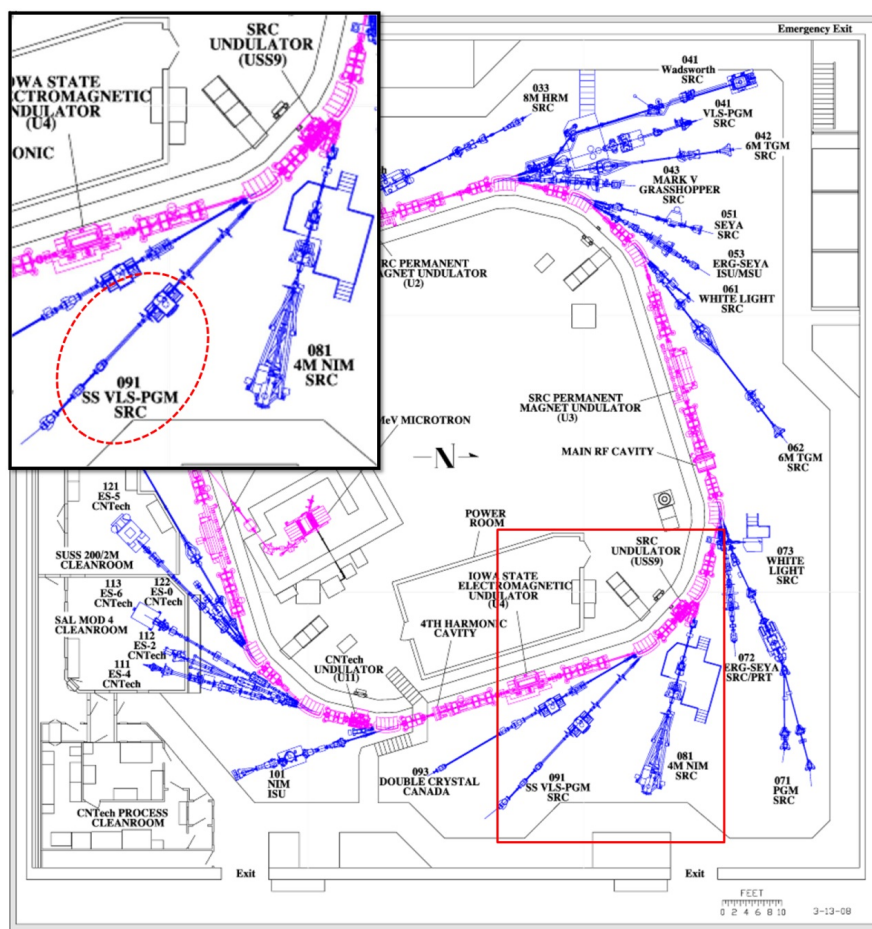


Figure 2.17: SRC-Synchrotron - The structure of Alaadin Storage Ring in SRC, Wisconsin, USA. The inset is a zooming of the red square region showing the VLS-PGM beamline (red dotted circle). Taken from SRC Webpage.

2.5.2.3 ARPES at ISA:

The ARPES setup at the Institute of Storage Ring (ISA, Aarhus, Denmark) is basically the same as the previous one. A Schematic description of the setup is shown in Fig.

2.18. The advantage of this setup is the presence of a load-lock in the preparation chamber. This is of critical importance while dealing with samples that have to be cleaved in vacuum, as it is the case for the topological insulators presented in the last chapter. It also allows samples to be inserted into the preparation chamber without breaking the vacuum. The transfer of the sample between the two chambers is done by moving the preparation chamber manipulator, through a valve, into the main chamber. In the main chamber the sample can be grabbed by a wobble-stick, and transferred to the main chamber manipulator. One more advantage of Aarhus setup is the presence of a garage for storing samples within which up to 10 samples can be stored. As the ARPES at Nanophysics Lab, the electron analyzer used in this setup was Phoibos 150, the description of which is already mentioned. The source used in ISA (ASTRID) is the

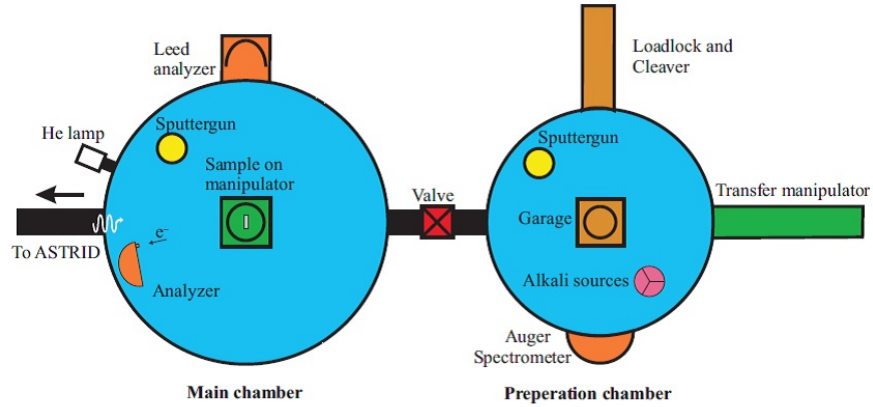


Figure 2.18: ARPES Setup at ISA - Schematic top view of the ARUPS setup in ISA. Taken from Ref. [94]^[94].

synchrotron^[95]. ASTRID is a small storage ring with four 10 m straight sections, and a bending magnet in each corner, Fig. 2.19. An undulator source is installed in one of the straight sections. The electrons are stored at 580 MeV, and the synchrotron radiation is most intense in the low energy x-ray range. The undulator source of ASTRID is characterized by high flux and low divergence of the beam in the (12-140 eV) energy range. The ARPES beamline is a branch line at the undulator source, as illustrated in Fig. 2.19. The monochromator (called SGM III) is a spherical grating monochromator (SGM) of the Dragon type with three gratings and a movable exit slit. The elements in the beamline are: horizontal focusing mirror, vertical focusing mirror, entrance slit, and setup with three interchangeable gratings, movable exit slit, and post focusing

2. EXPERIMENTAL TECHNIQUES

mirror. The horizontal focusing mirror is rotatable; it allows switching between the three branch-lines at the undulator section. The exit slit moves over 0.4 m . The three gratings (called LEG, MEG, and HEG) cover the energy range from 8 eV to 160 eV .

The photon flux in the case of medium- and high-energy gratings (MEG and HEG) is severely reduced and, therefore, the maximum usable photon energy for the AREPS experiments has in practice been limited to less than 80 eV . The vertical and horizontal spot sizes in the experimental chamber are less than 0.5 mm and 1 mm , respectively.

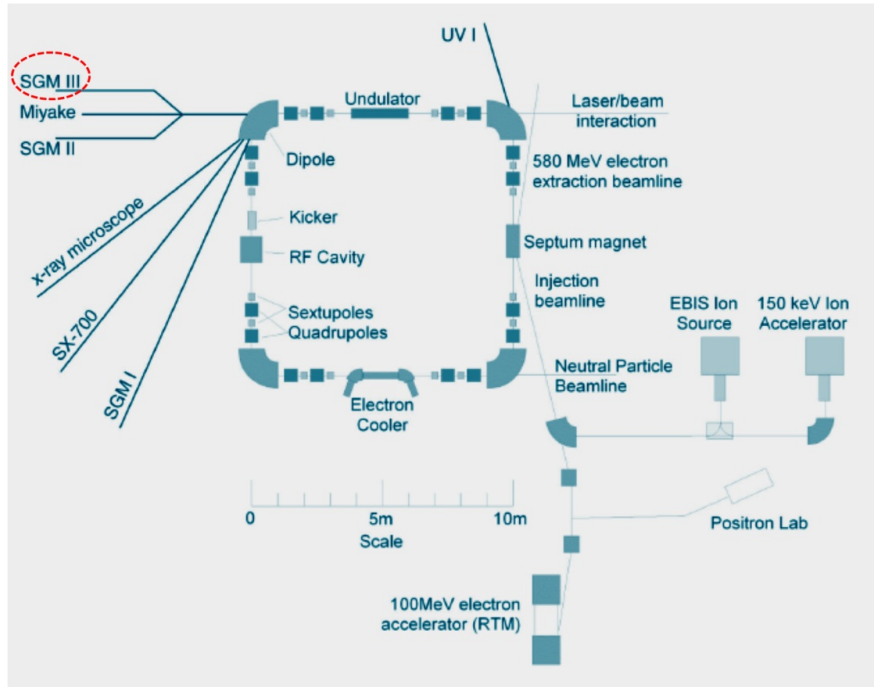


Figure 2.19: ISA-Synchrotron - A schematic illustration of the ASTRID layout. The ARUPS beamline is SGM III in the upper left corner (red dotted circle). Taken from ISA Webpage.

3

Results and Discussion I

This chapter is divided into two connected parts. Part I, entitled “*Tunable Cu(111) Surface State Induced by Au Alloying*”, concerns the surface geometric and electronic structure of the Au/Cu(111) system. Different Au coverage (from 0 ML to 5 ML) and annealing temperatures are used. Part II, entitled “*Lifshitz Transition across the 1 ML Ag/Cu(111) Superlattice Band Gap Tuned by Interface Au alloying*”, discusses the possible tuning of the 1 ML Ag/Cu(111) surface state by replacing the Cu(111) substrate with the Au/Cu(111) discussed in part I. In part II, the line width analysis of the surface state in the 1ML Ag/Cu(111) and 1 ML Ag/Au/Cu(111) as a function of the measuring temperature will be briefly presented.

3. RESULTS AND DISCUSSION I

Part I: Tunable Cu(111) Surface States Induced by Au Alloying

3.1 Introduction and Literature Survey I:

Surface states on noble metal (111) surfaces are among the most often studied surface electronic states. These, Shockley type^[28], surface states are placed inside the bulk projected gap at the center of the surface Brillouin zone and its dispersion relation is closely related to the band gap boundaries^[96]. In particular, the energetic position of the surface states band minima is essentially related to the lower edge of such projected band gap of the supporting bulk. This issue is further discussed in more details in appendix A of the present thesis. Being localized in the outermost atomic surface layers, such states represent an almost ideal example for two-dimensional electron systems. While the Shockley states at simple noble metal (111) surfaces have been intensively studied long ago, the effect of impurities/defects has attracted more attention due the formation of standing wave patterns originated by the Shockley state in scanning tunneling microscopy/spectroscopy that enables detailed surface science studies^[97–100]. In this respect, the Cu(111) crystal which features a Shockley surface state with a binding energy and effective mass of, respectively, 0.39 eV and $0.41 m_e$ ^[100], has been one of the most active surfaces compared to other noble metals. Both organic molecules and metallic adatoms/layers have been extensively tested on Cu(111). For example, deposition of some organic molecules on Cu(111) surface has led, in contrast to Ag and Au crystals, to a metallization between the molecular layer and the Cu substrate^[101]. Combination of noble metal interfaces in the form of adatoms, overlayers, or alloys/compounds revealed certain influence to the Shockley state. Adsorption of Cu adatoms on Cu(111) surface has shown to induce a localization of the latter surface state^[102,103].

3. RESULTS AND DISCUSSION I

Overlayers of metals on metal substrates with similar^[104] or different lattice parameters^[105] has been long subject to investigation due to the rich growth modes and the subsequent emergent new electronic states, such as Rashba-split states^[106–108], gapped surface states^[50], quantum well states^[109], etc. An example for a large lattice mismatch noble metal combinations is the 1 ML Ag/Cu(111) system that will be investigated in the second part of this chapter. The system undergoes an irreversible phase transition from a moiré to triangular dislocation network following a slight annealing of the sample^[51,110,111]. The Shockley state of this system shows an \bar{M} -point gap at the Fermi energy, the finding of which has triggered the claim of an electronic/structure interplay in that system^[50]. In fact, the moiré like patterns are very common for most overlayers with large lattice mismatch with the substrate^[112–114]. The present chapter deals with the overlayer growth of Au on top of Cu(111). Such combination belongs to the large lattice mismatch class (typically 11.4 %), where the in-plane lattice parameters (d) of Au(111) and Cu(111) are, respectively, $d=2.88$ Å (very similar to Ag(111) $d=2.89$ Å), and $d=2.55$ Å^[115]. Such mismatch is analogue to that in Ag/Cu(111), and hence the formation of moiré and/or dislocation pattern in the Au/Cu(111) system is expected. In fact, a scanning tunneling microscopy (STM) study of 0.6 ML Au/Cu(111) deposited at room temperature (RT) showed a dislocation network similar to the one seen in Fig. 3.1, with much higher periodicity, but poorer homogeneity compared to Ag/Cu(111)^[116–118]. One should keep in mind, however, that Au and Cu are miscible and therefore the formation of AuCu alloy cannot be discarded. A combined X-ray and Ultra-violet photoemission spectroscopy (XPS and UPS) concluded the formation of Au islands on top of Cu(111) for RT deposition^[119,120]. Alloy formation and Au segregation inside the Cu bulk have been also reported for Au/Cu(111) surfaces annealed to temperatures higher than RT^[121]. A similar work on a multilayer combination of Au and Cu has also been done and information concerning the morphology of the Au-Cu alloying at different annealing temperature and different Au/Cu ratios in such multilayer combination has been extracted^[122]. This in fact means that the surface structure in Au/Cu(111) is not as simple as for Ag/Cu(111), and contradictory results concerning the structure are common in literature^[123–125].

Apart from structural studies, we are not aware of any surface electronic structure characterization of Au/Cu(111) system. This may be due to the large in-homogeneity

3.2 Sample Preparation and Characterization Tools I :

of the prepared films, as seen in Fig. 3.1, Fig. 3.2, so as a very weak ARPES signals are expected in such cases. We, therefore, would like to question the possible existence and/or modification of a Shockley surface state characteristic for the grown film and its dispersion parameters compared to both Cu(111) and Au(111) surfaces. The Au(111), as a noble metal, also shows a Shockley state with a binding energy and effective mass of 0.44 eV and $0.255 m_e$, respectively^[100]. As a rule of thumb, after the deposition of noble metal monolayer(s) on top of other metal, the resulting Shockley state acquires a binding energy half way in between the surface states of both the thin film and the substrate^[126]. We shall show that, the Au/Cu(111), interestingly, exhibits a remarkable deviation from this criterion.

To this aim, we present a combined STM/ARPES study on ultrathin films of Au on top of the Cu(111) surface. Information regarding the growth mode and the surface electronic structure as a function of Au coverage as well as the annealing temperature will be given in the following sections.

3.2 Sample Preparation and Characterization Tools I ¹:

The Cu(111) crystal was cleaned using repetitive cycles of sputtering and annealing as described in chapter two. The Au metal was deposited on top of the clean substrate using a home-made evaporator. The substrate temperature was kept at 180 K during Au evaporation, and then softly annealed to different temperatures for a few minutes. In ARPES experiments, the Au was deposited as a wedge with thickness of ~ 0.2 ML to ~ 1.0 ML. The Au thickness calibration was done by monitoring the surface state between 0.7 ML and 1.2 ML in the Ag/Cu(111) system till the Cu surface state peak quenches^[50,105,127]. Since the Au and Ag crucibles are enclosed within the same evaporator, relying on the Ag coverage and the QMB reading serve as a good approximation to Au coverage, taking the density difference between Ag and Au into account. The ARPES measurements were then performed across the Au wedge while the sample is kept at different temperature, from 180 K to 300 K. The sample was then annealed to 400 K, 510 K, 600 K, and 660 K and then cooled down to RT. A clean Cu(111)

¹All STM measurements in the whole chapter were done by M. Corso. The XPS data was measured at SRC by M. Ormaza and F. Schiller. M. Matena has contributed to most of the ARPES data presented here.

3. RESULTS AND DISCUSSION I

stripe is left free at one side of the sample for a straightforward comparison of surface states and LEED patterns. ARPES experiments were carried out at two different UHV systems, the ARPES setup in San Sebastián using Helium I light (21.22 eV) and at the Apple PGM beamline of SRC using horizontal light polarization. In both cases the angular and energy resolution was set to 0.1° and 40 meV, respectively. Apart from a slight offset in Au coverage and the annealing temperature, both data sets reproduce the same findings. Therefore, ARPES data presented here mostly belong to those measured in San Sebastián, unless specified. In the STM experiments, the Au thickness calibration was done by evaporating a tinny amount of Au atoms (typically < 0.2 ML) at 150 K, to avoid both, island growth and diffusion/alloying between Cu and Au atoms. The Au coverage was then estimated using the floating method algorithm in WSxM software^[84].

3.3 Results and Discussion I:

3.3.1 Au/Cu(111) Surface Alloy:

Figure 3.1 shows STM images taken for ~ 0.15 ML Au deposited at room temperature and annealed to ~ 600 K. In Fig 3.1(a) one clearly sees two distinct areas: flat patches with few single protrusions and patches with a moiré like pattern. The former is assigned to a clean Cu(111) with few gold atoms, whereas the latter is identified as AuCu surface alloy induced by annealing. The stoichiometry of the AuCu alloy, as estimated from the relative areas in the STM image, was found to be $\sim \text{Au}_{0.3}\text{Cu}_{0.7}$. The small scale STM images, shown in Fig. 3.1(b-c), indicate the absence of long range order of the moiré pattern in most of the cases.

For higher Au coverage and for slightly higher annealing temperature (650 K), the areas with the moiré like pattern increases but a second layer appears before covering completely the un-alloyed Cu(111) regions, Fig. 3.2(a). A closer view, displayed in Fig. 3.2(b), reveals a sort of several short range ordered moiré like pattern ranging from ~ 3 nm in the dense areas to 6 nm close to the step upper edges. We attribute this difference to a change of Au concentration in the alloy. We also notice that the second layer islands are also alloyed and present the moiré like pattern with, similar to the dense area in the first layer, ~ 3 nm periodicity, Fig. 3.2(c).

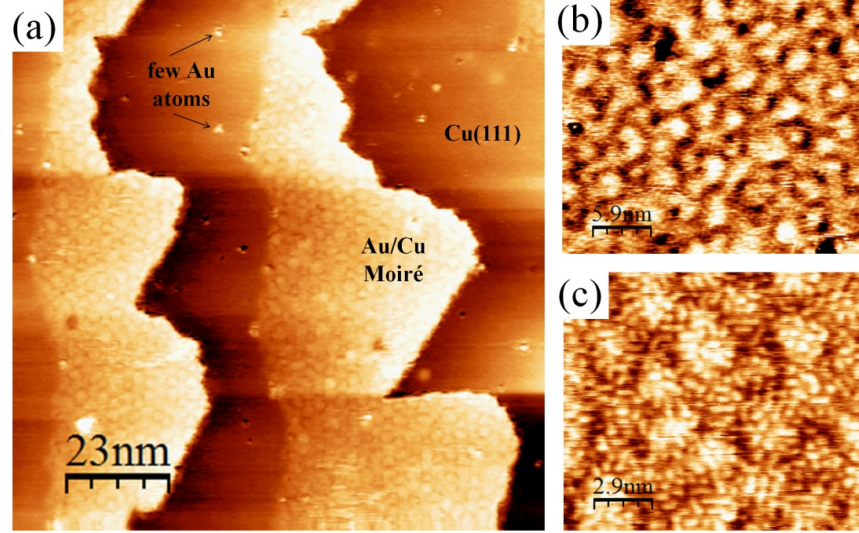


Figure 3.1: STM Images: 0.15 ML Au/Cu - (a) Large scale STM image for 0.15 ML Au/Cu after annealing to 600 K. (b-c) Zoomed scan in different areas showing the Au/Cu moiré in (a).

Higher annealing temperatures (e.g., 700 K, Fig. 3.3(a)) results in a complete alloying of the whole surface with, now, joined and flatter alloyed second layer contribution and almost no free Cu(111) patches. The moiré like pattern is also observed for such high annealing temperature, Fig. 3.3(b), together with a kind of distorted short range ordered hexagonal pattern of triangles with ~ 10 nm periodicity, Fig. 3.3(c). The latter pattern is not frequently observed in our STM images (compared to the moiré like one), and we shall omit it from our discussion. For all Au coverages up to 1.3 ML and at different annealing temperature, the moiré like pattern with its short range order is always present. For higher annealing temperatures, the moiré like areas become larger and flatter.

However, since only short range order is observed, superlattice spots (in LEED) and umklapps effects (in ARPES) can be completely shaded. The LEED patterns, for example, for the annealed Au/Cu samples only show a single set of spots that belongs to the Cu(111) crystal with almost no change in the Cu lattice parameters neither the appearance of superstructure related spots. Only for the as-deposited samples ($T = 180$ K) that two sets of spots are coexisting, see Fig. 3.4. The relative separation between them allows their assignment as bulk Cu(111) (red) and Au(111) (yellow) spots with no

3. RESULTS AND DISCUSSION I

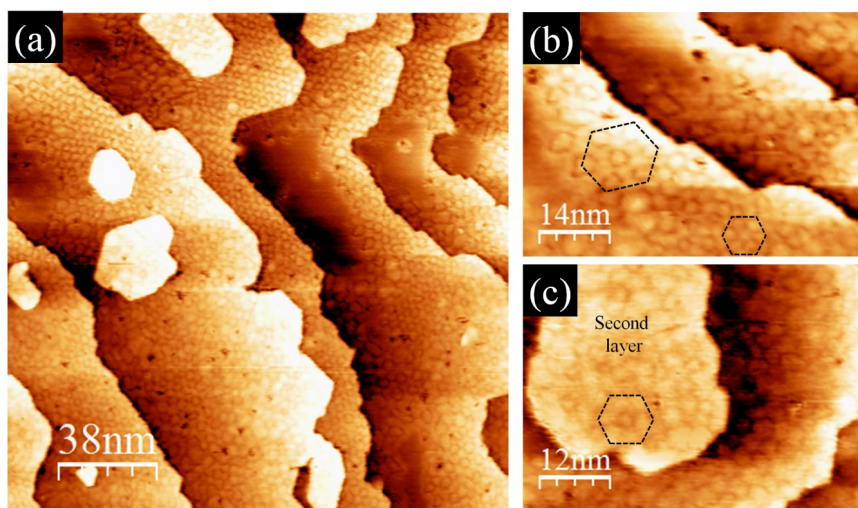


Figure 3.2: STM Images: 0.8 ML Au/Cu - (a) Large scale STM image for 0.8 ML Au/Cu after annealing to 650 K. (b-c) Zooming in different areas of (a).

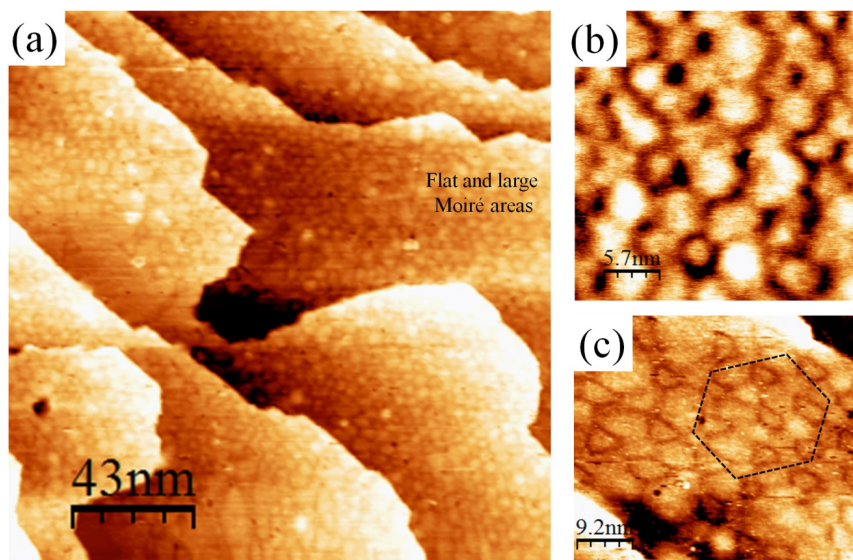


Figure 3.3: STM Images: 1.3 ML Au/Cu - (a) Large scale STM image for 1.3 ML Au/Cu after annealing to 700 K. (b-c) Zooming in different areas of (a).

change in their corresponding lattice parameter^[115]. The intensity of the spot profile of the Au(111) spots was found to increase as we scan through the Au wedge (increasing the Au coverage). We concluded that for such low temperatures (< 400 K) the Au atoms do not intermix with the Cu(111) matrix.

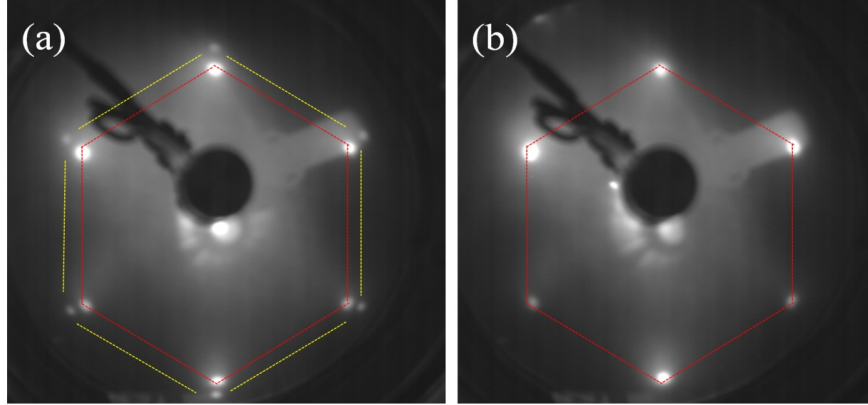


Figure 3.4: LEED Patterns: Cu vs. Au/Cu - LEED patterns of the as deposited (a) 0.5 ML Au on top of Cu(111) and after annealing to 650 K(b). In (a) the two set of spots are assigned to the Cu(111)(red) and Au(111) (yellow) spots, whereas in (b) only the Cu-like set of spots are seen. Electrons energy of 130 eV was used.

To gain further insight into the growth process, the Au-4*f* core level as a function of Au coverage and annealing temperature, has been measured with the photoemission setup in the SRC using photon energy of 125 eV. Figure 3.5 summarizes the results of such measurements after fitting the corresponding peaks with Doniach-Sunjc profiles and linear background, Fig. 3.5(a). When Au is evaporated at low temperature one observes a spin-orbit split peak at binding energies of 83.90 eV (Au 4*f*_{7/2}) and 87.57 eV(Au 4*f*_{5/2}), respectively, for low Au coverage (up to 0.2 ML) that slightly increases by ~ 30 meV for the nominal monolayer coverage. This situation resembles the 1 ML Au/Ru(0001) case where the 4*f*_{7/2} binding energy was at 83.88 eV for a non-alloyed gold layer^[120] and is distinct from the 1 ML Au/ 3 ML Cu /Ru(0001) situation (4*f*_{7/2} binding energy of 83.99 eV) where already for room temperature deposition some alloying takes place. We, therefore, concluded that the observed 4*f* peaks belongs to Au atoms only at the surface in agreement with LEED observations.

Annealing of the low coverage Au/Cu(111) system leads to alloy formation (shown in all STM images) that results in a core level shift of ~ 240 meV to higher binding

3. RESULTS AND DISCUSSION I

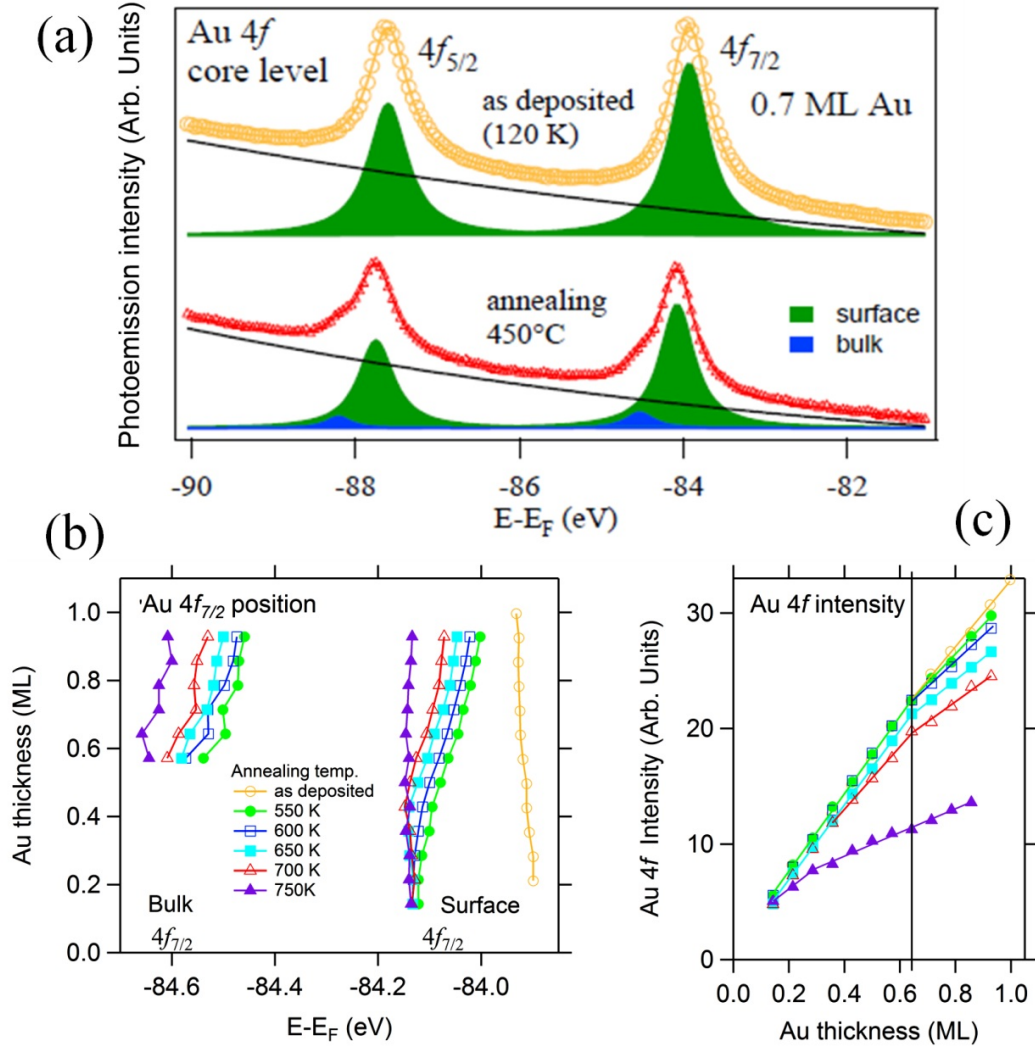


Figure 3.5: Core-Levels Spectra: Au/Cu - (a) XPS measurements of the Au 4f core-levels for as deposited (top) 0.7 ML Au on top of Cu(111) and after annealing to 750 K (bottom). The profile for as-deposited sample is fitted with single doublet that correspond to surface (green) Au atoms, where two doublets are used to fit the annealed sample profile for which extra bulk (blue) contribution is developed. The binding energy, (b), and the intensity (peak height), (c), of the 4f_{7/2} core-level as a function of Au thickness after fitting the corresponding spectra with single/two doublets for different annealing temperature.

energies: the binding energy of $4f_{7/2}$ and $4f_{5/2}$ were found, respectively at 84.14 eV and 87.81 eV independent of the annealing temperature, Fig. 3.5(b). The situation is now similar to the 1 ML Au/ 3 ML Cu /Ru(0001) situation^[120] where a $4f_{7/2}$ binding energy of 84.16 eV has been estimated after annealing to 600 K. At the same time, for such low Au coverage, the total $4f$ area remains constant indicating that the Au is still at the surface but now forming an alloy. This situation can be observed in Fig. 3.5(c).

An increase of the coverage up to ~ 1 ML has two consequences in the core level positions, (i) the appearance of a second contribution at the high binding energy side, Fig. 3.5(a), and (ii) the slight downward shift of the main peak at lower annealing temperatures, Fig. 3.5(b). The first point is attributed to the formation of the second bulk alloyed layer (below the surface alloy) that gives rise, similar to that in pure Au, to a “surface” and “bulk” contribution of the $4f$ peak^[128], in agreement with STM observations. Here this “bulk” contribution is small due to the fact that the kinetic energy of the Au $4f$ core level electrons (~ 35 eV) is close to the minimum of the electron mean free path of electrons and therefore the measurements are very surface sensitive^[129]. For increasing Au coverage the bulk peak increases in intensity with respect to the “surface” peak. The slight downward shift with coverage can be attributed to the increasing Au-Au bonding contribution (higher Au amount in the alloy) that pushes the peak position toward the binding energies for low temperature deposition. The high annealing temperature increases the Au atom mobility, reduces the areas with a high Au amount. Coming back to the Au $4f$ intensity one can observe that in the latter case the intensity is lower compared to samples annealed at lower temperature. This is generally attributed to alloy formation in the second and successive layers. Nevertheless such a situation would result in an earlier onset of the appearance of the bulk contribution of the $4f$ core level that was not observed. We rather believe in a re-evaporation process at such elevated temperatures (750-800 K).

We summarize our current understanding of the Au/Cu(111) growth modes by the schematic representation of Fig. 3.6. For all Au coverage and at temperatures less than the alloying onset ($T < 400$ K), Au follow an island growth mode, the vertical and lateral size of the islands scale with Au coverage. For Au coverage below 0.3 ML, AuCu surface alloying takes place upon annealing, with almost no change of the

3. RESULTS AND DISCUSSION I

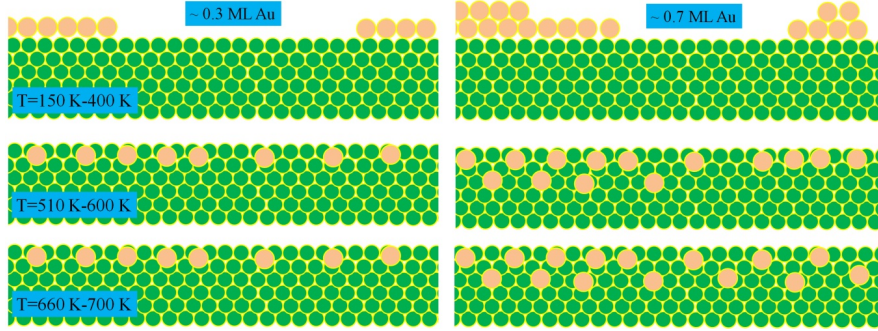


Figure 3.6: Growth Mechanism: Au/Cu(111) - Sketches illustrating the growth mechanism of Au on top of Cu(111) at different annealing temperatures. The left panel describes the low Au coverage region (≤ 0.3 ML), where the description of the high Au coverage region (≥ 0.3 ML) is shown to the right.

composition when increasing the temperature of annealing. For Au coverage > 0.3 ML, the depth of the alloy increases with the annealing.

The growth process just analyzed by means of STM and core-level photoemission is directly related to the band structure, especially to the Shockley surface state. Figure 3.7 shows the energy distribution curves (EDCs) at the band minima, for the Cu(111) surface state as a function of Au coverage and annealing temperature.

At temperature between 200 K and 400 K, the surface state band minima were found to shift toward the Fermi level as a function of Au. The shift is bigger as the Au coverage exceeds 0.3 ML. At 0.7 ML, the surface state was very broad with a band minimum of -0.33, hence 60 meV shifted toward the Fermi level as compared to Cu surface state band minima, shown by the dotted peak. Since the deposition of Au was done at LT (180 K) where the Au atoms are not supposed to be mobile yet, this can be explained as disordered Au small islands which, in turn, scatter the Cu(111) surface state. The more the Au coverage, the higher the dimension of those islands, as schematically shown in Fig. 3.6, and hence the scattering. This, in fact, agrees with the two sets of spots observed by LEED. Upon annealing the sample to 510 K, the surface state was found to shift towards higher binding energies as a function of Au coverage (dotted red line). The shift of the band minimum is actually significant. For 0.45 ML Au and after annealing to 510 K, the band energy was found to be -0.520 eV (after fitting the corresponding EDC), i.e. much higher compared to both Cu(111) and Au(111) surface states. For Au coverage > 0.45 ML, a second lower binding energy peak

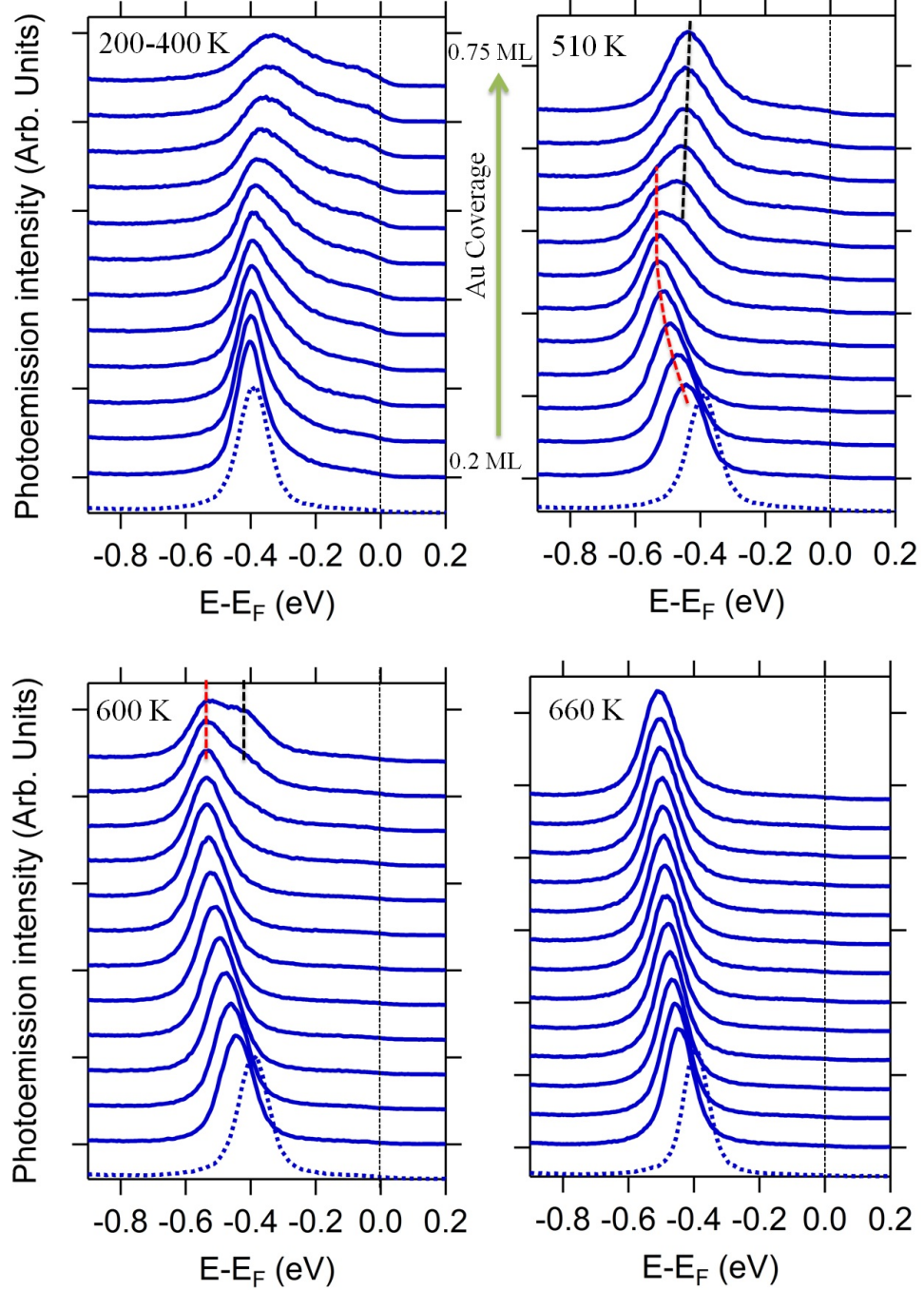


Figure 3.7: ARPES Data: Band Minima EDCs: Au/Cu - EDCs at the band minima for Cu(111) as a function of Au coverage (0.2 to 0.9 ML) at different measuring (150-300 K) and annealing temperature (400-660 K). The annealed samples are cooled down and measured at room temperature.

3. RESULTS AND DISCUSSION I

(black dotted line) appears that is attributed to the buildup of the second alloyed layer as confirmed from STM images. Annealing to 600 K results in the disappearance of the second layer contribution and, similarly, significant downward shift of the Shockley state. At 0.65 ML we estimated a band minimum with binding energy of 0.530 meV. The second monolayer contribution starts to, then, reappears for higher Au coverage. At 660 K the EDCs can nicely be fitted with a single peak for all Au coverage up to ~ 1 ML, with, however, lower binding energy (0.5 eV) compared to the 510 K and 600 K annealed sample. We believe in simultaneous dissolution of Au atoms from the second layer islands together with a slight re-evaporation of Au atoms.

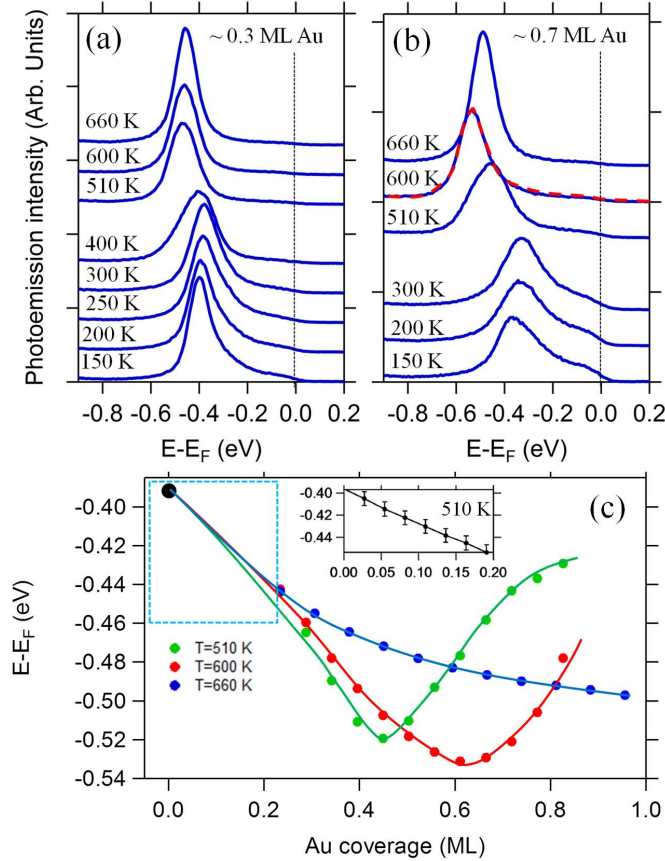


Figure 3.8: Band Minima: Data Points: Au/Cu - EDSs at the band minima for (a) 0.3 ML Au and 0.7 ML Au (b) on top of Cu(111) as a function of different measuring (150 K - 300 K) and annealing temperature (400-660 K). (c) The band minima after fitting the EDCs on the top panel for the 510 K (green), 600 K (red) and 660 K annealed samples. The results for the low Au coverage (< 0.2 ML) are shown in the inset for the 510 K annealed sample.

The top layers of the AuCu alloy in the latter case becomes Cu rich as the annealing temperature increases^[120] and finally when annealing to ~ 750 K a clean Cu(111) surface state is completely recovered. This is further confirmed by a recent work on 1 ML Ag on top of this Au/Cu(111) substrate annealed to 660 K, where the growth of Ag on top of the Au/Cu(111) was found to be exactly the same as Ag/Cu(111) with only differences in the surface electronic structure^[130].

We can then divide the Au coverage regime into two main regions (Fig. 3.8): $\text{Au} < 0.3$ ML, where the annealing temperature has almost no effect on the Shockley surface state of the AuCu alloy (see also the inset in Fig. 3.8(c)), and $\text{Au} > 0.3$ ML where the annealing temperature results in a downward shift in the binding energy continuously up to a certain re-evaporation temperature (660 K and higher). The data points presented in Fig. 3.8(c) nicely demonstrate this conclusion. The dashed red EDC in Fig. 3.8(b) and the corresponding minimum in the red data points in Fig. 3.8(c) represent the highest accessible binding energy (0.530 eV) for the present interplay between the Au coverage (~ 0.65 ML) and annealing temperature (600 K). A similar minimum (0.52 eV) also takes place for ~ 0.45 ML Au after annealing to 510 K. For Au coverage above these two minima, the EDCs need to be fitted with two peaks including the second layer contribution into account. The latter's data points are not included in the plot shown in Fig. 3.8(c).

A detailed analysis of the Shockley surface state dispersion along the $\overline{\Gamma M}$ direction, Fig. 3.9(a), reveals a clear correspondence between the binding energy shift, just analyzed, and the full parameters of the dispersion, such as the size of the Fermi surface, Fig. 3.9(b), the effective mass, Fig. 3.9(c), and the Fermi wavevector, Fig. 3.9(d-e), and their dependence on the Au coverage and annealing temperature. Figure 3.9(a) shows the photoemission intensity of the Shockley surface state along $\overline{\Gamma M}$ direction for (left) Cu(111) and (right) 0.45 ML Au/Cu(111) annealed at 660 K. One clearly sees the free-electron-like dispersion of both states together with the obvious difference in the binding energy. To further confirm the free-electron-like character of the dispersion, a FSM for 0.45 ML Au/Cu(111) annealed to 660 K is displayed in Fig. 3.9(b), which takes the form of a perfect ring, with a slightly larger Fermi wavevector than Cu(111). Since the dispersion is free-electron-like, we are able to extract the dispersion parameters of the observed surface state. An effective mass of $0.412 m_e$ and binding energy

3. RESULTS AND DISCUSSION I

of 0.39 eV fits very well the Cu surface state dispersion (hence the same as reported in literature), whereas $m_* = 0.37 m_e$ and $E_B = 0.48$ eV, respectively, are needed to fit the data set of the 0.45 ML Au/Cu(111) system annealed to 660 K. The parabolic fit is superimposed on Fig. 3.9(a) (black lines).

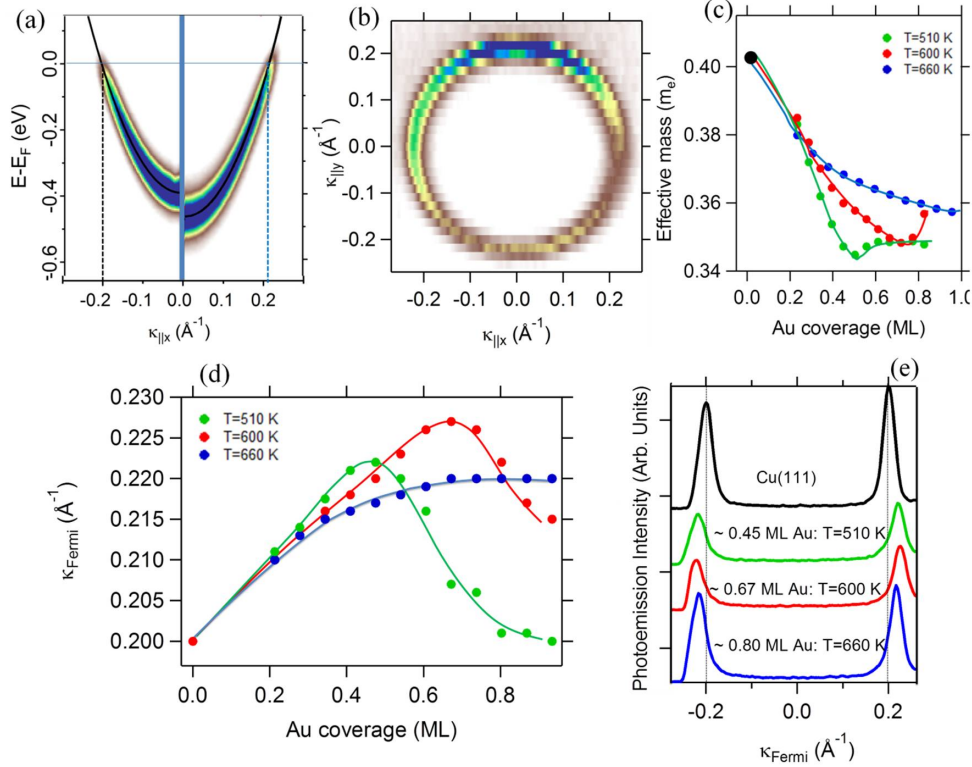


Figure 3.9: Summary of the Dispersion Parameters: Au/Cu - (a) Photoemission intensity of the surface state along $\bar{\Gamma}\bar{M}$ direction for (left) Cu(111) and (right) 0.45 ML Au/Cu(111) annealed at 660 K. The black lines represent the parabolic fit to these surface states. (b) Circular FSM for the 0.45 ML Au/Cu sample. (c-d) Variation of the effective mass and Fermi wavevector, respectively, with Au coverage at different annealing temperature. (e) The MDCs at E_F for the Au coverages with the highest band minimum for the three different annealing temperatures compared to Cu(111).

Apart from an obvious difference in the binding energy, the effective mass value was found in between that of Au(111) and Cu(111). The same analysis is applied for all Au coverage and the three different annealing temperatures, and the effective mass values are extracted and presented in Fig. 3.9(c). We notice that, there is a minimum in the effective mass at the exact same Au coverage that leads to a maximum in the

binding energy, hence at 0.45 ML and 0.65 ML for, respectively, the 510 K and 600 K annealing temperature. Close to 0.3 ML Au the effective mass is nearly independent of the annealing but a strong deviation is observed for higher Au coverage. The simultaneous increase (decrease) of the binding energy (effective mass) is also reflected in the behaviors of the Fermi wavevector with Au coverage and annealing temperature, Fig. 3.9(d-e). The maximum values of the wavevector were 0.222 \AA^{-1} and 0.227 \AA^{-1} for, respectively 0.45 ML Au annealed to 510 K and 0.65 ML annealed to 600 K following the maximum (minimum) in the binding energies (effective masses). For higher annealing temperature (660 K) the maximum Fermi wavevector is slightly reduced (0.219 \AA^{-1}). These three extreme cases are further highlighted in the corresponding momentum distribution curves (MDCs) shown in Fig. 3.9(e).

In the following discussion we will try to explain the physical origin of such modifications on the surface electronic structure. Usually combinations of the noble metals due to depositions of one element on top of another one leads to Shockley states between the pure elements positions. Examples are Ag/Au(111)^[104] or Ag/Cu(111)^[105] where the position of the surface state moves toward the Ag(111) surface state position for increasingly thicker Ag layers. One exception is the case of 2 ML Ag/Pt(111), where a Shockley state with a higher binding energy than the one of Ag(111) and Pt(111) was observed^[106].

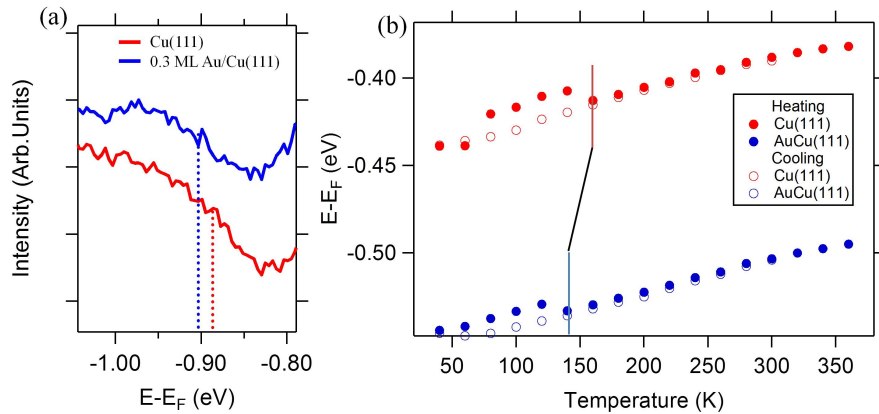


Figure 3.10: Bulk Projected Gap: Cu vs. Au/Cu - (a) EDCs showing the lower edge of the bulk project gap in (blue) Cu(111) and (red) 0.3 ML Au/Cu(111) annealed to 660 K. (b) The surface state band minima of (red) Cu(111) and (blue) 650 K annealed 0.7 ML Au/Cu(111) as a function of the measurement temperature.

3. RESULTS AND DISCUSSION I

In our case a maximum binding energy of 0.53 eV, much higher than both Cu(111) and Au(111), was found. The question of the origin of such unusual shift arises. One important point for the Shockley state energy is the position of the bulk projected bands that correspond to the L_4 - band gap edges (or L_2' in single group notation). A downward shift of the band gap energy for example by temperature variation also moves the Shockley state energy, but to a lower extent^[99]. In the case considered here the bulk band gap edge for copper was determined at $E-E_F = -0.89$ eV and moved to $E-E_F = -0.91$ eV, see Fig. 3.10(a), in the case of 0.3 ML Au/Cu(111) where the surface state is shifted by 85 meV. The surface state itself usually shifts less than the bulk band gap edges. In the case of low temperature experiments^[99] the surface state shift is only 55 % and 85 % of the bulk band gap shifts for Cu and Au, respectively. This would shift down the surface state by maximal 12 meV and will not even reaches the surface state position in Au(111). Low temperature measurements, shown in Fig. 3.10(b), also shows that both Cu and AuCu alloy follow the exact same temperature dependent with a downward shift rate of 0.16 meV/K, hence the same reported for Cu(111) crystal. The only slight different is during the heating cycles, where AuCu desorbs the adsorbates gases 20 K before Cu(111) and is, therefore, slightly less reactive than Cu(111) agreeing with a possible existence of Au atoms on the topmost layer surface. In conclusion, the reported tunable high binding energy for AuCu alloys cannot be explained by the bulk band gap shift.

The search for other possible reasons in order to explain such deviation in the trend of the binding energy, effective mass, and Fermi wavevector has led us to consider the following possible mechanisms. Several adsorbates, such as the electropositive alkali atoms^[131], on top of noble metal surfaces tend to increase simultaneously surface states binding energies and its Fermi wave vectors. By contrast, adsorption of CO molecules^[132], rare gases or dielectric NaCl^[133] overlayers were found to decrease both the binding energy and Fermi wavevector. Charge transfer, direct doping, dipole formation, work function variation, etc, in the previous systems are believed to be the essential reasons for surface state modification. We exclude similar interpretations in our case. We rather believe that the observed shift is induced by the combination of random alloy formation and the moiré itself, which lowers the surface potential felt

by the electrons. The later is being tested now by our theory collaborators ². However, we would like to mention our motivation to favor such interpretation. For 2 ML Ag/Pt(111) for example^[106], a similar downward energy shift has been reported. The system shows a moiré superstructure for such coverage. The authors then observed this shift for 2 ML and not for 1 ML, 3 ML or higher coverage. In fact, the signature of the surface potential variation due to the moiré was also reflected in the enhancement of the spin-orbit split of the Pt(111) surface state. Similar artificial binding energy shift can be seen by reexamining the moiré superstructure of the 1 ML Ag/Cu and 2 ML Ag/Cu and their comparison with the respective Ag coverage on Au(111), where no moiré like pattern is observed. One notices that the binding energy of the moiré like superstructure deviates by ~ 100 meV (similar to our values) from the expected behavior due to the quantum size effect variations with the film thickness. The corrugation of the moiré, the common surface structure in the present case and the examples, might induce an effective surface potential that triggers such shift. More supporting findings in literature are a recent STS study which has shown that the surface state in Ag/Si(111) locally shifts toward higher binding energy in the proximity of a dislocation site, but not a step^[134]. There is also a clear analogy with the shift of the Cu surface state in $\text{Cu}_{0.9}\text{Al}_{0.1}$ alloy, which is terminated with a 1×1 or a $\sqrt{3} \times \sqrt{3}$ R30 superstructure^[135]. In spite of the fixed Al concentration in the two cases, the $\sqrt{3} \times \sqrt{3}$ R30 phase was shown to induce an extra shift of the surface state toward higher binding energy with narrower line shape compared to the 1×1 phase. We believe that all these systems exhibit the same behavior as the AuCu surface alloy has.

The shift of the surface state in the presence of a moiré corrugation maybe simply explained as due to an effective increase of the quantum well that contains the surface state (see appendix A). Such variation of the surface quantum well is sketched in Fig. 3.11(a-b) together with atomic representation of the moiré corrugation. According to the phase accumulation model, bound surface states (crystal and/or barrier induced) reflected backward and forward across the crystal-vacuum interface occur when^[98];

$$\phi_B + \phi_C = 2\pi n \quad (3.1)$$

²Due to our anticipation of the generality of this effect, the calculation is intended to be done on Cu ML on top of Cu(111). We ignore the actual situation of Au, and rather examine the surface state energy as a function of interlayer separation and lateral displacement and analyze the corresponding LDOS for the on-top and on-site positions.

3. RESULTS AND DISCUSSION I

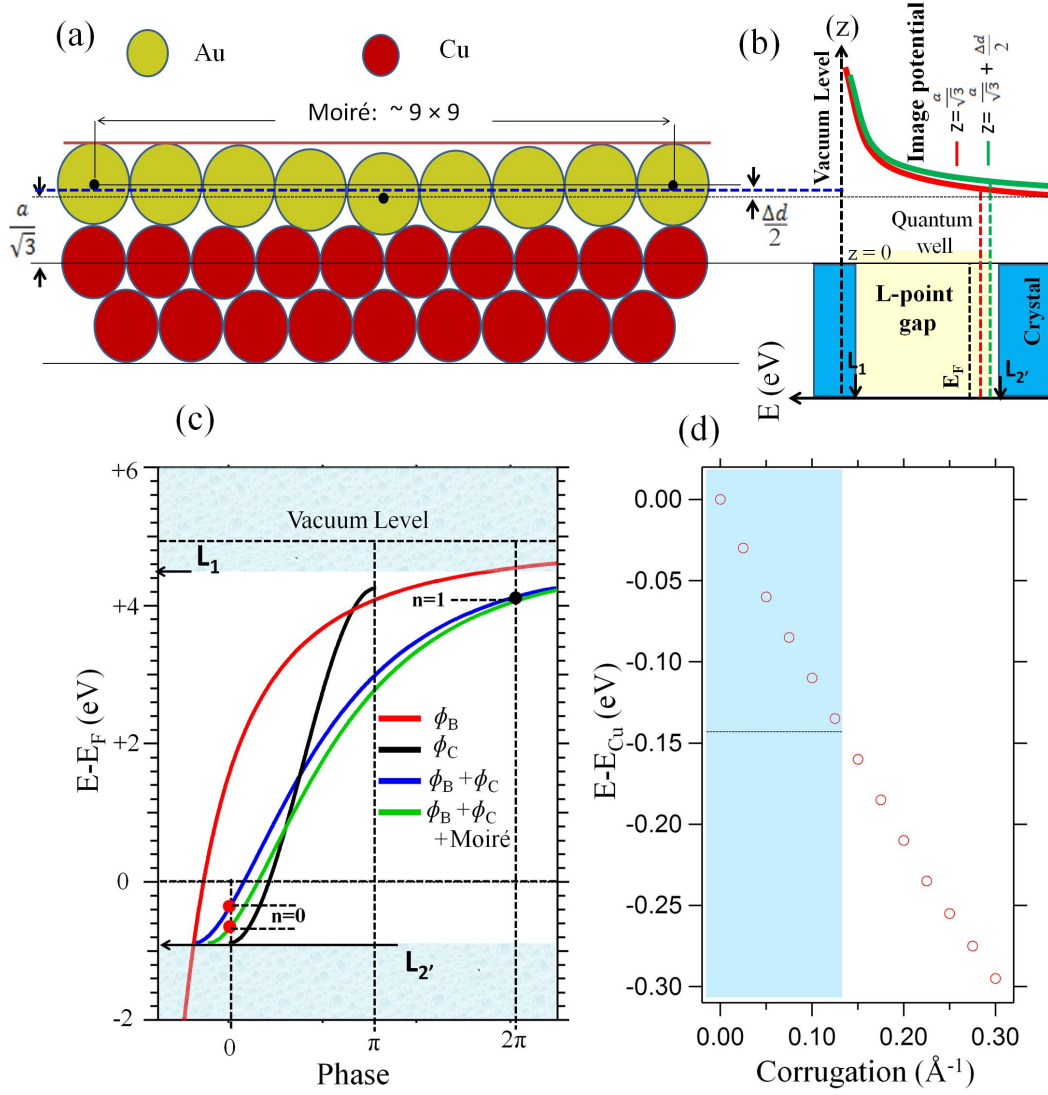


Figure 3.11: Phase Accumulation Model: moiré Corrugation Effect - (a) Hard-ball model representation of the 9×9 moiré pattern for 1 ML Au/Cu(111) excluding the actual situation of the alloy formation. (b) Schematic drawing of the potential in the vicinity of the flat (red) and corrugated (green) surface shown in (a). Their corresponding surface states (confined in the quantum well formed by the image potential and crystal gap defined at the L-point edges) are marked by dashed red and green lines, respectively. (c) Energy variation of the reflection phase changes at the image potential ϕ_B , crystal barrier ϕ_C , and $\phi_B + \phi_C$ for the $L_2'-L_1$ gap in Cu(111) without and including some corrugation due to the moiré. (d) The energy shift with respect to Cu(111) band minima as a function of the moiré corrugation.

where ϕ_C and ϕ_B are the crystal and barrier phase changes, respectively, and n is an integer number. The energy dependence of both ϕ_C and ϕ_B were estimated to be^[96,98];

$$\phi_C = 2\arcsin\sqrt{\frac{E - E_L}{E_U - E_L}}, \phi_B = \pi\left(\sqrt{\frac{3.4\text{eV}}{E_V - E}}\right) - 1 \quad (3.2)$$

where E_L , E_U and E_V , are the lower and upper edges of the crystal bulk gap (at the L -point) and the vacuum energy defined by the sum of Fermi energy and work function, respectively. If a thin film is inserted between the solid-vacuum interfaces, Equ. (3.1) reads^[136,137];

$$\phi_B + \phi_C + 2k_{\perp}d = 2\pi n \quad (3.3)$$

where k_{\perp} is the momentum perpendicular to the surface and d is the film thickness.

To consider the corrugation of the moiré we have used Equ. (3.3) by replacing k_{\perp} by the ΓL wave vector $(\pi\sqrt{3})/a$ and $d = a/\sqrt{3} + \Delta d/2$, where Δd is the corrugation due to the moiré, as sketched in Fig. 3.11(a)^[138]. Increasing the moiré corrugation, thus Δd , results in increasing the width of the quantum well that confines the surface state, Fig. 3.11(b). Using $E_L = -0.89$ eV, $E_U = 4.25$ eV, and $E_V = 4.95$ eV as reported for Cu(111)^[98], the phases in Equ. (3.1) and (3.3) are plot in Fig. 3.11(c-d). The surface state solution occurs at a total phase of $\phi = 0$ ($n = 0$). The blue (green) line is the total phase shift in the absence (presence) of moiré. Using ~ 0.25 Å^[126] as a corrugation, similar to the one reported for Ag/Cu(111), a shift of 300 meV is obtained; see red dots in Fig. 3.11(c). We also plot the energy downward shift as a function of the corrugation in (d). The shaded area encloses the energy shifts reported here for AuCu alloy, where a maximum shift of 140 meV was obtain. This value corresponds to a corrugation of about 0.13 Å.

We observed in the STM images different regions with different corrugations reflected, then, in ARPES as broad peak features. The roughness varies as well with the annealing temperature and, therefore, combination of highest binding energy and sharp profiles represent a stable phase of AuCu alloy, explaining the minima positions in Fig. 3.8. Since in the present case of AuCu alloy, the Cu and Au atoms corrugations can be in the range from 0 Å to 0.25 Å, the estimated roughness of 0.13 Å represents the average value, which is half the moiré corrugation in Ag/Cu(111).

3. RESULTS AND DISCUSSION I

3.3.2 Quantum Well States on Au/Cu(111) Surface Alloy:

So far the Au coverage reported in the present chapter was limited to a maximum of 1 ML Au. The LEED pattern recorded in this coverage regime reveals a Cu(111)-like pattern with the same lattice parameter as for Cu(111). The STM images, on the other hand, show a disordered quasi-Moiré superstructure between the AuCu surface alloy and the supporting Cu(111) substrate. The homogeneity of the alloy and the moiré-like pattern were found to be dependent on coverage and annealing temperature. We also noticed that, for < 1 ML Au coverage, patches of 2 ML Au coexist with 1 ML Au and clean Cu(111) patches. The 2 ML Au patches were also found, as seen by STM, to form AuCu surface alloy with the same quasi-moiré like pattern. It is such observation that motivates the study of higher Au coverage, where one can tune the depth of the alloyed layers (the thickness of the AuCu alloy on the supporting Cu(111) substrate) via Au coverage and the annealing temperature. Sharpe interface between Ag multilayer and, for example, Cu(111) and Au(111) substrate have been subject to intensive studies, due to the formation of quantum well states dispersing with the film thickness [109,136–141]. Similar studies on Au multilayer on Cu(111) annealed to different temperature are not reported in previous works. For low temperature (100 K) deposition of ~ 4 ML Au

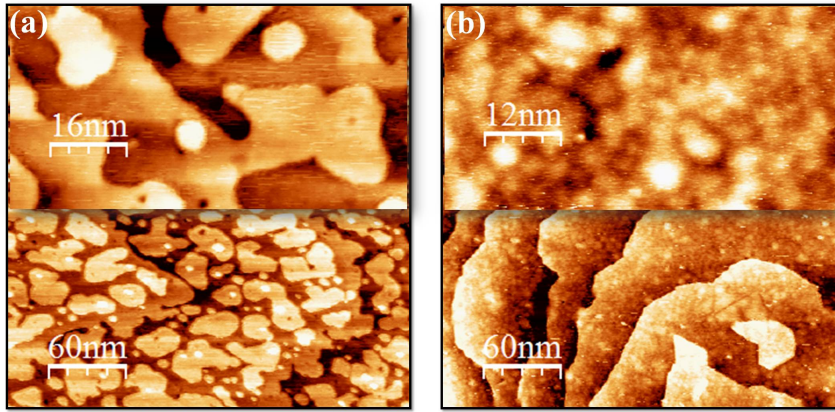


Figure 3.12: STM Images: 3 ML Au/Cu - STM images for 3 ML Au/Cu(111) after deposition at 100 K(a) followed by annealing to 600 K (b). The upper halves in (a) and (b) are small scale scan showing the absence (a) and existence (b) of superstructures.

on top of Cu(111), our STM images show an island-growth mode for Au without any detectable alloy formation, Fig. 3.12(a). After annealing to ~ 600 K, the merging

and smoothing of the islands together with the formation of the AuCu alloy and the quasi-moiré like pattern was formed, Fig. 3.12(b). Apart from the large inhomogeneity of the alloyed surface, the large scale STM image shows almost flat surface with few, alloyed, islands. This, in turn, allows working with surface averaging techniques, such as LEED and ARPES, meaningful.

In order to investigate the dependency of both the surface geometry and electronic structure on Au coverage as well as the annealing temperature, we have prepared (at 180 K) Au wedge of thicknesses from ~ 2 ML to ~ 5 ML, as schematically described in Fig. 3.13. We then performed a systematic analysis of the geometric and electronic structure by scanning the electron beam (in LEED) and the light spot (in ARPES) across the wedge annealed to different temperature. The results presented here are the data taken across the wedge shown in Fig. 3.13, where a Cu(111) stripe is left free for direct comparison of lattice parameters and surface state dispersion in both LEED and ARPES, respectively. The spot at the edge of the wedge, between Cu and the 2 ML Au/Cu, was used in LEED for accurate mapping of possible tiny lattice parameter changes.

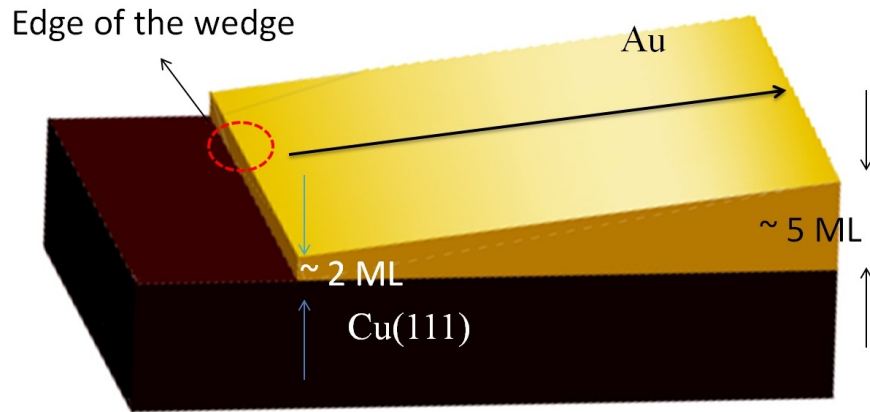


Figure 3.13: Schematic Drawing of Investigated Samples: Au/Cu Wedge - Schematic representation of the investigated Au wedge on top of Cu(111) substrate. The Au coverage dependent LEED and ARPES data were taken along the black arrow. The Cu free stripe and the edge of the wedge, between Cu and 2ML Au/Cu, (red circle) are used for comparison.

Figure 3.14 shows the LEED patterns recorded across the Au wedge at different annealing temperature. The as deposited case will be used as a reference to assign

3. RESULTS AND DISCUSSION I

the Cu and Au related spots. These are represented by the vertical blue and yellow dotted lines for Cu(111) and Au(111), respectively. We notice that, for coverages ≥ 2 ML Au, only the (1×1) spots of Au are seen, the sharpness of which increase with annealing temperature up to 550 K. This indicates no noticeable surface alloying up to this temperature. Annealing to higher temperatures results in the smooth evolution from Au(111)-like spots, at 550 K, to almost Cu(111)-like spots, at 800 K. The lattice parameter at 650 K and 750 K was estimated to be ~ 2.70 Å and ~ 2.65 Å, respectively, in comparison to the surface lattice parameter of Cu(111), 2.55 Å, and Au(111), 2.88 Å. At 800 K, the lattice parameter was the same as Cu(111). Such LEED findings together with the UPS study of the *d*-bands of Au and Cu can shed some light into the structural evolution with the Au coverage and annealing temperature.

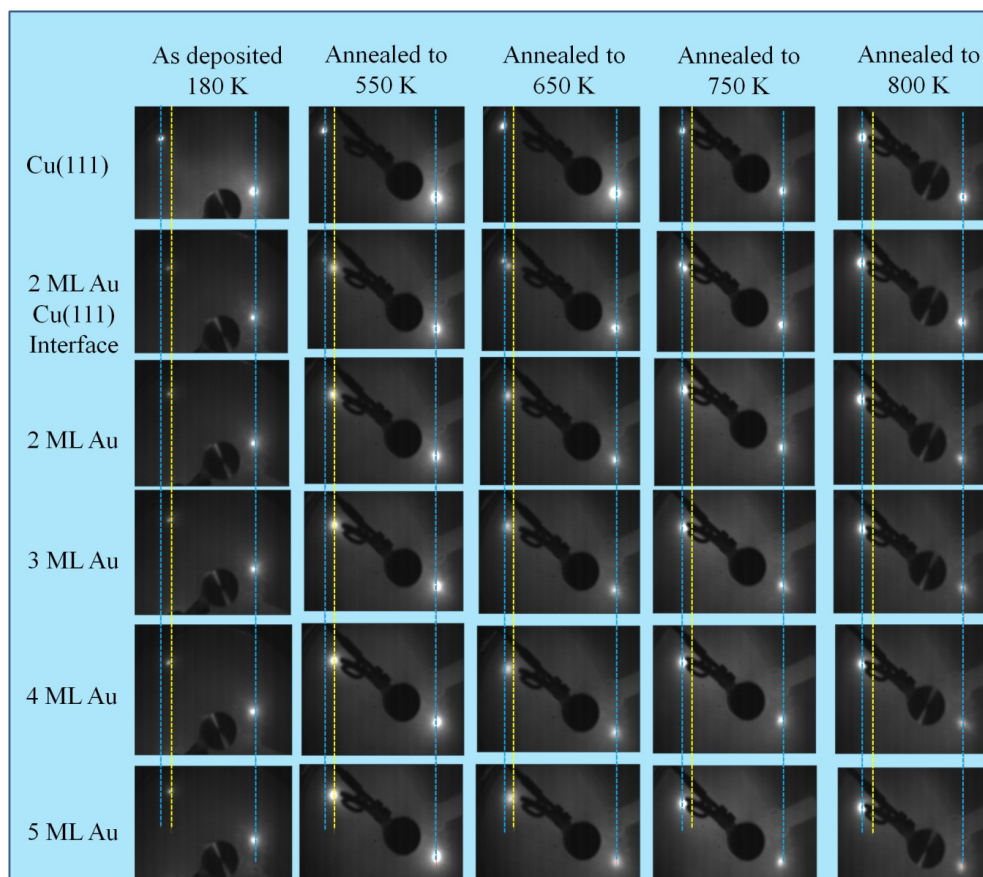


Figure 3.14: LEED Patterns across the Au/Cu Wedge - LEED patterns for the as prepared and subsequently annealed Au/Cu system as a function of Au coverage. Electron energy was 100 eV.

In Figure 3.15 we display the valence-band spectra for Au films of different coverage annealed to increasing temperature taken at normal emission. All photoemission data were taken at 180 K and with He I line (21.22 eV). The binding energy of the Cu(111) *d*-bands (the black spectra and the shaded pink area) is between 2.96 eV and 3.9 eV. For Au, the binding energy read of the *sd*-bands is between 3.0 eV and 6.2 eV (see the 5 ML Au deposited at low temperature, in this spectrum due to the mean free path of the photoelectrons of approx. 2-3 ML only the Au electronic structure is observed). That energy region is identified by a shaded yellow area. There is a small overlap with the Cu energy region; nevertheless both spectral features from Cu and Au are easy to distinguish. We notice that, all Au coverages follow, qualitatively, the same trend with the annealing temperature. For the as deposited and the 550 K annealed cases, the Cu(111) *d*-bands are completely quenched, indicating a complete wetting of Au starting already from 2 ML. Going from the as deposited to the 550 K annealed sample, only the quality of the spectra is slightly improved agreeing with the sharpness of the LEED pattern without any change in the observed Au lattice parameter.

For higher annealing temperatures, the *d*-bands spectra change toward Cu(111)-like with, however, less intense *d*-bands and different relative intensities. It is only for the 800 K annealed sample where the *d*-bands profile is very close to that of the Cu(111). We conclude that, at this annealing temperature the Au atoms, to large extent, leave the surface agreeing with the LEED observation, where the Cu(111) lattice parameter is completely recovered. The contribution from the Au *d*-bands is hardly visible for the annealed samples.

The left panel of Fig. 3.16 shows the *d*-bands of the 4 ML Au annealed to 650 K, 750 K, and to 800 K. The energetic position of the Cu and Au bands are, respectively, marked with the red and blue lines. We attribute the new broad peaks (black arrows) observed at - 5.3 eV and - 6.7 eV to Au atoms alloyed within the Cu substrate^[120]. At 650 K a little contribution from the un-alloyed Au patches is still visible close to - 4.8 eV. This feature is quenched with annealing to 750 K together with enhancement of the alloy related peaks intensities. At 800 K, only little contribution from the alloy related peaks is still visible and the overall spectrum is mainly Cu-like. These observations can be explained by the schematic representation shown in Fig. 3.16(b), which also show good agreement with the LEED patterns. The Au atoms that constitute the

3. RESULTS AND DISCUSSION I

Au islands (or bigger flat Au islands when slightly annealed up to 550 K) diffuse and alloy with the Cu atoms in the bare Cu substrate when annealed to temperatures higher than 550 K. The depth (thickness) and the quality of the alloy can be tuned by annealing, for example, as we go from 650 K to 750 K in the present case. The Au film represents the source of Au atoms, and the temperature serves as top-down tool for the formation of alloyed thin films with tunable thicknesses on top of the Cu substrate. We cannot, however, completely exclude a possible variation of the alloy composition (rather than alloy thickness) with the annealing temperature, where $\text{Au}_x\text{Cu}_{1-x}$ can be formed. Information regarding the alloy composition is not available at the moment, and further studies, such as XPS, are still required.

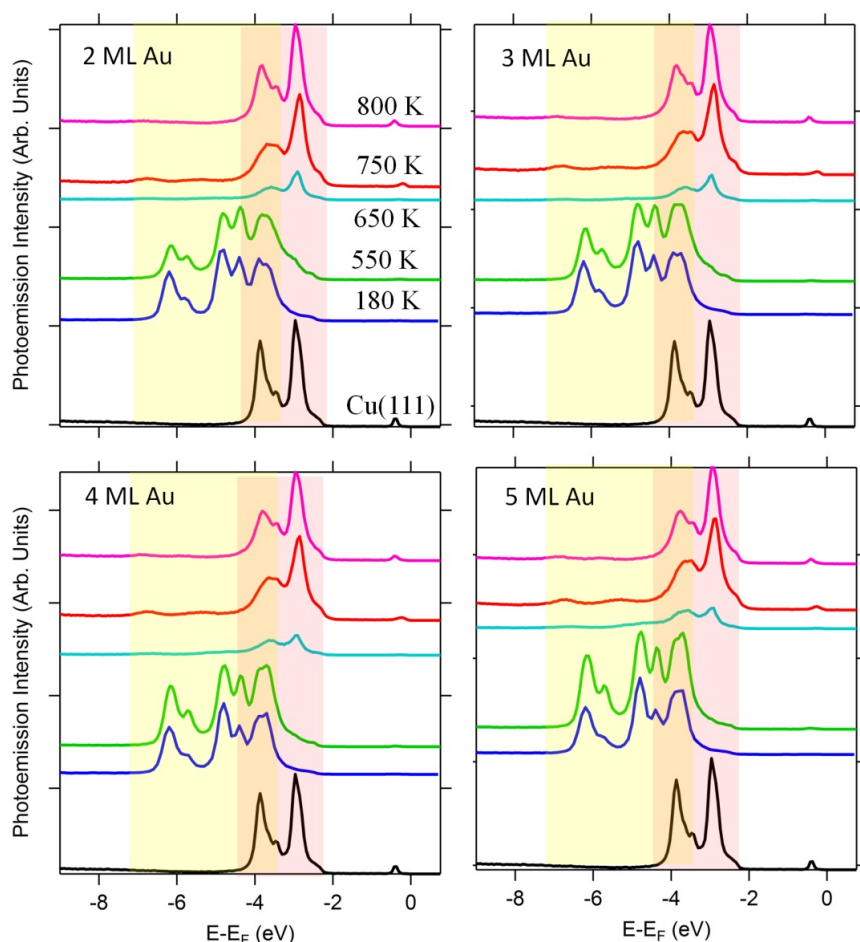


Figure 3.15: Valence Band: Au/Cu Wedge - Valence-band spectra for 2 ML-5 ML Au/Cu(111) with the annealing temperature.

In Fig. 3.17 photoemission intensity plots showing the surface state dispersion as a function of Au coverage for the as deposited (top panel) and the 550 K annealed sample (middle panel) are displayed. The lower panel of the figure shows a series of EDCs taken at the band minima as function of Au thickness. The band minima of Cu(111) and the 2-3 ML Au/Cu surface state (as deposited) are , respectively, -0.415 eV and -0.471 eV measured at 180 K. The latter value agrees with the value reported for the Au(111) crystal^[100], indicating no alloying with the Cu substrate. For the as prepared sample and for higher Au coverage the Au-like surface state shifts toward the Fermi level indicating higher amount and height of Au islands. After annealing to 550 K, the Au-like surface state has the binding energy of the Au(111), indicating a smoothing, rather than alloying, of the Au islands into bigger and flat Au covered regions. We have seen from the low coverage (< 1 ML) AuCu system, that at 550 K

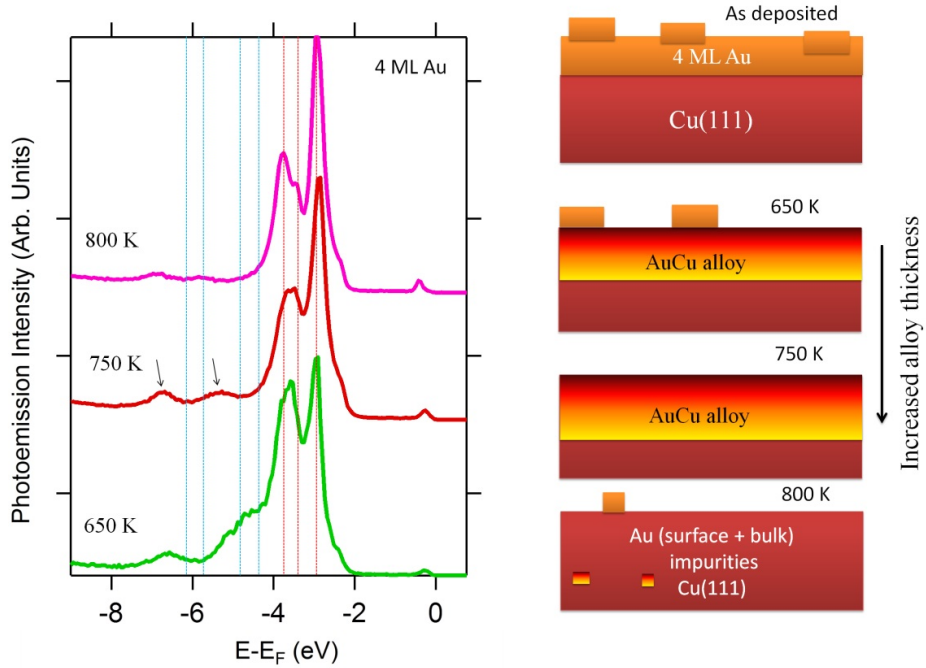


Figure 3.16: Valence Band and Growth Mechanism - Left: Valence-band spectra of 4 ML Au/Cu(111) after annealing to 650 K, 750 K, and 800 K. Right: Schematic representation of the proposed growth mechanism and alloy formation with annealing.

a slight alloy of 0.2 ML at the Au/Cu interface takes place, which in turn shifts the Cu surface state by ~ 20 meV to higher binding energy. We cannot, therefore, exclude a

3. RESULTS AND DISCUSSION I

possible tinny alloying at the Au/Cu interface, which insignificantly shifts the surface of the Au adlayers.

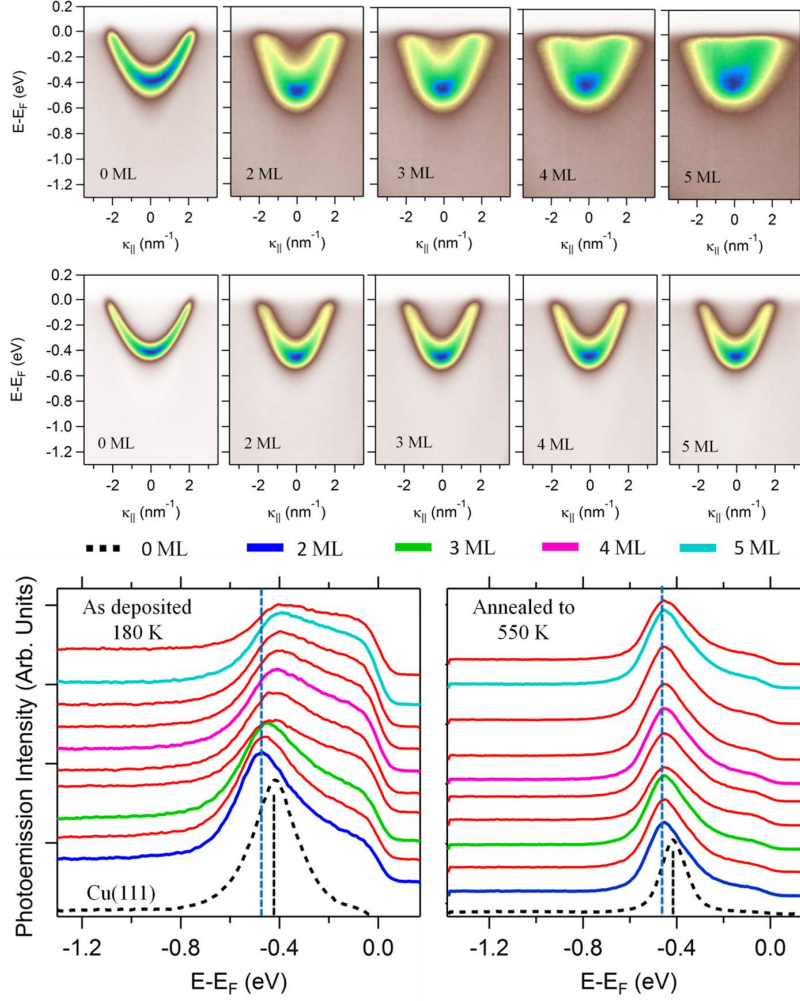


Figure 3.17: ARPES Data: As-Deposited Au/Cu - ARPES photoemission intensity plot of the Au wedge/Cu(111) for the as deposited (top panel) and the 550 K annealed (middle panel) sample. The lower panel display EDC series at the band minima in the two cases.

The combined analysis of LEED, valence bands, and surface states in ARPES confirm, therefore, the Au termination of the surface. A closer view to both LEED and ARPES spectra for the as deposited 3 ML Au is displayed in Fig. 3.18. Moiré like superstructure spots are seen with, however, much smaller periodicity (11×11) compared to the herringbone ($22 \times \sqrt{3}$) characteristic for the Au(111) crystal^[142]. In ARPES,

on the other hand, the intensity variation and the broadening from the band bottom up to the Fermi level points toward un-resolved spin-orbit split surface state (hardly visible even in the second derivative), where the dispersion parameters of Au(111) surface state (dashed parabolas) coincide on the photoemission intensity plots shown in Fig. 3.18.

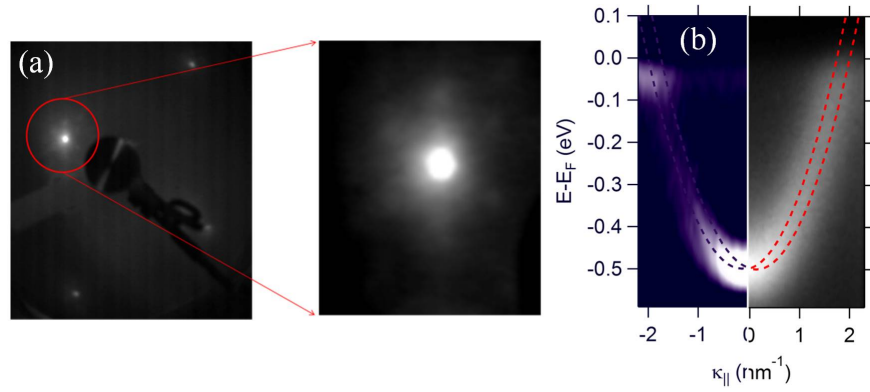


Figure 3.18: LEED Pattern vs. Dispersion Plot: 3 ML Au/Cu - A close view to the as-deposited 3 ML Au/Cu(111) LEED pattern (a) and the corresponding ARPES intensity plot of the surface state (b). The second derivative of the ARPES image is displayed to the left.

After annealing to 650 K, the Au-like surface state acquires a lower binding energy than Cu(111) and becomes, significantly, dependent on Au coverage, see Fig. 3.19. Quantum well/resonance states are also developed and were found to disperse with the alloy thickness across the Au wedge. The same states are still there after annealing to 750 K with, however, different binding energies. The surface state for the 750 K annealed sample is, now, almost Au coverage independent with a binding energy of 0.3 ± 0.01 eV. The fixed energetic position of this state indicates that the thickness of the formed alloy has established its bulk value, where only the quantum well/resonance states are dispersing with Au coverage. For Au coverage > 3 ML only two broad quantum wells are observed.

After annealing to 800 K, and at all Au coverages, the quantum well states completely vanish and the surface states shift towards higher binding energies and getting close to the value of Cu(111), Fig. 3.20. We argue that Au desorption takes place, as commented in Fig. 3.16, where few Au atoms are still doping the substrate (for less

3. RESULTS AND DISCUSSION I

than 3 ML Au) and/or forming tinny clusters on top (for ~ 5 ML Au). Such ARPES finding is confirmed by LEED and the valence band data.

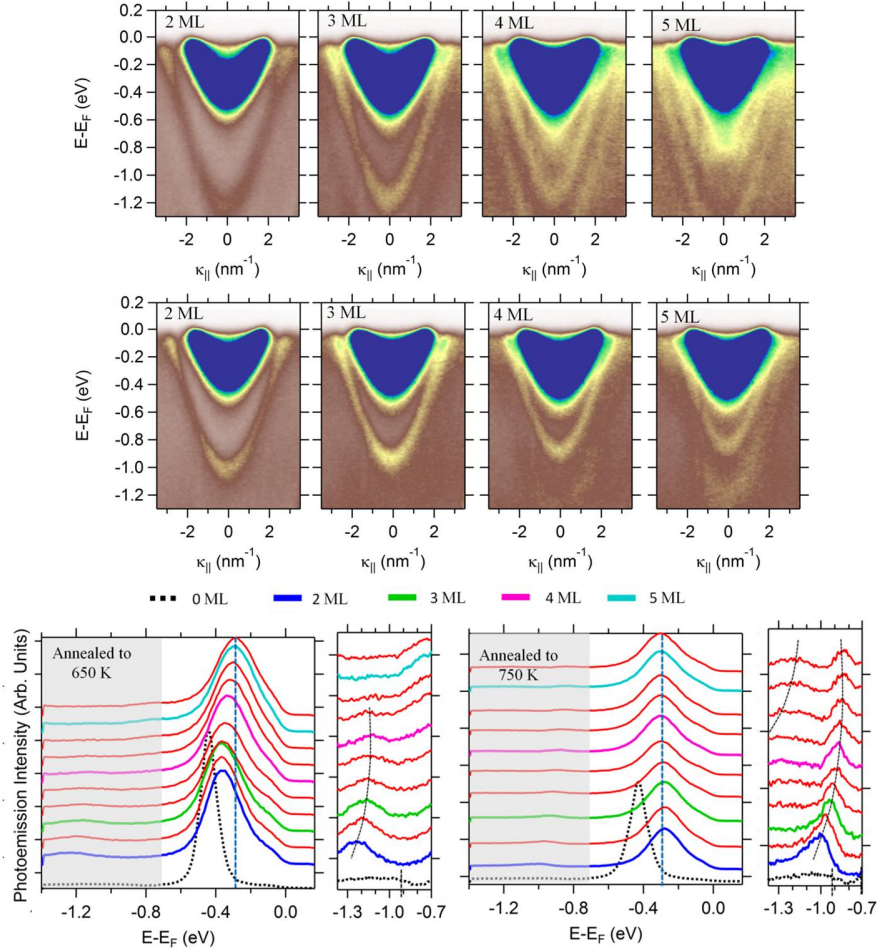


Figure 3.19: ARPES Data: 650 K-700K Annealed Au/Cu - ARPES photoemission intensity plot of the Au wedge/Cu(111) for the 650 K (top panel) and the 750 K (middle panel) annealed sample. The lower panel display EDC series at the band minima in the two cases. The gray shaded areas are zoomed in to the right of each EDC series.

Coming back to the region of interest, at 650 K and 750 K, where all evidences point toward surface alloy formation with thickness (or rather probably composition) dependent Au coverage and annealing temperature. Figure 3.21 summarizes the energetic position of the quantum well/resonance states ($n = 1$ and $n = 2$) after fitting the corresponding EDCs for the 650 K and 750 K annealed cases. We note that, the band minima of the second quantum well states were always out of detection. We,

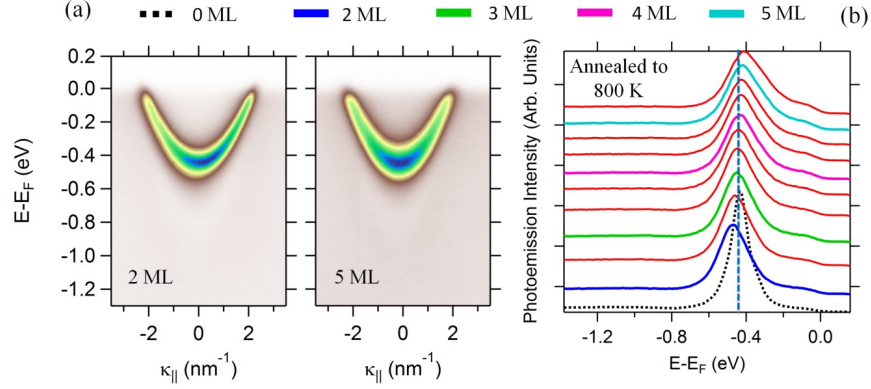


Figure 3.20: ARPES Data: 800 K Annealed Au/Cu - (a) ARPES photoemission intensity plot of the 2 ML and 5 ML Au/Cu(111) annealed to 800 K. (b) EDC series at the band minima as a function of Au coverage.

however, extracted the energetic position of their band minima by fitting the visible part of the state with a free-electron-like parabola with the same effective mass as the first quantum well states. We also used the phase accumulation combined with the two band model, see appendix A, to have an estimation of the AuCu alloy thickness. The results of such model calculation are represented by the black solid lines in Fig. 3.21. In the model we fix the lower (E_L) and upper(E_U) edges of the bulk projected gap (L_2 - L_1) of Cu(111) as explained in Fig. 3.11. The average interlayer separation calculated using the lattice parameters obtained from LEED (these are, 2.21 Å and 2.16 Å for 650 K and 700 K annealed samples) was fixed. The variable parameters within the model were, the vacuum energy (E_V), the reciprocal lattice vector of the overlayer (G), the Fourier-coefficient of the overlayer crystal potential(V_g), and the film thickness (d). The fit of the data points to the model was found to be very sensitive to these parameters, although all combination of parameters does not fit to the data if the Au/Cu alloy formation is not taken into account. The Au film thickness is, therefore, rescaled to account for Au/Cu alloy formation assuming an initial stoichiometry close to $\text{Au}_{0.3}\text{Cu}_{0.7}$ for the 2 ML Au annealed to 650 K. This assumption was based on the XPS and STM analysis, discussed in the previous sections, where a similar stoichiometry was obtained for 1 ML Au. A single scaling parameter to account for such fixed stoichiometry of Au/Cu alloy was not possible, indicating a certain variation in the stoichiometry, however, with defined QWSs; see the x-axes in Fig. 3.21(a). Using $V_g = 2.15$ eV, E_G

3. RESULTS AND DISCUSSION I

$= 8.7$ eV, and $E_V = 11.18$ eV, we obtained a reasonable fit to the data points; see black solid lines in Fig. 3.21(a). The resulting bulk dispersion along the ΓL direction is also shown in Fig. 3.21(b), with the lower and upper edges of the bulk gap of the alloy are, respectively, at -0.5 eV and $+3.9$ eV, hence the $L_{2'}$ gap edge (that defines the surface state energy) is shifted by 0.39 eV towards lower binding energy compared to the Cu(111) substrate (red dashed lines). Therefore, the estimated -0.3 eV band minima for the alloy surface state can be attributed to the shift in the bulk projected gap of the bulk Au/Cu alloy.

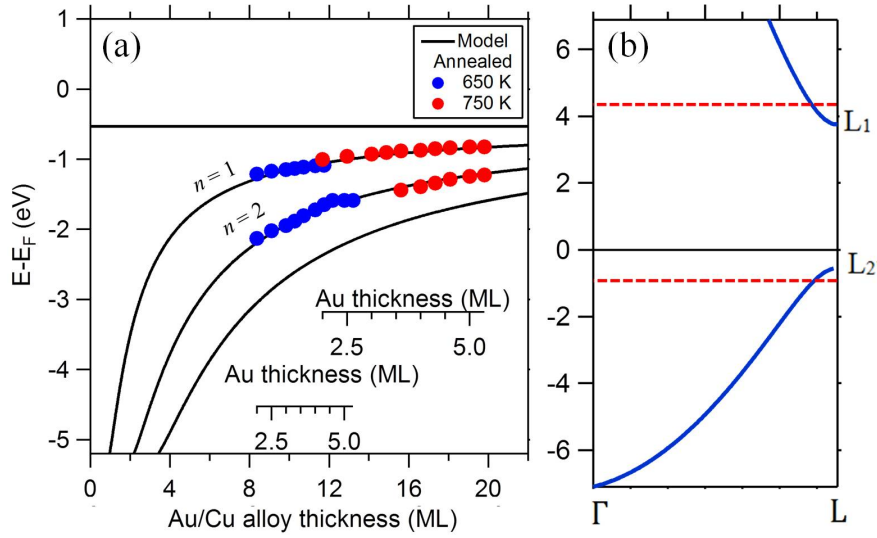


Figure 3.21: Phase Accumulation Model: 650 K and 750 K Annealed Au/Cu - (a) The band minima energetic position of $n = 1$ and $n = 2$ QWSs for the 650 K (blue) and 750 K (red) annealed Au wedge (2 ML-5 ML) on top of Cu(111). The black lines are fit to the data using the phase accumulation model. (b) The resulting bulk dispersion along the ΓL direction of the Au/Cu alloy as obtained from the phase accumulation model. The red dashed lines defined $L_{2'}$ and L_1 for Cu(111).

3.4 Conclusions:

We have shown that the sub-monolayers deposition of Au on top of Cu(111) allows us to tune the dispersion of the Shockley type surface state with respect to its binding energy, effective mass, and Fermi wavevector. The annealed Au/Cu system led to a surface alloy that presents a moiré pattern with respect to the Cu(111) substrate. The

presence of such moiré pattern changes the effective surface potential and causes the modification of the surface electronic structure. We estimated a significant (~ 140 meV) downward shift of the surface state band minimum for 0.67 ML Au annealed to 600 K. An effective mass of $0.35 m_e$ was obtained in the latter case.

We have also shown that, for Au coverage above 2 ML similar alloy and moiré like pattern formation takes place. Annealing the multilayer Au/Cu(111) allows us to fabricate an Au/Cu alloy with tunable thicknesses. Since the source for Au atoms that form the alloy was the un-alloyed Au thick layers, we considered this approach as a “*top-down*” fabrication induced by the annealing temperature. The alloyed multilayer Au/Cu(111), after annealing to 600 K or 750 K, features QWSs that disperse with Au/Cu alloy thickness for each temperature. The presence of such QWSs, on one hand, allows us to estimate the alloy thickness using the phase accumulation model and, on other hand, serve as a proof to the homogeneity of the Au/Cu alloy.

3. RESULTS AND DISCUSSION I

Part II: Lifshitz Transition across the 1 ML Ag/Cu(111) Superlattice Band Gap Tuned by Interface Au alloying

3.5 Introduction and Literature Survey II:

Of major importance in modern technology are solid interfaces between ultra thin films and solid substrates. Generally speaking, three markedly different modes of film growth can be distinguished. These are schematically represented in Fig. 3.22. In the layer-by-layer growth mode the interaction between substrate and layer atoms is stronger than that between neighboring layer atoms. In this case, each new layer starts to grow only when the last one has been completed. In contrast, in island growth mode, the interaction between the neighboring film atoms exceeds the overlayer substrate interaction. The layer-plus-island growth mode (Stranski-Krastanov, SK), however, is an interesting intermediate case. After formation of one, or sometimes several complete monolayers, 3D islands grow on top of the first complete layer or layers. Many factors might account for this mixed growth mode: A certain lattice mismatch between substrate and deposited film may not be able to be continued into the bulk of the epitaxial crystal. Alternatively, the symmetry or orientation of the overlayers with respect to substrate might be responsible for producing this growth mode^[31].

The system of interest in the present chapter is a metallic monolayer on top of metal substrate, namely 1 ML Ag on top of Cu(111). The growth of Ag on top of Cu(111) follows the Stranski-Krastanov growth mode, where a layer-by-layer is observed up to Ag film thicknesses of 2 ML. Due to, in contrast to Au and Cu, the immiscibility and the large lattice mismatch (13 %) between the Ag ($d = 2.89 \text{ \AA}$) deposit and the Cu(111) substrate ($d=2.55 \text{ \AA}$), the 1st and 2nd Ag MLs were found to form a moiré pattern. In fact, 1 ML Ag/Cu(111) features a hexagonal moiré pattern with a (9×9) periodicity

3. RESULTS AND DISCUSSION I

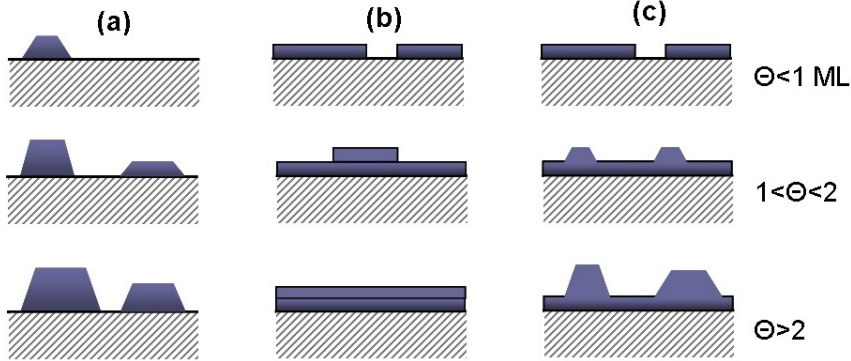


Figure 3.22: Growth Modes - Schematic drawing illustrating the three important growth modes of a thin film for different coverage (Θ) regimes (ML stands for monolayer). (a) Island growth (Vollmer-Weber, VW). (b) Layer-by-layer growth (Frank-van der Merve, FM). (c) Layer-plus island growth (Stranski-Krastanov, SK). Taken from Wikipedia.

when deposited at low temperature (LT). A soft annealing to room temperature (RT), or equivalently, deposition at RT followed by soft annealing to 400 K results in a superstructure of a dislocation network with $\sim 9.5 \times 9.5$ periodicity. This irreversible evolution of the moiré into dislocation network is theoretically understood as a result of Cu atoms removal of the substrate^[143]. These findings concerning the structure have been theoretically and experimentally (STM, LEED, and SXRD) examined^[143–146]. Such ordered superstructure with nanoscale periodicity is of obvious importance, since it can be used as a template for self-organization of magnetic dots, quantum dots, organic molecules, etc, in the same analogue to other well-known strained metallic layers^[128,147,148].

Of particular interest is the surface electronic structure of such 2D lateral superlattices. The 1 ML Ag/Cu(111) system features a Shockley type surface state with a binding energy in between those of the clean Ag(111) and Cu(111), see appendix A. Using Angle Resolved Photoemission Spectroscopy (ARPES) and Scanning Tunneling Spectroscopy (STS), the transformation from moiré into a dislocation pattern has been nicely reflected in the energetic position of the surface state band minimum. The strong scattering of surface electrons by the dislocation network has led to a surface state with lower binding energy (~ 0.190 eV) as compared to the weakly scattering

moiré superstructure ³ (~ 0.290 eV)^[45,46,127,149]. In fact, the effect of the moiré to dislocation transformation was only seen as defects inducing an upward shift of surface states. The effect of such “*periodic*” array of scatterers (dislocations) on the dispersion of the surface state was first reported by Schiller et al.^[50,51]. They observed a band back-folding of the surface state and a gap opening at the \bar{M} -point. This is actually the case when a surface presents a superstructure, since the potential has nonzero component at the surface Brillouin zone (SBZ) boundaries. Interestingly, the \bar{M} -point gap was found to lie at the Fermi energy, the finding of which can explain why the incommensurate 9.5×9.5 dislocation superstructure (which costs 1.3 % lattice compression) that characterizes this system is favored compared to the gapless moiré commensurate 9×9 reconstructions (which costs only 0.4 % lattice compression)^[50,51]. The periodicity of the moiré and dislocation superstructures was then deduced from the dispersion along $\bar{\Gamma}\bar{M}$ direction, where a wavevector at the \bar{M} -point of 0.16 \AA^{-1} (i.e. 9×9) and 0.15 \AA^{-1} (i.e. 9.5×9.5) for the moiré and the dislocation, respectively, have been estimated^[50–52,111]. Using ARPES and by performing an angular scan, the Fermi surface (FS) as well as the band structure of the Ag/Cu(111) system were determined. In case of the dislocation superstructure, it is shown that the FS is nested (gapped) with small hole pockets at the \bar{K} -points. Interestingly, the measured band structure reveals the presence of a tiny gap at the \bar{K} -point, and an overall gap $\bar{\Gamma}\bar{M}\bar{K}\bar{\Gamma}$ of 25 meV was, then, found to be a direct gap^[51,53]. Later, it has been shown that it is the three-fold symmetry of the dislocation network that lifts the degeneracy at the \bar{K} -point, compared to the gapless six-fold symmetry moiré superstructure^[53]. The observed band structure is thus quite similar to the technologically interesting gapped-graphene^[55]. Although electron scattering and transport properties in such noble metal dislocation networks have not been investigated yet as for graphene, the discovery of this novel band structure, and, in particular, the presence of gaps, has prompted the concept of surface state nanoelectronics^[54], in analogy to nano-optics and plasmonics. The difficulties within this area concern, however, the way the energetic position of the band gaps can be tuned without affecting the spectral features, hence without significant decrease of the life time^[54].

³We have shown in part I of this chapter, that the moiré superstructure (contrary to the dislocation scatterers) shifts the surface state towards higher binding energies.

3. RESULTS AND DISCUSSION I

Motivated by these findings, this chapter mainly reports the possibility of further engineering the surface electronic structure of the 1 ML Ag/Cu(111) dislocation system by means of interface Au doping. The chapter can then be divided into two sections. First, the surface electronic structure of the clean 1 ML Ag/Cu(111) will be reexamined and to be used as a reference for the Au doped system. Second, the effect of Au doping (alloying) on the electronic structure of the 1 ML Ag/Cu(111) system will be discussed. Attention will be paid to the “*Liftshitz Transition*” induced by a certain amount of Au doping. The electronic structure as a function of the temperature, in the undoped and Au doped systems, will be discussed and information concerning the lifetime of the hole states will be extracted. The Au doping or Au multilayer’s grown on the 2 ML Ag/Cu(111) and the 1 ML Ag/Cu(111) will be, qualitatively, discussed.

In the two sections, STM images and LEED patterns for each system will be analyzed. They appear throughout the text, when required, to facilitate the interpretation of the ARPES data, and allow for structural/electronic interplay to be clearly seen. A theoretical calculation for the electronic band structure, constant energy surfaces (CES) and local density of states (LDOS) will be presented and compared to ARPES data for the un-doped and Au doped 1 ML Ag/Cu(111) systems.

3.6 Sample Preparation and Characterization Tools II:

The Cu(111) crystal was cleaned using repetitive cycles of sputtering and annealing as described in chapter two. The Ag and Au metals were deposited on top of the clean substrate using a home-made evaporator. In order to allow for a systematic study and accurate comparison, we take advantage of the large size of the Cu(111) crystal to grow different wedges on the same substrate, as shown in Fig. 3.23. In one direction, the Ag wedge from 0.7 ML up to 1.3 ML (arrow 1 in Fig. 3.23) was grown and annealed to 500 K. A clean Cu(111) stripe is left free at one side of the substrate. In the other direction, a Au wedge from 0 ML up to 1 ML (arrow 2 in Fig. 3.23) was then grown on top, leaving a free Cu(111) area together with a free Ag/Cu(111) wedge (arrow 1 in Fig. 3.23). Since the Cu(111) surface state is very well studied, as discussed in appendix A, area 0 will be kept as a reference to better calibrate both the energy and momentum for the other investigated regions. The whole sample is then annealed to different temperatures, ranging from 400 K up to 700 K. Arrow 3 samples the 1 ML Ag (after

the investigation of arrow 1) on top of the Au/Cu(111) wedge. Therefore, the electronic structure along the three different arrows will be detailed in the subsequent sections. The Au/Cu system (arrow2) is already investigated in section one of this chapter and, therefore, data will be called for comparison. We note, however, that, after investigating the electronic structure along each arrow grown on the same sample, each system can be then prepared separately for more investigations. All the measurements presented here have been taken in San Sebastián (LEED, STM, and ARPES). The measurements were carried out at room temperature, unless specified. In ARPES, the He-I α line ($h\nu = 21.22$ eV) has been used. The surface state has been measured in low angular (LAD) and/or wide angular (WAM) modes, and data were prepared according to the routines described in appendix B.

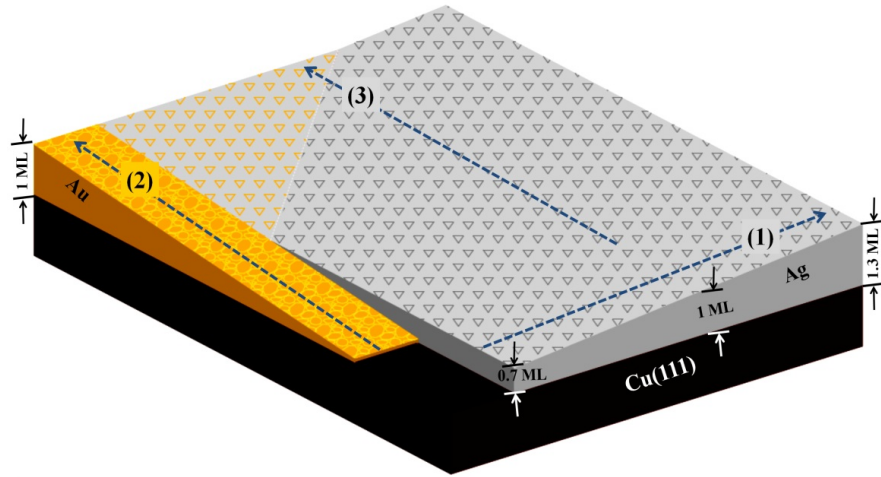


Figure 3.23: Wedges Preparation: Ag/Au/Cu(111) - Schematic description of the sample preparation procedure showing the Ag and Au wedges grown on top of the Cu(111) crystal.

3.7 Results and Discussion II:

3.7.1 1 ML Ag/Cu(111) Gapped Superlattice:

In order to know the exact position of the 1 ML Ag over the wedge, an ARPES scan is taken along the Ag wedge (Arrow 1) and the EDSs at the band minima are shown in Fig. 3.24(a). The scan was taken in LAD mode with pass energy of 10 meV and HeI line (21.2 eV). For the partially Ag covered Cu(111) substrate incoherent emission

3. RESULTS AND DISCUSSION I

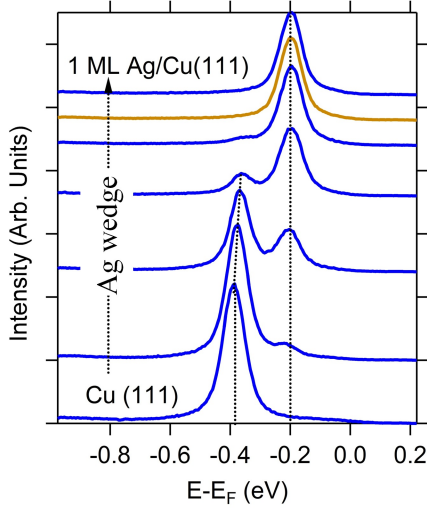


Figure 3.24: Ag Thickness Calibration. EDC spectra of the band minima across the 1 ML Ag/Cu(111) wedge (arrow1) showing the Cu(111) surface state, the 1 ML Ag/Cu(111) surface state (brown EDC), and emission from both Ag and Cu surface states for less than 1 ML Ag.

from Cu and Ag patches is seen due to the emissions of their respective surface states at approx. - 0.39 and - 0.20 meV^[47]. At the 1ML Ag coverage, only one emission peak is seen (brown EDC) with a binding energy of - 0.195 eV, as reported for the 1 ML Ag/Cu(111) dislocation network system.

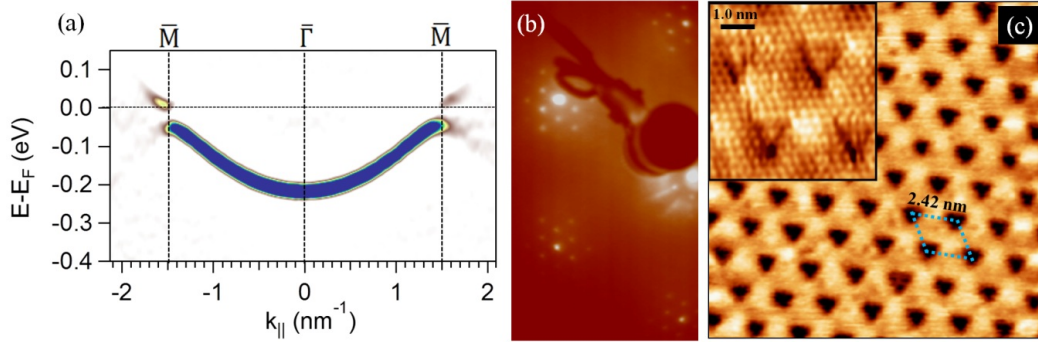


Figure 3.25: ARPES, LEED and STM: 1 ML Ag/Cu - (a) ARPES data showing the band dispersion along the $\bar{\Gamma}\bar{M}$ direction for the undoped 1 ML Ag/Cu(111) annealed to 450 K. Data are shown in the second derivative. (b) The dislocation network as seen by LEED, with approximate periodicity of 9.5×9.5 . (c) STM image ($20 \times 20 \text{ nm}^2$) showing the 1 ML Ag on top of Cu(111) crystal. The unit cell is marked by the dotted blue lines. The 1 ML Ag/Cu dislocation pattern is better seen in the atomic scale image shown in the inset of (c)^[126].

Here we are interested to look at the electronic structure of the dislocation network system. Figure 3.25(a) shows the surface state dispersion of the 1 ML Ag/Cu(111)

dislocation network. The reported \bar{M} -point gap is clearly seen with its size (65 ± 10 meV) and location in momentum space (1.5 nm^{-1}) in a good agreement with the literature^[50–54]. The existence of such gap is triggered due to the formation of the 9.5×9.5 dislocation network superstructure, as shown in the LEED pattern and STM image in Fig. 3.25(b-c)^[126]. The Fermi surface, shown in Fig. 3.26(a), is clearly nested over a large portion of the BZ with electron pockets at the \bar{K} -points. The band structure over the $\bar{\Gamma}\bar{M}\bar{K}\bar{\Gamma}$ directions is plotted in Fig. 3.26(b), where the existence of a small gap (25 meV) slightly above the Fermi level (+50 meV) is clearly seen at \bar{K} -point.

The geometric and electronic structure of the 1 ML Ag/Cu(111) dislocation network superlattice presented here are in excellent quantitative agreement with previous works [13-15, 19]. For the investigations here, only the systematic low temperature measurements, aimed to construct some information about the lifetime due the presence of gaps, will be examined and compared to the Ag/Cu(111) doped with different amounts of Au.

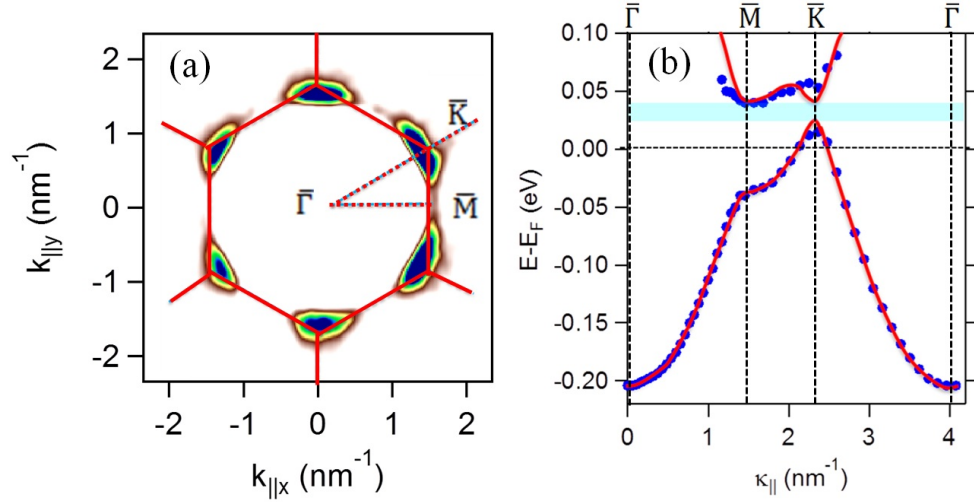


Figure 3.26: FS and Band Structure: 1 ML Ag/Cu - (a) Fermi surface map of the undoped 1 ML Ag/Cu(111). The red solid lines mark the BZ edges and defining $\bar{\Gamma}\bar{M}$ and $\bar{\Gamma}\bar{K}$ directions. (b) Surface band dispersion of the 1 ML Ag/Cu(111) along the $\bar{\Gamma}\bar{M}\bar{K}\bar{\Gamma}$ direction. Data points (blue) are obtained from fits to individual EDC spectra. The solid lines (red) represent the band structure derived from a model calculation using the surface potential shown in Fig. 3.30(b). The shaded region indicates the presence of a full gap.

3. RESULTS AND DISCUSSION I

3.7.2 Au doped-1ML Ag/Cu(111) Gapped Superlattice:

We have shown in section 3.I that the Au/Cu(111) system at specific annealing temperatures is mainly Cu terminated and the corresponding surface state is tunable, and has higher binding energy as compared to the bare Cu(111) surface. This section investigates the surface electronic structure of the 1 ML Ag on top of such Au/Cu(111) system. Figure 3.27 shows the position of the normal emission surface state position as obtained by ARPES along arrow 2 of the wedge sketched in Fig. 3.23. The data points represent the band minima after fitting the corresponding EDC, shown in the inset, with a Lorentzian peak convoluted with a Gaussian to account for the finite energy resolution of the machine.

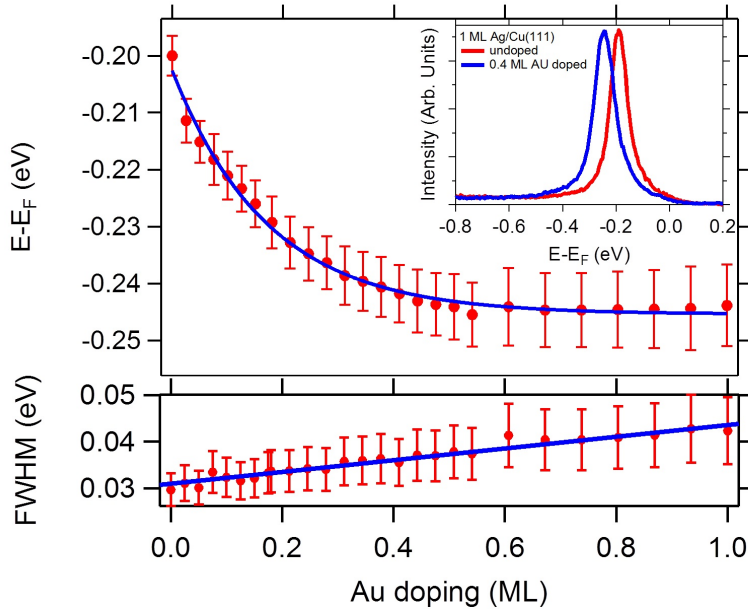


Figure 3.27: Band Minima and FWHM: Au Doped 1 ML Ag/Cu - Top panel: Fits of the EDCs at band minima across the Au/Cu(111) wedge for 1 ML Ag (arrow 2 in Fig. 3.23). The inset shows EDCs at the band minima for (red) 1 ML Ag/Cu(111) and (blue) 1 ML Ag/0.4 ML Au/Cu(111). The lower panel shows the insignificant increase of the line width as a function of Au doping.

The surface state band minimum clearly shifts down as a function of Au doping. At a Au coverage of 0.4 ML the surface state band minimum reaches saturation at $E_B = 0.245$ eV. The maximum shift of the Ag/Cu(111) band minimum is ~ 50 meV (compared to ~ 100 meV shift of the Cu(111) surface state with the same Au doping in

Au/Cu(111) alloy). This is actually expected, since the 1 ML Ag is far separated from the AuCu alloyed layer compared to the top layer of Cu(111) surface. The observation of the band minimum shift is, in fact, similar to the traditional way of doping with alkali metal atoms, such as potassium (K) [54,150,151]. However, the Au “*interfacial*” doping in our case is preferred to the alkali metals “*surface*” doping regarding the inelastic scattering lifetime. This is seen in the lower panel of Fig. 3.27. We estimated a maximum of 17 % percent increase of the Full Width at Half Maximum (FWHM) of the surface state width for Au coverage up to 0.4 ML compared to 300 % increase for the 0.2 ML K doped case [54,126].

Figure 3.28(a) shows the surface band of the 0.4 ML Au doped 1 ML Ag/Cu(111) system along the $\bar{\Gamma}\bar{M}$ direction. In order to extract the energetic position of the lower and upper edges of the \bar{M} -point gap, and hence the gap width, an EDC is taken at the \bar{M} -point (1.47 nm^{-1}) for different Au doping which, in the pure Ag/Cu(111) system, two separate peaks are observed. For small FWHM increase due to the Au atoms, scattering broadens the two peaks making a distinction by eyes, only, not easily possible. Each EDC is then fitted with two Lorentzian peaks, which define the gap edges, a Fermi edge, and convoluted with a Gaussian peak to account for the energy resolution of the machine, as shown in Fig. 3.28(b). The Fermi edge position was determined by a measurement that consisted of moving the light and analyzer spot to the tantalum foil position of the proper sample holder under exactly the same experimental conditions right before or after the measurement of Ag(Au/Cu(111)). The results of such fit for different Au coverages are displayed in Fig. 3.28(c). Both the lower and upper edges of the gap shift towards higher binding energy at almost the same rate as the band minimum. The \bar{M} -point gap width ($80 \pm 10 \text{ meV}$) is thus nearly independent of the Au doping. This in turn proves that the Ag/Cu(111) bands shift “*rigidly*” with Au doping, as the bands of (111)-oriented noble metal surface does with the measurement temperature [99]. We conclude that the Au doping only changes the substrate crystal potential that defines the surface state energy rather than the triangular superlattice potential that opens the gap. The black data points in Fig. 3.28(c) are the gap edges of the undoped Ag/Cu(111) system measured at room temperature (RT), 180, and 40 K, taken from Ref. [50,52] [50,52]. As observed from Fig. 3.28(c) by picking up the appropriate Au doping, the energetic position of the gap can now be tuned a RT without significant increase of the line width.

3. RESULTS AND DISCUSSION I

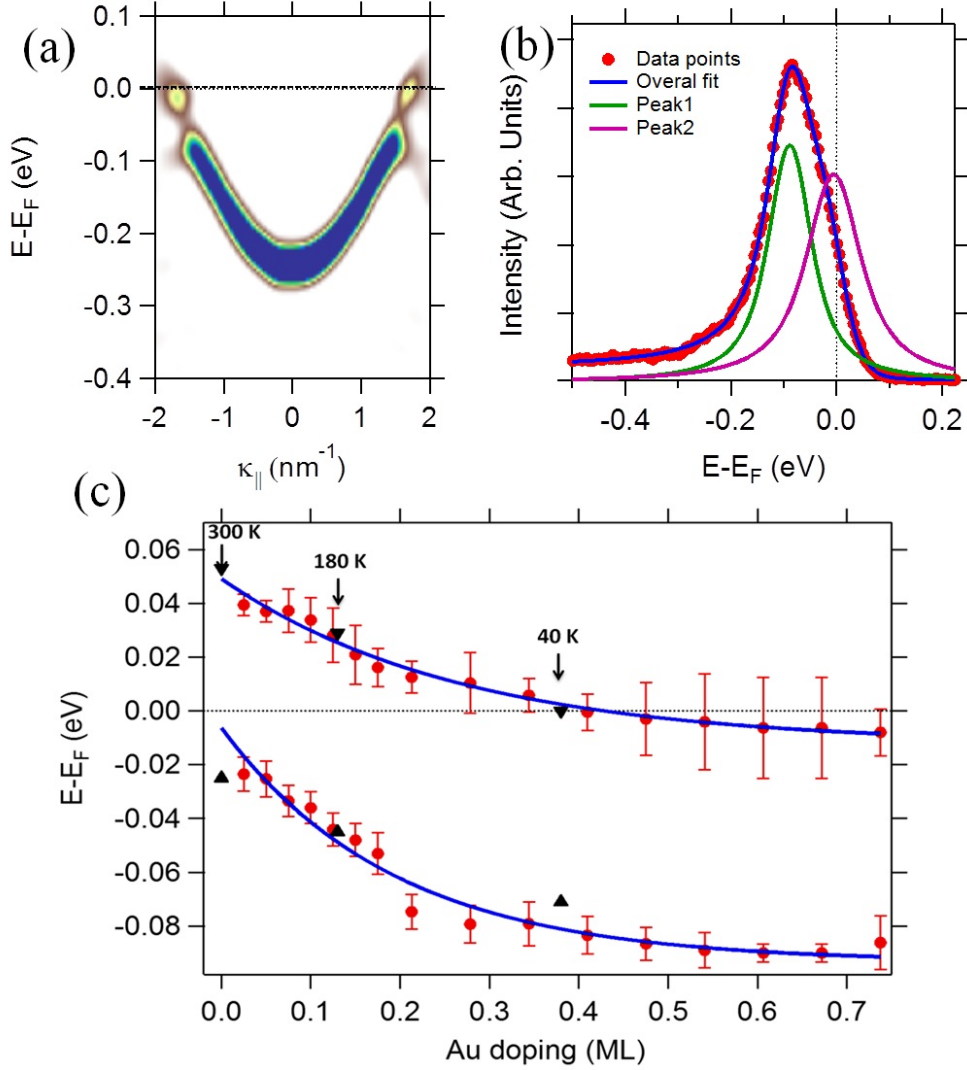


Figure 3.28: \bar{M} -Point Gap Analysis: Au(Wedge)/1 ML Ag/Cu - (a) The surface state of the 0.4 ML Au doped 1 ML Ag/Cu(111) along the $\bar{\Gamma}\bar{M}$ direction. (b) A line profile at the \bar{M} -point fitted with two Lorentzian peaks, which defines the lower and upper edges of the \bar{M} -point gap, divided by a Fermi function, and convoluted with a Gaussian peak to account for the energy resolution (40 meV). (c) Upper and lower edges of the \bar{M} -point gap as a function of Au doping, after fitting the corresponding EDCs in (b). The black triangles in (c) and the arrows indicate the \bar{M} -point gap edges for the un-doped 1 ML Ag/Cu(111) system measured at different temperatures in literature.

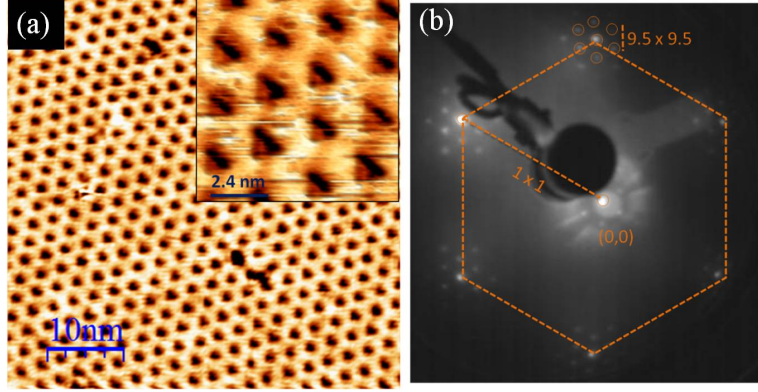


Figure 3.29: STM and LEED: Au doped Ag/Cu - (a) STM image of 0.5 ML Au doped 1 ML Ag/Cu(111) showing the same triangular dislocation network as for the undoped system with the same periodicity (-1.0 V, 1.0 nA). The inset shows a small scale image where the triangular shape is better resolved. (b) LEED pattern of the 0.5 ML Au doped sample revealing a $\sim 9.5 \times 9.5$ superstructure.

The wavevector corresponding to the \bar{M} -point was found to be independent of Au doping with a value of $\sim 1.47 \text{ nm}^{-1}$. This value corresponds to a superstructure with (9.6×9.6) periodicity, close to the 9.5×9.5 superstructure reported for the undoped system. The later finding is further supported by the STM images and LEED pattern shown in Fig. 3.29. The STM image shows a long-range-ordered hexagonal network of triangular dislocations (better resolved in the inset) with a periodicity of $\sim 2.5 \text{ nm}$ compared to $\sim 2.43 \text{ nm}$ in Ag/Cu(111). The STM images correspond to $\sim 0.5 \text{ ML}$ Au doped 1 ML Ag/Cu(111). The LEED pattern also shows a $\sim 9.5 \times 9.5$ superstructures that is independent, within the error limit, on the Au doping. These findings, suggest that the same substrate and atom removal mechanism claimed^[143] to originate the triangular dislocations in the undoped system appear to be valid at the interface doped with Au atoms, which therefore intermix with Cu(111) surface without affecting its lattice parameters.

In the following paragraphs we will further investigate the 1 ML Ag/Cu(111) doped with 0.4 Au ML, hence where the \bar{M} -point barely crosses the Fermi level, as shown in Fig. 3.28(c). In this case, the upper edge of the gap lies at $\sim 2 \text{ meV}$ below the Fermi level. To explore the band topology in more details, we have performed a Lorentzian peak fit analysis to the EDC spectra along $\overline{\Gamma MK\Gamma}$ directions for the 0.4 ML Au doping

3. RESULTS AND DISCUSSION I

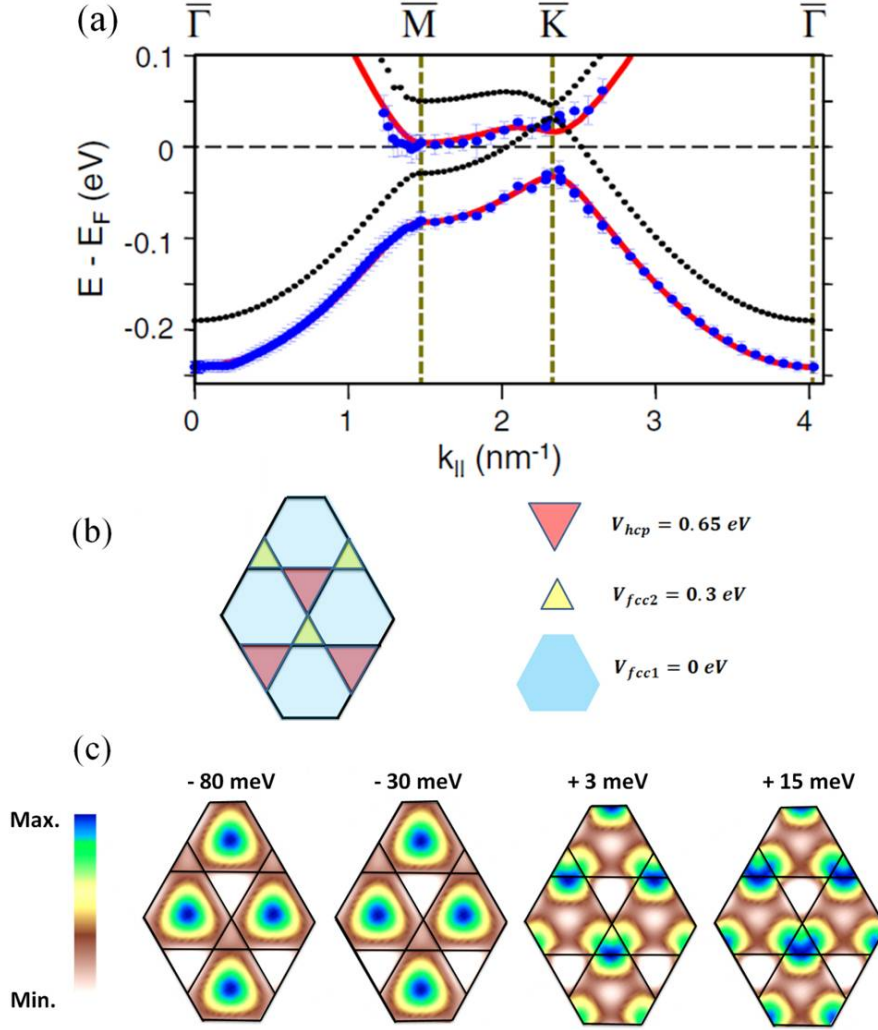


Figure 3.30: Band Structure and LDOS: EBEM - (a) Surface band dispersion of the 1 ML Ag/0.4 ML Au/Cu(111) along the $\bar{\Gamma}\bar{M}\bar{K}\bar{\Gamma}$ direction. Data points (blue) are obtained from fits to individual EDC spectra. The solid lines (red) represent the band structure derived from a model calculation using the surface potential shown in (b). The dotted lines (black) are the theory fit to data of the undoped 1 ML Ag/Cu(111) networking keeping $V_{fcc2} = 0$. (c) Local density of states (LDOS) at the lower \bar{M} (-80 meV) and \bar{K} (-30 meV) and the upper \bar{M} (+2 meV) and \bar{M} (15 meV) edges, as determined using the boundary element method (BEM) approach and the surface potential in (b).

case. The results of these fits are display as data points (blue points) in Fig. 3.30(a). Due to the thermal occupation, bands within $\sim 2k_B T$ (where k_B is Boltzmann constant and T is the temperature of the measurement) above the Fermi level can be probed in ARPES, i.e. up to + 50 meV at RT^[152]. This allows us to reliably define the gap edges along $\overline{\Gamma M K \Gamma}$ region. The solid red lines are a single fit to the data using a plane wave (PW) calculation to solve the Schrödinger equation:

$$(\nabla^2 + k^2 - \frac{2m_*}{\hbar^2})\Phi = 0, \quad (3.4)$$

with the 2D surface potential V shown in Fig. 3.30(b). V is divided into three different regions, which correspond to Ag atoms on *fcc* and *hcp* sites of the *fcc* Cu(111) surface, that is *fcc1* and *fcc2* respectively, and Ag atoms on the Cu *hcp*-packed triangles (*hcp*).

The PW fit uses the measured effective mass of Ag(111) ($m_* = 0.41 m_e$) and two fitting parameters, namely, the potential energy within the *hcp* triangular dislocations ($V_b = V_{hcp} - V_{fcc1}$) and at *fcc2* sites ($V_c = V_{fcc2} - V_{fcc1}$). The latter is justified from the potential step found between *hcp*-like and *fcc*-like packing, which gives rise to different contrast in STM images of dislocation patterns on (111) surfaces^[127,153,154]. We obtain $V_b = 0.65$ eV and $V_c = 0.3$ eV. The triangular step barrier is the same found for the undoped system, although V_{fcc2} is much larger than the *fcc-hcp* surface state offset (30 meV) observed in Au(111)^[127].

The photoemission data and the corresponding fit in Fig. 3.30(a), indicates that the full gap along $\overline{\Gamma M K \Gamma}$ direction of the Au-doped superlattice is now indirect, with its lower edge at \bar{K} in the first band (-30 meV in both data and model), and its upper edge at \bar{M} in the second band (-2 meV and +2 meV in the data and model, respectively). We note however that, if V_c is made equal to zero in the PW calculation, the \bar{K} point of the second band falls slightly below the \bar{M} -point, making the full $\overline{\Gamma M K \Gamma}$ gap direct at \bar{K} . This is shown by the dotted black lines in Fig. 3.30(a). These lines correspond to the calculated band structure of the undoped 1 ML Ag/Cu(111) system in Ref. [54]^[54]. The data in Fig. 3.30(a) prove that the V_{fcc2} discontinuity is required in the model calculation for a good agreement between the theory and experiment.

The sensitivity of the upper \bar{K} -point to the V_{fcc2} potential is actually expected from the real space properties of the surface state wave function at \bar{K} , which in turn are derived from the triangular symmetry of the surface potential^[53]. To gain more insight

3. RESULTS AND DISCUSSION I

into the surface state wave function for the particular case of the Au-doped system, of Fig. 3.30(c) we show local density of states (LDOS) maps at different energies. They have been calculated from the 2D potential of Fig. 3.30(b) using the boundary element method (BEM⁴) as explained in Refs. [54,155]^[54,155]. The energies correspond to the lower \bar{M} (-80 meV) and \bar{K} (-30 meV) and to the upper \bar{M} (+3 meV) and \bar{K} (+15 meV) points. The 2D potential of Fig. 3.30(b) appears superimposed on the LDOSs shown in Fig. 3.30(c). At \bar{K} , we observe changes in the LDOS analogous to those probed with STM in the undoped system^[53], i.e., the probability density maxima shift from the *fcc1* (-30 meV) to the *fcc2* (+15 meV) sites when crossing the gap. At \bar{M} , the orthogonality is also observed at both sides of the gap.

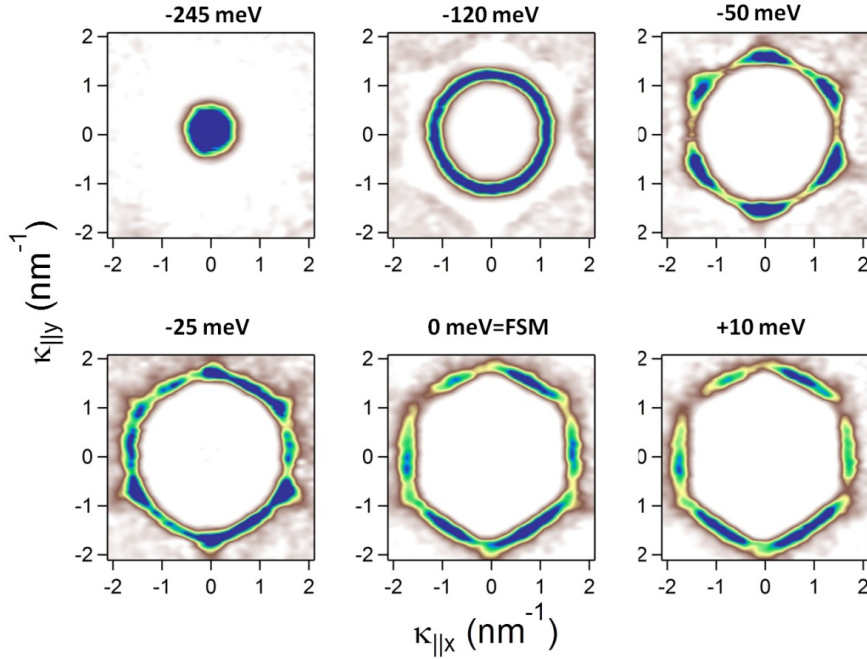


Figure 3.31: Experimental CESs: 0.4 ML Au/Ag/Cu - Experimentally measured constant energy surfaces (CES) for the 1 ML Ag/Cu(111) doped with 0.4 ML Au.

The fact that the full $\overline{\Gamma MKT}$ gap is indirect has an interesting consequence on the constant energy surfaces (CES) close to the Fermi energy (FS). Figure 3.31 and 3.32 show, respectively, the experimental and theoretical CESs including the FS for

⁴The EBEM code together with a user friendly input file were provided by Prof. F. J. García de Abajo, from Instituto de Optica-CSIC, Madrid.

the 0.4 ML Au doped system. The CESs were simulated using the BEM method in photoelectron 2D parallel-momentum space. The overall agreement between the experiment and theory is remarkable. The CES at 120 meV proves clearly the six-fold symmetry of the system, where photoemission from 2nd Brillouin zones (BZ) is seen. The CES at -50 meV is identical to the FS of the undoped system, proving the rigid shift induced by Au doping.

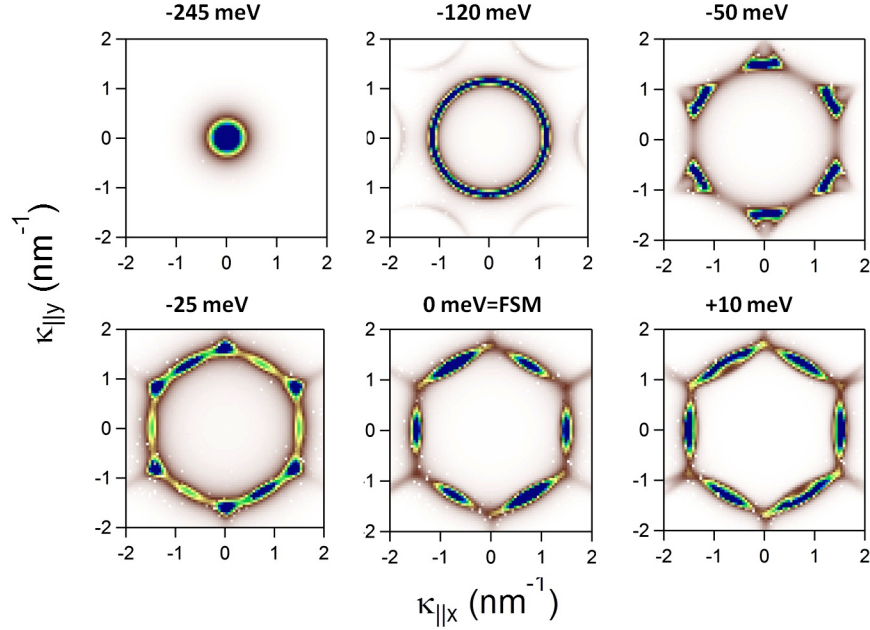


Figure 3.32: Theoretical CESs: 0.4 ML Au/Ag/Cu - Theoretically simulated constant energy surfaces (CES) for the 1 ML Ag/Cu(111) doped with 0.4 ML Au.

Of particular interest are the shapes of the FS for the doped and undoped system. These are further highlighted in Fig. 3.33. The figure shows the deep transformation of the free electron-like Cu(111) surface state and its ring-like FS, see appendix A, in the presence of the 2D triangular dislocation network. For the undoped 1 ML Ag/Cu(111) system the network periodicity (2.43 nm) allows nesting of the FS at \bar{M} -points. A gap is observed at \bar{M} in the FS shown in Fig. 3.33(a), extending over a large portion of the BZ edge, and giving rise to quasi-parabolic hole pockets (i.e. a small fraction of the occupied surface states leaks above the Fermi level) at \bar{K} -points. The hole pocket radius ($k_F=0.22 \text{ nm}^{-1}$) and its effective mass ($m_*=0.24 m_e$) are determined from the \bar{K} band dispersion in Fig. 3.33(b). For a Au-doping level of 0.4 ML the surface state

3. RESULTS AND DISCUSSION I

band minima shifts down by ~ 50 meV to -245 meV, Fig. 3.33(d). The upper edge of the \bar{M} gap for the undoped system lies at 45 meV above the Fermi level, such that Au doping moves this upper edge barely below Fermi level, as seen in Fig. 3.33(d), Fig. 3.28(c), and Fig. 3.30(a). As a result, hole pocket at \bar{K} in Fig. 3.33(a) become electron pocket at \bar{M} in Fig. 3.33(c). The latter exhibits a clear asymmetry, namely, a low effective mass in the \bar{M} direction ($m_*=0.03 m_e$) and a heavy effective mass in the $\bar{M}\bar{K}$ direction ($m_*=0.58 m_e$).

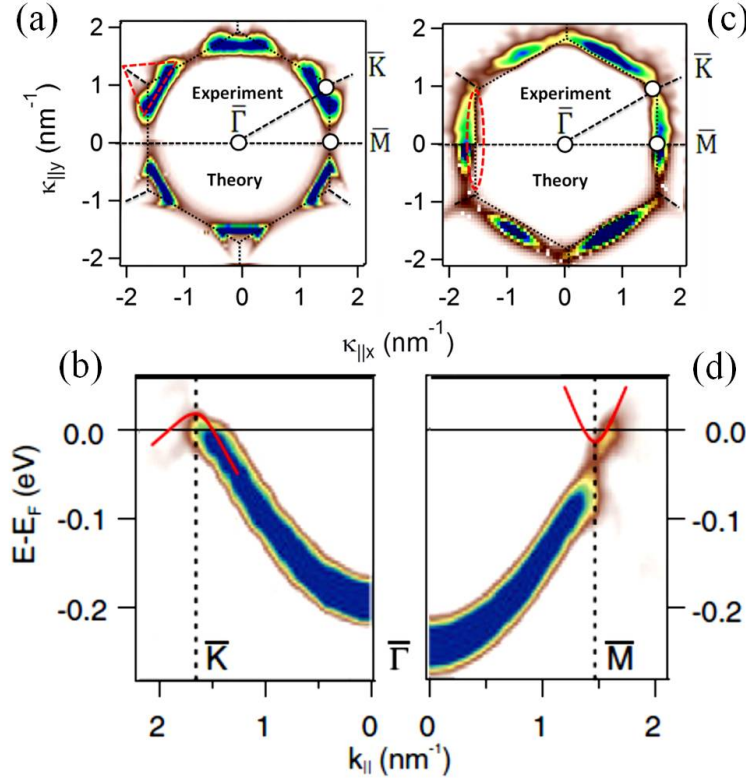


Figure 3.33: Lifshitz Transition: Ag/Cu vs. Au/Ag/Cu - FSM of (a) 1 ML Ag/Cu(111) that significantly changes after doping with (c) ~ 0.4 ML of Au. The upper and lower halves of (a) and (c) corresponds, respectively, to experimental measurements and theoretical simulations. The dotted lines mark the BZ edges and the dashed lines define the hole and electron pockets at \bar{K} and \bar{M} , respectively. The corresponding bands are shown along (b) $\bar{\Gamma}\bar{K}$ and (d) $\bar{\Gamma}\bar{M}$ symmetry directions. All images present the second derivative of the photoemission intensity.

The transformation of the hole pocket-like FS, of the undoped system, to an electron pocket-like FS, for the 0.4 ML Au doped one, is a natural consequence of the indirect

character of the full gap induced by the non-zero value of the $fcc2$ potential, Fig. 3.30. Such radical transformation, which can be tuned further by Au doping, is called “*Lifshitz Transition*” and might have interesting applications.

The pocket like FS of the undoped 1 ML Ag/Cu(111) superlattice is analogous to the FS in the technologically interesting gapped epitaxial graphene^[156], which in fact is linked to many of its exotic properties. A Lifshitz transition similar to the present one has recently been observed in magnetic semiconductors, where hole-pocket filling leads to a radical ferromagnetic-to-superconductor transition^[157]. In Ag/Cu(111) the surface state belongs to a projected bulk band gap; i.e., the supporting gap is metallic, and hence any exotic surface excitation would be screened. We still expect a different behavior in hole lifetimes of the present undoped and doped dislocation lattices with respect to a standard noble metal surface. Interband transitions contribute to 80 % of the hole screening near the Fermi level^[158], and hence a strongly featured FS may lead to significant lifetime changes. In this context, the fact that Au doping allows superlattice FS tuning without introducing additional inelastic scattering appears of obvious importance.

The search for exotic electron scattering properties and plasmonics like surface nanoelectronics effects^[54] in the Ag/Cu(111) superlattice will require sophisticated techniques, such as four-probe STM and cryogenic temperatures, since the size of the full gap (~ 30 meV) closely matches the thermal broadening $k_B T$. For example, in Fig. 3.28(c) electron pockets exhibit sign of thermal broadening at \bar{K} , i.e., emission from the lower \bar{K} band edge at -30 meV. We have seen in Fig. 3.27(c), that in Ag/Cu(111) the \bar{M} -point gap, and hence the full surface state, shifts towards higher binding energy at LT, as marked by the three black arrows. This is actually equivalent to the effect of Au doping with, of course, less thermal broadening in the LT case. Hence both temperature and doping can be combined to fine tune the hole or electron pockets occupation, and hence to investigate the lifetime effects and the consequences of the Lifshitz transition in the 1 ML Ag/Cu(111) superlattice. The coming section deals with the LT measurements of the pure and Au doped Ag/Cu(111) system.

3. RESULTS AND DISCUSSION I

3.7.3 Temperature Dependent Measurements:

In the present section the surface state line width as a function of temperature for three different samples will be discussed. These are the undoped 1 ML Ag/Cu(111), the 0.2 ML Au doped Ag/Cu(111), and the 0.7 ML Au doped Ag/Cu(111). The 0.2 ML and 0.7 ML Au doped samples were prepared simultaneously by depositing the respective Au amount on the same Cu(111) crystal, to allow direct comparison. The choice of the Au coverage was, also, intended to follow smoothly the energetic positions of the upper and lower edges of the \bar{M} -point gap, especially close to the Fermi energy crossing. The three systems have been measured with the He I line (21.22 eV) in low angular dispersion mode with 7 eV pass energy. The pressure in the main chamber was always better than 8×10^{-11} mbar, and increases to $\sim 1.7 \times 10^{-10}$ mbar during the measurement. The finite energy resolution of the machine is estimated by measuring the Fermi edge on the sample holder and at low temperature (LT), typically ~ 40 K. We estimated an energy resolution of ~ 29 meV. At measuring temperatures below ~ 120 K the surface states were found to get slightly broaden with time. This can be attributed to a possible condensation of residual gases in the main chamber at LT. A recent study^[159] performed with synchrotron radiation relates this effect to a chemisorbed hydrogenation induced by the light source itself. In the study shown here, at 140 K, the sample left 8 hours clearly showed no condensation or hydrogenation effects (only 1 meV upward energy shift and 2 meV broader line width). Below 140 K we observed broadenings with time and, therefore, we have tried to minimize the measurements time as possible while maintaining a reasonable statistics for accurate fitting, especially at the \bar{M} -point. At temperatures close to 80 K, the condensation effect is rather significant. By changing the light spot to a different point on the sample, roughly 5 mm, a complete recovery of the surface state is possible. At this temperature and down to 40 K we softly anneal the samples and re-measure after the sample is cooled down. During the time it takes to go from one temperature to another and since the source of condensation is not precisely know to us, we kept the valve of the light source closed and moved the sample relatively far from the analyzer entrance. This slightly reduced the effect of the broadening.

In Fig. 3.34 we display the second derivative of the photoemission intensity plot showing the Shockley surface state dispersion along $\bar{\Gamma}\bar{M}$ for the undoped Ag/Cu, the 0.2 ML Au, and 0.7 ML Au doped Ag/Cu, taken at three different temperatures; 300

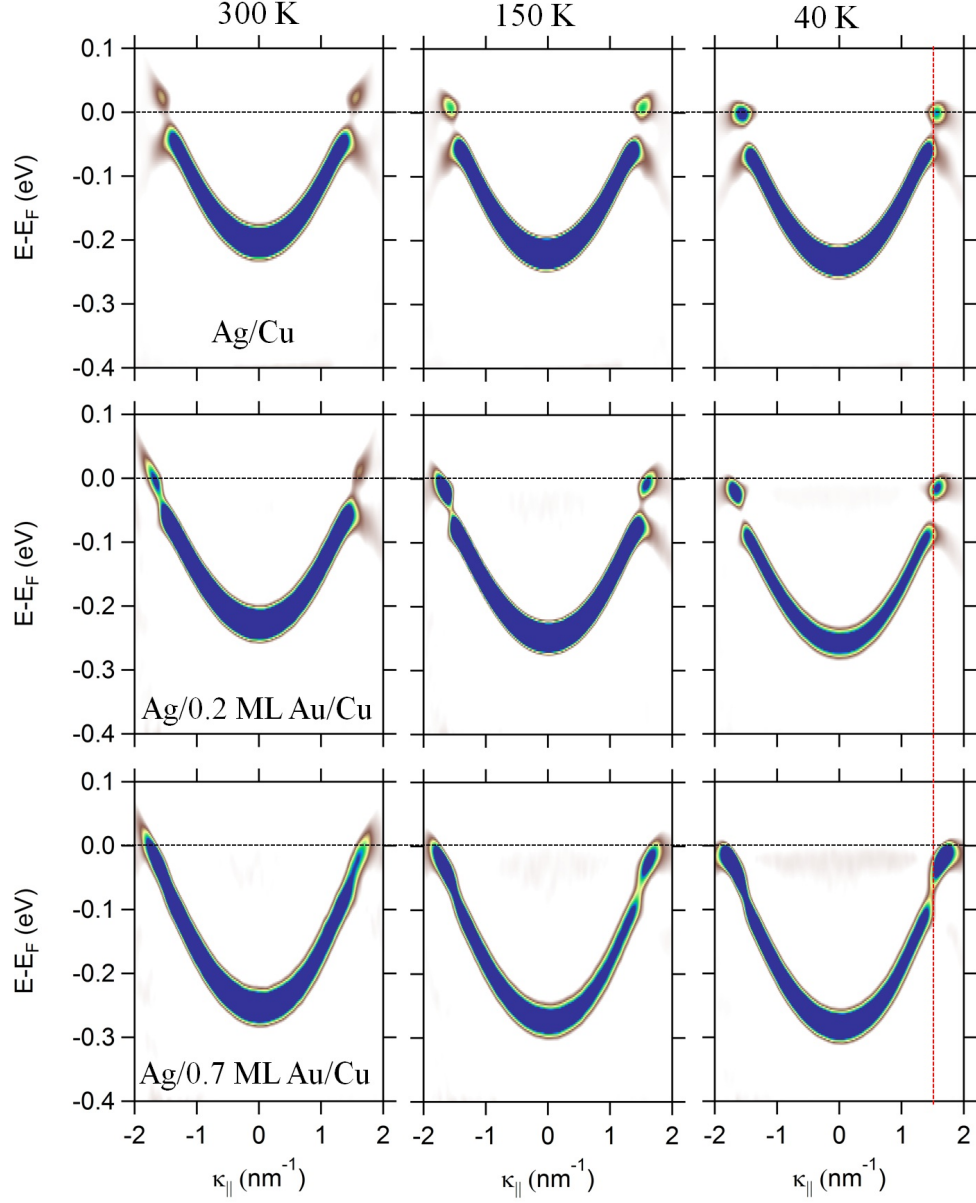


Figure 3.34: LT Measurements: Dispersion Plots: Ag/Cu vs. Au/Ag/Cu - Surface state dispersion along $\bar{\Gamma}\bar{M}$ direction as measured by ARPES at three different temperatures (300 K, 150 K and 40 K) for (1st row) 1 ML Ag/Cu(111), (2nd and 3rd rows) 0.2 ML Au and 0.7 ML Au doped Ag/Cu(111), respectively. The horizontal/vertical dashed black/red lines mark, respectively, the Fermi level and the \bar{M} -point. Images are shown as second derivatives.

3. RESULTS AND DISCUSSION I

K, 150 K, and 40 K, respectively. The black (horizontal) and red (vertical) dotted lines mark, respectively, the Fermi energy and the \bar{M} -point position. The latter was found to be $\sim 1.52 \text{ nm}^{-1}$ in all three cases. In the following we compare the evolution of the binding energy and line width at $\bar{\Gamma}$ as function of the temperature for the three different cases. Figure 3.35(a) displays the EDC series for the 0.2 ML Au doped Ag/Cu case taken at $\bar{\Gamma}$. The data points in Fig. 3.35(b) are the corresponding fit for each EDC in the undoped and doped cases. Each EDC is fitted with a Lorentzian peak convoluted with a Gaussian (of 29 meV width) to account for the finite energy resolution.

We notice that the band minimum of both the undoped and Au doped systems follow the same trend as reported for the (111) oriented noble metal surfaces, hence a downward shift of the band minimum with decreasing the measuring temperature. The only difference is an offset toward higher binding energy while increasing the Au coverage. The rate of such downward shift (the temperature coefficient) as determined from the slope of $(E - E_F)$ versus (T) plot was found to be $(1.45 \pm 0.03) \times 10^{-4} \text{ eV/K}$ in the three cases. This value is similar to the $1.6 \times 10^{-4} \text{ eV/K}$ reported for Cu(111) and quite different from $2.6 \times 10^{-4} \text{ eV/K}$ reported for both Ag(111) and Au(111)^[99].

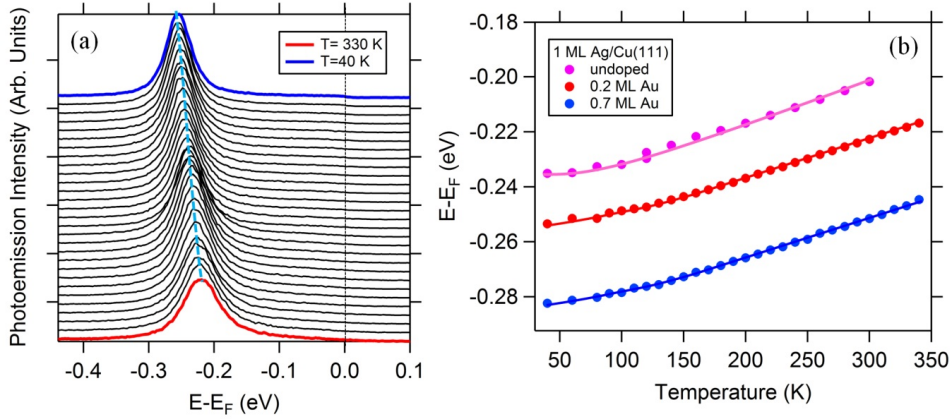


Figure 3.35: EDCs: Band Minima: 0.2 ML Au/Ag/Cu - (a) EDCs taken at the band minimum for 0.2 ML Au doped sample at different temperature from 330 K (red) to 40 K (blue) in steps of 10 K. (b) Data points after fitting these EDCs for the undoped and the 0.2 ML and 0.7 ML Au Ag/Cu(111).

This finding agrees with the fact that the surface state band minimum is mainly coupled to the lower edge of the bulk projected gap of the supporting substrate^[98], which is related to the bulk lattice constant variation (Cu in the present case) and

hence the projected bulk gap size and position (see appendix A for basic information regarding this issue). The data points after fitting the EDCs defining the upper and lower edges of the \bar{M} -point gap (see Fig. 3.36(a)) for the 0.2 ML Au doped sample as a function of the measurement temperature are shown in Fig. 3.36(b). The choice of this coverage was, actually, intended to observe the gap size (see Fig. 3.36(c)) while crossing the Fermi level. For temperatures where the gap has crossed the Fermi level ($T < 220$ K), the lower and upper edges of the gap shift toward higher binding energy with a rate of $1.0 \pm 0.03 \times 10^{-4}$ eV/K (red dashed line in (b)).

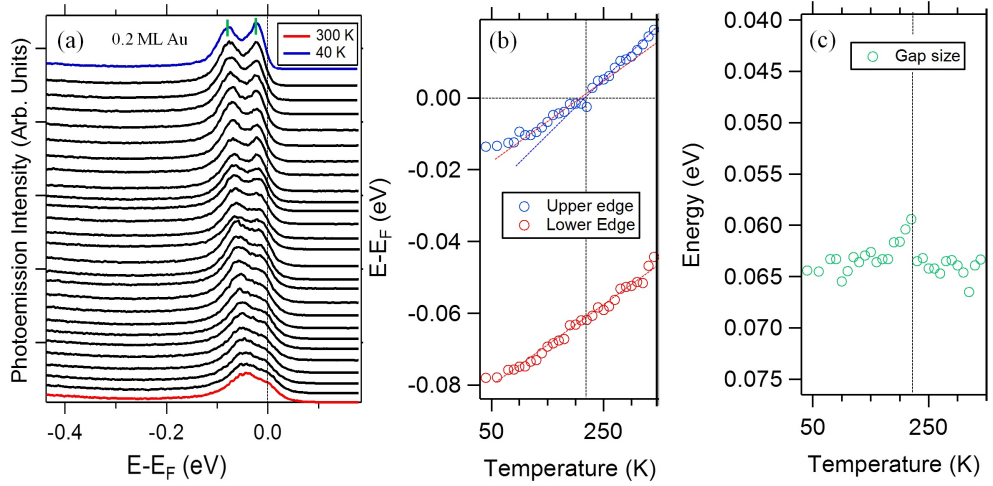


Figure 3.36: \bar{M} -point Gap Analysis: 0.2 ML Au/Ag/Cu - (a) EDCs taken at the \bar{M} -point for 0.2 ML Au doped sample at different temperature from 330 K (red) to 40 K (blue) in steps of 10 K. (b) Data points, after fitting these EDCs, defining the lower (red) and the upper (blue) edges of the \bar{M} -point gap for the 0.2 ML Au doped sample as a function of measurement temperature. The red line is a linear fit to the lower edge (and the upper edge below 200 K) with slope of 1.0×10^{-4} eV/K, where the blue line is the fit for the upper edge for temperatures higher than 200 K. (c) The size of the \bar{M} -point gap (green) as a function of the measurement temperature.

For higher temperatures, however, the upper edge of the gap shows a higher downward shift rate of $1.5 \pm 0.03 \times 10^{-4}$ eV/K (blue dashed line in (c)) suggesting a tinny distortion of the gap due to mass renormalization after crossing the Fermi level. The gap size (green open circles) was found to slightly shrink (from ± 65 meV to ± 60 meV) close to the crossing temperature. A 5 meV reduction of the gap size is very tinny and within our error limits. The same analysis has been applied for different

3. RESULTS AND DISCUSSION I

EDCs at different momentum going from the $\bar{\Gamma}$ -point toward the \bar{M} -point. Each EDC can be fitted with a single Lorentzian peak, thus, reducing the uncertainties of defining the \bar{M} -point gap that requires two Lorentzian convoluted with a Fermi function. The resultant fit for these EDCs series are displayed in Fig. 3.37(a) together with the downward shift rate expressed as the temperature coefficient in (b). For both the 0.2 ML and 0.7 ML Au doped samples almost constant temperature coefficient of 1.45×10^{-4} eV/K is obtained for $k_{||}$ from 0 to 0.8 nm^{-1} . Close to the \bar{M} -point this value is reduced to 1.0×10^{-4} eV/K.

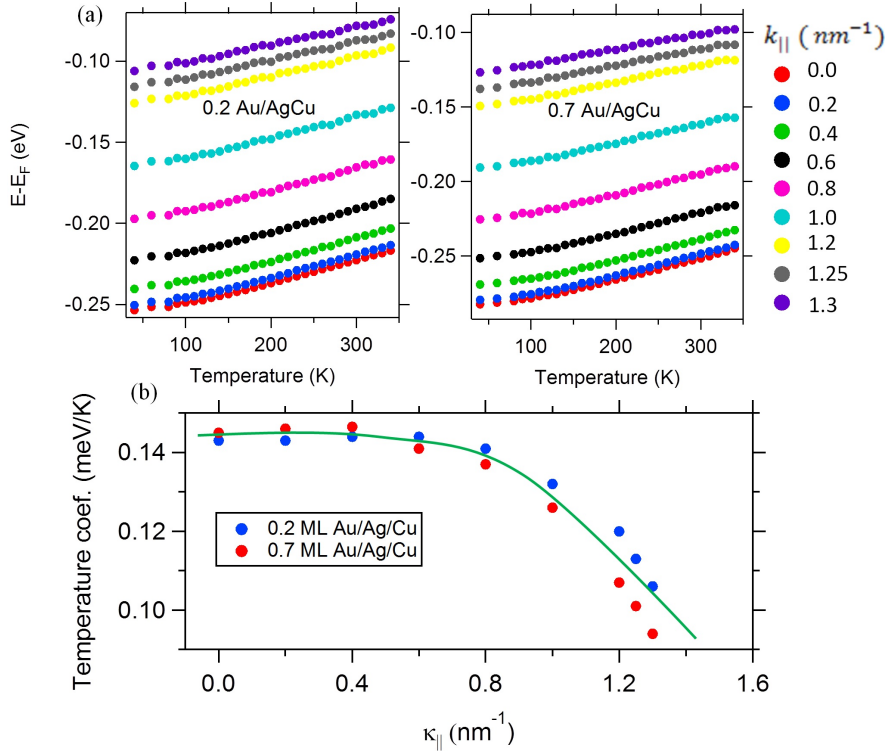


Figure 3.37: The Rate of the Downward Shift: Band Minima - (a) The energetic position of the surface state after fitting the EDCs for the undoped and the 0.2 ML and 0.7 ML Au Ag/Cu(111) at different momentum as a function of the temperature. (b) The rate of downward shift (temperature coefficient) as function of the momentum for the two samples. The green line is just a guide to the eyes.

Therefore, we conclude that the surface state is slightly modified in the proximity of the \bar{M} -point and the estimated shrink of the gap size can be acceptable. The same analysis has been done for the non-gapped Cu(111) and 0.7 ML Au/Cu(111) surface

states and the same observation was obtained. This suggests that the renormalization effect is not induced due to the presence of the gap, but rather, slightly, affecting this gap which accidentally happens to exist at high momentum value (1.52 nm^{-1}) where the mass renormalization effect is pronounced.

So far we have discussed the effect of the measuring temperature on the energetic position of the surface state for different Au coverage. Here we further present the line width analysis for the two doped Au cases. Apart from the finite energy and momentum resolution, the experimental line width of surface states is a sum of three main contributions, namely, the electron-phonon, the electron-electron, and electron-impurity scattering^[160–162]. Each of these has its own signature on a given spectral feature making the separation between them experimentally accessible. Assuming that both the electron-electron and electron-defect scattering are independent of the measuring temperature, the variation of the line width with the temperature can be used to identify the electron-phonon interaction contribution. Figure 3.38 shows a plot of the experimental line width (FWHM or Γ) as a function of the measurement temperature for the Au doped systems. The undoped Ag/Cu was measured in a separate experiment, and the width was found to be higher than the 0.2 ML Au doped sample. Such anomalous behavior, contrary to all our previous findings, is attributed to a worse prepared Ag/Cu surface and will, therefore, be omitted from our results.

In general, the broadening due to electron-phonon coupling is related to the Eliashberg spectral function via the following equation^[163];

$$\Gamma_{e-ph}(\varepsilon, T) = 2\pi\hbar \int_0^{\omega_{max}} \{\alpha^2 F(\omega)[1 + 2n(\omega) + f(\varepsilon + \omega) - f(\varepsilon - \omega)]\} d\omega \quad (3.5)$$

where ω_{max} is the maximum phonon frequency and $\alpha^2 F(\omega)$ is the Eliashberg spectral function. The later is approximated to $\lambda(\omega/\omega_D)^2$ or $\lambda(\omega/2\omega_D)$ for 3D or 2D systems^[160], respectively, where λ and ω_D are, respectively, the electron-phonon coupling constant and Debye frequency. Here we will use the 2D Debye approximation. Rewriting Equ. (3.5)^[164]

$$\Gamma_{exp}(\varepsilon, T) = \Gamma_{e-e} + \Gamma_{e-imp} + \pi\hbar\lambda \int_0^{\omega_D} \left\{ \left(\frac{\omega}{\omega_D} \right) [1 + 2n(\omega) + f(\varepsilon + \omega) - f(\varepsilon - \omega)] \right\} d\omega \quad (3.6)$$

3. RESULTS AND DISCUSSION I

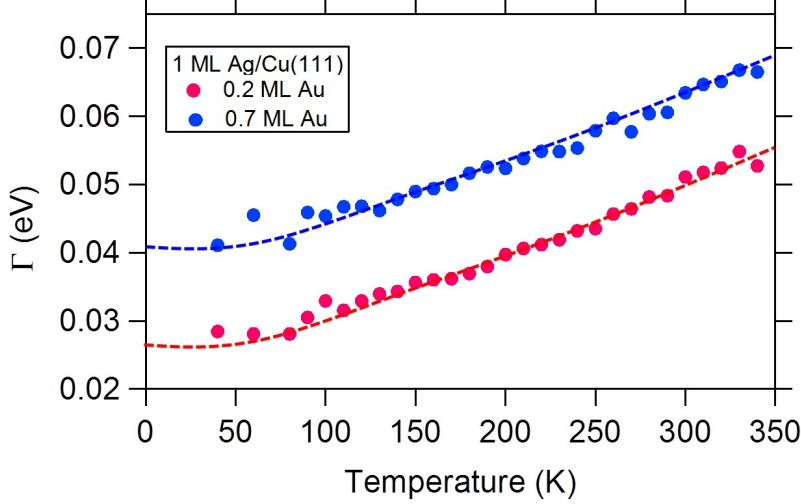


Figure 3.38: Line Width: Band Minima - Experimental line width at band minimum as a function of temperature for the 0.2 ML Au, and 0.7 ML Au Ag/Cu(111). The dashed red and blue lines are the fit to the data for the two Au doped samples using Equ. (3.7).

where Γ_{exp} is the experimental line width, including the electron-electron (Γ_{e-e}), electron-impurity (Γ_{e-imp}), and electron-phonon (the last term in the equation) line width. The broadening due to electron-electron scattering is given by^[164];

$$\Gamma_{e-e} = \beta[(\pi k_B T)^2 + E_b^2] \quad (3.7)$$

where β is a very small proportionality constant and E_b is the hole binding energy. For phonon frequencies less than Debye energy, the electron-electron interaction can be considered almost temperature independent. It is only important when the Debye energy is close to the hole binding energy (e.g., ~ 25 meV for Debye temperature of 300 K), hence close to the Fermi level. We also consider the electron-impurity broadening temperature independent, for temperatures low enough not to generate thermal defects. Therefore, the first two terms in Equ. (3.6) will be constants. Fitting the experimental line width with Equ. (3.6) using Debye temperature of 260 K^[165] and using $\Gamma_{e-e} + \Gamma_{e-imp}$ and λ as free fit parameters, good agreements are obtained with the parameters given in table 3.1. The dashed lines, superimposed on the data points, are the result of fitting Equ. (3.6) to the data.

The broadening due to electron-phonon coupling was found to be the same for both samples (8.5 meV). The 0.2 ML and 0.7 ML Au doped samples have a band minimum

3.7 Results and Discussion II:

	$\Gamma_{e-e} + \Gamma_{e-imp}$ (meV)	Γ_{e-ph} (meV)	λ
0.2 ML Au Ag/Cu(111)	17.5	8.5	0.2 ± 0.02
0.7 ML Au Ag/Cu(111)	33	8.5	0.19 ± 0.02

Table 3.1: Fitting Parameters: Electron-Phono Coupling - The resulting parameters after fitting the experimental line width with Equ. (3.6).

difference of ~ 40 meV and, therefore, the strong increase in the $\Gamma_{e-e} + \Gamma_{e-imp}$ value for the 0.7 ML Au doped sample is likely attributed to higher concentration of defects (Γ_{e-imp}) rather than a real increase of Γ_{e-e} . Assuming the same Γ_{e-e} , for both samples, we estimated a higher limit for Γ_{e-e} , that is $\sim 12 \text{ meV} \leq \Gamma_{e-e} < 17.5 \text{ meV}$. This value is similar to the one reported for Cu(111), see table 3.2, and very different from Ag(111). The λ parameter is also the same, within error limits, for both samples, with slightly/significantly higher values than reported for, respectively, Cu(111) and Ag(111). An experimental work on a multilayer Ag on Cu(111) estimated about the same value for λ with some oscillations with the film thickness around this value, see table 3.2.

Physical Quantity	Γ_{e-e} Γ_{e-ph}	Γ_{exp}	λ	λ	Ref.
Techniques Samples	Theory meV	ARPES meV	Theory	ARPES	
Ag(111)	2/3.7	6 ± 0.5	0.12	0.12	[165] ^[165]
Cu(111)	14/7.3	23 ± 1	0.16	0.14 ± 0.02	[165] ^[165]
20ML Ag/Cu(111)	\times	< 40	0.1	0.2 ± 0.02	[166] ^[166]
1ML Ag/Cu(111)	\times	19	\times	0.14	[159] ^[159]
1ML Ag/Cu(111)	\times	19	\times	0.19 ± 0.03	Present
0.2ML Au/Ag/Cu	\times	26	\times	0.19 ± 0.02	Present
0.7ML Au/Ag/Cu	\times	40	\times	0.19 ± 0.02	Present

Table 3.2: Life Time Contributions: Theory & Experiment - Compilation of the experimental (ARPES) and theoretical values of Γ_{e-e} , Γ_{e-ph} and Γ_{exp} . The values of the electron-phonon coupling constant (mass enhancement factor) λ are also included. The Ag(111), Cu(111) and their combination are only presented and compared to our experimental values.

3. RESULTS AND DISCUSSION I

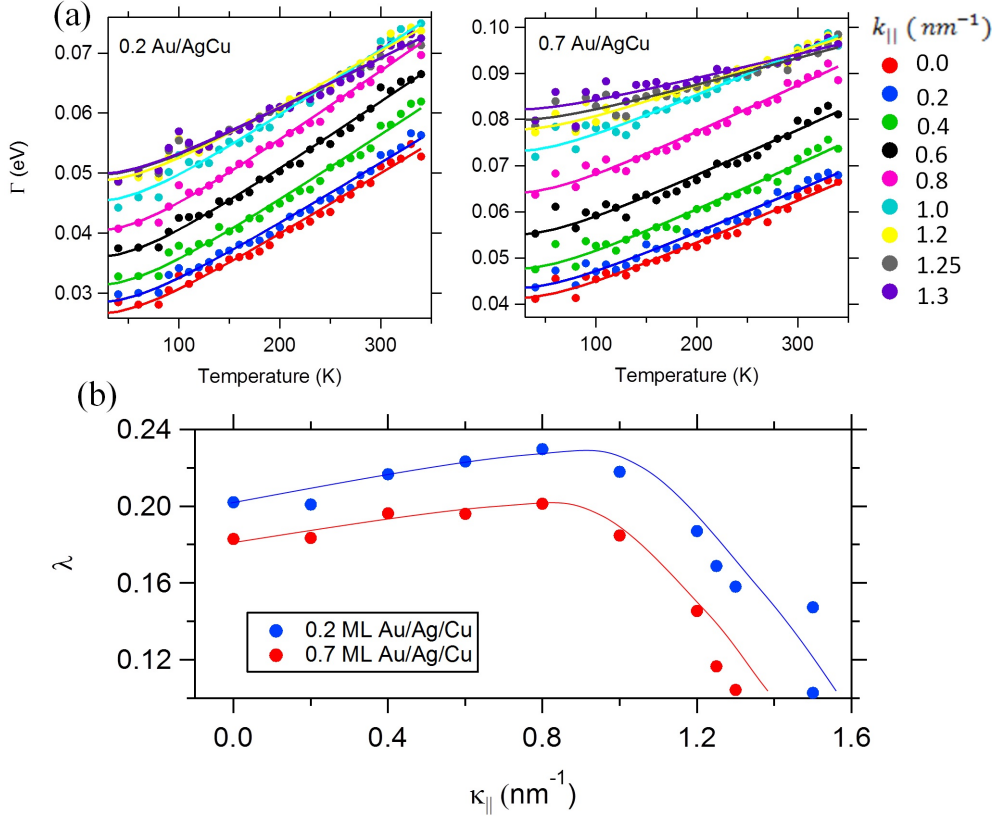


Figure 3.39: Experimental Line Width: Electron-Phonon Coupling - (a) The experimental line width after fitting the EDCs for the undoped and the 0.2 ML and 0.7 ML Au Ag/Cu(111) at different momentum as a function of the temperature. (b) The electron-phonon coupling parameter as a function of the momentum for the two samples obtained after fitting the data points in (a) using Equ. (3.6). The solid lines are just guide to the eyes.

The same analysis was applied to a series of EDCs taken at off-normal geometry. These are shown in Fig. 3.39(a) for the 0.2 ML and 0.7 ML Au doped samples, where the data points are the experimental data and the solid lines are the corresponding fit using Equ. (3.6). The estimated λ value and its variation with the parallel momentum are seen in Fig. 3.39(b). For $k_{||}$ ranging from 0 to 0.1 nm⁻¹ λ parameter was found to, very slowly, increase and suddenly decrease approaching the \bar{M} -point. The momentum dependent electron-phonon coupling parameter in the proximity of the gap cannot be, in the frame work of the present data, be ascribed to the presence of the gap. The same analysis for un-gapped surface states, such as the Cu(111) and Au/Cu(111) are

required. Unfortunately, the later have shown to be very much affected by condensation, Fig. 3.40, rendering the estimation of the λ parameter impossible.

We believe that the Ag(111) surface state or equivalently the 2 ML Ag/Cu(111), where the gap is completely above the Fermi level, can be used to quantify this effect. The drawback of using Ag(111) is the close proximity of the Ag surface state to the Fermi level, which can cause further artifacts to the estimated width, specially, at off-normal configuration. The 2 ML Ag/Cu(111) has a surface state band minimum of -0.165 eV with, however, the disadvantage of the un-avoided broadening due to variations from the nominal 2 ML Ag coverage. A careful preparation of the 2 ML Ag/Cu(111) is critical, since a slight deviation from the perfect coverage might screen the variation of λ ^[166].

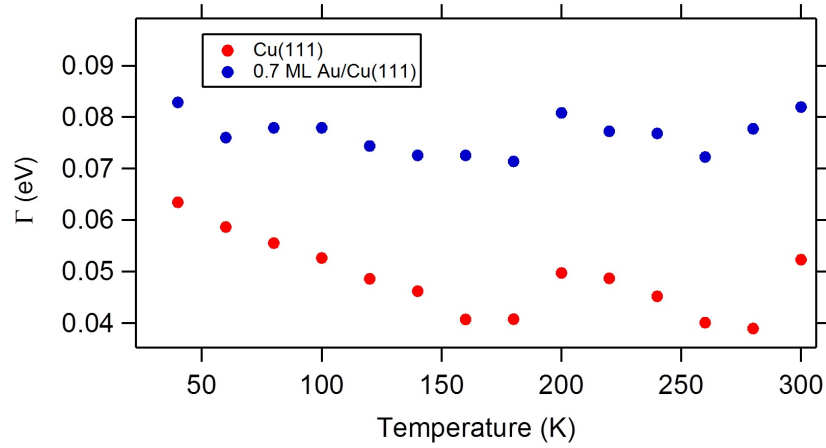


Figure 3.40: Experimental Line Width: Au/Cu(111) - Experimental line width at the $\bar{\Gamma}$ -point as a function of temperature for the undoped (red) and the 0.7 ML Au (blue) Cu(111). Apart from an offset, they both follow the same random trend. The random variation of the line width, compared to the Ag/Cu cases, render extracting the separate contributions to the line width.

3.8 Outlook:

This section contains further work which is mainly inspired from the Au/Cu alloying as well as the Ag/Cu(111) system. The results discussed throughout this section are intended to highlight some possible extension of the previous work presented in a qual-

3. RESULTS AND DISCUSSION I

itative background. The experimental observations reported here are not yet reported in literature. A better experimental conditions and/or a theoretical description of the presented results are, to some extent, still needed to present our understanding to the results in more quantitative way. We, therefore, document these results here for further continuation in future work.

3.8.1 Au Doped-2ML Ag/Cu(111) Moiré Superlattice:

The previous findings and the way that Au doping affects both the Cu substrate and the 1 ML Ag/Cu(111) surface states can be generalized to different systems. For example, it has been shown that the moiré superstructure of the 2 ML Ag/Cu(111) systems features an \bar{M} -point gapped Shockley surface state^[50]. Since the gap position is energetically above the Fermi level, a quantitative analysis of the gap size and, even a complete proof of its existence, are still missing. We have shown that ~ 0.4 ML of Au shifts down the Cu(111) surface state by ~ 100 meV, and the 1 ML Ag/Cu(111) by ~ 50 meV when annealed to 600 K. One would, however, expect that the effect of the same Au coverage on the 2 ML Ag/Cu(111) system shifts the band structure down by a smaller amount. Therefore, we study the effect of Au doping followed by different annealing temperature on the surface electronic structure of the 2 ML Ag/Cu(111) system. Figure 3.41 show the EDCs at the band minimum for the 2 ML Ag/Cu(111) as a function of Au doping. The sample was annealed to 550 K following the Au deposition. The energetic position of the band minimum, -0.15 eV for the un-doped 2 ML Ag/Cu(111), was found to shift down by ~ 25 meV at the maximum Au coverage (1 ML Au), Fig. 3.41(a-b). The FWHM was found to increase by 50 % for the 1 ML Au coverage compared to the un-doped system, Fig. 3.41(c).

Actually, the energetic position of the gap was claimed to starts at 26 meV above the Fermi level as stated by Schiller et al.^[50]. The measurement temperature in their work was 150 K, and hence roughly 25 meV shifted down as compared to our room temperature measurements. Due the weaker scattering by corrugation of the moiré as compared to the dislocation network, the gap size is also expected to be smaller than the one reported for the 1 ML Ag/Cu(111) dislocation pattern. Figure 3.42(a), clearly shows the umklapp of the surface state after doping with 0.5 ML Au and subsequent

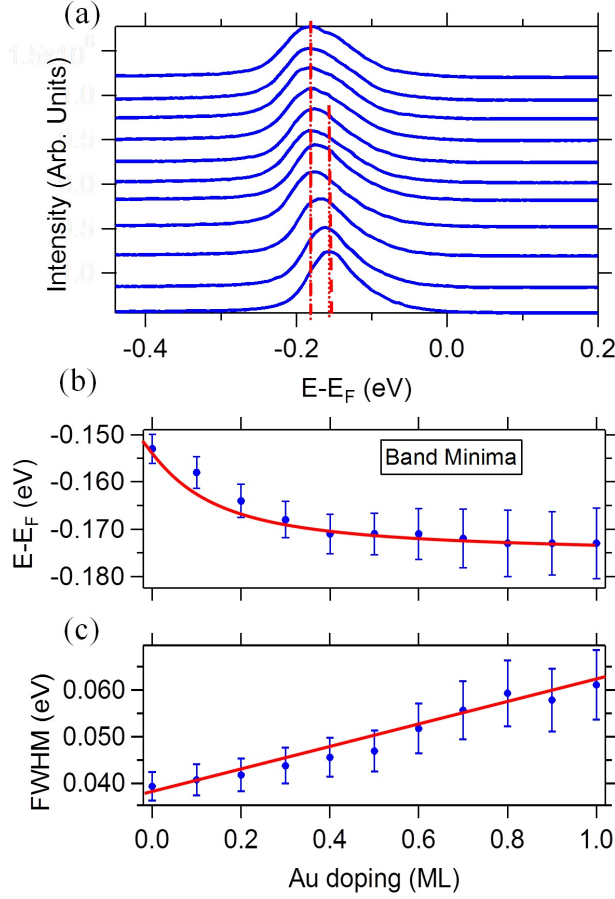


Figure 3.41: ARPES Data: Band Minima-Au/2 ML Ag/Cu(111). a) EDCs at the band minimum of the 2 ML Ag/Cu(111) as a function of Au doping and subsequent annealing to 550 K. (b) The energetic position of the band minimum and (c) the corresponding FWHM for the surface state as a function of Au doping.

annealing to 550 K. The features are, however, rather broad to extract the exact dispersion of the surface state. Upon annealing to 650 K, Fig. 3.42(b-c), the features get narrower with nearly the exact band minima as for the 550 K annealed sample. Fitting the surface state as well as the umklapp branches using the free-electron parabolic dispersion, the band crossing was estimated to take place at 23 meV above the Fermi level.

In order to visualize the different symmetry directions, we have measured the constant energy cuts for the 0.5 ML Au doped sample (annealed at 550 K), Fig. 3.43. The FS does not show gapping over the entire momentum range with, however, a slight depletion of intensity close to the \bar{M} -points. The constant energy cut taken at 23 meV above the Fermi level looks hexagonally shaped and, slightly, resembles the FS of the 1 ML Ag/Cu(111) system. This, in fact, means that the \bar{M} -point gap for the doped system is close to 23 meV above the Fermi level at room temperature.

3. RESULTS AND DISCUSSION I

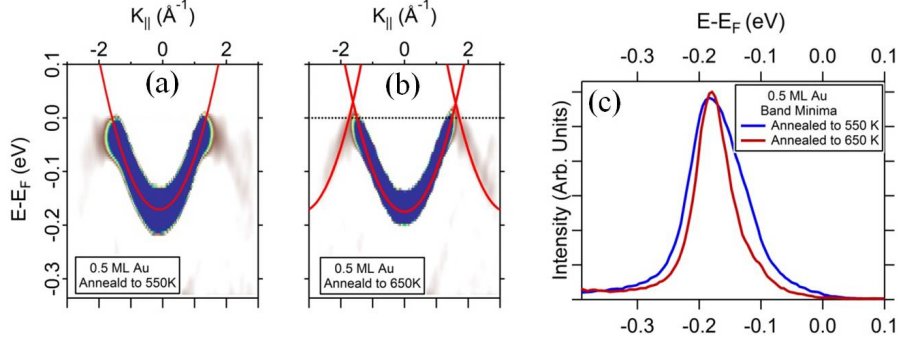


Figure 3.42: ARPES Data: Dispersion Plots: Au/2 ML Ag/Cu(111) - The surface state band dispersion for the 0.5 ML Au doped 2 ML Ag/Cu(111) after annealing to (left) 550 K and (middle) 650 K, and (right) the corresponding EDCs at the band minimum.

One should note that the constant energy surfaces measured here are for the 550 K annealed sample where the surface state is rather broad. Therefore, the Au doping scenario can be optimized to allow for quantitative analysis of such gap. First, the annealing temperature has to be chosen in such a way that the surface state is as narrow as possible with its binding energy as high as possible. This will bring the gap close to 20 meV above the Fermi level.

Second, a low temperature measurement (150 K) will further shift the full surface state by the required ~ 20 meV and the gap will lie completely at the Fermi level. We expect a smaller gap size in this special case of the moiré superstructure, and at 150 K the upper edge of the gap is most probably accessible. For even bigger gap sizes, a combination of both very low temperature (40 K) and the perfect choice of the Au coverage and the annealing temperature can shift the surface state further down while maintaining its FWHM reasonable enough to perform quantitative analysis.

3.8.2 Tunable Periodicity in 1 ML Ag/n-ML Au/Cu(111):

We have seen in the last section that the Au and Cu atoms in multilayers of Au on top of Cu(111) diffuse/segregate into the bulk/surface resulting in an alloyed structure, similar to the one reported for the submonolayers Au doped Cu(111). Our STM measurements showed that the deposition of 1 ML Ag on top of such alloyed multilayer Au/Cu system results in, similar to the slightly doped samples, a dislocation like

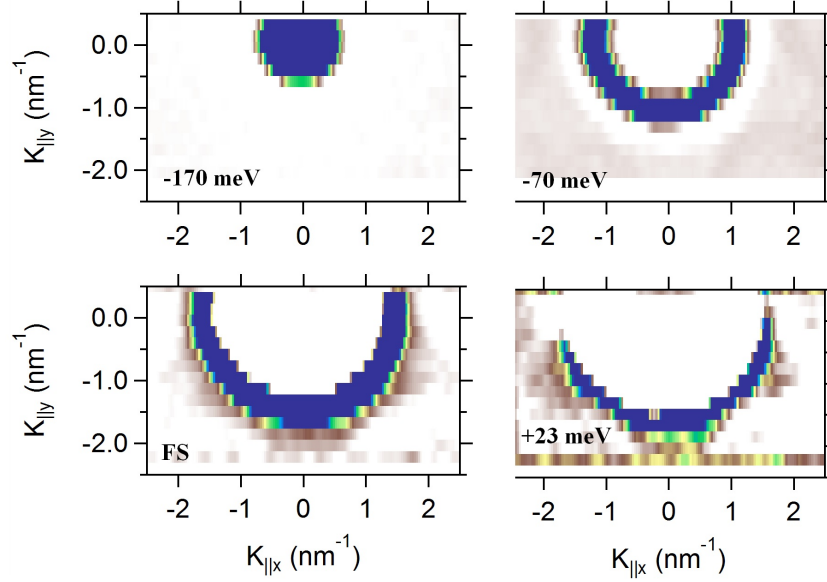


Figure 3.43: ARPES Data: CESs: Au/2 ML Ag/Cu(111) - Constant energy cuts for the 0.5 ML Au doped 2ML Ag/Cu(111) after annealing to 550 K taken at the band minimum, -170 meV, -70 meV, the FS (0 meV) and at + 23 meV above the Fermi level.

pattern with higher periodicity (~ 3.2 nm), Fig. 3.44. On one hand, the formation of the dislocation pattern on the multilayer Au/Cu system can be considered as an additional proof for Cu segregation to the surface. That is so, because the formation of the dislocation pattern is believed to be due to the removal of Cu atoms. The slightly larger periodicity obtained in the multilayer Au case opens the possibility toward engineering the dislocation network pattern, and hence the re-shaping of the FS. The later is essential for further generalization of the theoretically proposed surface state nano-electronics. In the STM images the dislocation patterns are covering the full surface, however, with a high degree of inhomogeneity. This full wetting of the Ag layer(s) is further confirmed from the shape of the d -bands, shown in Fig. 3.45, for the Ag films compared to the as deposited and the 650 K annealed 5 ML Au/Cu. The main bands for Au and Cu (-2.0 eV to 4.5 eV) quenches significantly after the deposition of 1 ML and 2 ML Ag while the main d -bands of Ag (-5.0 eV to 6.3 eV) increase according to their respective coverage. Therefore, we conclude an almost complete wetting of the Ag films on top of the 5 ML AuCu alloy. The LEED pattern clearly shows a moiré-like superstructure pattern, the brightness of the spots, however, were not as sharp as

3. RESULTS AND DISCUSSION I

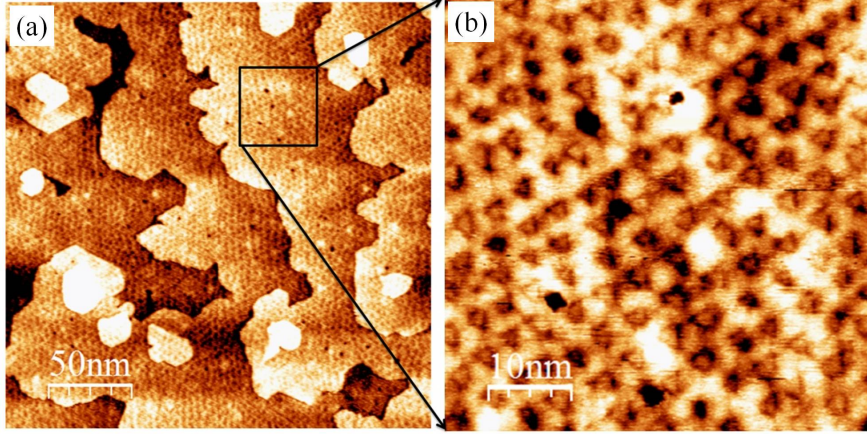


Figure 3.44: STM Images: 1 ML Ag/3 ML Au/Cu(111) - STM images for 1ML Ag/ 3 ML Au/Cu(111) after deposition at 100 K followed by annealing to 600 K . The image to the right is a zoom from the large scale image (black square), showing the dislocation network more clearly.

observed for the low Au doped samples (not shown).

The ARPES results for the 1 ML and 2 ML Ag on top of the alloyed 5 ML Au/Cu are shown in Fig. 3.46. The quantum well states (QWSs), previously seen in the 650 K annealed 5 ML Au/Cu, are still present, together with a new surface state, different from the Au/Cu one, characteristic for the 1 ML and 2 ML Ag. The latter two are further displayed in Fig. 3.46(b), and the corresponding EDCs at the band minima are shown (blue and red) in (c) compared to the 5 ML Au/Cu (black). The band minimum was found at $E = -0.17$ eV and $E = -0.125$ eV for, respectively, the 1 ML and 2 ML Ag films. The lower binding energies in the two cases are ascribed to a worse quality of the surface, rather than a stronger potential of the triangular dislocations themselves. The variation of the energetic position of the QWSs with Ag thickness, seen in the inset of (c), follow the usual behavior, where for higher thicknesses the QWSs shift toward lower binding energies^[137]. Concerning the 3.2 nm periodicity observed in the STM images, this would lead to a back-folding of the surface state at $k_{||} = \sim 1.1 \text{ nm}^{-1}$. This is not observed in ARPES, where very broad umklapps are hardly seen, in the second derivative, close to the usual $k_{||} = \sim 1.5 \text{ nm}^{-1}$ reported for Ag/Cu. We believe that a large random size distribution of the dislocation network periodicity at the surface is taking place. A more systematic study, for wide range of annealing temperatures

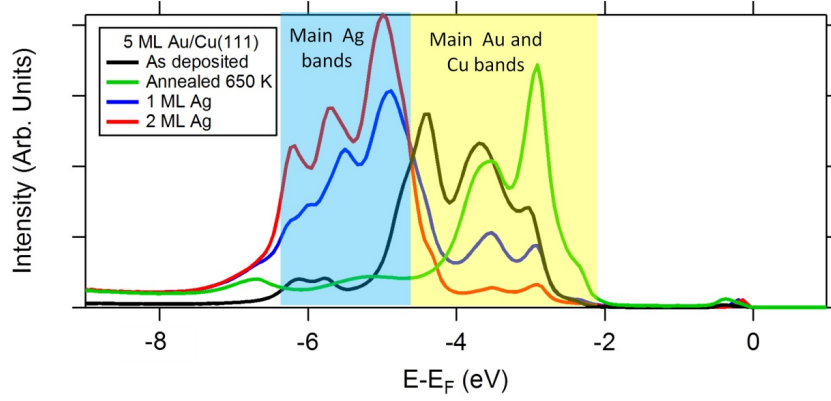


Figure 3.45: Valence Band Spectra: Au/Cu vs. Ag/Au/Cu - Valence-band spectra of as deposited (black) 5 ML Au/Cu(111) and after annealed to 650 K (green). The same for 1 ML Ag (blue) and 2 ML Ag on top of the annealed 5ML Au/Cu alloy. The yellow (blue) shaded regions highlight the main bands of Au and Cu (Ag).

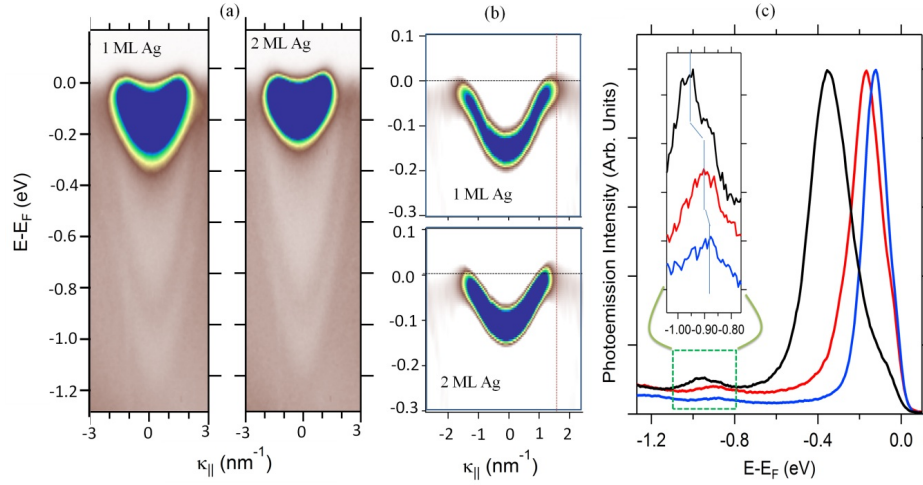


Figure 3.46: ARPES Data: QWSs: Ag/Au/Cu - (a) Surface and QWS states of the 1 ML and 2 ML Ag on top of 5 ML Au/Cu(111) annealed to 650 K. (b) Only the surface states of the two systems are shown with better energy resolution and displayed in their second derivative. (c) the band minima EDCs for 5 ML Au/Cu (black), 1 ML Ag (red), and 2 ML Ag (blue) in top of 5 ML Au/Cu surface alloy. The inset in (c) shows the QWSs for the three systems.

3. RESULTS AND DISCUSSION I

and Au coverage, are required to control the periodicity of the Ag/Cu(111) dislocation network.

3.9 Conclusions:

We have shown that by an appropriate combination of Au doping and annealing temperature, the surface state band minimum of the 1 ML Ag/Cu(111) can be tuned without significant changes of its line width. In particular, we were able to relocate

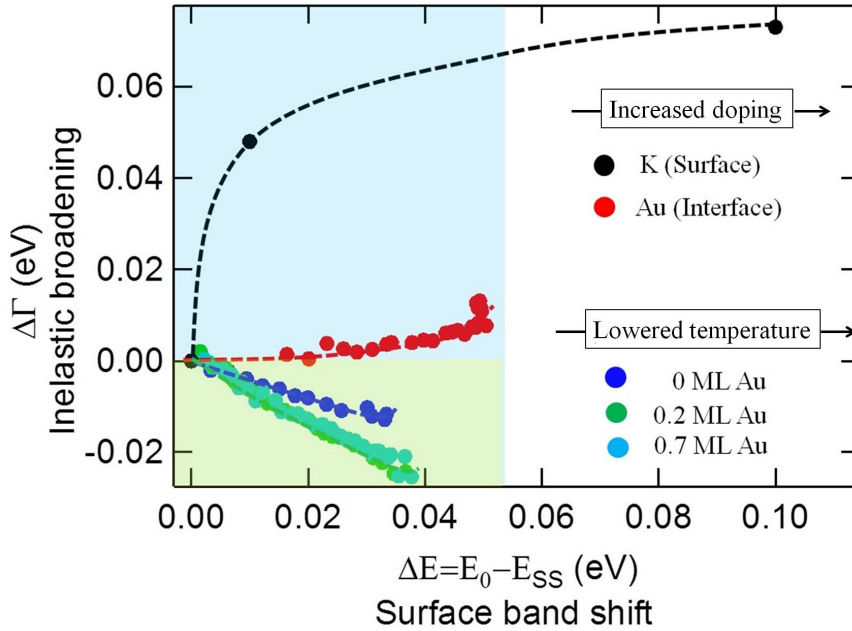


Figure 3.47: Line Width vs. Band Minima Shift: Summary - (a) Inelastic broadening (line width) versus the surface band shift for surface/interface doping with K/Au doping (black/red). The same plot for different temperature for the undoped (dark blue), 0.2 ML Au (green), and 0.7 ML Au (light blue) doped 1 ML Ag/Cu(111).

the \bar{M} -point gap in a wide energy range even completely below the Fermi level. The later allows us to observe a complete Lifshitz transition at 300 K, where the hole pockets at the \bar{K} -point fill up and the Fermi surface become electron-pocket like at the \bar{M} -point. Using low temperature measurements the contributions to the hole lifetime; the electron-electron, electron-phonon, and electron-impurity scattering, have been determined for the 1 ML Ag/Cu surface state doped with different Au amount. We

concluded that, the strength of the electron-electron and electron-phonon interactions are nearly independent on Au amount and are similar to the bare Cu(111) substrate, rather than the Ag(111) surface. To the accuracy limit of our measurements, we have not detected noticeable change on the lifetime while scanning the \bar{M} -point gap across the Fermi level.

The power of the Au “*interface*” doping approach and low temperature measurement compared to the usual “*surface*” doping with alkali metal, can be nicely seen in Fig. 3.47, where one clearly notices the possible tunability of the band minima with the resulting line width (i.e., lifetime). We have also tested the possible generalization of Au interface doping for thicker Ag films on top of Cu(111). Whereas in the 1 ML Ag case a maximum of ~ 50 meV shift of the surface state has been obtained, only a 25 meV shift for the 2 ML Ag film was obtained for the maximum Au coverage. This allows us to, barely, recognize a hexagonally distorted constant energy surface (at +23 meV) similar to the FS characteristic for the 1 ML Ag/Cu(111). For thicker surface Ag films (not shown) the interface Au doping has no effect on the Ag surface state.

3. RESULTS AND DISCUSSION I

4

Results and Discussion II

4. RESULTS AND DISCUSSION II

Coexistence of 1D and 2D Lateral Periodicities on the Surface of 1 ML Ag/v-Cu(111)

4.1 Introduction and Literature Survey:

In the previous chapter, the importance of having 2D nanostructured substrates has been explained from a basic research point of view. For technological applications, however, one can consider most of the patterned (e.g. reconstructed) surfaces as templates for the growth of inorganic and/or organic architectures. This way of self-organization has been shown to be a successful alternative to the top-down nanostructurization techniques (e.g. lithography techniques). As a consequence, a special attention has been paid to the possibility of systematically tuning the periodicities of such templates as well as the minimization of their final patterns size distribution. The 1 ML Ag/Cu(111) template presented in the previous chapter represents one of such 2D templates with, interestingly, nanoscale periodicity. However, the tunability of the dislocation network periodicity for that system has not been so far reported.

Vicinal surfaces, on the other hand, have been shown to be interesting candidates as tunable 1D templates. A vicinal surface of a single-crystal is a surface whose orientation is close to that of a low-Miller index surface. It is usually obtained by polishing a single crystal slightly off a high symmetry low-Miller indices direction, by an angle called the miscut angle (α). When suitably prepared, at the atomic scale a vicinal surface consists of a regular array of parallel atomic steps separating atomically flat terraces of the high symmetry plane^[41]. Due to the repulsive stepstep interaction these steps generally appear regularly spaced, as shown in the schematic description of Fig. 4.1(a). The most important geometric parameters for a vicinal surface are the step array periodicity d , the terrace width L , the step height h , and the miscut angle α . All these parameters are combined together in one equation, $\tan(\alpha) = \frac{h}{L}$, characteristic of vicinal surfaces^[42].

4. RESULTS AND DISCUSSION II

Obviously, by just tuning the miscut angle, it is quite easy to control the step-step separation and so the terrace width as well. In some cases, especially for large miscut angles, steps tend to bunch together and form a “*faceted surface*”, i.e. segregation of two alternating phases with different step lattice constants. However, the simplest case of a vicinal surface is a regular array of one-atom-height steps separated by flat terraces. As mentioned in chapter two, two different types of minifacets at steps are originated, namely A- $\{100\}$ and B- $\{111\}$ minifacets, when the miscut is toward the $[1\ \bar{1}\ \bar{2}]$ and $[11\ \bar{2}]$ directions, respectively. Assuming periodic monatomic step arrays, terraces will contain $m + \frac{2}{3}$ atomic rows for $\{100\}$ -type steps, and $m + \frac{1}{3}$ for $\{111\}$ -type steps, where m is an integer number. The Miller indices are then $(m+1\ m-1\ m-1)$ and $(m-2\ m\ m)$ for $\{100\}$ and $\{111\}$ -like vicinals, respectively^[42].

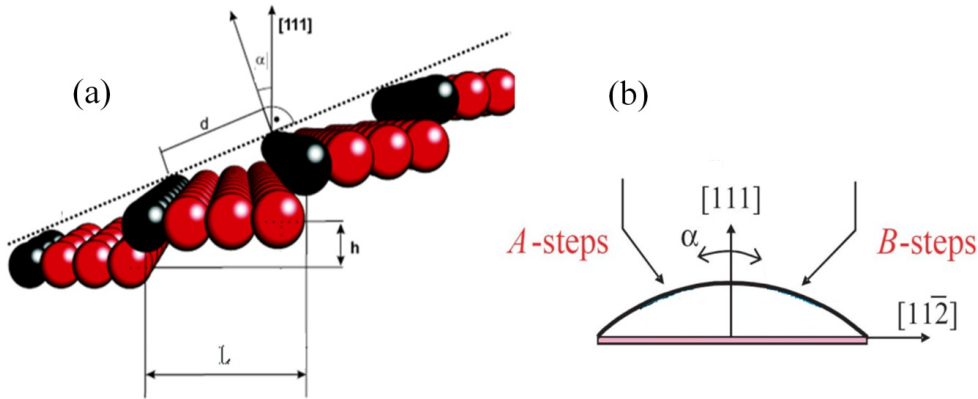


Figure 4.1: Schematic View: Curved Crystal - Schematic side view of a vicinal surface, indicating the relevant parameters (a)^[41], and of curved Cu(111) crystal (b). The Cu(111) curved crystal shows no facets for all miscut angles at both sides of the sample.

In the very same analogue, “*curved crystal surfaces*”, as schematically described in Fig. 4.1(b), and in Fig. 2.10 of chapter 2, allow a smooth variation of the miscut angle in the same sample and hence appear as the rational way to explore and tune the properties of vicinal surfaces that depend on d ^[43,44].

Practically and due to the presence of steps which can strongly alter atomistic process of adatoms diffusion, the growth on a vicinal surface can be very different compared to a flat one^[167,168]. Moreover, the vicinal surfaces may preserve the reconstruction in the flat terrace adding extra periodicity and hence a different growth mechanism within

the terraces as well^[42]. Therefore, vicinal, faceted, and/or reconstructed vicinal surfaces have been successfully used to grow a vast amount of technologically interesting highly ordered nanostructure architectures, such as nanodots, nanowires, naomesh, nanochains, nanostripes, etc^[169–181].

So far the above discussion mainly concerned the technological application of such vicinal surfaces as templates. The vicinal surfaces, however, can be considered as model nanostructures themselves with tunable 1D nanoscale periodicity. This, in fact, made them interesting candidates to study the electronic structure of low dimensional systems. In the present work, the vicinal surfaces of interest are the (111) noble metal surfaces. Flat noble metal surfaces feature Shockley type surface states with Fermi wavelength in the nanoscale, see appendix A. The presence of periodic arrays of steps with a periodicity close to the Fermi wavelength can lead to the exotic modification of those surface states. It has been shown that, by varying the terrace width, hence at different miscut angles, the dispersion of the electrons can be tuned from free electron like (in flat surfaces) to a 1D superlattice, and to 1D quantum well states^[41,182–189]. For potential applications, the terrace width can be finely tuned in order to set the superlattice gaps at the Fermi energy^[44,190]. This critical terrace width was shown to vary for different noble metal surface^[190,191]. The size of the superlattice gaps was shown to vary depending on the magnitude of the step potential^[44]. The ability to modulate electronic states at metallic surfaces will lead to new materials and practical applications because it enhances the effective chemical contrast on the surface, especially when the modulation occurs around the Fermi energy, which in turn can add a new driving force, electronic in origin, for self-organization processes^[82,191].

In the previous chapter, it has been shown that the 1 ML Ag on top of “*flat*” Cu(111) surface led to the formation of moiré and/or dislocation superstructure. In particular, the formation of the dislocation network was ascribed to the removal of Cu atoms from the substrate. On vicinal Cu surfaces, the formation of such dislocation networks was also observed, together with the extra periodicity of the steps. For vicinal surfaces with very narrow terrace width, the misfit between the size of the dislocation triangles and the terrace width has found to induce a periodic faceting of the substrate^[178]. For Ag coverage less than 1 ML, such faceting consists of alternative Cu-free and Cu-Ag covered stripes, the relative terrace width of which can be nicely tuned by Ag coverage^[178,179].

4. RESULTS AND DISCUSSION II

Apart from the technologically interesting application of such template, the electronic structure was found to be of particular interest as well. A progressive transition, as a function of Ag coverage, from 2D surface bands into 1D quantum well states has been observed^[192,193]. It has also been shown that, Ag stripe boundaries become, surprisingly, “transparent” to Cu-like states, since they display band dispersion as in flat Cu(111)^[194]. The Cu substrates used in Ref. [192]^[192], [193]^[193], and [194]^[194] were the vicinals Cu(223), Cu(335), and Cu(10 10 11), respectively. Detailed studies, however, for a large variety of vicinals is not so far reported in literature. In fact, the curved crystal approach allows such study to be done in a precise way.

In this context, this chapter mainly investigates the electronic structure of 1 ML Ag on top of the curved Cu(111) crystal. First the electronic structure as a function of the miscut angle of the clean curved Ag(111) and Cu(111) crystals will be briefly discussed. In particular, the magnitude of the step potential and its effect on the energetic position and the broadening of the surface state will be extracted. Second, the electronic structure of the 1 ML Ag/Cu(111) system will be discussed in more detail. The magnitude of the step potential will be compared to the clean curved crystal. The size effect and the broadening of the surface states will be discussed. More attention is paid to the situation at which the step superstructure lattice vectors coincide with the one or two dislocation triangles. The STM data for the clean and 1 ML Ag covered curved crystal will be analyzed and appear throughout the text, when required, to facilitate the interpretation of the ARPES data, since they allow for structural/electronic interplay to be clearly seen. A theoretical calculation for the electronic band structure, local density of states (LDOS), and the photoemission intensity will be presented and compared to ARPES data.

4.2 Samples Preparation and Experimental Tools:

The clean Cu(111) and Ag(111) curved crystals have been cleaned by repetitive cycles of sputtering and annealing. The Ag wedge (0.7 ML to 1.2 ML) was deposited on top of the curved Cu(111) substrate while the substrate was kept at 150 K. The sample is then softly annealed to 400 K for few minutes. The wedge is grown parallel to the steps, Fig. 4.2, and the position of 1 ML Ag coverage is determined on the flat area of

the curved crystal by following the surface state (in ARPES) or the dislocation pattern (in STM).

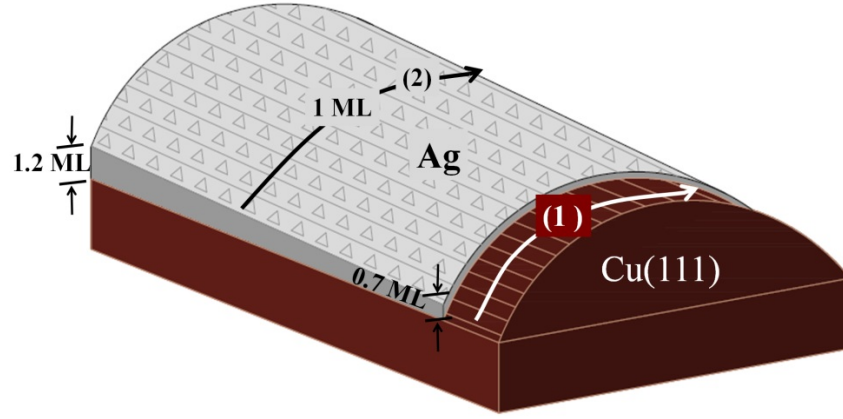


Figure 4.2: Invetsigated Samples: Wedge Preparation - Schematic description of the sample preparation procedure showing the Ag wedge (0.7 ML to 1.2 ML) grown on top of the curved Cu(111) crystal. Arrow 1 represents the scan across the clean curved crystals, whereas arrow 2 is the scan across the 1 ML Ag on top of the curved Cu(111) crystal.

All the photoemission measurements were done at the SRC, while STM and LEED measurements presented here were all performed at Nanophysics laboratory.

4.3 Results and Discussion:

4.3.1 Curved Cu(111) and Ag(111) Crystals¹:

In order to characterize the surfaces corresponding to different areas on the curved crystal (i.e. different miscut angles), we have performed characteristic STM measurements on different points of both Ag and Cu curved crystals (arrow 1 in Fig. 4.2). These are shown in Fig. 4.3 and Fig. 4.4 for Ag and Cu(111) curved crystals, respectively. The LEED patterns are also recorded, by scanning the electron beam from one to the other

¹The contribution of the present author to this subsection is limited to the STM measurements of the curved Ag(111) crystal together with the LEED pattern for both Ag(111) and Cu(111) curved crystals, in collaboration with M. Corso and E. A. Goiri. ARPES measurements and analysis were done by F. Schiller and J. E. Ortega.

4. RESULTS AND DISCUSSION II

side of the sample, for both crystals at different points. These are displayed in Fig. 4.5 for Cu(111) curved crystal.

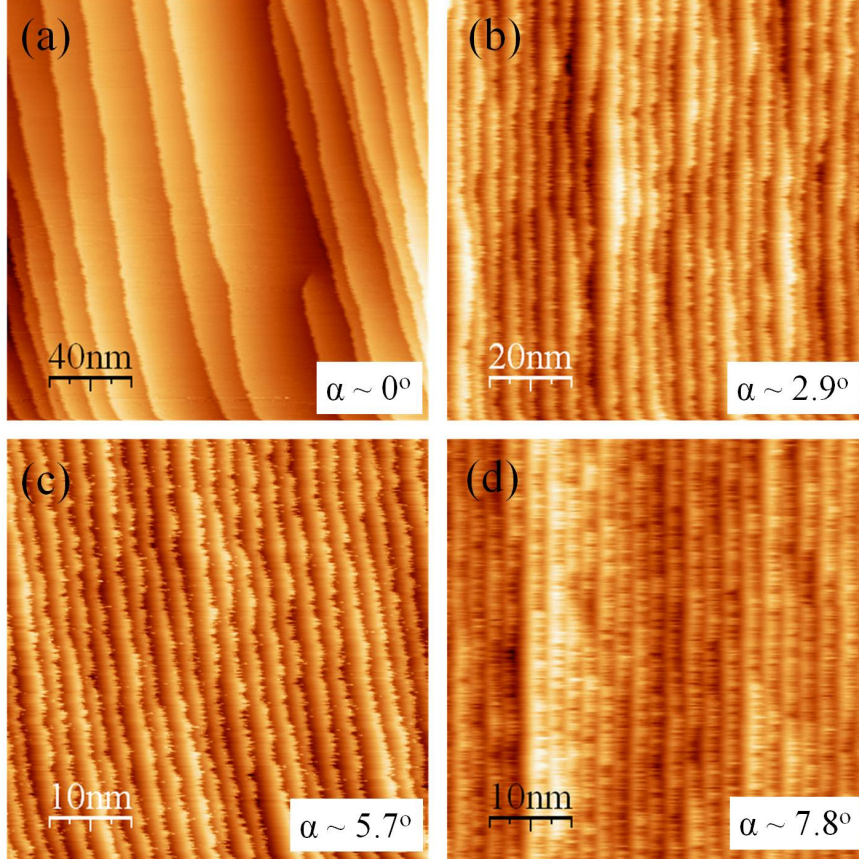


Figure 4.3: STM Images: Curved Ag(111) - STM images on some areas of the curved-Ag(111) clean substrate, where the miscut angle increases as one goes from (a) to (d) toward the right side of the sample.

While scanning the STM tip over the surface, starting close to the flat area of the surface (Fig. 4.3(a) and Fig. 4.4(a)), a highly ordered monatomic periodic array of steps is clearly seen, the separation of which decreases with increasing the miscut angle. No facets have been observed at any miscut angle for Ag and Cu crystals, in contrast to the clear faceting reported for the reconstructed curved Au(111) crystal^[43]. The LEED pattern in the flat part of the sample reflects the hexagonal closed packed structure of Ag(111) and Cu(111) and the sharpness of the diffraction spots confirms that the samples are clean in a macroscopic scale. Only the LEED patterns on the curved Cu(111) crystal are shown in Fig. 4.5.

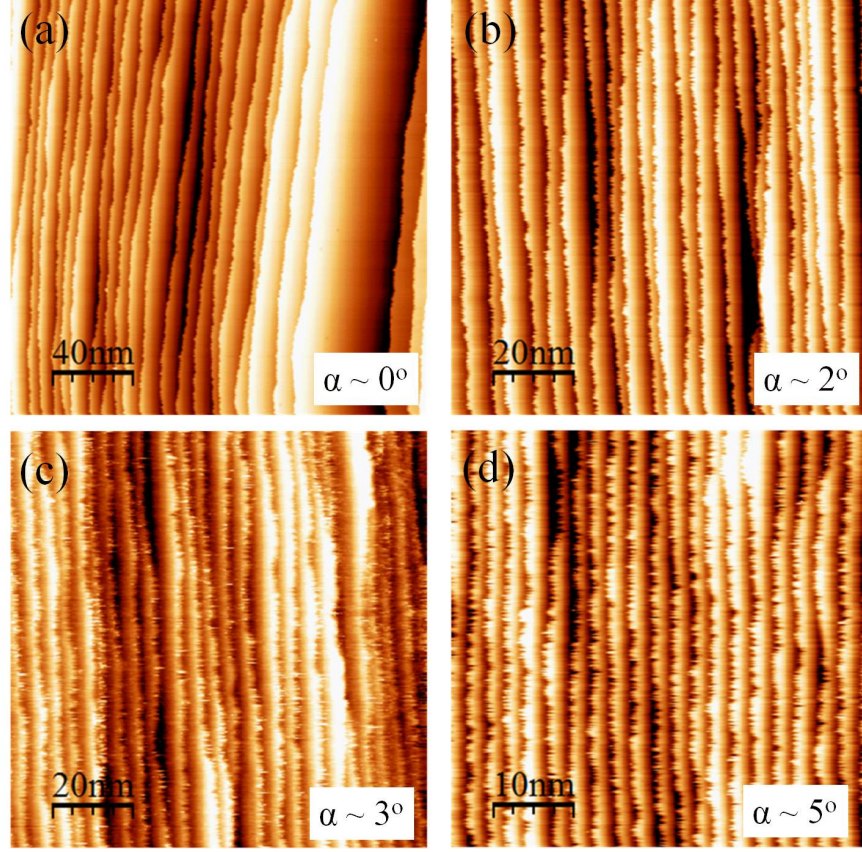


Figure 4.4: STM Images: Curved Cu(111) - STM images on some areas of the curved-Cu(111) clean substrate, where the miscut angle increases as one goes from (a) to (d) toward the right side of the sample.

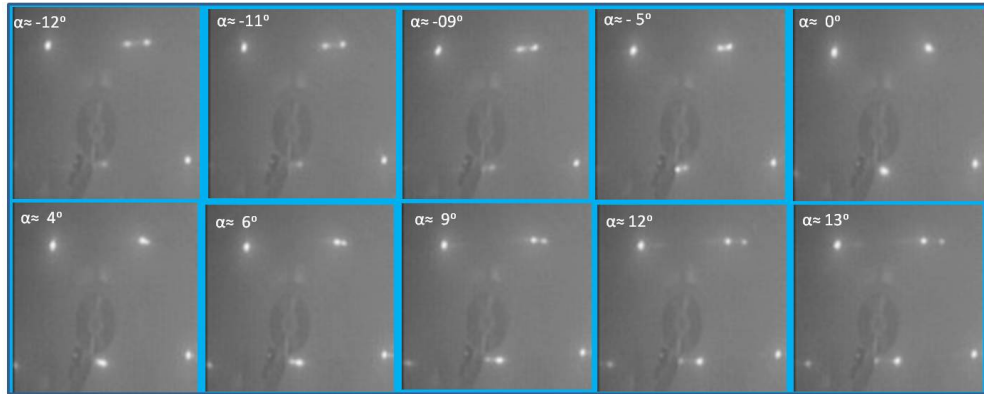


Figure 4.5: LEED Patterns: Curved Cu(111) - LEED images of the curved-Cu(111) clean substrate. The 1×1 spots at $\alpha = 0^\circ$ split into two spots the separation of which increases with the miscut angle at both sides of the crystal.

4. RESULTS AND DISCUSSION II

Scanning the electron beam along the vicinal part of the sample leads to a splitting of the diffraction spots due to the presence of an extra periodicity corresponding to the regular step arrays. The magnitude of the splitting was found to increase as the miscut angle decreases, i.e. with smaller step-step separation. The observed spots, again, indicate the absence of any facet in both sides of the sample in contrast to the vicinal^[42] and curved^[43] Au(111) single crystals.

The surface electronic structure of the curved Ag(111) and Cu(111) crystal was then investigated with ARPES. Taking advantage of the narrow size of the synchrotron light spot in the SRC, one can systematically sample different points on the surface. Figure 4.6 summarizes the important aspects of the surface electronic structure for both crystals and its dependence on the miscut angle. The top panel of the figure shows photoemission intensity plots for the Shockley surface state dispersion in the direction perpendicular to the step array, taken at two different miscut angles (left). When the terrace width is closer to the Fermi wavelength of the Cu substrate ($\lambda_{F/2} = \sim 17 \text{ \AA}$)^[182], an energy gap is opened at the Fermi level.

This critical miscut angle for Cu, as estimated from the vicinal surface equation, is $\sim 7^\circ$. The white dashed lines in the top and middle panels of Fig. 4.6 clearly indicate the presence of a Fermi gap. This is also seen in the middle panel, where the FSs intersect (white dotted lines) close to this miscut angle leading to a FS nesting (i.e. depletion of intensity at the circles crossing). At higher miscut angles, e.g. the one shown at 9° , the energetic position of the gap is far above the Fermi level, and the two circles, that represent the FS rings, are not intersecting anymore.

We note that the magnitude of the gap depends on the step potential, which is different for the three noble metals. The step potential can be experimentally determined by following the EDC spectra at the band minimum as a function of the miscut angle. The energetic position of the band minimum with respect to the (111) band (E_o) shifts by an energy (ΔE) toward lower binding energy as a function of the miscut angle, as shown on the top panel (right) for Cu(111) crystal at 5° and 8° miscut angles compared to the flat Cu(111). The relation between the energetic shift (ΔE), the terrace width and the step potential can be deduced within the simplest approach of a 1D superlattice, i.e. a periodic succession of δ -like potential barriers of strength $U_o b$ located at the steps. Here the step potential will be represented by a finite barrier of height U_o and

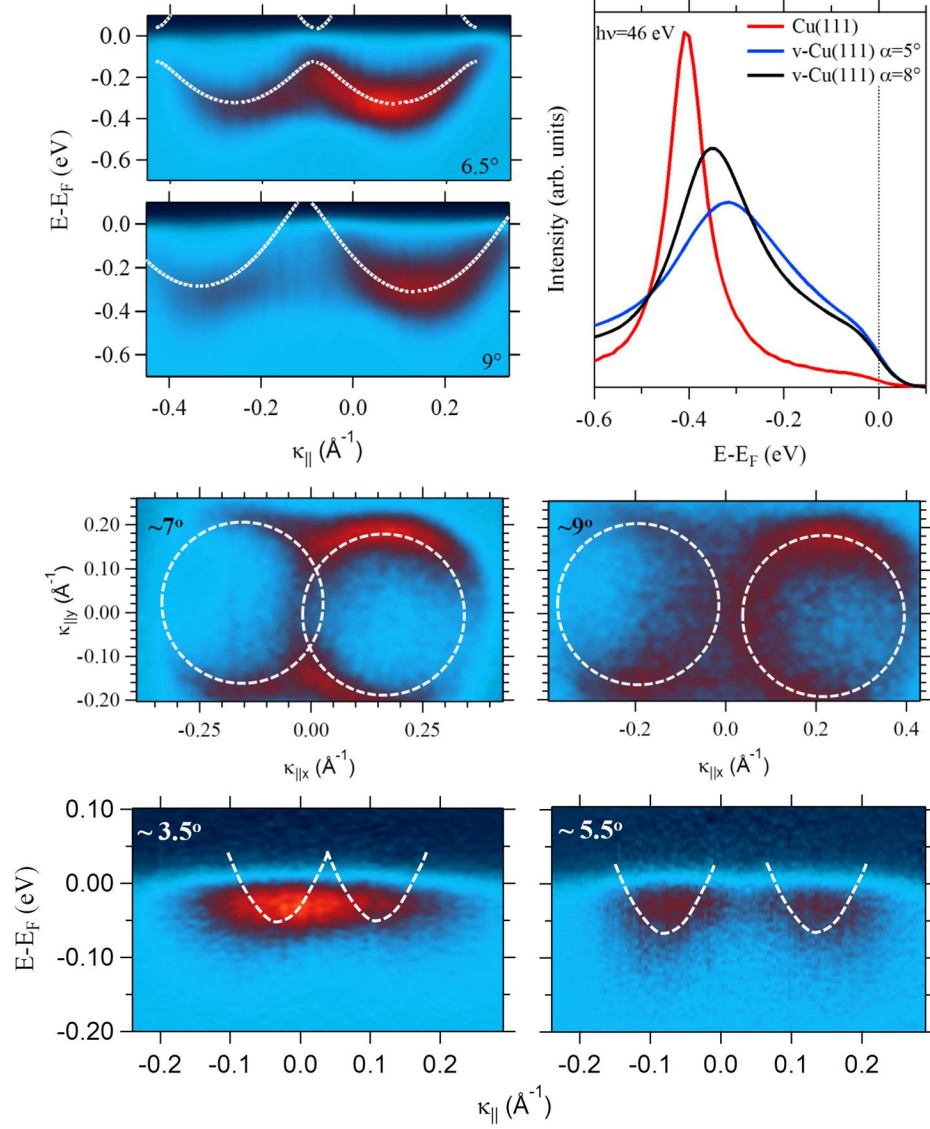


Figure 4.6: ARPES Data: Curved Ag(111) and Cu(111) - The top panel shows (left) photoemission intensity plots of the surface band dispersion at $\sim 6.5^\circ$ and 9° miscut angles in curved Cu(111) crystal, and (right) EDC spectra for band minima at different miscut angles. The middle panel shows FS plots for (left) $\sim 7^\circ$ and (right) $\sim 9^\circ$ miscut angles in Cu(111). The lower panel shows (left) photoemission intensity plots of the surface band dispersion at $\sim 3.5^\circ$ and $\sim 5.5^\circ$ miscut angles in curved Ag(111) crystal. The white dashed curves (circles) are the KP model bands (the intensity maxima) in all the panels. The Fermi level gap opening in curved Cu(111) is clearly seen from the dispersion and FS plots close to $\sim 7^\circ$ miscut. In case of curved Ag(111) the crossing is above the Fermi level. Read the text for further details.

4. RESULTS AND DISCUSSION II

width b , where the 1D Kronig-Penney model can be applied^[44]. At the surface state band minimum ($k_{||B.M.} = 0$), the following expression applies;

$$\Delta E = E(k_{||B.M.} = 0) - E_o = \frac{2\hbar^2}{m_*} \frac{1}{d^2} [\arctan(\frac{q_o}{q})]^2 \quad (4.1)$$

where $q_o = \frac{m_*}{\hbar^2} \times U_o b$ and $q = \sqrt{\frac{2m_*}{\hbar^2} \Delta E}$.

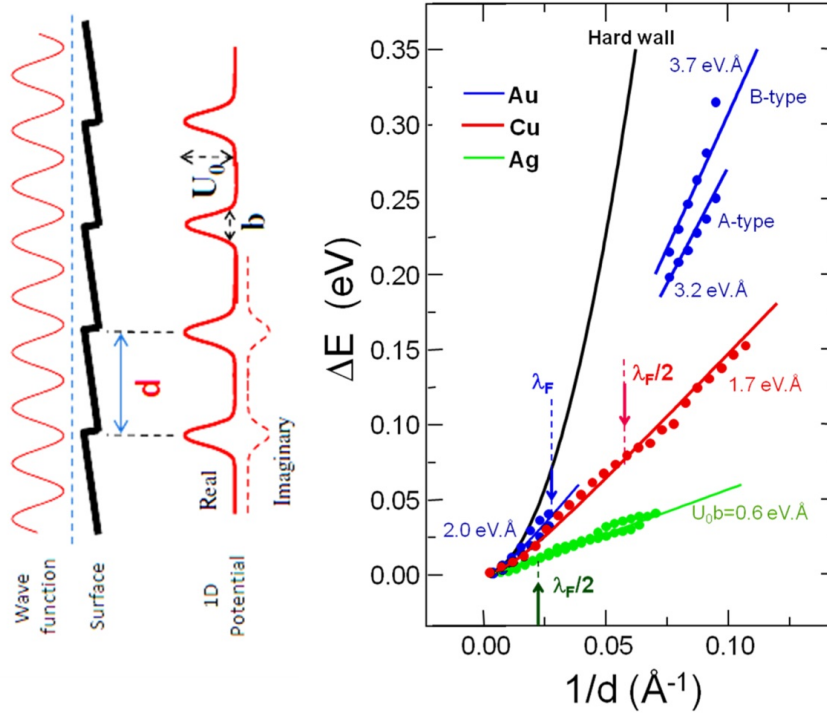


Figure 4.7: Kronig-Penney Model: Curved Ag(111) and Cu(111) - Left: Side-view sketch of the 1D periodic potential in a step superlattice with lattice constant d and $U_o b$ barriers at step edges. Right: The size confinement effect (expressed as ΔE) as a function of the terrace width (expressed as $1/d$) for Ag, Cu, and Au crystals. The solid lines are the KP model fit to the experimental data. The black line represents the hard wall potential, where $U_o b$ goes to infinity. Data points in the faceting range of Au are not included.

In Fig. 4.7 the data points represent the experimental energy shift ΔE as a function of $(1/d)$ for the curved Ag(111), Au(111), and Cu(111) crystals. The data points were extracted by fitting each EDC with a Lorentzian peak multiplied by a Fermi function to eliminate the proximity effect of the Fermi level (especially in the case of Ag(111))

crystal), and convoluted with a Gaussian peak to account for the energy resolution. The reference energies E_o measured on the flat (111) crystals, i.e. $\alpha = 0^\circ$, were -0.056 eV, -0.408 eV, and -0.464 eV for Ag(111) (at 100 K), Cu(111) (at 180 K), and Au(111) (at 150 K), respectively. The lines in Fig. 4.7 represent the fit to the data points using Equ. 4.1, where we assumed $m_* = 0.41 m_e$ for both Cu and Ag, $0.27 m_e$ for Au, and using U_{ob} as the single fitting parameter. The agreement between the simple KP model and the experimental findings is, indeed, remarkable for the three crystals. The values of the potential U_{ob} as comes from this fit were 0.6 eV.Å and 1.7 eV.Å for the Ag and Cu crystals, respectively. The same potential applies to both sides of the crystal, hence the scattering by A-type and B-type steps is, quantitatively, the same. In case of Au, and due to the presence of herringbone reconstruction, the step potential was found to be 3.2 eV.Å and 3.7 eV.Å for A-type and B-type step, respectively. The strength of the step potential is, thus, weaker in Ag, making the corresponding superlattice gaps hardly visible compared to Cu crystal, Fig. 4.6. We also note that the same small value of the Ag step potential has been also reported for the 2D dislocation potential on the Ag/Cu(111) system, as we will see later.

To establish the interplay between the geometric and electronic structure, we have done a statistical analysis on the STM images for both Cu and Ag crystals, as the ones shown in Fig. 4.3 and Fig. 4.4. The average terrace width (\bar{d}) and their size distribution or standard deviation (σ) have been calculated for each miscut angle for both the Cu and Ag crystals. The results are displayed in Fig. 4.7(a-b). Electronic instabilities in vicinal surfaces are expected at 1D nesting values $d = n \times \lambda_{F/2}$, for which superlattice gaps occur at the Fermi level. The calculated terrace widths that correspond to ($n \times \lambda_{F/2}$), are marked in Fig. 4.7 for the three crystals. In Cu we obtain $\lambda_{F/2} = 17$ Å, for Ag $\lambda_{F/2} = 45$ Å and for Au $\lambda_{F/2} = 20$ Å. In the framework of classical elastic model, and for a constant dipole-like step potential strength, a linear proportionality between σ and \bar{d} is a direct indication of elastically stable step lattice. In Fig. 4.8, one clearly sees that in Ag crystal and for both A and B-type steps the relation between σ and \bar{d} is indeed linear. Such linear behavior discards any electronic/structure instability and hence agrees with the measured smallest potential strength for Ag, Fig. 4.7(b). In Cu crystal, on the other hand, a deviation from linearity between $\lambda_{F/2}$ and λ_F with a dip of a minimum at ~ 23 Å is observed. In fact, the step array with step lattice

4. RESULTS AND DISCUSSION II

parameter close to this value, i.e. at 23.5 Å, is visually sharper than other terrace width distribution, as shown in Fig. 4.8(c-d).

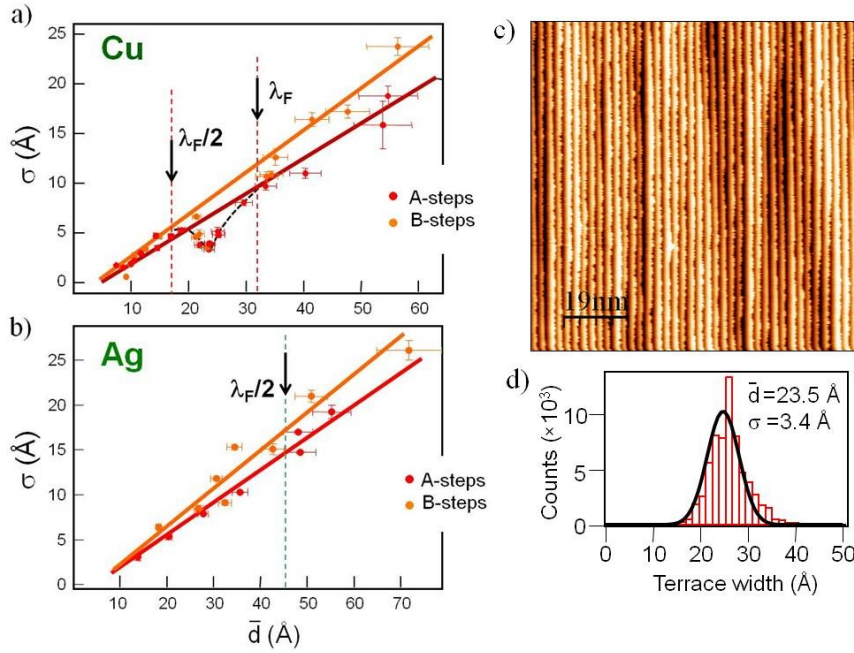


Figure 4.8: STM Statistical Analysis: Curved Ag(111) and Cu(111) - Terrace width variation σ as a function of the average superlattice constant \bar{d} for (a) Cu and (b) Ag, as determined with STM. The deviation from linear behavior is only seen in Cu case, where a dip is observed between $\lambda_F/2$ and λ_F , suggesting a structure instability triggered by the surface state. In (c) a characteristic STM image from Cu crystal with average terrace width (23.5 Å) in the nesting region, showing the sharp size distribution (3.4 Å) as depicted in (d).

For further details concerning the electronic/structure interplay in the three Ag, Cu, and Au curved crystal the reader is referred to Ref. [43,44]^[43,44].

4.3.2 1 ML Ag/Curved-Cu(111)²:

The section concerns the measurements taken along arrow 2 in Fig. 4.2, hence the 1 ML Ag on top of the curved Cu(111). The calibration of the Ag coverage was mentioned already in the previous chapter. We start by examining the size effect (the magnitude of

²A number of people have contributed to this work; M. Corso and J. Cordon (STM) and M. Matena, J. Lobo, and the present author (ARPES at SRC).

the upward shift of the band minimum), the corresponding quantity in ARPES is ΔE , and the resulting step potential, comparing it to Ag(111) and Cu(111), Fig. 4.7. Figure 4.9(a) shows a series of EDC spectra taken at the band minima for different miscut angles. These are fitted with a combined Lorentzian-Gaussian, and the resulting fit parameters for the Lorentzian determined ΔE and ΔW . The size effect (ΔE) and the relative line width (ΔW) is then plotted as a function of the inverse terrace width ($1/d$) and the miscut angle, which is shown on the top scale, Fig. 4.9(b-c).

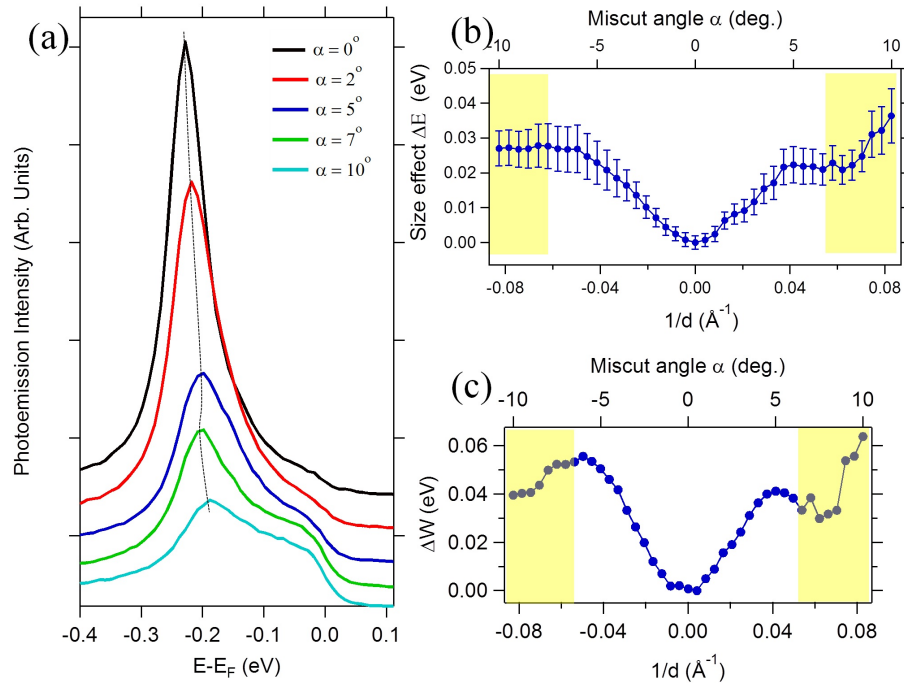


Figure 4.9: ARPES Data: 1 ML Ag/Curved-Cu(111) - (a) EDC spectra at the band minimum for different miscut angles. (b-c) The size effect (ΔE) and the line width (expressed as (ΔW)) as a function of the terrace width (expressed as $1/d$) for 1 ML Ag on top of the curved Cu(111) crystal. The yellow shaded regions in (b-c) are the faceting areas where EDC fitting is not meaningful.

For miscut angles $> 6.5^\circ$ a perfect fit with a single Lorentzian was not possible but the fitting parameters are also included in the figure (yellow shaded regions). The artificial lowering of the width for such miscut angles is, therefore, unphysical. Indeed, the existence of triangular dislocation within the terraces induces a strong faceting of the substrate for narrow terraces. That is the situation of miscut angles close to 6.5° and, therefore, the yellow shaded areas will be excluded from our discussion. Within

4. RESULTS AND DISCUSSION II

this limit, both sides of the crystal reveal similar results, apart from the different quality of both sides, which is shown in Fig. 4.9(c) as differences in the line width. The features that belong to the positive side (positive miscut angles) were always qualitatively the same, but better resolved than the negative side and therefore will be used throughout the chapter, unless specified.

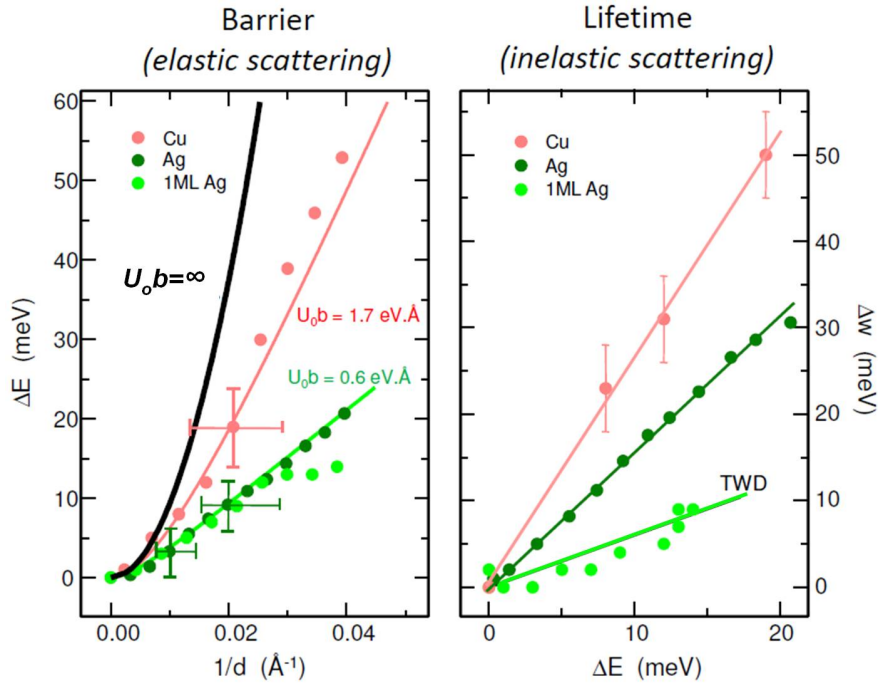


Figure 4.10: Elastic vs. Inelastic Scattering - Left: The size effect (ΔE) as a function of the terrace width (expressed as $1/d$) for Ag (dark green), Cu (red), and the 1 ML Ag/Cu (light green) systems. The solid lines are the KP model fit to the experimental data. The black line represents the hard wall potential, where $U_0 b$ goes to infinity. Right: The line width variation (ΔW) as a function of the corresponding size effect (ΔE) for the three systems defined in the right panel.

In Fig. 4.10 we re-plot the size effect and the relative line width for the Ag(111), Cu(111), and 1 ML Ag/Cu(111) as a function of $(1/d)$. The solid lines are the 1D KP model fit to the data using Equ. 4.1, which yield the magnitude of the scattering potential ($U_0 b$). The same $U_0 b$ (0.6 eV. \AA) value was found to fit both Ag crystal and 1 ML Ag/v-Cu(111) quite well, Fig. 4.10(left). Both ΔE and ΔW are known to be the signature of scattering in an ARPES experiment, apart from intrinsic line width variations. The value of ΔE gives information about the barrier strength and the

elastic scattering, whereas ΔW is related to the inelastic scattering and contains life time information. In fact there should be a correlation between these two, which is not included in the KP model. The ΔW vs. ΔE shown in Fig. 4.10(right), however, points toward a particular difference between the Ag crystal and the 1 ML Ag/Cu system. For the latter, the variation of ΔW with the miscut angle is of the order of the broadening due the terrace width distribution (TWD), light green line in Fig. 4.10(right)^[195]. Therefore, we conclude that both elastic and inelastic scattering at Ag-covered Cu steps is almost negligible, which in turn implies that Cu steps become highly transparent to surface electrons when covered with the Ag monolayer. This property is of particular interest in the search of the so-called surface state nanoelectronics (SSNE) phenomena^[54], namely electron-guiding and focusing by scattering at nanopatterned 1 ML Ag/Cu-Cu(111) systems, where the loss of information via inelastic scattering at the steps is almost negligible .

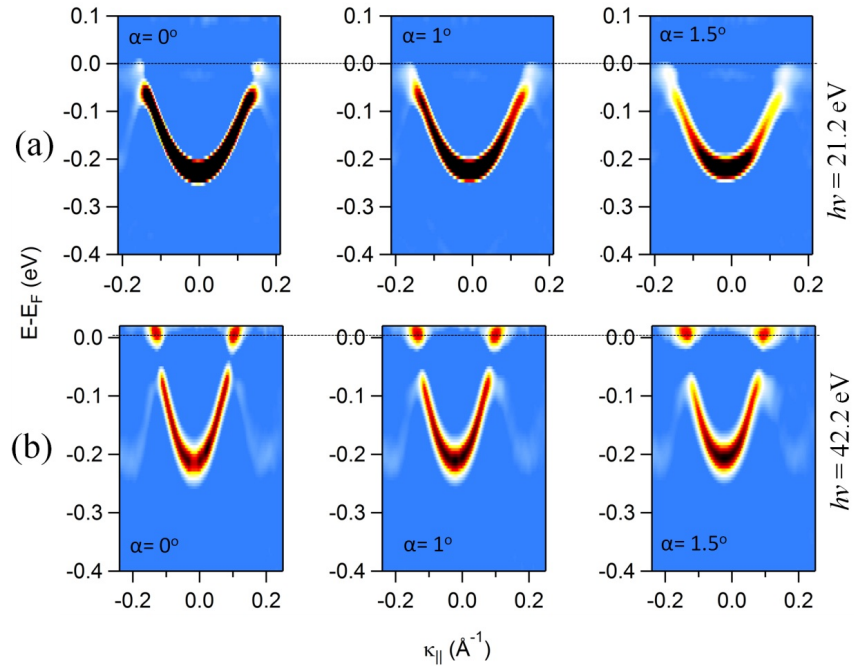


Figure 4.11: Surface States Dispersions: Small Miscut Angles - Photoemission intensity plot for the surface state dispersion perpendicular to the step array on the 1 ML Ag/v-Cu and different miscut angle measured with 21.2 eV (a) and 42.2 eV (b).

In the following we examine the variation of the surface state dispersion due to the

4. RESULTS AND DISCUSSION II

presence of the combined 1D step and 2D dislocation superlattices. Figure 4.11 shows the photoemission intensity plot of the Shockley surface state on the 1 ML Ag/v-Cu(111) for miscut angle from 0° to 1.5° . All the photoemission data presented here are taken in the direction perpendicular to the step lattice. Each image is taken with two different photon energies (21.2 eV) and (42.2 eV) to allow better fitting of the main surface state and visualization of umklapps bands, respectively. One notices that, for this range of terrace width (≥ 80 Å), the gapped surface states look, basically, the same as the flat 1 ML Ag/Cu(111) where the effect of the steps slightly lower its binding energy and the \bar{M} -point gap is barely affected. The high photon energy images, Fig. 4.11(b), show clear umklapps bands due to the dislocation network. Here the steps act as random defects or impurities. No back-folding due to the presence of steps is observed, such that the final shape of the surface state is mainly set by the dislocation network. In fact, our STM measurements on such wide terraces shows randomly spaced steps together with relatively wide areas of the dislocation network, therefore, supporting ARPES findings. We also note that for 1.5° miscut, the terrace width is about 80 Å, thus, in the limit of ARPES ability to detect interference effects^[195].

The interplay between the 1D step lattice and the 2D dislocation network is visible for step-step separations that host one or two triangles per terrace, and it is barely seen in three triangles per terrace. These situations were shown to form a highly ordered and stable superstructure as judged from our STM. Figure 4.12 and Fig. 4.13 show STM images for a terrace width fitting one and two triangles, respectively³. A closer view is also shown in (b) together with the Fourier transform (FT) of the large scale images (c). The distorted hexagonal patterns seen in the FT plots ensure the reliability of ARPES data. One also sees that the splitting induced by the step superlattice is nicely visible in the FT of Fig. 4.13(c), and coincides with the dislocation lattice spots in Fig. 4.13(c). The periodicity of the dislocation pattern parallel to the steps is the same as on flat surfaces (24.2 ± 0.3) Å, for all miscut angles below the faceting onset. The other unit cell axis deviates from this value with a magnitude that depends on the terrace width. In Fig. 4.12(b) the length of this unit cell vector is (31.5 ± 0.3) Å at an angle of 68° to the step axis.

³Close to the step edges half-triangles are also observed in the STM images of Fig. 4.12 and Fig. 4.13. These can be considered as part of the step edge.

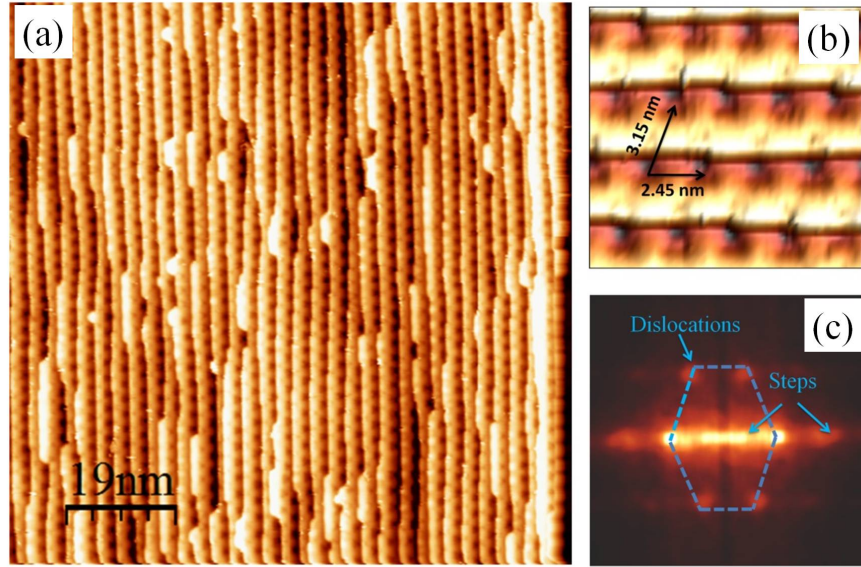


Figure 4.12: STM Images: Miscut Angle = 5.5° : $\{111\}$ Step - (a) STM image for the 1 ML Ag/Cu taken at miscut angle of 5.5° on the 111 minifacets side of the crystal. (b) Small scale STM image, where the dislocation lattice is better resolved. (c) The Fourier transform of the large scale STM image, where the hexagonally distorted reciprocal lattice is marked by the blue lines. The two different set of spots, indicated by the arrows, are due to the coexistence of the step and dislocation lattices.

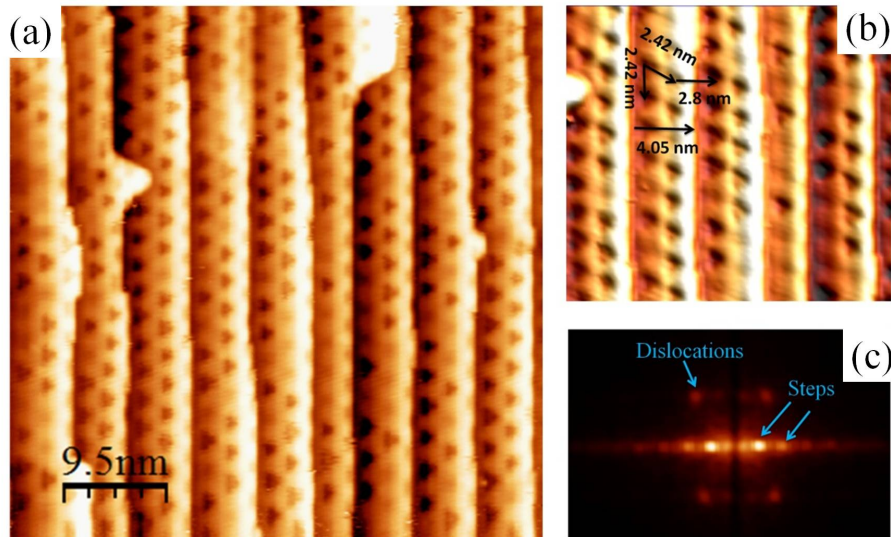


Figure 4.13: STM Images: Miscut Angle = 3° : $\{100\}$ Step - Same as Fig. 4.12 but at a miscut angle of 3° and on the $\{100\}$ minifacets side of the crystal.

4. RESULTS AND DISCUSSION II

Such deviations results in the distortion of the hexagonal lattice, shown in FT, and the subsequent deformation of the BZ. In Fig. 4.13(b) where two triangles are enclosed within the same terrace, the periodicity within each terrace is kept at $(24.2 \pm 0.3 \text{ \AA})$ while the triangle-triangle separation at the boundaries of the step is slightly larger $(28.0 \pm 0.3 \text{ \AA})$. Actually, at both sides of the steps, the triangles are forming a rectangular lattice deviating from the usual hexagonal ordering of the triangles in the flat surface. This might be due to the $\{100\}$ minifacets of this side of the crystal. In fact, STM measurements on different sides of the crystal reveal some differences, where the triangles ordering were found to depend on the step type. Figure 4.14, for example, shows an STM image taken at the same miscut angle of the STM image shown in Fig. 4.12, but on the opposite side of the crystal.

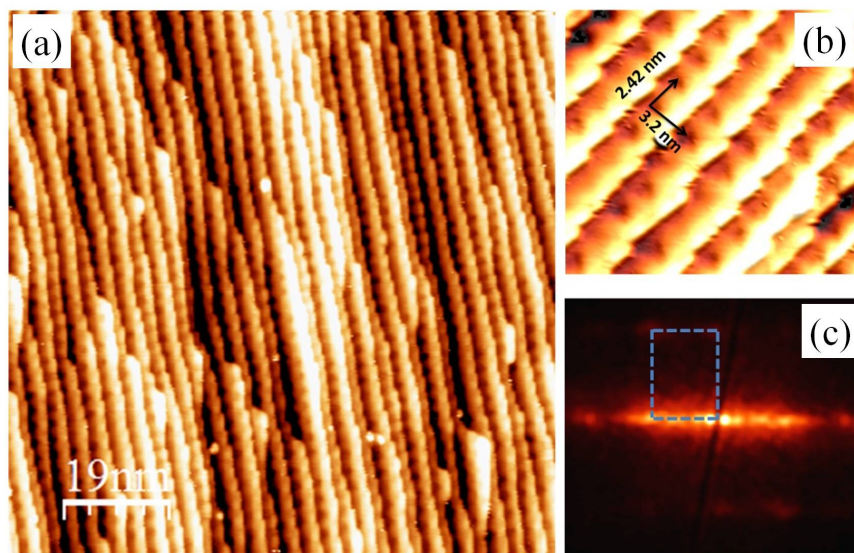


Figure 4.14: STM Images: Miscut Angle = 5.5° : $\{100\}$ Step - Same as Fig. 4.12 but on the $\{100\}$ minifacets side of the crystal, where a square lattice of the triangles is observed.

The same superlattice parameters, 24.2 \AA parallel to the steps and 32 \AA across the steps, have been obtained with the triangles, however, forming a rectangular lattice. The reproducibility of the STM measurements on the $\{100\}$ -type step side was difficult. The formation of such rectangular lattice seems to depend strongly on the sample preparation. On the other hand, different annealing temperatures allow imaging the hexagonal ordering on the $\{111\}$ -type step side and STM results were reproducible.

The signature of a rectangular lattice should be quite distinct from the hexagonal one in ARPES, although we have not detected any difference, i.e., ARPES results in both sides of the crystal are nearly the same, with the exception of the quality of one side compared to the other. Therefore our discussion, and theoretical modeling, will only investigate the hexagonal superstructure formed by the dislocations and the effect of insertion of a tunable step lattice.

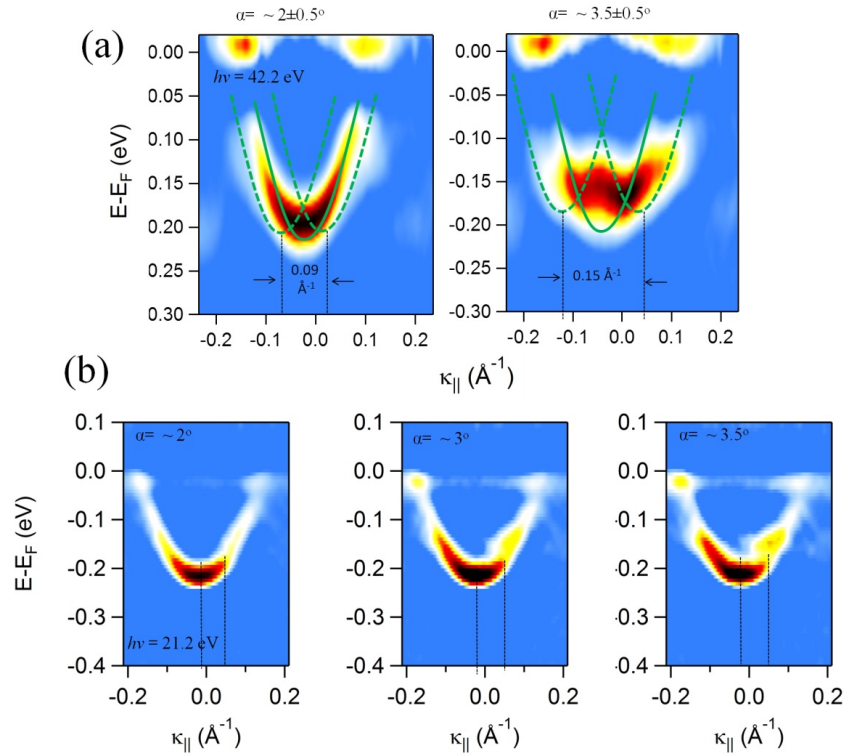


Figure 4.15: Surface States Dispersions: Medium Miscut Angles - Photoemission intensity plot for the surface state dispersion perpendicular to the step array on the 1 ML Ag/v-Cu at different miscut angles measured with 42.2 eV (a) and 21.2 eV (b). The dashed green lines in (a) mark the umklapp bands whereas the solid ones mark emission from 1 ML Ag on top of large flat areas. The dashed black lines in (b) mark the difference between the band minima and the step induced gap.

Figure 4.15 shows the photoemission intensity plot of the Shockley surface state for miscut angles $> 2^\circ$ taken at 42.2 eV (a) 21.2 eV (b). The back-folding due to the presence of the step lattice is seen (dotted green lines) together with residual contribution from Ag on flat Cu(111) terraces (solid green lines). The latter has been also

4. RESULTS AND DISCUSSION II

observed for the clean vicinal copper substrate in our experimental work and by other groups^[196]. For $\alpha = 2^\circ$ the separation between the umklapp bands was found to be $\sim 0.09 \text{ \AA}^{-1}$, hence a terrace width of 70 \AA . For such wide terraces, three triangles per terrace can fit. The crossing of the umklapp bands is seen in Fig. 4.15(b), as a tinny gap (apparently kink) also close to -0.045 \AA^{-1} . This gap is named “*step gap*”, due to the folding by the step lattice. The main \bar{M} -point gap of the dislocation network is, apparently, not affected. The step gap gets better resolved as we increase the miscut angle. At $\alpha = 3.5^\circ$ the separation between the step lattice umklapps shown in (b) was found to be $\sim 0.15 \text{ \AA}^{-1}$. This corresponds to a step superlattice with $\sim 41 \text{ \AA}$, hence can host no more than two triangles per terrace. In fact the step gap nearly keeps its momentum position fix from $\alpha = 3^\circ$ to $\alpha = 4^\circ$. We argue that the step periodicity is set to fixed size due the stability of the two triangles per terrace phase. For a terrace width that is too small to host two triangles, only one triangle fits into the terrace and the step lattice gap nearly coincides with the hexagonal dislocation lattice. This situation takes place for $\alpha = 5^\circ - 6^\circ$.

In Fig. 4.16 we further highlight these situations, namely one and two triangles per terrace. The dotted lines are the band structure calculation along $\bar{\Gamma}\bar{M}$ direction using the geometries shown in Fig. 4.17 as an input. The calculations were performed with the EBEM code briefly mentioned in the previous chapter and the code details can be found in Ref. [54]^[54]. The right side in (a) and (b) are the simulated photoemission intensity plots. From Fig. 4.10 we learned that the step potential in the 1 ML Ag/Cu system is the same as the Ag(111) step potential and, therefore, we use $0.6 \text{ eV}\cdot\text{\AA}$ for both the triangles and step potentials keeping the effective mass to the one of Ag ($0.41 m_e$).

Although our STM images show a deviation from the perfect hexagonal geometry, which is not included in the model, but both fits reasonably well with each other. The simulated photoemission intensity also describes well the massive depletion of intensity^[57] close to the Fermi level, apart from the real gap at the \bar{M} -point. We also note that, the size distribution due to the step lattice is of crucial importance for better visualization of gaps, especially the dislocation gap. For example, in the case of two triangles per terrace, shown in Fig. 4.16(b), a tiny deviation from the perfect geometry will result in a second repetition by the step lattice taking place at momentum values

different from the \bar{M} -point of the dislocation lattice, leading therefore to extra umklapp. This can be seen in Fig. 4.16(b) as a low intensity inside the gap and close to the main umklapps of the dislocation lattice.

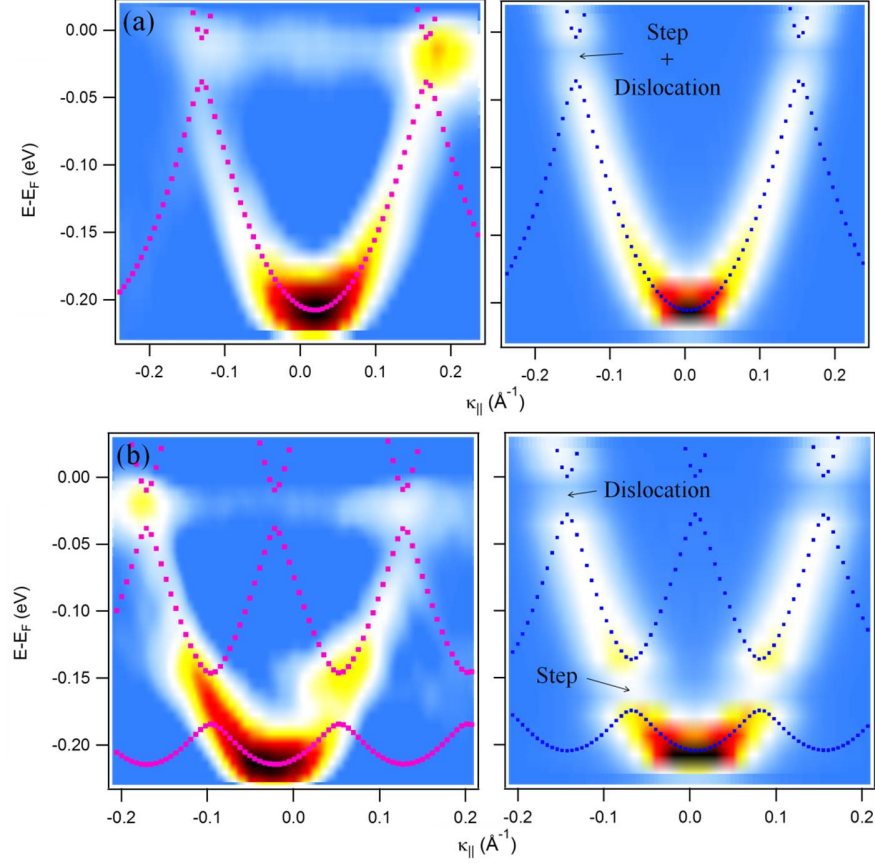


Figure 4.16: Surface States Dispersions: Theory vs. Experiment - Experimental (left) and simulated (right) photoemission intensity of the surface state dispersion perpendicular to the step array for miscut angles of (a) 5.5° and (b) 3.5° which, respectively, correspond to one and two triangles per terrace. The dotted lines are the calculated dispersion perpendicular to the step array in the two cases including the dislocation lattice. In (b) a tinny emission due to terrace width distribution is visible close to the main dislocation network umklapp band.

Our STM images showed that order superstructures are confined within a tinny window close to the nominal miscut, and broader terrace width distribution is easily observed. The $100 \mu m$ light spot in ARPES, therefore, is sampling different regions and the results include significantly the terrace width distribution effect. Although the

4. RESULTS AND DISCUSSION II

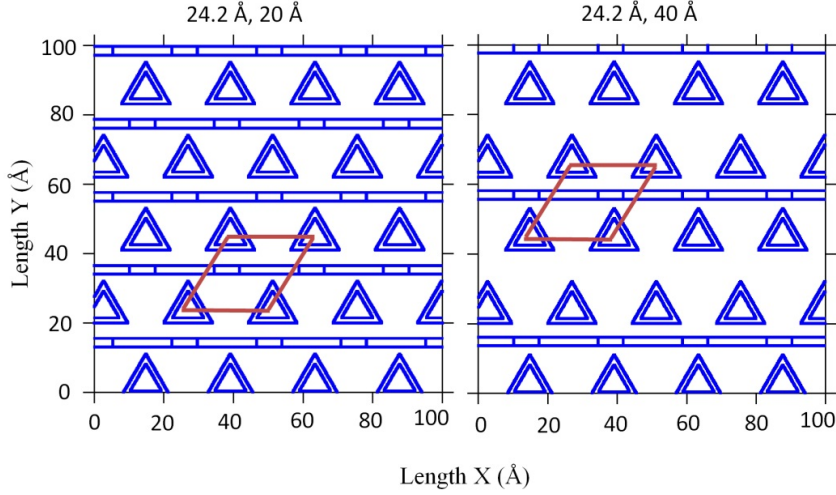


Figure 4.17: EBEM Input Geometries - The input geometry used by EBEM code to simulate the photoemission intensity and the surface state dispersion perpendicular to the step array, which are displayed in Fig. 4.16.

theoretical model nicely describes the possibility of the coexistence of both 1D and 2D periodicities, better quality of the data is indeed required, particularly, for FS scans that require rotation of the manipulator and, therefore, tinny change of the spot being sampled. For this purpose we believe that flat vicinal crystals with well defined miscut angles serve better in this specific case. Table 4.1 shows the step-step separation as a function of miscut angle for Cu(111) vicinals. The terrace width that fits perfectly integer number of triangles per terrace and the corresponding miscut angles are given. We notice that for small miscut angles a variation of 0.5° in the miscut angle results in a 20 \AA change in the terrace width, and therefore, uncertainty of at least better than 0.25° is required to be able to resolve some features in ARPES.

The tunability of the triangular dislocation network can be of interest in the context of SSNE. Therefore, we will proceed, in the following, to theoretical modeling of some of the cases given in table 4.1 and their comparison to the single dislocation and step superlattices.

Figure 4.18 shows the simulated CESs for the step superlattice (top) and the dislocation network superlattice (bottom) taken at different energies. The CESs are taken at energies below (left), inside (middle), and above (right) the step (top) or dislocation

Triangles per terrace	α (deg.)	d Å
1	6.0	20
2	3.0	40
3	2.0	60
4	1.5	80

Table 4.1: Step-Step Separation in a Curved Crystal - The step-step separation (d) as a function of the miscut angle (α) for the curved Cu(111) crystals. Only miscut angles for which an integer number of triangles can fit into the corresponding terraces are tabulated.

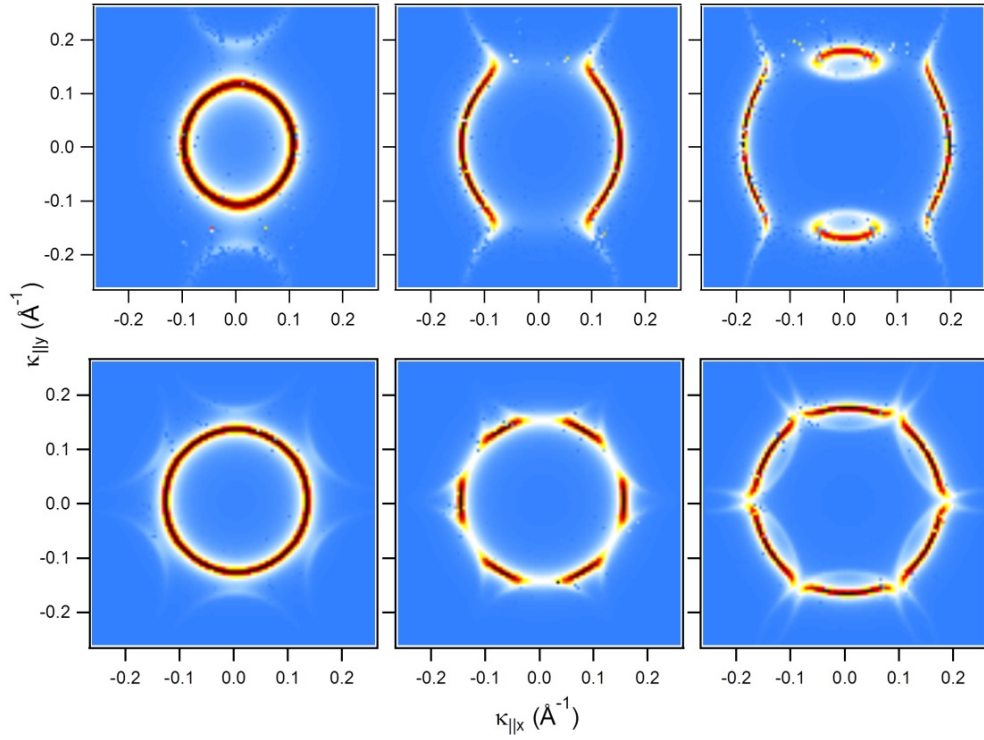


Figure 4.18: Theoretical CESs: 1 ML Ag/Cu(111) - Simulated CESs for vicinal Cu(111) crystal (top) and the 1 ML Ag on top of flat Cu(111) (bottom) with the same 24.2 Å periodicity. The CESs were taken at energies barely below (left), inside (middle) and above (right) the step and dislocation gaps.

4. RESULTS AND DISCUSSION II

(bottom) gaps. These CESs are in good agreement with the experimental ones shown in Fig. 4.6 for the step lattice and Fig. 3.31 for the dislocation lattice. The calculated dispersion parallel and perpendicular to the steps (a), as well as the CESs (b) based on the geometries shown in Fig. 4.17 (where step lattice are inserted with the same (left) and twice (right) the dislocation network periodicity), are shown in Fig. 4.19 and Fig. 4.20, respectively. The wavevectors $k_{||x}$ and $k_{||y}$ denote the momentum parallel and perpendicular to the step lattice, respectively. The energy is referred to the bottom of the surface state of Cu(111). The Fermi level is close to 300 meV. The calculated LDOS (c) at different energies are also included.

In Fig. 4.19, where the terraces enclose only one triangular row, one clearly sees that the effect of the step lattice is almost negligible, and the calculated CESs and LDOS^[53] resemble the situation of the pure triangular dislocation lattice. In Fig. 4.19, where the step lattice is twice the periodicity of the triangular one, both the CESs and LDOS are quite different from the pure step or triangular lattices. For CESs close to and at the energetic positions of the step gap, the situation resembles the pure step superlattice. The LDOS at these energies are also quite different, where the maximum intensity leaks in the region between the two triangular rows enclosed within terraces forming a wavy like pattern. Upon crossing the step gap, the LDOS were found to be the same as the normal triangular lattice up to the lower edge of the dislocation gap. After crossing this gap, the LDOS takes a complicate distribution, quite distinct from the previously mentioned situations. One also qualitatively sees that, both the step and dislocation superlattices manifest in the highly featured CESs. These CESs might, therefore, be tested as candidates for further sophistication of the SSNE approach.

In the current state of the experimental ARPES data, only good agreement is obtained for the dispersion perpendicular to steps. The simulated LDOS could, however, be used to further confirm the validity of the model, e.g. by direct comparison with STS measurements, where the terrace width distribution is irrelevant. In spite of the blurred effects of ARPES data one can, actually, identify the simultaneous signature of both the steps and dislocation on some experimentally measured CESs. Figure 4.21 shows experimental (top) CESs including the FS for the 1 ML Ag/Cu for miscut angle of 5.5° . The corresponding real space STM image for this vicinal surface is shown in Fig. 4.12, where a hexagonally distorted geometry was obtained.

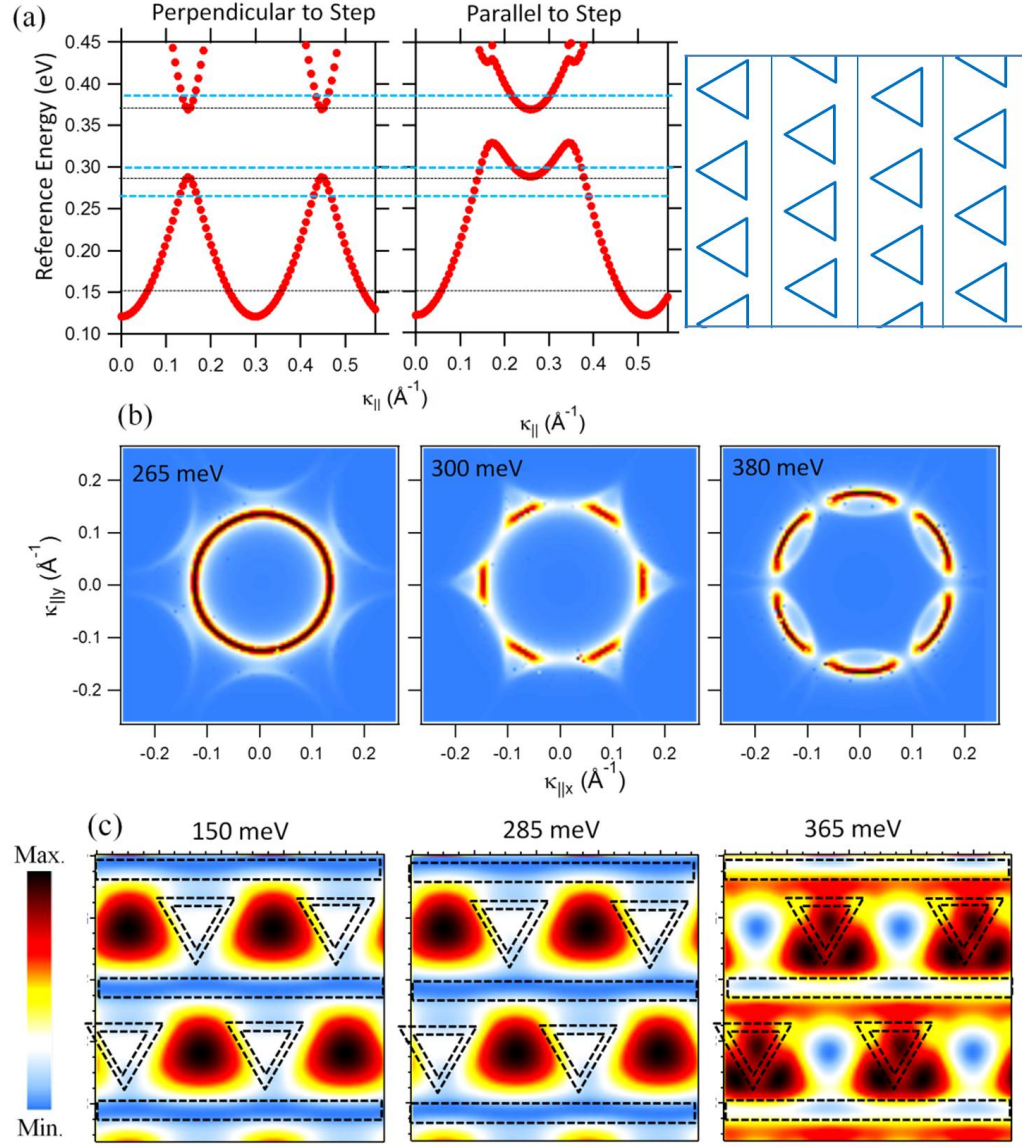


Figure 4.19: Theoretical CESs: 1 ML Ag/v-Cu(111): One Triangle/Terrace -
 (a) Calculated band structure perpendicular (left) and parallel (middle) to the step array using the geometry shown to the right (i.e. one triangle per terrace). (b) Simulated CESs at the energies marked by horizontal blue dotted lines in (a). (c) Simulated LDOS at the energies marked by horizontal black dotted lines in (a).

4. RESULTS AND DISCUSSION II

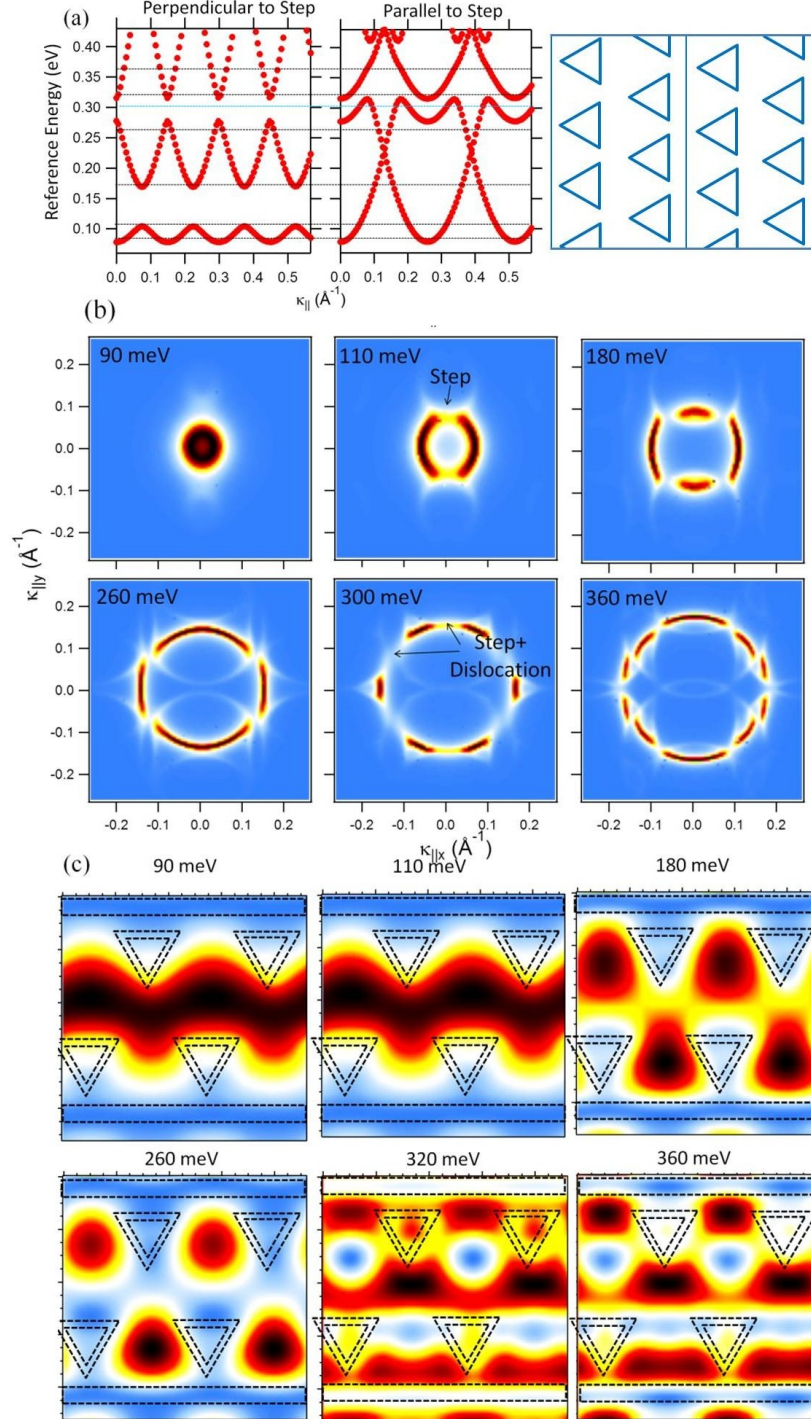


Figure 4.20: Theoretical CEs: 1 ML Ag/v-Cu(111): Two Triangle/Terrace - Same as Fig. 4.19 but for two triangles per terraces case. The CEs and LDOS are all taken at the energies marked by the dashed black lines. One CE is also added at the energy marked by the dashed blue line (inside the dislocation gap).

Including these distortions (68° , instead of 60° , between the unit cell vectors, with 24.2 \AA and 31 \AA lattice constants parallel and across the step axes, respectively) in the theoretical model, the resulting CESs are shown in Fig. 4.21 (bottom). Since the terrace width is slightly larger than the dislocation periodicity, the step gaps are first visible for the high binding energy CESs. At these energies, one can see the emission from the dislocation umklapps confirming, therefore, the coexistence of both 1D and 2D hexagonal lattice. For lower binding energies CESs including the FS, the emission from the second BZ barely intersects with the main first BZ emission and the FS appears hexagonally shaped. To further confirm the reliability of the theoretical model, we show the experimental FS for the 1 ML Ag/Cu taken at 6° miscut angle, Fig. 4.22. For this miscut we expect the geometry shown in Fig. 4.17 (left), and hence a hexagonally shaped FS similar to the 1 ML Ag on top of flat Cu(111). Fig. 4.22 clearly supports this expectation.

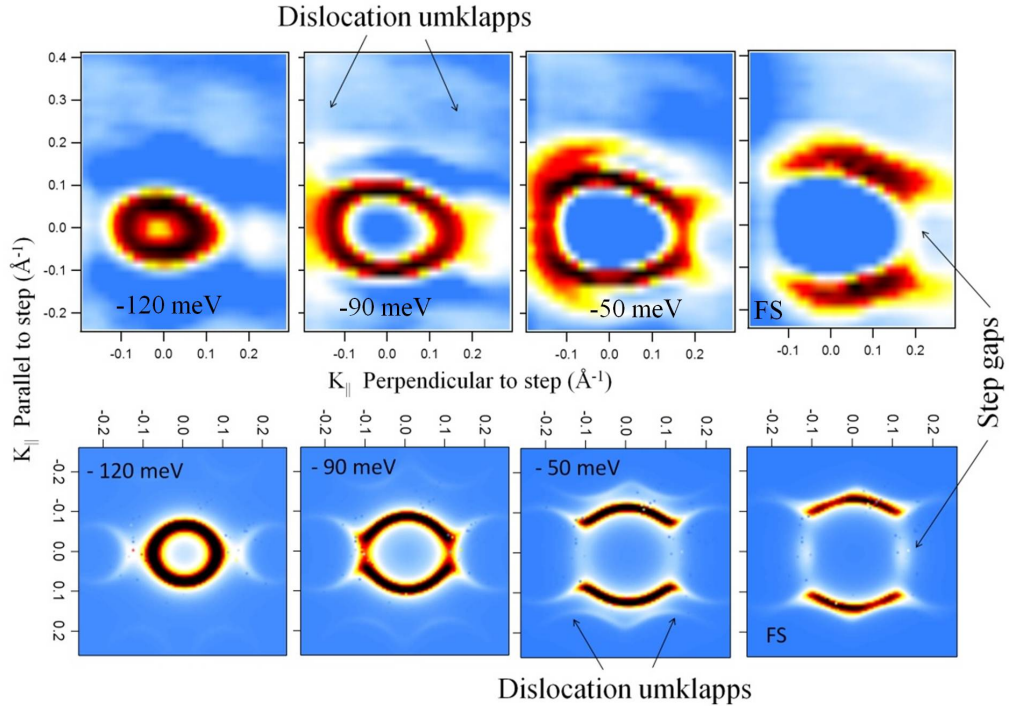


Figure 4.21: Experimental CESs: Miscut Angle = 5.5° - Experimental (top) and simulated CESs for 1 ML Ag on top of vicinal Cu(111) at 5.5° miscut angle. The input geometry shown in Fig. 4.17 was used including some distortion. The length of the unit cell vectors were 24.2 \AA and 31 \AA making an angle of 68° in between. $h\nu=21.2 \text{ eV}$.

4. RESULTS AND DISCUSSION II

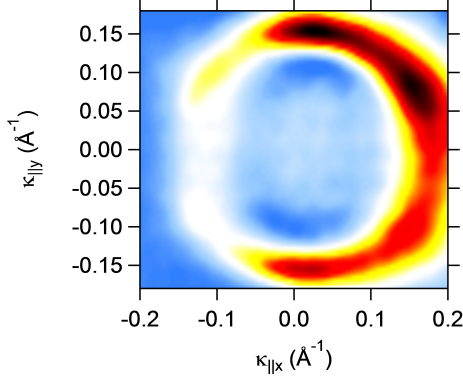


Figure 4.22: Experimental FS: Miscut Angle = 6° . Experimental FS for the 1 ML Ag/v-Cu(111) for a miscut angle of 6° , where the periodicity of the step and dislocation superlattices coincides. The faint emission enclosed within the hexagonal FS can be ascribed to the presence of terrace width distribution. $h\nu = 21.2$ eV.

We have mentioned that, for better quality of the data a flat vicinal sample with precise miscut angles are required. The drawback of this approach is the extreme precision required for large miscut angles, as discussed in table 4.1. Actually, the qualitative agreement between theory and experimental ARPES data clearly seen in the surface state dispersion as well as the CESs, just discussed, motivates the curved crystal approach. Quantitative data analysis, e.g. band structure fitting, is not possible. A better alternative to the single flat vicinals is the fabrication of a curved crystal with bigger radius of curvature. A curved crystal with $12 \text{ mm} \times 12 \text{ mm}$, hence double the size of the one used throughout this work but with the double radius of curvature is already fabricated by A. Magaña, a Ph.D student in our group. We believe that such crystal will allow minimizing the averaging of the nearby miscut angles in ARPES measurements, especially when angular scans are concerned.

4.4 Conclusions:

We have shown that the curved crystal approach can substitute the flat vicinal surfaces and allow for systematic analysis of the physical and electronic surface structure. In particular, the magnitude of the step potential for the three noble metals was determined. The Ag steps were found highly transparent. Similar step potential, of $0.6 \text{ eV} \cdot \text{\AA}$, was deduced for both v-Ag(111) and the 1 ML Ag/v-Cu(111) system, with significant quenching of the inelastic scattering in the latter. We also showed that, both the step superlattice and the dislocation network coexist in the 1 ML Ag/v-Cu(111) system. The umklapps bands, step gaps, and dislocation gaps were clearly seen in the photoemission intensity from the surface state dispersion perpendicular to the steps,

and with poorer quality in the CESs. Using EBEM code we have calculated the band structure, CESs, and LDOSs and the results were found to be in qualitative agreement with the experimental data. For a more quantitative analysis a well defined bigger curved crystal, or flat vicinal surfaces, are required in order to minimize the terrace width distribution that arises due to the averaging over the miscut angles in question.

4. RESULTS AND DISCUSSION II

5

Results and Discussion III

5. RESULTS AND DISCUSSION III

Apparent Spin-Orbit Split of the 1 ML Ag/Cu/Ni(111) Surface State: Qualitative View

5.1 Introduction and Literature Survey:

In this section we further explore the 1 ML Ag/Cu(111) superlattice for a thin Cu film on Ni(111). Both Cu and Ni have the same FCC crystal structure with quite similar lattice parameters (3.524 Å and 3.615 Å for Ni and Cu, respectively)^[197]. Due to the large lattice mismatch (16 %) between Ag(111) and Ni(111), the 1 ML Ag deposition on Ni(111) does, therefore, show moiré pattern with $\sim (7 \times 7)$ periodicity similar to the 9×9 moiré seen on Cu(111)^[112,198,199]. Neither surface alloying nor dislocation network formation has been reported for this system^[200]. In the contrary, the Cu deposition on Ni(111) was shown to grow pseudomorphically, such that thick Cu films can be grown without alloy formation (for annealing temperatures $< 800\text{K}$)^[201]. Therefore, we expect similar surface electronic states for 1 ML Ag on top of thick enough Cu films grown on Ni(111). In spite of the structural similarities between Cu(111) and Ni(111), their surface electronic structure is, however, significantly different. The Ni(111) crystal supports a spin-polarized Shockley surface state, with the majority and minority states being below and above the Fermi level, respectively^[202]. Brief comments about the surface states on Ni(111) will appear in-line with the text.

Our goal is to investigate the surface electronic structure of the 1 ML Ag/Cu-buffer/Ni(111) with variable Cu buffer thicknesses; thus bringing the 1 ML Ag surface state closer to the magnetic Ni(111) substrate, even in direct contact (without Cu spacer). Except for the clean Ni(111), we are not aware of any previous surface electronic structure studies on these systems. However, noble metal overlayers on top of Ni(111) crystal have been widely used as substrates for graphene growth^[203–206] without prior characterization of the surface states on the substrates themselves. In this case,

5. RESULTS AND DISCUSSION III

noble metals are generally deposited after graphene and the system is subsequently heated to produce metal intercalation^[204]. Although Au and Cu are known to form surface alloys with Ni^[126,201] at the intercalation temperature, the intercalated layers are considered as pure single layers of the noble metal. Note that the Dirac cone of graphene is centered at the \bar{K} -point of the SBZ^[207], thus, far away of being affected by surface states commonly centered at $\bar{\Gamma}$ -point in noble metal surfaces^[100]. The intercalation of such noble metals and other atoms were found to significantly modify the energetic position of the Dirac point in graphene^[203], decoupling the graphene from the bare substrate (becoming free standing graphene), and opening gaps at the Dirac point by breaking the symmetry of the graphene atomic lattice^[208]. Moreover, sizable spin-orbit splitting was observed which raises the hope towards graphene based spintronics^[209,210]. Although the surface electronic structure of the graphene-support (i.e., the noble metals/Ni substrate) was not so far concerned, we believe that characterizing these substrates can be of fundamental and technological importance.

5.2 Sample Preparation and Experimental Tools:

The schematic representations of the samples are shown in Fig. 5.1. A Cu wedge (~ 1 ML to ~ 5 ML) has been grown on the Ni(111) single crystal leaving a free Ni stripe. The wedge was annealed to ~ 600 K in most of the cases, i.e., below the critical temperature for Cu-Ni alloying. For the latter, annealing beyond 800 K is needed. The 1 ML Ag was then deposited on top of the Cu wedge and the free Ni stripe, followed by annealing to 600 K, Fig. 5.1(b). LEED patterns, valence bands spectra, and surface states have been acquired at different points on the wedges. All the measurements presented here were carried out at the Nanophysics laboratory's ARPES chamber. In ARPES, two photon energies (21.2 eV (Helium I) and 10.2 eV (Hydrogen Lyman α)) were used, where both the bulk and surface features can be, respectively, highlighted. Since the Ni d -band emissions are rather strong close the surface states energy window (close to Fermi level), the low photon energy was used to increase the surface state-to-Ni- d -bands relative intensity. The d -bands itself were always measured with the He line (21.22 eV) to enhance bulk features.

For the purpose of this study, we have used the surface states and valence bands of Ni(111), the 1 ML Ag/Ni(111) without Cu buffer, thick (5 ML) Cu/Ni(111), and the

1 ML Ag/thick Cu/Ni(111) as references, to later follow the variation of the electronic surface states with the Cu film thicknesses. These references are, respectively, marked by (1), (2), (3), and (4) on Fig. 5.1.

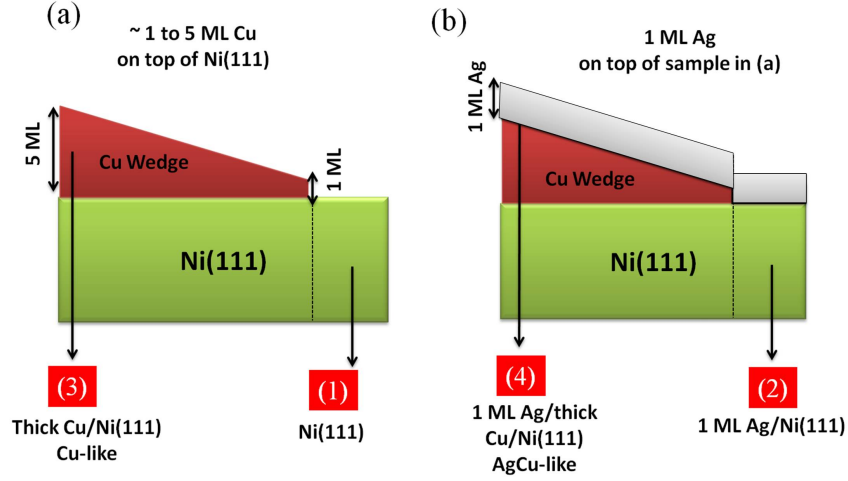


Figure 5.1: Schematic Diagram of Investigated Samples - Schematic drawing of the Cu wedge grown on top of the Ni(111) crystal (a) and after deposition of 1 ML Ag on top. Free Ni stripe, marked by (1) in (a) and 1 ML Ag/Ni stripe, marked by (2) in (b) are left at one side of the sample. The Cu wedge starts from ~ 1 ML up to ~ 5 ML. The points (3) and (4) mark the position of the 5 ML Cu/Ni and 1 ML Ag/5 ML Cu/Ni, respectively.

5.3 Results and Discussion:

5.3.1 Surface States on Ni(111):

Since the Ni(111) crystal has been long characterized in the literature, we start by a quick review of its surface electronic structure.

The calculated bulk band structure for majority and minority spin, taken from Ref. [211]^[211], are shown in Fig. 5.2(a). The solid (dotted) lines denote the majority (minority) spin polarized bands. The blue (red) lines mark bands with $\Lambda 1$ ($\Lambda 3$) symmetry. In the present study, we are only interested in identifying the surface related states that take place in the inverted gap at the L -point. In Fig. 5.2(b) the experimentally observed exchange split surface states marked by S1, S2, are shown, apart from the

5. RESULTS AND DISCUSSION III

recently observed S3 (not shown). The S1 states are *sp*-Shockley type surface states that occur in the bulk projected gap (L_2 - L_1 ; -0.9 eV to +6.0 eV) of Ni(111). The exchange splitting of S1 state was experimentally (at room temperature) estimated to be 100 meV^[211,212]. The dispersion parameters for the occupied spin-majority surface state of Ni(111) are $E - E_F = 0.04$ eV, $m_* = 0.18 m_e$, and $k_F = 0.044 \text{ \AA}^{-1}$. Due to the high reactivity of Ni, the surface state is strongly affected, and different values are reported in literature and, therefore, we will be referring in the rest of the chapter to our experimental values. The S2 state is classified as a Tamm surface state/resonance first reported by F. J. Himpsel et al^[213]. This surface state disperses downward in energy when increasing the parallel momentum in all directions and takes place in the inverted (L_2 - L_3) gap. Its surface nature was recognized due to its degradation after oxygen or hydrogen adsorption, together with the absence of dispersion with photon energy. The binding energy for this state was estimated to be ~ 0.25 eV.

In the present work, we will pay more attention to the occupied S1 and S2 states, which are displayed in Fig. 5.2(c). The green dashed parabolas mark the dispersion of the S1 and S2 surface states, where the inclined line marks the bulk *d*-band of Ni. Estimated binding energies, effective masses, and Fermi wavevectors for S1 and S2 are given in table 5.1 together with the values obtained in other works¹. The dispersion parameters for the S1 surface state are clearly different compared to the full agreement observed for the S2 state. That actually stems, apart from different surface quality and different measurement temperatures, from the complexity of the Ni band structure, where the L_2 - L_1 gap is traversed by the upper spin-split *d*-band ($L_{3\uparrow}$; -0.15 eV, $L_{3\downarrow}$; +0.16 eV) that obscures the S1 state (Fig. 5.1(a))^[213].

These upper spin-split *d*-bands can barely be seen as unquenched emission in the vicinity of the S1 state, and in between the S1 and S2 states. The ARPES data shown in Fig. 5.2(c) were recorded with a photon energy of 21.2 eV. The relative intensity of both bulk and surface emission changes when the photon energy of 10.2 eV is used, but the surface state energies do not change.

¹The tabulated values are all collected from spin-integrated measurements except for Ref. [212]^[212] where a spin-resolved experiment was done. The Ni(111) crystal used here was the same one used in Ref. [126]^[126] but measured at the SRC with lower temperature (150 K). Clearly, for the same sample but different measuring temperature, cleaning procedure, photon energy, and vacuum conditions the dispersion parameters are significantly different.

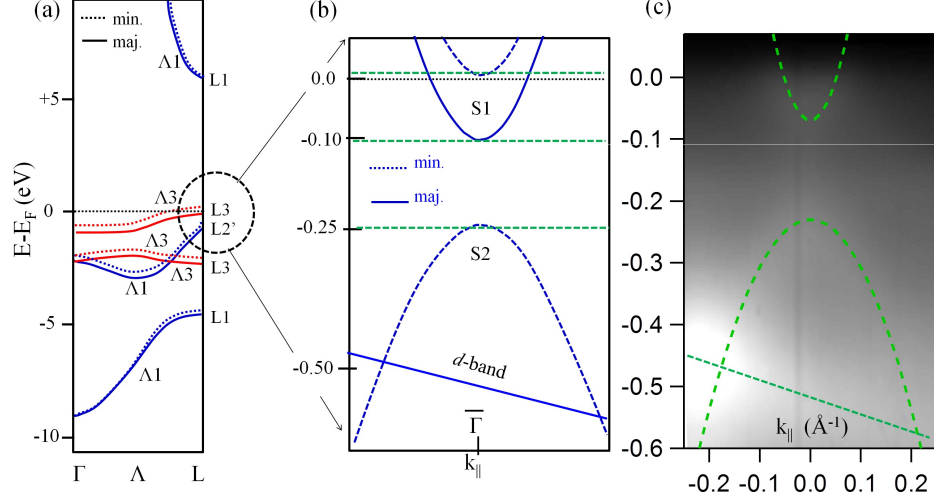


Figure 5.2: Bulk Band Structure and Surface States on Nickel - (a) Spin-resolved bulk band structure of the Ni crystal along the ΓL direction. The blue (red) lines mark the $\Lambda 1$ ($\Lambda 3$) bands, whereas the solid (dotted) lines mark the majority and minority spin bulk bands. Adapted from Ref. [211]^[211]. (b) Schematic representation of the experimentally reported surface states on Ni(111) for majority and minority spin. (c) Photoemission intensity plot along $\bar{\Gamma M}$ direction of Ni(111) surface. The green dashed parabolas mark the S1 and S2 surface states, whereas the inclined line marks the bulk emission from the Ni d -band close to -0.5 eV. ARPES data in this case was taken with photon energy of 21.22 eV and at 180 K.

T (K)	S1			S2	
	$E - E_F$ (eV)	$m_*(m_e)$	k_F (\AA^{-1})	$E - E_F$ (eV)	$m_*(m_e)$
Unknown ^[213]				-0.25	
RT ^[202]	0.02 ± 0.01			-0.25 ± 0.03	
140 ^[214]	-0.11 ± 0.01	0.14 ± 0.05	0.06	-0.23 ± 0.02	-0.35
Unknown ^[211]	0.0				
Unknown ^[211,212]	$0.0(0.1)$				
RT ^[215]	-0.03 ± 0.02	0.17	0.03	-0.23	-0.31
150 ^[216]	-0.082	0.23	0.069	-0.25	-0.35
180[Present]	-0.04	0.18	0.044	-0.25	-0.35

Table 5.1: Dispersion parameters of Ni(111) Surface States - Dispersion parameters of the S1 and S2 surface states along $\bar{\Gamma M}$ direction as reported in the literature and the present work.

5. RESULTS AND DISCUSSION III

5.3.2 Surface States on 1 ML Ag/Ni(111):

Figure 5.3 shows the LEED patterns across the Ag wedge (0.6 ML to 1.2 ML) on top of Ni(111) after annealing to 600 K. The wedge was prepared in a separate experiment in order to define the 1 ML Ag coverage (point (2) in Fig. 5.1). The moiré superlattice (blue) was estimated to be $(7\pm0.2 \times 7\pm0.2)$ of the Ni (red) substrate. This finding is in agreement with previous studies where a layer-by-layer growth and similar moiré superstructure were reported^[112,198,199]. The central spot of the moiré superstructure gains intensity across the wedge at the expenses of the Ni spots, allowing for a first rough estimation of the 1 ML Ag coverage. A quick ARPES scan across the wedge (not shown), and close to the 1 ML Ag coverage estimated from LEED, allows better identification of the 1 ML Ag coverage, where the sharpest emission is obtained, without detectable contribution from other coverage higher or less than 1 ML.

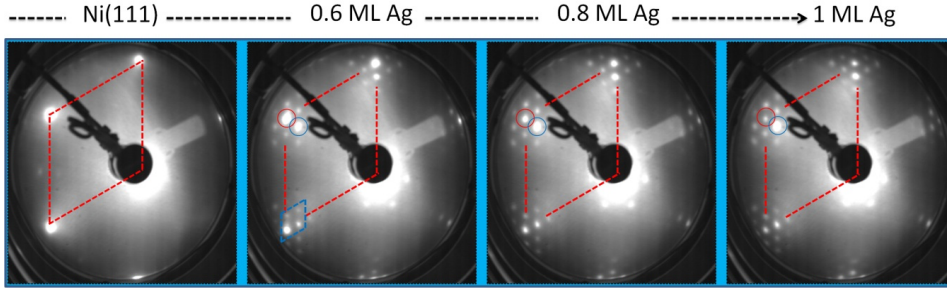


Figure 5.3: LEED Patterns: Ag/Ni(111) - LEED patterns across the Ag wedge on top of Ni(111). The red dashed lines mark the reciprocal space vectors of Ni(111), whereas the blue dashed lines encloses the main Ag/Ni moiré spots.

The ARPES measurements on the 1 ML Ag/Ni(111) are summarized in Fig. 5.4. In (a) we show different constant energy surfaces (CESs) taken at the energies marked by dashed yellow lines in (b). The faint circular intensity in the CES at -0.35 eV belongs to the dispersion of the S2 Tamm-like surface state which, compared to Ni, is shifted toward lower binding energy (now at ~ -173 meV). The accuracy of determining the binding energies at band minima is limited by the bright strong emission at the bottom and top of the S1 and S2, respectively. The CES at -0.09 eV is taken close to the S1 Shockley surface state band minimum (0.066 eV), which is shifted towards higher binding energy compared to Ni. The estimated Fermi wavevector and effective mass

were found to be $k_F = 0.053 \text{ \AA}^{-1}$ and $m_* = 0.16 m_e$, respectively, and are therefore similar to clean Ni(111).

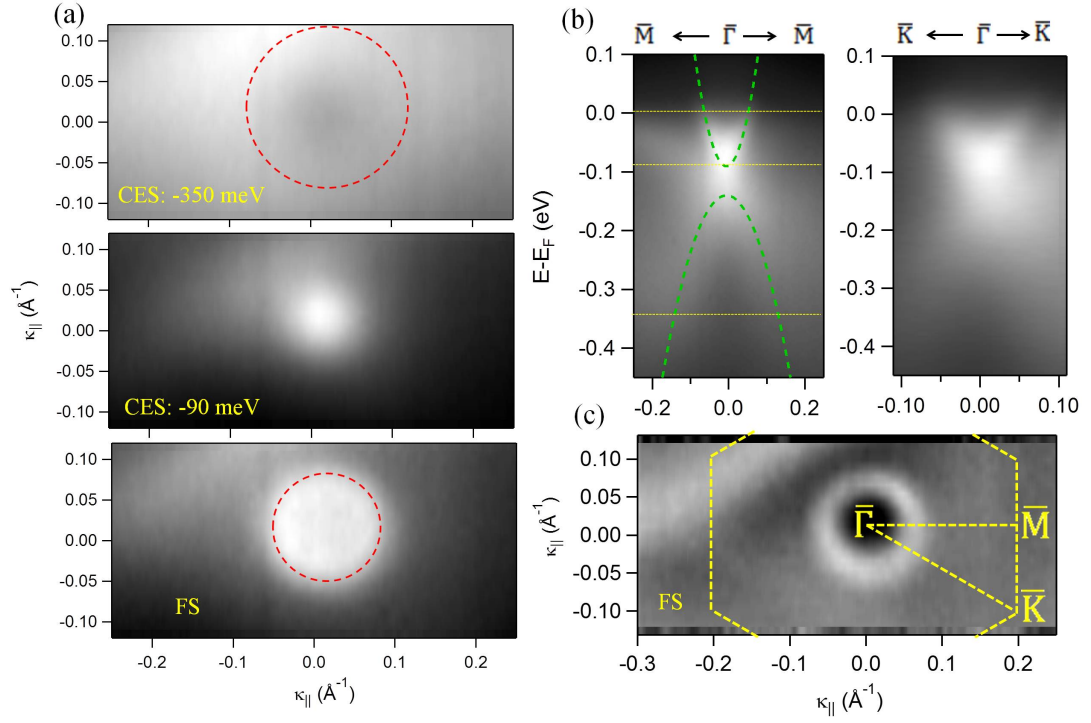


Figure 5.4: ARPES Data: 1 ML Ag/Ni(111) - (a) CESs taken at different binding energies marked by the horizontal lines in (b). The red circles marks the CESs of S2 (top) and S1 (bottom) surface states. (b) Surface states dispersion along $\bar{\Gamma}\bar{M}$ (left) and $\bar{\Gamma}\bar{K}$ (right) direction. The green dashed parabola shows the dispersion of the S1 and S2 states. (c) Second derivative plot of the FS. The yellow dashed lines define the hexagonal 7×7 superstructure surface Brillouin zone (SBZ).

Actually, this downward shift is at first glance surprising, since the Ag(111) surface state position is $\sim 60 \text{ meV}$. Nevertheless, this finding supports our conclusion from the Au/Cu system reported in chapter three, i.e., the presence of a moiré pattern induces a downward shift of surface states. Figure 5.5 displays the Ni and the 1 ML Ag/Ni EDCs taken at the band minimum. These were fitted by two Lorentzian peaks for the surface states (1 ML Ag/Ni) and one more Lorentzian peak for the d -band (Ni), where the difference in the S1 and S2 surface states band minima is clearly seen.

The FS shown in Fig. 5.4(a), and its second derivative in Fig. 5.4(c), exhibits a circular free-electron-like character, and hence the dispersion is isotropic along both the

5. RESULTS AND DISCUSSION III

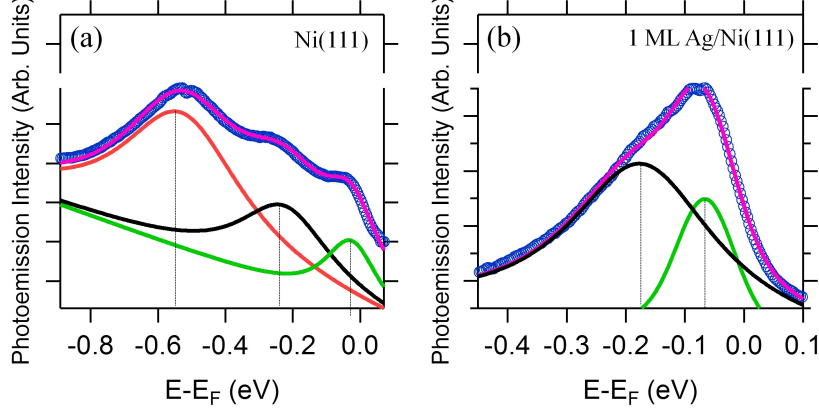


Figure 5.5: EDC Spectra: Ni(111) vs. 1 ML Ag/Ni(111) - EDC spectra for Ni(111) (a) and 1 ML Ag/Ni(111) taken at the band minima. The green, black, and red denote, respectively, the S1, S2 surface states, and the d -bands, after fitting the corresponding EDC (blue circles).

$\overline{\Gamma M}$ and $\overline{\Gamma K}$ directions shown in Fig. 5.4(b). The “*slope-like*” feature close to the Fermi level at negative and positive momentum along $\overline{\Gamma M}$ and $\overline{\Gamma K}$, respectively, belongs to the Ni bulk bands. These are also seen as linear intensities around the circular FS. The FS is completely enclosed within the surface Brillouin zone (SBZ), marked by dashed yellow lines, of the moiré superlattice (assuming 7×7 superstructure) and is not nested over the entire momentum space, in contrast to the 1 ML Au/Ni(111) system^[126].

In conclusion, the 1 ML Ag/Ni(111) surface states are similar to the Ni(111) with slightly different dispersion parameters. We have not detected any signature of the unoccupied minority S1 state, most probably due to the significant reduction of the exchange interaction upon 1 ML Ag deposition, or rather unlikely the splitting is large enough to push the minority S1 state far above the Fermi level. .

To further confirm the dispersion of the Tamm-like surface state we display, in Fig. 5.6, the MDC cascade (a) that correspond to the photoemission intensity plot in (b) for the 1 ML Ag/Ni(111) taken slightly off-normal emission ($k_{||y} = 0.015 \text{ \AA}^{-1}$). The Tamm-like state is better seen in these plots, and its circular shape is also seen in the CESs displayed in (c).

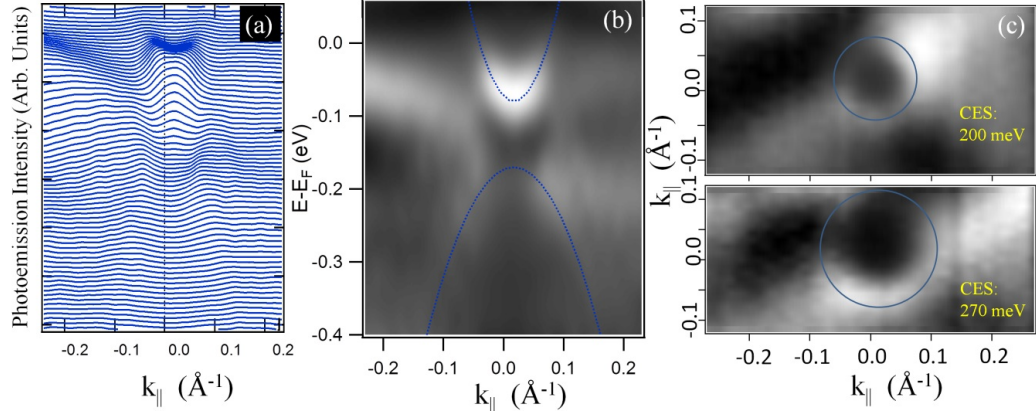


Figure 5.6: ARPES Data: 1 ML Ag/Ni(111) - MDC cascade of the 1 ML Ag/Ni(111) (a) for the photoemission intensity plot in (b). In (c) two CESs are shown. The blue lines mark the dispersion of the S1 and S2 states, and the blue circles mark the circular shape of the S2 state. Photoemission data are displayed as second derivative plots.

5.3.3 Surface States on 1 ML Ag/5 ML Cu/Ni(111):

Figure 5.7 shows the surface state dispersion along the $\overline{\Gamma M}$ direction for (a) 5 ML Cu/Ni(111) and (b) after 1 ML Ag deposition on top. The systems were annealed to 600 K, i.e., below the surface alloy formation temperature reported in the literature. The surface state in Fig. 5.7(a) clearly resembles the Cu(111) surface state, with slightly lower binding energy ($\Delta E = \sim 30$ meV), further supporting a complete wetting without noticeable alloy formation. Also the surface state of the 1 ML Ag grown on top is characterized by a 1-ML-Ag/Cu(111)-like surface state with ~ 15 meV lower binding energy. The LEED pattern (not shown) taken on the 1 ML Ag case shows a clear Moiré superstructure with $(8.5 \pm 0.2 \times 8.5 \pm 0.2)$ periodicity. The back folding due to such Moiré (or dislocation network) is, however, hardly visible in the present case. Actually, for such high Cu coverage the oblique feature close to the Fermi level is still visible, as can be seen in the saturated intensity plot in Fig. 5.7(c). The left half in (c) is the Cu/Ni surface state. On the right half (1 ML Ag/Cu/Ni) one can hardly see some umklapp intensity shadowed by the oblique band. These findings suggest that the dislocation network is still present in 1 ML Ag on thin Cu films.

We must, however, note that the annealing temperature is of crucial importance to reproduce the features seen in Fig. 5.7. In fact, increasing the annealing temperature to ≥ 800 K results in significant modification of these surface states. Figure 5.8 shows

5. RESULTS AND DISCUSSION III

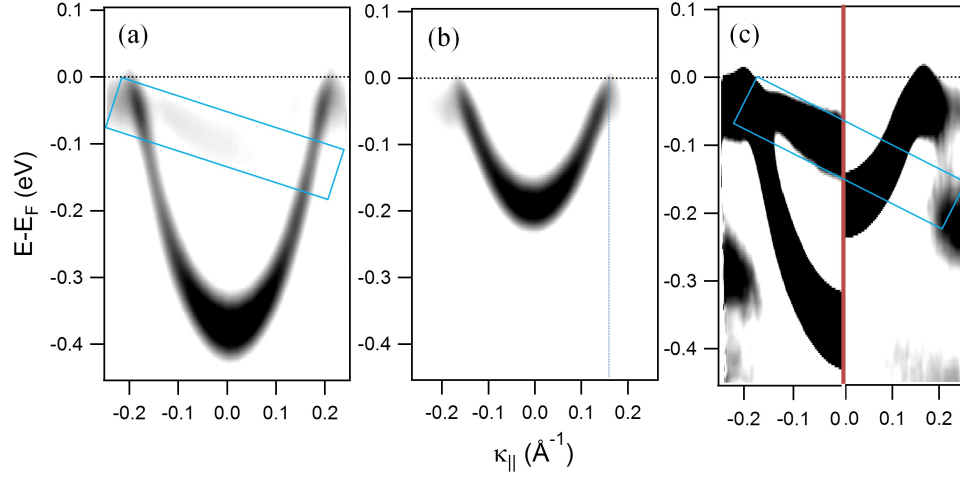


Figure 5.7: ARPES Data: 5 ML Cu/Ni vs. 1 ML Ag/ 5 ML Cu/Ni: Annealed to 600 K - Shockley surface state dispersion along $\bar{\Gamma}\bar{M}$ direction for (a) 5 ML Cu/Ni(111) and (b) 1 ML Ag on top. In (c) we compare (a) and (b), on the left and right halves, respectively. The photoemission intensities were saturated in (c) to highlight the Ni bulk emission enclosed by the blue rectangle. The data are displayed as second derivative images.

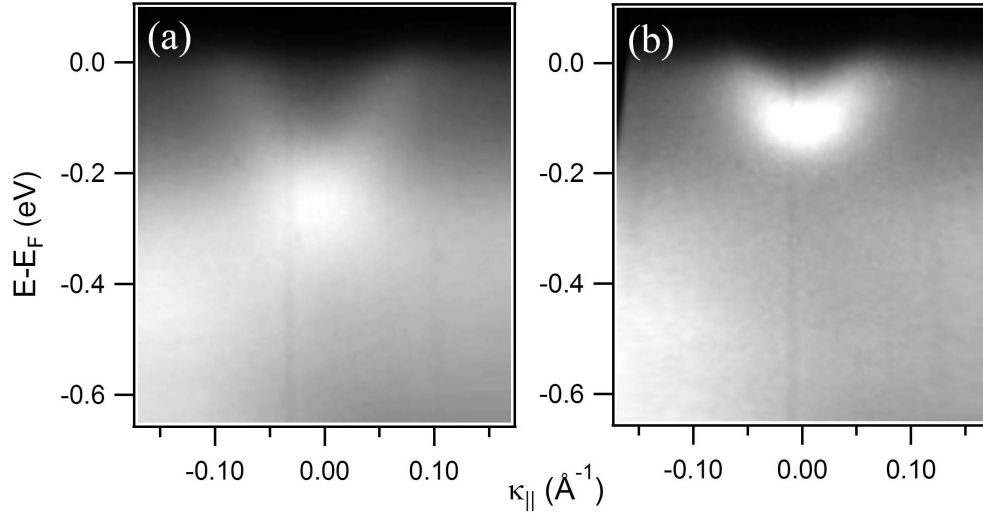


Figure 5.8: ARPES Data: 5 ML Cu/Ni vs. 1 ML Ag/ 5 ML Cu/Ni: Annealed to 800 K - Same as Fig. 5.7(a-b), but after annealing to 800 K, where surface alloy formation takes place. The second derivative is not performed in this case.

the dispersion of these states along $\overline{\Gamma M}$ direction after annealing to 800 K. The 5 ML Cu/Ni(111) evolves toward a Ni-like surface state with, however, higher binding energy (0.2 eV). The 1 ML Ag sample also becomes similar to the 1 ML Ag/Ni(111), with slightly higher binding energy; see Fig. 5.4(b). These findings strongly suggest an alloy formation due to either Cu or Ag atom segregation into the Ni matrix.

The analysis of the valence band of the two samples, shown in Fig. 5.9, can clarify whether alloying takes place between Ag and Cu or with both of them with Ni. We notice that the *d*-bands of Ag (silver shaded region) do not undergo any changes in both the shape and the binding energy, indicating that no Ag atoms are re-evaporated neither alloyed with Cu/Ni substrate. The Cu *d*-bands (red shaded region), on the other hand, shift toward lower binding energy and, significantly, lose intensity when annealed to 800 K. In contrast Ni *d*-bands grow (light green shaded region, close to the Fermi level), further confirming a significant alloy formation between Cu and Ni. The CuNi alloy surface states rapidly age, similar to Ni, in contrast to the unalloyed Cu/Ni surface state, indicating a higher amount of reactive Ni atoms on the surface.

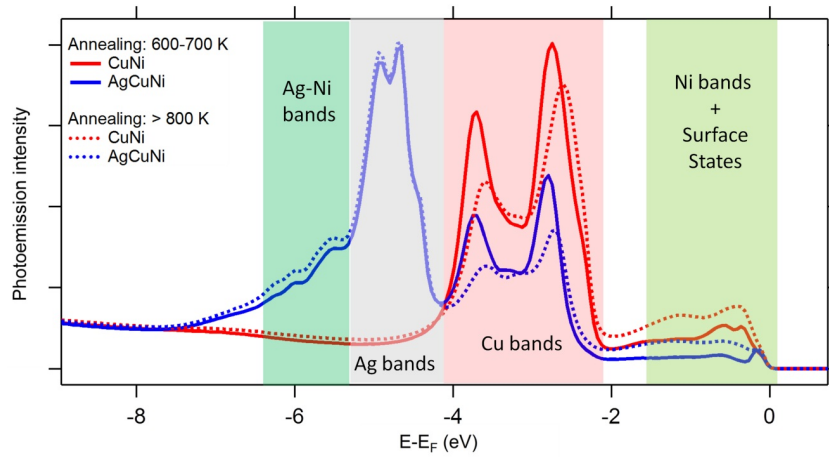


Figure 5.9: Valence Band Spectra: 5 ML Cu/Ni vs. 1 ML Ag/ 5 ML Cu/Ni - Angle-integrated valence band spectra for the Cu/Ni (red) and Ag/Cu/Ni (blue) after annealing to 600 K-700 K (solid) and to 800 K (dotted).

The small peaks close to ~ 6 eV (dark green shaded region) gain intensity after annealing to the alloying temperature. They are only seen on the Ag covered samples and gain more intensity after alloy formation. To understand the nature of these

5. RESULTS AND DISCUSSION III

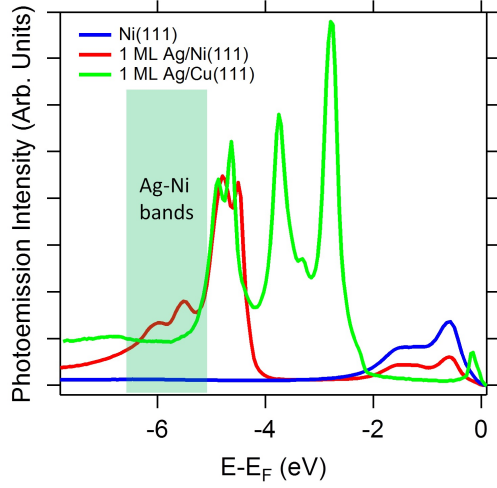


Figure 5.10: Valence Band Spectra: Ni, Ag/Ni, and Ag/Cu/Ni. Angle-integrated valence band spectra for clean Ni(111) crystal (blue), the 1 ML Ag/Ni(111) (red), and the 1 ML Ag/Cu(111) (green). The green shaded energy window highlights the Ag bands on Ni.

bands, we compare the valence band spectra just analyzed with the one shown in Fig. 5.10. Clearly, no such bands are observed for the clean Ni(111) (blue) nor for the 1 ML Ag/Cu(111) (green). For 1 ML Ag/Ni(111), however, these bands are present with better defined profile shape. All in all, these bands are only seen in the presence of both Ag and Ni and they lose intensity with increasing the Cu spacer thickness. The appearance of these bands in the case of Ag/Ni using the same photon energy, however, indicates partial contribution from 2 ML islands of Ag on top of Ni(111)^[217,218]. Comparing the profile shape to a recent work on Ag thin films on Ni(111), the contribution from the 2 ML Ag is very tinny^[219] (< 0.3 ML in Ag/Ni and much smaller in the presence of Cu spacer). This is also supported by the surface states shown in Fig. 5.4 and Fig. 5.7, where only single emission is seen.

5.3.4 Surface States on 1 ML Ag/1-3 ML Cu/Ni(111):

In the following we will restrict the discussion to Ag, Cu, and Ni(111) combinations annealed to ~ 600 K, assuming a sharp interface without alloy formation. Figure 5.11(a) shows the dispersion along $\overline{\Gamma M}$ and $\overline{\Gamma K}$ directions (left) and their second derivatives (right) for the 1 ML Cu/Ni(111) annealed to 600 K. Apart from the strong d -band emission (blue dashed line), surface states are marked by dashed yellow, red, and green lines. The surface states marked by yellow are actually due to residual Ag coverage, as deduced from the d -band spectra in Fig. 5.12. These surface states will be discussed later.

The hole-like dispersing surface state (dashed green lines) looks similar to the Ni Tamm state (S2) with, however, much higher binding energy (~ 0.420 eV). A CES at this energy is displayed in (b) showing its isotropic dispersion. The apparent doublet (marked by red) is assigned to Shockley surface states (S1) of 1 ML Cu/Ni. The doublets are better seen in the CES taken at +10 meV, shown in (b). The overlap between these states, the Tamm state, and the d -bands of Ni makes it difficult extracting the correct position of the band minima. Apparently, the band minimum of the Shockley states looks similar to the -0.4 eV obtained for Cu(111).

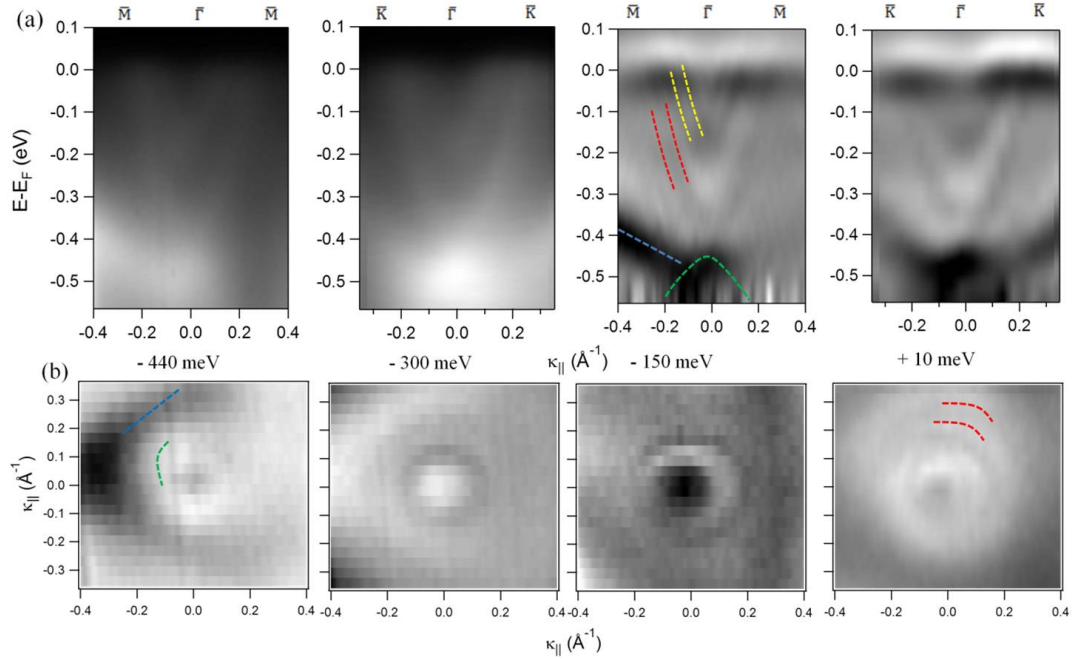


Figure 5.11: ARPES Data: 1 ML Cu/Ni - (a) Shockley surface state dispersion for 1 ML Cu/Ni(111) along $\overline{\Gamma M}$ and $\overline{\Gamma K}$ directions (the two images to the left) and their second derivatives (right). (b) CESs taken at different binding energies. The red (green) lines in (a) and (b) mark the Cu/Ni surface states and CESs, respectively. The yellow dashed lines in (a) mark the surface state in Ag/Cu/Ni due to partial Ag coverage. The bulk emission due to Ni bands is highlighted in (a) and (b) by the blue dashed lines.

The states marked by yellow dashed lines are identified by measuring the ARPES spectra for the 1 ML Ag/1ML Cu/Ni(111) spot on the sample (Figs. 5.12 and 5.13). Figure 5.13(a) shows the dispersion along $\overline{\Gamma M}$ direction and its second derivative. The surface state is clearly composed of two branches. The estimated binding energy at the band minima is 0.155 eV. The separation between the Fermi wavevectors of the two

5. RESULTS AND DISCUSSION III

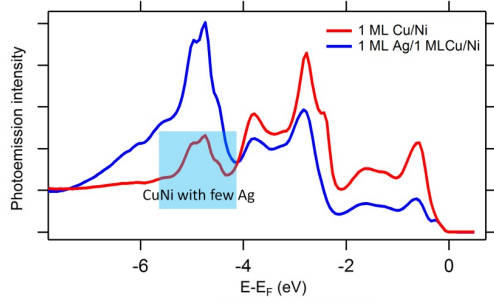


Figure 5.12: Valence Band Spectra: Cu/Ni vs. Ag/Cu/Ni. Angle-integrated valence band spectra for 1 ML Cu/Ni (red), and the 1 ML Ag/ 1 ML Cu/Ni (blue). The blue shaded energy window indicates the presence of some Ag atoms on the, nominally clean 1 ML Cu/Ni system.

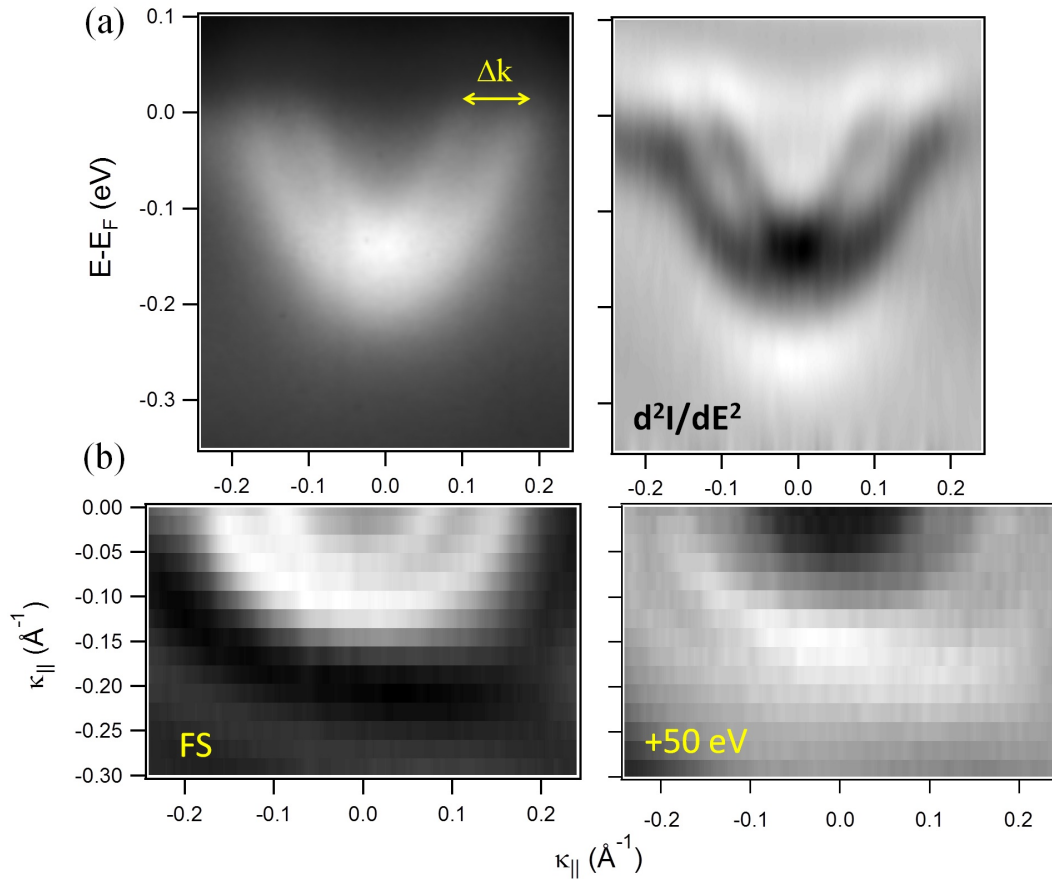


Figure 5.13: ARPES Data: 1 ML Ag/ 1 ML Cu/Ni - (a) Shockley surface state dispersion of the 1 ML Ag/ 1 ML Cu/Ni(111) system along $\overline{\Gamma M}$ direction (left) and its second derivatives (right). (b) CESs taken at the Fermi level (FS) and +0.05 eV.

branches is $\Delta k_F = 0.06 \text{ \AA}^{-1}$. We note, however, that the estimated value of the binding energy is, again, largely uncertain due to the strong intensity close to the crossing or the common minima of these doublets. The FS, in (b), is composed of two concentric contours. The contours are, apparently, hexagonally shaped, (this is better seen in the CES at +50 meV). A straightforward explanation of the origin of these states is missing; however, we will discuss possible candidates by the end of this chapter.

Figure 5.14 shows the dispersion along $\overline{\Gamma M}$ (a) and $\overline{\Gamma K}$ (b) directions for the 3 ML Cu/Ni(111) annealed to 600 K. The surface states dispersions look analogous as for 1 ML Cu/Ni, Fig. 5.11, apart from stronger quenching of the Ni d -bands. The corresponding CESs are shown in Fig. 5.15. The CES at -480 meV belongs to the Tamm surface state, whereas the -365 meV is a CES close to the band minima of the main Shockley surface state. For other CESs, including the FS, the dispersion of the Ni d -bands which appear as linear intensity around the contours, significantly enhance the intensity at the crossing points, making it difficult to draw appropriate conclusions about its real topology.

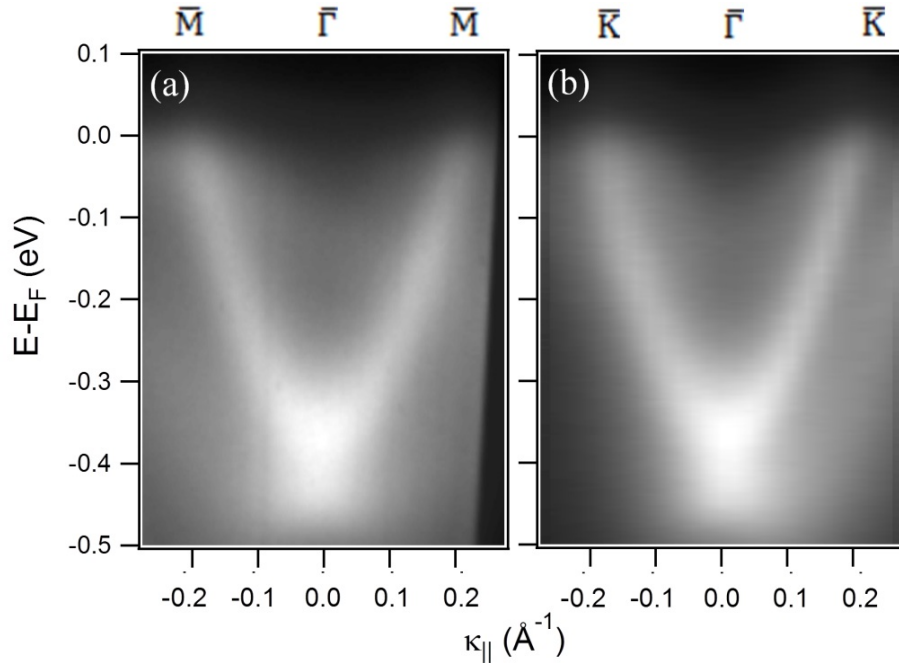


Figure 5.14: Dispersion Plots: 3 ML Cu/Ni - Shockley surface state dispersion of the 3 ML Cu/Ni(111) system along $\overline{\Gamma M}$ and $\overline{\Gamma K}$ directions.

5. RESULTS AND DISCUSSION III

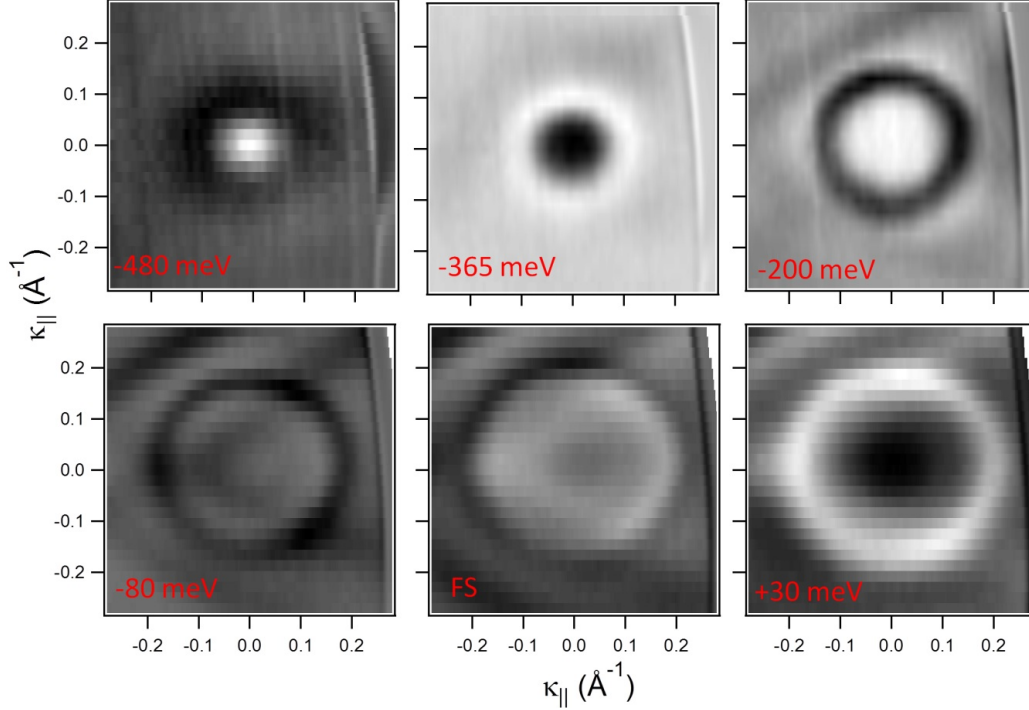


Figure 5.15: CES Plots: 3 ML Cu/Ni - CESs taken at different energies for the 3 ML Cu/Ni(111) system.

Figures 5.16 and 5.17 display the band dispersion/constant energy surface results for the 1 ML Ag/ 3 ML Cu/Ni(111) system. The dispersion along $\overline{\Gamma M}$ and $\overline{\Gamma K}$ directions (a) and their second derivatives (b) for the 1 ML Ag/ 3 ML Cu/Ni(111) annealed to 600 K feature again two branched surface states, with a binding energy close to 0.165 eV, i.e., 10 meV downward shifted from the 1 ML Ag/1 ML Cu/Ni pair of bands, Fig. 5.16. The difference in the Fermi wavevector between the two branches is also reduced ($\Delta k_F = 0.03 \text{ \AA}^{-1}$) with respect to the 1 ML Ag/1 ML Cu/Ni case. The CESs are shown in Fig. 5.17. Due to the smaller radius of the Fermi contours in the present case, the far lying emission from the Ni *d*-bands does not significantly alter the intensity distribution at the FS boundaries, allowing us to, barely, observe a slight hexagonal shape of the two concentric Fermi contours.

In summary, for the 1 ML Ag/Cu /Ni(111) system, the surface state is Ag/Cu like, and the presence of the Ni substrate does not significantly influence the dispersion parameters. For thin Cu buffers (1-3 ML) the surface states in both Cu/Ni and Ag/Cu/Ni

systems can be described by two crossed parabolas.

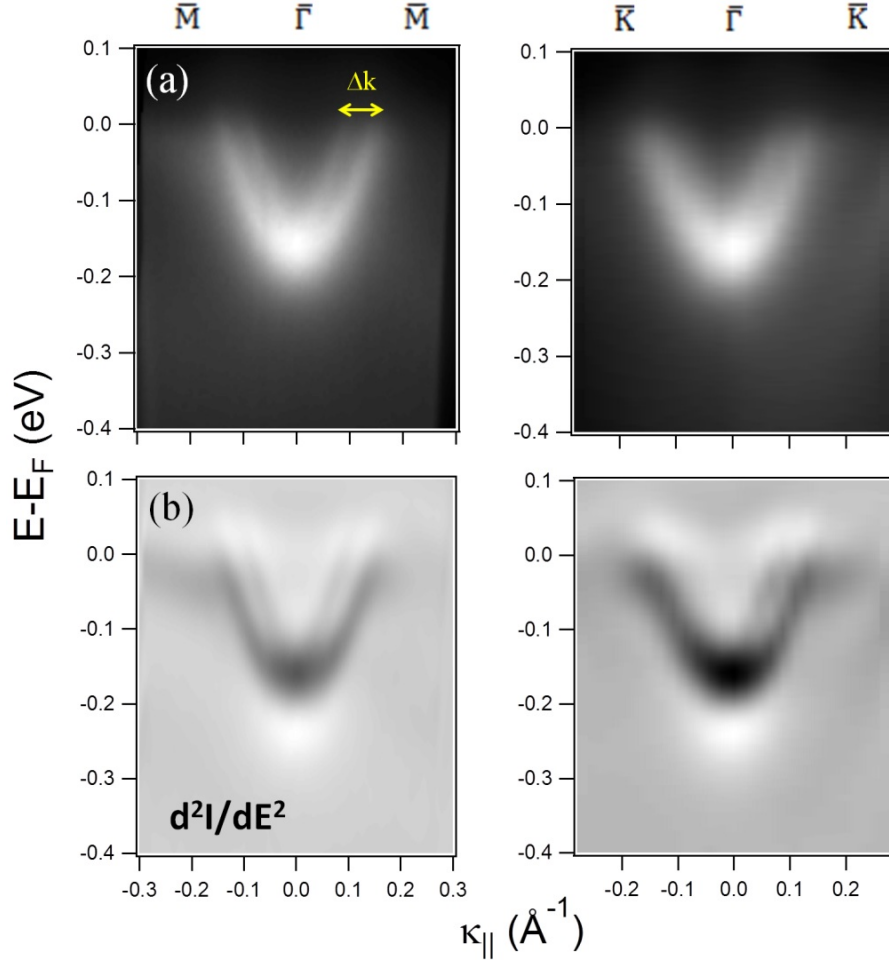


Figure 5.16: Dispersion Plots: 1 ML Ag/ 3 ML Cu/Ni - (a) Shockley surface state dispersion of the 1 ML Ag/ 3 ML Cu/Ni(111) system along $\bar{\Gamma}\bar{M}$ (left) and $\bar{\Gamma}\bar{K}$ (right) directions (left) and its second derivatives (right), and their second derivatives shown in (b).

We exclude that these states are induced by the magnetic character of the substrate, i.e., we discard magnetic exchange splitting, since an even stronger splitting would be seen in the case of the Ag/Ni monolayer system. The 1 ML Ag/Ni(111) exhibits a Ni-like surface state without any, likely, signatures of magnetism, as expected from the observed reduction of the Ni magnetic moment when covered by single layer of Ag, Cu^[220], and Ag/Cu. The lack of magnetic exchange splitting for the 1 ML Ag/Cu

5. RESULTS AND DISCUSSION III

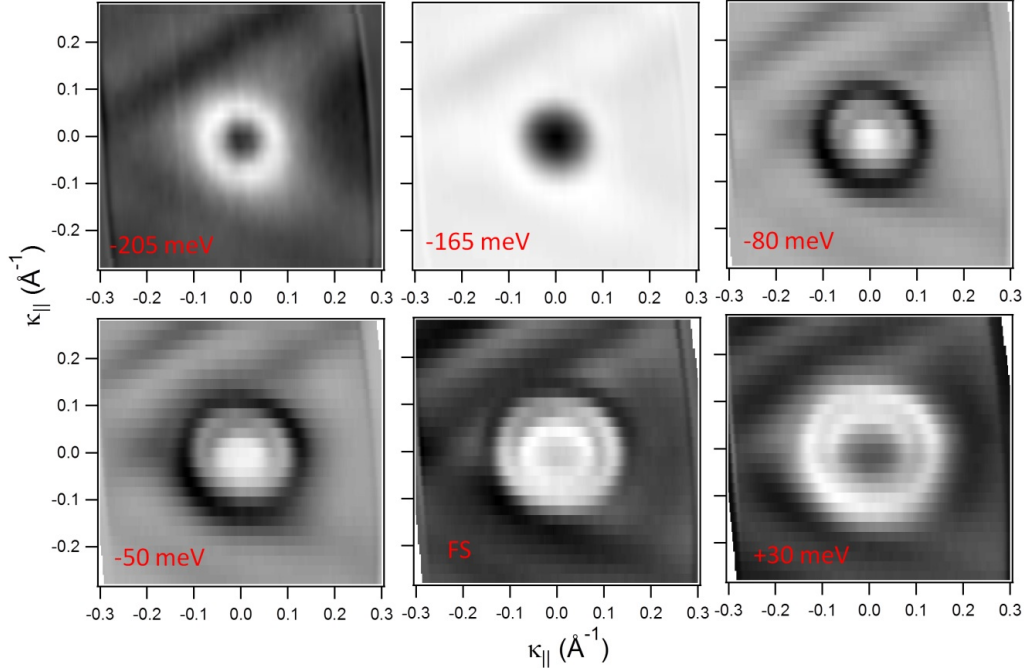


Figure 5.17: CES Plots: 1 ML Ag/ 3 ML Cu/Ni - CESs taken at different energies for the 1 ML Ag/ 3 ML Cu/Ni(111) system.

/Ni(111) system can also be drawn from the DFT calculations² shown in Fig. 5.18. It corresponds to a Ni slab of 15 layers thickness compared to the same slab terminated on both sides by Cu and Ag single layers. We notice that, for clean Ni the magnetic moment (blue dots) is slightly enhanced at the surfaces. After 1 ML Cu (green dots), the magnetic moment of the uppermost Ni layer is reduced and goes to zero at the Cu overlayer. The same happens when a Ag ML is deposited on top (red dots).

Since the split states only occur in the presence of the Cu spacer, a possible assignment is that these states are spin-split quantum well states within the Cu film. This is, however, rather unlikely for two reasons. First, if the observed states are to be considered as two parabola offsets by some energy, the effective masses will be quite different. This can be seen in Fig. 5.19(a). The red circles are the data points after fitting the corresponding MDCs by four Voigt peaks. The parabolic fit to the inner and outer branches are shown in purple and blue, respectively. The fitting parameters

²The calculations were done by E. Cannuccia, a post-doc in Nano-bio Spectroscopy Group, San Sebastián.

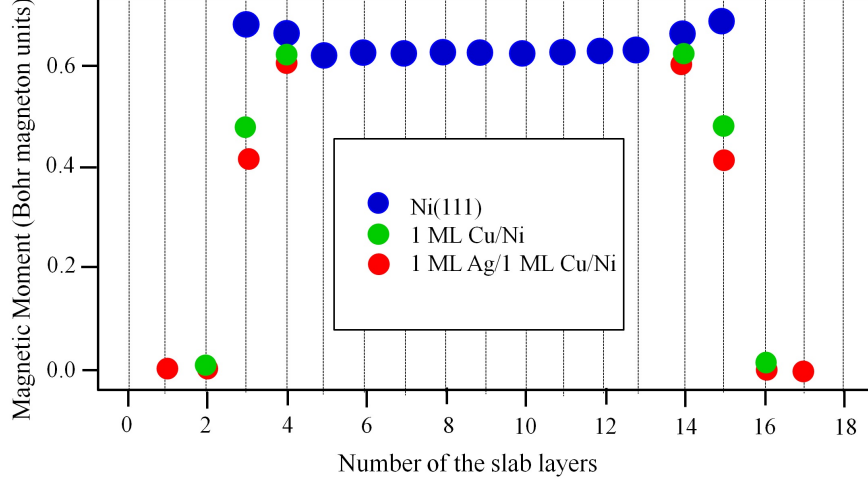


Figure 5.18: Calculated Magnetic Moments - The calculated magnetic moment as a function of the layer number in the slab for Ni (blue), 1 ML Cu/Ni (green), and 1 ML Ag/ 1 ML Cu/Ni (red).

are ($m_* = 0.4 m_e$ and $E - E_F = -0.101$ eV) for the inner branch and ($m_* = 0.78 m_e$ and $E - E_F = -0.190$ eV) for the outer branch. Although, the energy split of the two states are of the order of the exchange splitting in Ni (~ 100 meV), the large difference in the effective masses makes the QWS or the exchange splitting interpretation rather unlikely. Second, with increasing the Cu spacer thickness these states shift towards higher binding energies, in contrast to the common upward shift observed in Cu films at this energy range.

In reality, the topology of the two branches points toward an apparent Rashba-type spin-orbit splitting, as shown in Fig. 5.19(b). The blue curves are the fit to the experimental data (red circle), where the two branches are of equal effective mass ($0.43 m_e$) and split in the k -axis around the $\bar{\Gamma}$ -point by $\sim 0.038 \text{ \AA}^{-1}$. Such splitting is considered quite large if compared to, for example, Au(111) [221].

A spin-orbit split of such magnitude in the class of metals discussed here, would not be expected. The main ingredients for the spin orbit split to occur are the presence of heavy atom elements together with the broken inversion symmetry. These two ingredients can be seen by looking into the atomic spin-orbit interaction and Rashba equations. The energy of an electron in a magnetic field generated by its nucleus; due to the atomic spin-orbit coupling is given by [222];

5. RESULTS AND DISCUSSION III

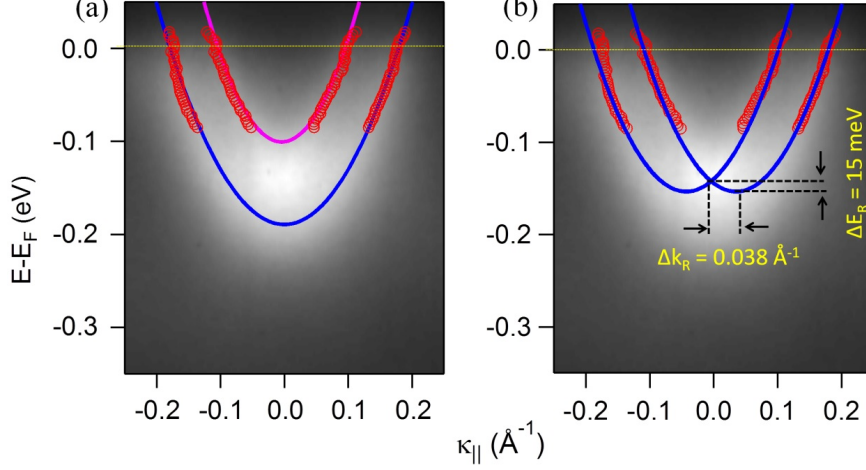


Figure 5.19: ARPES Data: 1 ML Ag/ 1 ML Cu/Ni - Shockley surface state dispersion of the 1 ML Ag/ 1 ML Cu/Ni(111) system along $\overline{\Gamma M}$ direction. The red circles are data point after fitting the corresponding MDCs by four Lorentzian peaks convoluted with Gaussian. In (a) the data points are fitted with two parabola offset in energy and with different effective masses, whereas in (b) Rashba-like spin-orbit split fit were applied.

$$\vec{E} = \frac{\mu_B}{\hbar m_e c^2} \frac{\vec{r} dV}{r dr} (\vec{l} \cdot \vec{s}) \quad (5.1)$$

where μ_B is Bohr magneton, \hbar Planck's constant divided by 2π , e electronic charge, m_e electron mass, c is the speed of light, l orbital angular momentum, and s is the spin angular momentum. The term $(\vec{E} = \frac{1}{e} \frac{\vec{r} dV}{r dr})$ is the electric field generated by the nucleus, which is transformed in the rest frame of the electron to a magnetic field $(\vec{B} = -\frac{\vec{v} \times \vec{E}}{c^2})$. The dependency of the spin-orbit splitting on the atomic number is included within the $\frac{dV}{dr}$ term, where for heavy elements the potential gradient is higher. In solids, and due to the presence of combined time reversal and inversion symmetry, the spin-systems are degenerate. If the inversion symmetry is broken, the spin degeneracy could be lifted by the spin-orbit interaction.

A breakdown of the structural inversion symmetry for a 2D electron system due to the confinement by asymmetric potentials or due the presence of the surface (Rashba-Bychkov effect^[223]) will induce spin polarization. The Rashba Hamiltonian for the spin-orbit interaction in a 2D electron gas confined in a plane with inversion asymmetry perpendicular to the surface is commonly written as;

$$H_{RB} = \alpha_R \vec{\sigma}(\vec{k}_{||} \times \vec{e}_z) \quad (5.2)$$

where α_R is Rashba constant, $\vec{\sigma}$ are the Pauli matrices, $\vec{k}_{||}$ is the 2D momentum, and \vec{e}_z is a unit vector perpendicular to the surface. The solution of the Schrödinger equation with this perturbation Hamiltonian leads to the following energy dispersion^[222];

$$E(k_{||}) = \frac{\hbar^2 k_{||}^2}{2m^*} \pm (\alpha_R k_{||} = \frac{\hbar^2}{2m^*} (k_{||} \pm k_R)^2) \quad (5.3)$$

This equation describes two parabola with the same effective mass (m^*) and with an offset $\pm k_R$ from the $\bar{\Gamma}$ -point ($k_{||} = 0$), as illustrated in Fig. 5.19(b). The two parabolas have to cross each other at the time reversal invariant momenta ($\bar{\Gamma}$ -point, in the present case). For 2D electron systems, the presence of a surface potential barrier naturally breaks the inversion symmetry. The Au(111) surface state, for example was found to be best described within the framework of Rashba model^[221]. The Au splitting decreases when substituting the heavy element (Au) with a lighter one (Ag), thus proving the atomic character of the spin-orbit splitting^[224].

Recently, Bi/Ag(111)^[108,225] and Bi/Cu(111)^[226] surface alloys were shown to induce a giant Rashba splitting much bigger than that of Bi, even though the number of heavy elements (Bi) were replaced by lighter elements (Ag, Cu). This finding points toward another driving force for the spin-orbit split, since the atomic spin-orbit interaction and the out of plane inversion symmetry alone cannot put the correct scale for the observed splitting. In-plane inversion symmetry was proposed to explain this effect. In fact, theoretical calculations explained the giant spin-orbit split in Bi-based alloys as due to asymmetric charge around the nucleus due to the atomic compression in such alloys^[227]. A striking example of the role played by the in-plane inversion symmetry in Rashba splitting is the case of Sb(111) surface. Antimony has atomic number (Z) of 51, similar to that of Ag ($Z = 47$), and less than that of Au ($Z = 79$). Therefore, undetectable spin-orbit splitting is expected for Sb based on the size of the atomic spin orbit split alone^[228]. A twenty time bigger spin-orbit split ($\sim 0.03 \text{ \AA}^{-1}$) was, surprisingly, reported for Sb(111) which was then attributed to the atomic scale roughness of the Sb compared to Ag^[229].

In our case, the observed spin-orbit-split-like state is only reported for 1 ML Ag/1-3 ML Cu/Ni(111) where the Cu layer is compressed to match the Ni lattice parameter.

5. RESULTS AND DISCUSSION III

This opens the possibility for an in-plane induced roughness, which would lead to a Rashba-like splitting, as in the Sb(111) case. In Fig. 5.20 we show a schematic representation (left) of the systems studied here and the corresponding surface state dispersion along $\overline{\Gamma M}$ direction (right). Assuming that Cu atoms (red) on Ni(111) (green) grow with the same Ni lattice parameter that, in this hard ball model representation, would necessarily give rise to in-plane corrugated Cu layers. The superstructure corrugations seen in the schematic drawing are arbitrary, and are only intended for a better visualization.

The absence of such atomic corrugation in Ag/Ni and Ag/5 ML Cu/Ni, where the Cu layers recovers the lattice parameter of Cu, explains the absence of spin-split bands in these two cases. Also in the high annealing temperature (> 800 K) where surface alloying between Cu and Ni takes place, Fig. 5.8, no such splitting is observed. Since the corrugation is greater for the 1 ML Cu and decay to almost zero in the 5 ML Cu case, the strength of the spin-orbit splitting would be stronger for the 1 ML Cu, reduced in 3 ML Cu, and finally vanishes for higher Cu coverage, as exactly observed. Actually, for Cu/Ni case ($Z(\text{Cu}) = 29$) without the Ag layer, shown in Fig. 5.9, one can see a similar splitting, which is hardly visible due to the combined close proximity of the Cu/Ni surface state band minima to the strong emission from the Ni d -band, and the unintended partial Ag coverage. Theoretical calculations are in progress to test these experimental findings. STM measurements are also required to validate the assumption of the atomic scale roughness sketched in Fig. 5.20.

Now we would like to address some possible consequences of this work. Firstly, this finding suggests the possible generalization of the rough pseudomorphic substrates, made by combination of two elements with similar lattice parameter, to tune the strength of the spin-orbit splitting in light or heavy elements overlayers. We expect an even stronger spin-orbit split states for Bi full layer(s), for example, on top of atomically rough surfaces. In that respect, a Cu/Ni substrate would serve better than, for example, Ag/Ni to enhance the spin-split of a heavy element overlayer(s). We also believe that the present observations might help resolving the contradictions concerning the spin-orbit split of graphene grown on Ni(111) and intercalated with noble metal atoms. Actually, a recent theoretical study for graphene on Ni and other noble metal substrates concluded that the spin-orbit splitting does not sensitively depend

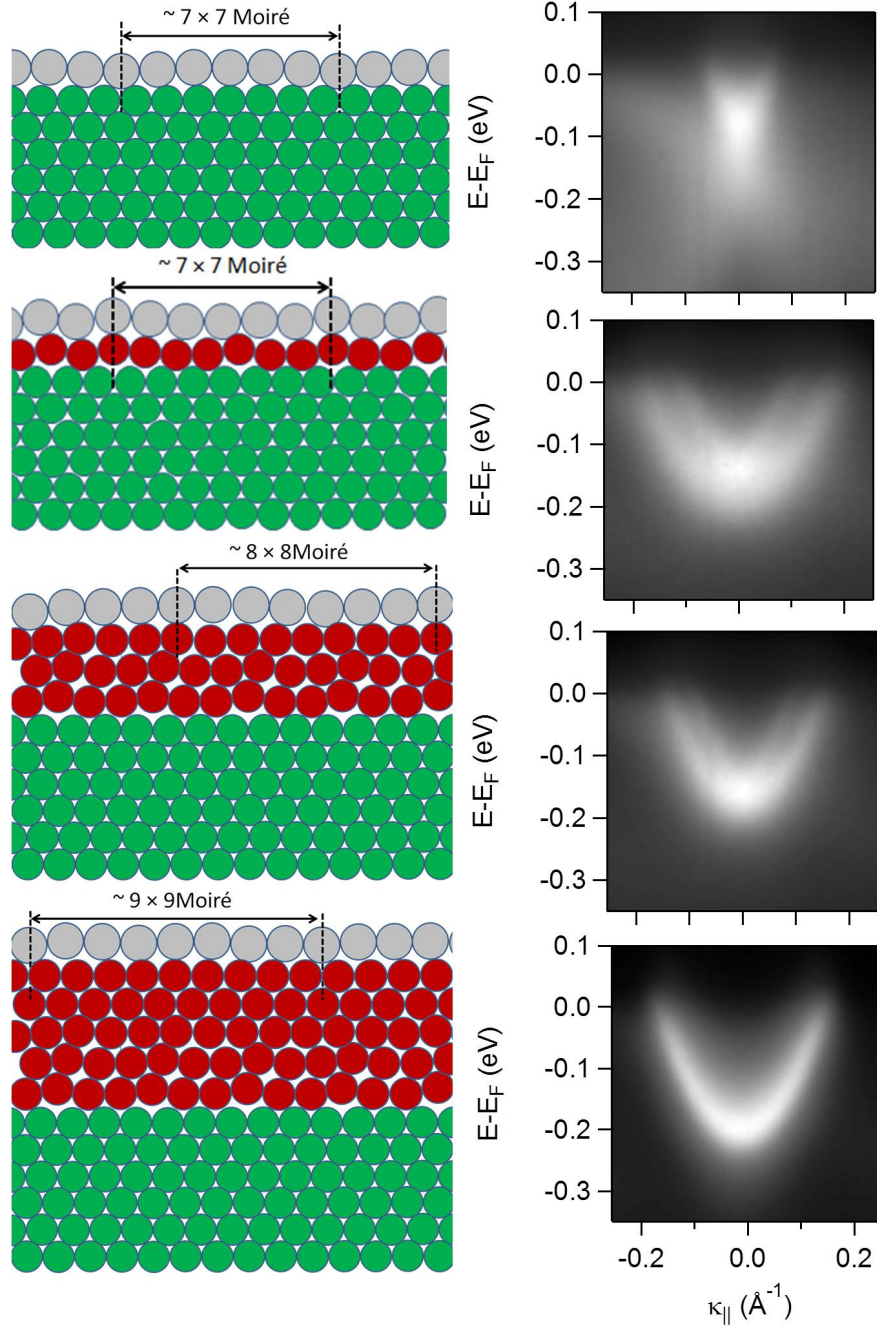


Figure 5.20: Structure vs. Dispersion Plots: Ag/Cu/Ni - Schematic drawing of the 1 ML Ag /Cu/Ni(111) system used in this work (left), and the corresponding surface state dispersion along $\overline{\Gamma M}$ direction. The Ni, Ag, and Cu atoms are shown in green, red, and silver colors, respectively.

5. RESULTS AND DISCUSSION III

on the charge transfer (as claimed for graphene on Ni) between the graphene and the substrates^[230]. They also found that the heavy metals are not always inducing large spin-orbit splitting in graphene^[230]. Therefore, the understanding of such noble metals combinations on Ni(111) is of critical importance.

Secondly, and more related to the main subject of the thesis, is the issue of the Ag/Cu dislocation network in these Cu/Ni(111) films. Up to 3 ML Cu, the surface state looks quite distinct from the 1 ML Ag/Cu(111) surface state. For 5 ML Cu and higher, the energetic position of the surface, together with weakly resolved umklapps, indicates the dislocation network formation. The surface electronic structure in these two cases is quite distinct: Rashba like in one case and gapped state in the other case. The exact surface structure for Cu thickness < 4 ML, though, needs to be characterized by STM, since the dislocation network formation (with Cu film thickness dependent periodicity (less than 9×9)) for such Cu thicknesses cannot be discarded. Such characterization might answer a fundamental question concerning the interplay between the electronic states and the surface structure.

At the end we would like to, briefly, comment on other alternative explanation of the physical origin of the reported double branched surface states, based on some findings in recent literature. For example, Ag films grown onto Pt(111) exhibit quantum well states with significant deviation^[231] from the nearly-free-electron behavior, which is otherwise characteristic of Ag films on Cu(111)^[136] or Au(111)^[140]. The dispersions of the QWSs in the Ag/Pt system were found to be flattened close to the $\bar{\Gamma}$ -point of the surface Brillouin zone^[231]. Even more, a negative effective mass was observed for the first QWS of small Ag film thicknesses (< 20 ML). These observations, together with first-principle calculations attributed such anomalous behavior to the hybridization between the QWSs and the Pt projected bulk bands of the same symmetry but different in-plane dispersion. More recently, a similar situation is observed for a Cu film on Pt(111). Interestingly, the flattening and band inversion of the QWSs were shown to, similarly, take place for the surface state on Cu/Pt(111) for a 3-4 ML Cu film^[232]. The same hybridization effect has been proposed as the origin of such unusual dispersions.

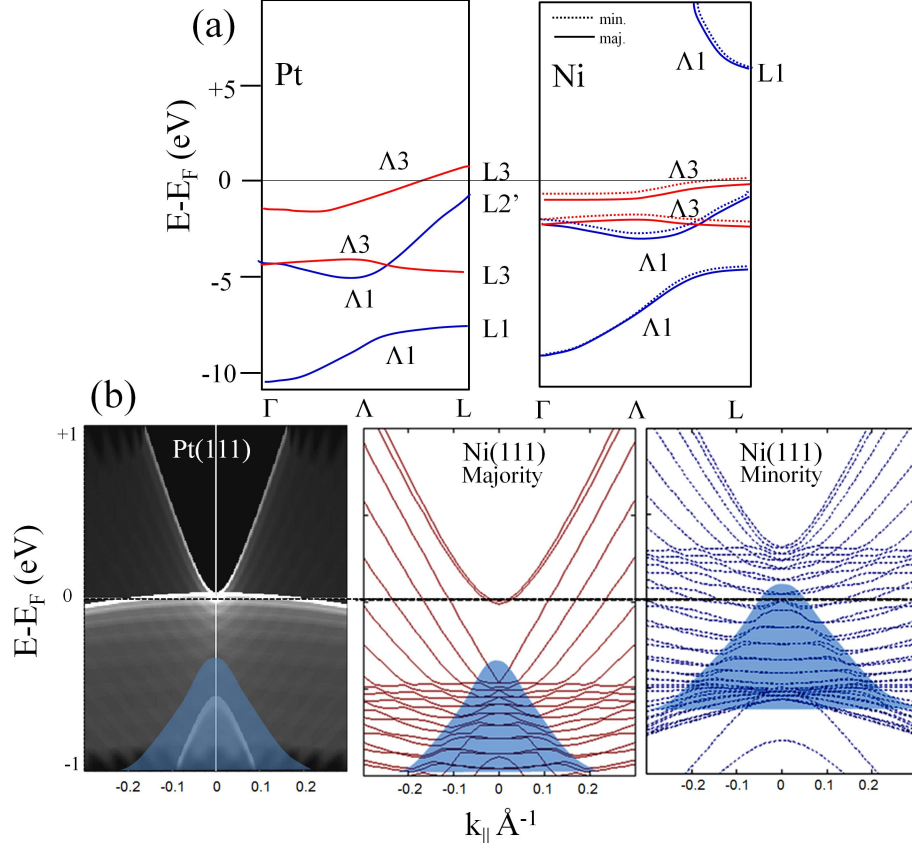


Figure 5.21: Band Structure: Pt vs. Ni - (a) Calculated bulk band structure of Pt and Ni. Red and blue lines mark bands with Λ_1 and Λ_3 symmetry, respectively. For Ni, solid and dotted lines stand for the majority and minority bands, respectively. Adapted from [211,233]. (b) The projection of the bulk band structure along the (111) direction for Pt(111) and Ni(111). The blue shaded regions highlight the projection of the low energy Λ_1 bands which have the same symmetry as the sp -derived surface states. See the footnote for the references.

Figure 5.21 shows the bulk band structure [211,233] and its projection onto the (111) direction for both Pt and Ni ³. Since Ni is magnetic, the majority- and minority-spin band structures are displayed. Clearly seen, both Pt and Ni have very similar band structure (Fig. 5.21(a)). Only the low energy bulk bands with the sp -character (Λ_1) are concerned here. Their projection onto the (111) direction are marked by the blue shaded regions, where downward dispersing bulk states are defined (Fig. 5.21(b)). In

³The calculated band structure of Pt(111) is obtained using ELAN 1.0 Energy Level Analyzer software, developed by V. Joco., whereas the Ni(111) band structures were provided by E. Cannuccia.

5. RESULTS AND DISCUSSION III

case of Cu and Ag films on Pt(111) it is the hybridization with this band that led to the anomalous dispersion of the surface and QW states.

The minority $\Lambda 1$ band of Ni(111) lies close to the Fermi level (Fig. 5.21(b)) where the Ag(111) and the 1 ML Ag/Ni(111) surface states exist. For 1 ML Ag/Cu/Ni(111), the surface state lies at higher binding energy for increased Cu film thickness. The hybridization between the surface or QW states and the $\Lambda 1$ bands is at its maximum when the QW/surface band minimum is close to the top of the $\Lambda 1$ band.

A schematic representation of the surface state of the 1 ML Ag on top of Cu (0 to 5 ML)/Ni(111) is shown in Fig. 5.22. In the absence of strong hybridization with the substrate bulk bands, nearly-free-electron surface states with their usual parabolic dispersion are expected (see black lines in the first column). Hybridization with the $\Lambda 1$ bands (blue shaded regions) results in a strong deviation from the parabolic dispersion close to the $\bar{\Gamma}$ -point (see red lines in the first column). Since the 1 ML Ag/Ni surface state lies close to the top of the $\Lambda 1$ band, the strong hybridization can result in a negative effective mass. For 1 ML Ag/5 ML Cu/Ni the parabolic dispersion can be fully recovered. For Cu thickness in between these extremes, flattened dispersions are expected.

By taking the hybridization alone into account, our photoemission data cannot be reproduced. However, if we consider the presence of both interface and surface states at the 1 ML Ag/Cu slab a good agreement between the schematic representation and our data can be obtained. Indeed, two parabolic surface states are present in a free-standing film, which merge into a single Shockley-like state for increasingly Cu film thickness (see black lines in the third column). In a real film, the two slab states become the surface and the interface state, as reported for Mg(0001) thin films grown on W(110)^[234]. For weakly interacting interfaces two parabolas with the same effective mass are expected, something that is not observed in our experimental data, as discussed in Fig. 5. 19. If one, however, considers that the interface state hybridizes strongly with the bulk band (see solid red lines in the fourth column), while the far laying surface state at the Ag layer is barely affected (see dashed red lines in the fourth column), a good agreement with the experimental data (the fifth column) can be obtained.

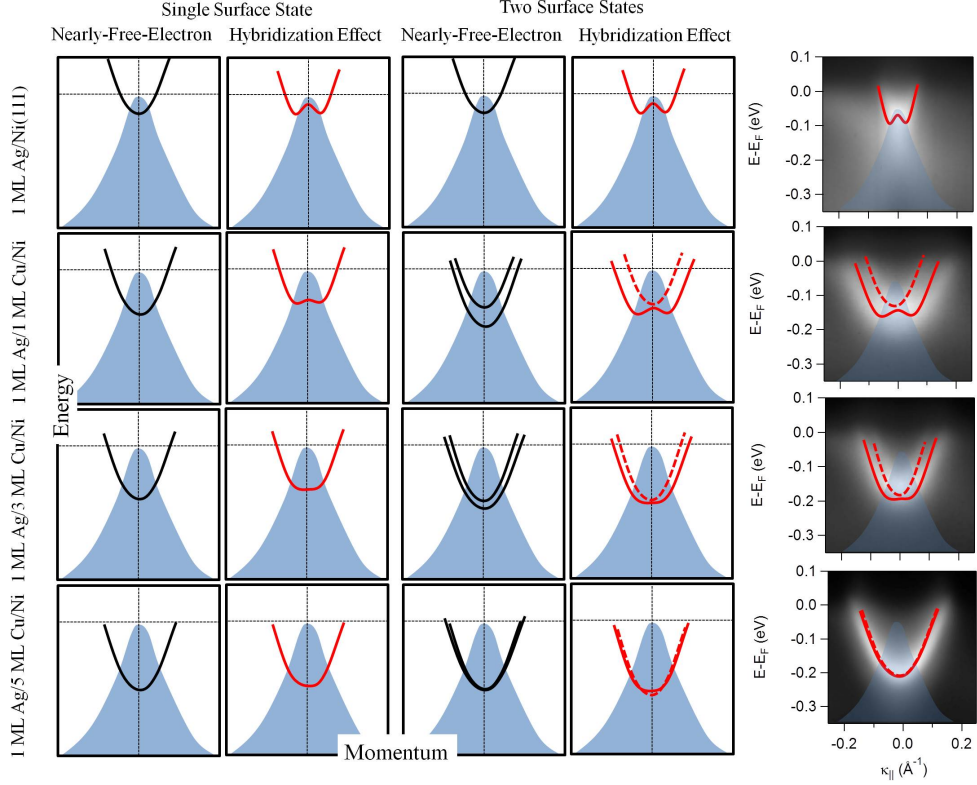


Figure 5.22: Hybridization Effect in Ag/Cu/Ni(111) - Schematic representation of the hybridization effect between the surface states in 1 ML Ag/Cu/Ni system and the $\Delta 1$ band of the Ni substrate. Surface/interface states are marked with the black (red) lines in the absence (presence) of hybridization. The blue shaded regions are the projection of the $\Delta 1$ band onto the (111) direction. The experimental data are shown to the right, where the surface states and the $\Delta 1$ bands are superimposed.

Although these physical effects are common for some metallic systems and does not involve new interpretation to our data, the photoemission intensity plots points, experimentally, may also be interpreted as spin-orbit like split bands. The latter actually is rather unlikely, from theory point of view. Since the surface state, interestingly, should acquire a spin-texture after hybridization with a magnetic substrate band, techniques such as spin-resolved photoemission can shed some light into the nature of the observed bands. The outer branches of the surface state should give an opposite spin polarization for spin-orbit split states, whereas the hybrid surface state should acquire the same polarization close to the $\bar{\Gamma}$ as the $\Delta 1$ minority band.

5. RESULTS AND DISCUSSION III

We note also that Ir has a similar band structure as Pt and Ni^[233], and therefore hybridization between surface or QW states of noble metal overlayers on top of Ir(111) and its bulk bands is expected. We are not aware of such studies on the surface of Ir(111) to further support the hybridization effect. However, the Ir(111) surface state itself has been recently claimed to be sort of topologically protected due to the linking between the spin-orbit branches of the surface state and the Ir bulk bands^[235]. It has claimed that this property arises from the nature of the bulk bands of Ir, where the L_3 and L_2 bands reverse order (L_3 higher in energy than L_2) compared to the situation in noble metals. Actually, Pt and Ni exhibit the same band inversion as Ir. Therefore, a detailed understanding of the real physical nature of the clean Ni and Pt surface states themselves would be necessary.

5.4 Conclusions:

In conclusion, we have shown that the gapped 1 ML Ag/Cu(111) surface state can be obtained on Ni(111) substrate for Cu thicknesses > 3 ML. The 1 ML Ag/Ni(111) system was found to be characterized by a Ni-like surface state with circular FS, whereas umklapps due to the Moiré superstructure were not visible. For 1 ML Ag on top of Cu/Ni(111) and for Cu thickness < 4 ML, an “*apparent*” spin-orbit splitting of surface states, with barely hexagonally shaped FS-s, were obtained. Similar states are expected due to hybridization between the surface/interface states and bulk bands. Theoretical calculations as well as other experimental techniques, beyond the scope of the present thesis, are required to test these findings. STM measurements are also required to answer the question of whether there is a critical Cu thickness at which the dislocation network starts to form, as well as to determine the surface structure of the 1 ML Ag/Cu/Ni(111) system.

6

Results and Discussion IV

6. RESULTS AND DISCUSSION IV

Robust Surface Doping of Bi_2Se_3 Topological Insulator by Rb Intercalation

6.1 General Introduction:

The surface states discussed in the previous chapters are called “*Shockley surface states*” and their origin is related to the broken symmetry at the crystal surface termination^[27,28]. They are fundamentally different from the robust edge (surface) states^[58] that, e.g., correspond to the integer^[236], fractional^[237], and spin^[238,239] quantum Hall (QH) effects. The state corresponding to the QH is an insulating state, which can be induced by applying a strong enough magnetic field to an electron gas confined in 2D at low temperatures. This leads to a circulation of the electrons in a direction determined by the magnetic field in which discrete energy levels, “*Landau levels*”, are formed^[236,240]. What distinguishes the QH state from the usual band insulating state, however, is the formation of a propagating current along the edges of the sample (i.e., edge states induced by magnetic field rather than symmetry breaking at the surface) when an electric field is applied. These states were found to be robust against scattering by impurities. This robustness is later attributed to their connection to the bulk occupied states rather than the edges and, therefore, getting rid of them involves extreme damage to the bulk of the material^[240–243]. Such unusual coupling with the bulk states is what is referred to as “*topological*” protection.

The search for a QH-like effects without applying a magnetic field^[238,243–246] has led to the discovery of the spin QH effect in HgTe quantum wells^[239], taking advantage of the “*spin-orbit coupling*” as being an intrinsic source of the magnetic field. Although, the QH effects are restricted to 2D electron systems, a new class of 3D insulating systems that host similar topologically protected surface states was, later, theoretically predicated^[247,248] and experimentally verified^[249], namely “*topological insulators*”. The

6. RESULTS AND DISCUSSION IV

main ingredients that are needed for 3D topological insulators are, in the presence of inversion symmetry, the presence of an insulating bulk band gap generated by a spin-orbit coupling strong enough to induce a band inversion. The strong spin-orbit coupling of these new 3D materials induces different parities at different time reversal invariant momenta (TRIMs). The surface states associated with such 3D topological insulator are named “*topological surface states*” and their properties and interaction with, e.g., surface defects are completely different from the, by now called, “*trivial surface states*” discussed in the previous chapters.

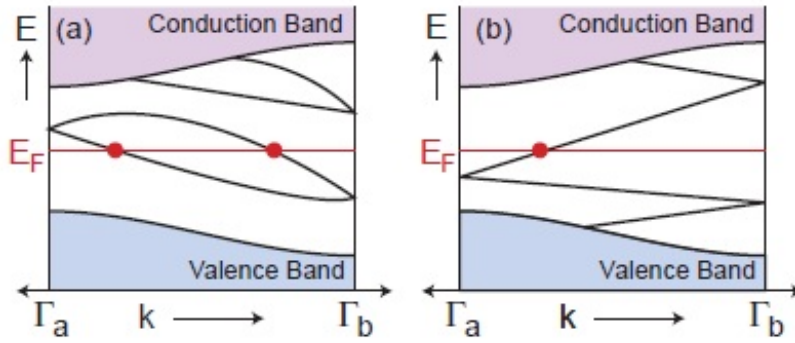


Figure 6.1: Trivial vs. Topological Surface States - Surface state dispersion between two Kramer’s degenerate points: in (a), the number of surface states crossing the Fermi energy E_F is even, whereas in (b) it is odd. An odd number of crossings lead to topologically protected metallic surface states. Taken from Ref. [58] ^[58].

The robustness of the topological surface states can be understood from the schematic representation in Fig. 6.1. The Shaded regions in the figure represent the valence and conduction bands of an insulator. The black solid lines are edges or surface states, and the Fermi level is marked by the horizontal line. According to Kramer’s theorem, time reversal symmetry implies that the electronic states are degenerate at the TRIMs (i.e., Γ_a and Γ_b). In the presence of spin-orbit interaction, the degeneracy of the twofold state is lifted except at these TRIMs. The (a) and (b) describe the only two possible ways of connecting these states. In (b) the Kramer’s pairs switch partners while in (a) they do not. The situation in (a) is the common one for topologically trivial states, where one can eliminate these states by placing the Fermi level in the full gap using, for example, adsorbates. In situation (b), however, there is no way of getting rid of these “*topological state*”. In 3D topological insulators, these states are Dirac-like with

its Dirac-points located at the TRIMs. The robustness of the topological state is ensured as long as the time reversal symmetry is present; otherwise a magnetic field (or magnetic impurity) can lead to a gap opening at the TRIMs.

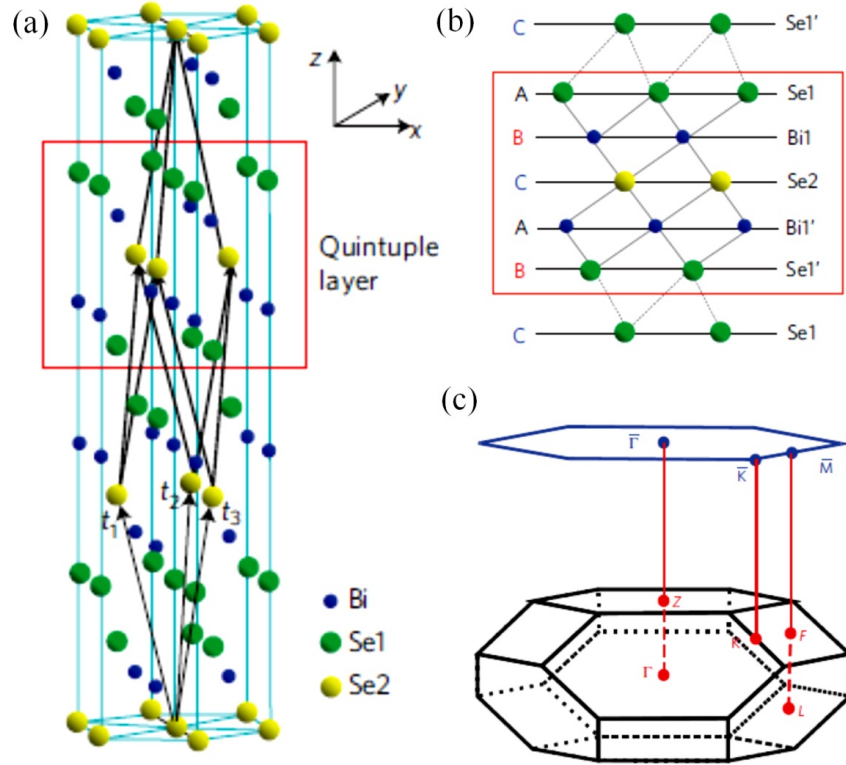


Figure 6.2: Real vs. Reciprocal Space of Bi_2Se_3 - (a) Crystal structure of Bi_2Se_3 with three primitive lattice vectors denoted by t_1 , t_2 , and t_3 . A quintuple layer Se1-Bi1-Se2-Bi1'-Se1' is indicated by the red square in (a) and a side view of it is further zoomed in (b). (c) The 3D Brillouin zone (BZ) of Bi_2Se_3 (black) and the 2D BZ of the project (111) surface (blue). The high symmetry k points are labeled. Adapted from Ref. [245]^[250].

In the following we briefly discuss the rule of the strong spin-orbit coupling using a case example on the Bi_2Se_3 crystal. The example can be generalized to most layered semiconductors A_2X_3 , where A is a heavy metal element (Bi, Sb, etc) and X is a metal chalcogenide (Se, Te, etc)^[250,251]. The Bi_2Se_3 has a rhombohedral crystal structure with five atoms per unit cell^[250] as shown in Fig. 6.2. The material consists of five-atom layers (quintuple layers) arranged along the z -axis each of them consist of five atoms with two equivalent Se atoms (Se1 and Se1'), two equivalent Bi (Bi1 and Bi1')

6. RESULTS AND DISCUSSION IV

atoms and a third Se atom (Se2). The coupling is strong between two atomic layers within each quintuple layer and much weaker, mainly van der Waals type, between adjacent quintuple layers. The primitive lattice vectors are t_1 , t_2 , and t_3 . The crystal has an inversion symmetry centered at the Se2 sites, a necessary condition for the topological state existence. The lattice parameters of the crystal are $a = 4.138 \text{ \AA}$ and $c = 28.64 \text{ \AA}$, with a quintuple layer width of 7.15 \AA measured from the centered of the van der Waals gap, and quintuple layer separation of 2.43 \AA measured between the Se layer atoms in adjacent quintuple. The bulk and the surface Brillouin zones (BZ) are shown in Fig. 6.2(c). The high symmetry points are given on the graph, where Γ , L , F , Z and $\bar{\Gamma}$ and \bar{M} are the TRIMs of the bulk and surface BZ, respectively.

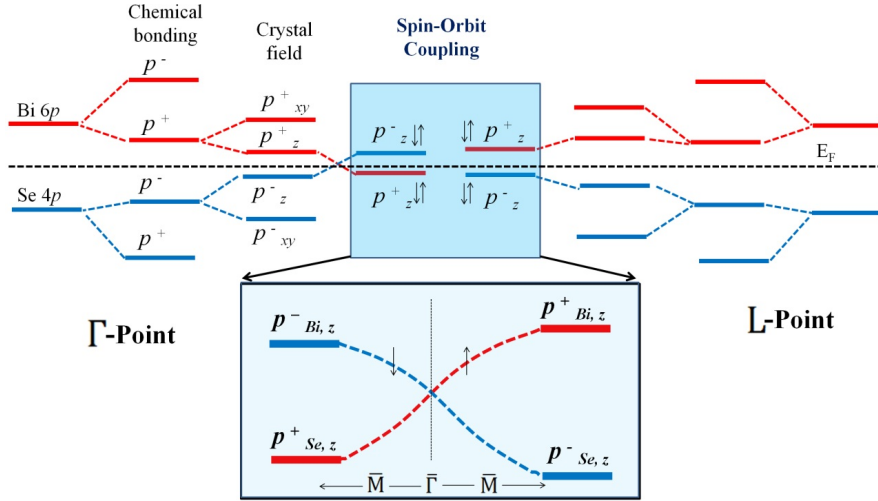


Figure 6.3: Parity Inversion in Bi_2Se_3 - Schematic diagram showing the evolution of the atomic $p_{x,y,z}$ orbitals of Bi and Se into the conduction and valence bands of Bi_2Se_3 at the Γ -point (left) and the L -point (right). The black dashed line represents the Fermi level. Beside the chemical bonding and crystal field splitting, the spin-orbit coupling induces a band inversion at the Γ , but not, the L -point. Modified from Ref. [245]^[250]. At the surface (bottom), spin-polarized topological states (dashed blue and red lines along the $\bar{\Gamma}\bar{M}$ direction) are formed inside the bulk gap produced by the spin-orbit coupling.

The Bi_2Se_3 crystal has the necessary ingredient for being a topological insulator in the framework of Kane's criterion. The first obvious one is the presence of a bulk insulating gap; the later in case of Bi_2Se_3 was estimated to be $\sim 0.3 \text{ eV}$ ^[252]. The second ingredient is the presence of band inversion induced by the spin-orbit splitting; the Bi as heavy element allows satisfying this condition. Theoretical calculations showed that

6.2 Sample Preparation and Experimental Tools:

it is only when the spin-orbit interaction is switched on, band inversion takes place and the parity (defined by (+) or (-) sign) at the Γ -point changes its sign to be opposite to the other TRIMs as depicted in Fig. 6.3 for Γ and L -points. At the crystal surface termination, and due to the presence of a gap induced by the spin-orbit coupling, a helical spin-polarized Dirac-like topological state connecting the valence and conduction bands is observed; see dashed blue and red lines in the bottom of Fig. 6.3.

The discovery of these topological states of matter, and due to their spin properties and extreme robustness, immediately triggered a variety of potential applications. In particular, the proximity of such topological insulators to other exotic state of matters, such as superconductivity, were suggested, aiming to achieve, e.g., topological superconductors^[253]. Exposure of topological crystals to different adsorbates, thin films of trivial materials, thin films from other topological materials, etc, have been extensively explored.

In the present work, we investigate the near surface electronic structure of Bi_2Se_3 (0001) crystal. In particular, the effect of alkali metal (Rb) deposition on the topological state, valence and conduction bulk bands will be detailed. We report a downward shift of the topological state together with the formation of a series of 2D spin-orbit split and M-shaped states in the vicinity of the conduction and valence band, respectively. These findings are in complete agreement with recent works using similar or completely different adsorbates. The physical origin of such near surface electronic structural modification is still questionable. Due to the great similarity of different adsorbates effects, the literature survey will appear in-line with our results and discussion.

6.2 Sample Preparation and Experimental Tools:

The Bi_2Se_3 with the structure shown in Fig. 6.2 are, due to excess Se or defects, commonly found as n -type doped semiconductors^[252]. Previous work has shown that the conduction band (and the topological state) is below the Fermi level. For the purpose of our work, an intrinsic or p -type crystal is more convenient. Bi_2Se_3 crystals doped with Ca are shown to be p -type semiconductors; hence, the conduction band is completely above the Fermi level. The p -doped and un-doped Bi_2Se_3 crystals were

6. RESULTS AND DISCUSSION IV

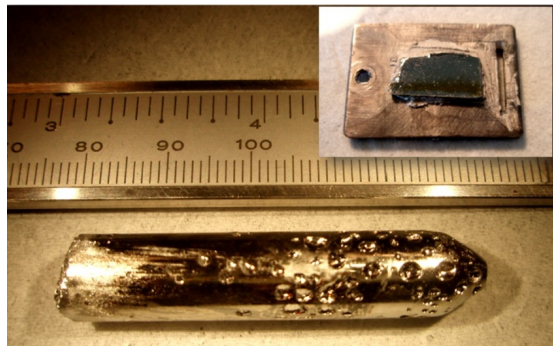


Figure 6.4: The Bi_2Se_3 Crystal. The crystal once taken out from the ampoule. The inset shows the sample attached to the Tantalum holder after gluing. Made by M. Bianchi.

produced by the following common strategy¹ [254]: Stoichiometric mixtures of 5N purity elemental Bi and Se were melted at 860°C for 24 hours in an evacuated quartz ampoule. The Ca-doped sample was synthesized by adding the respective amount of Ca with the mixture before melting. The mixture was then cooled down to 650°C at a rate of 2.5°C/h followed by annealing to 650°C for another two days. The sample was subsequently removed to another evacuated quartz ampoule with a conical bottom and zone melted through an induction coil with a rate of 1.2 mm/h . The quality of the resulting crystal was found to be dependent on the annealing and cooling conditions (time, rate, and/or temperature). After cutting the ampoule with a diamond wheel and breaking it delicately the crystal is taken out. It has the cylindrical shape presented in Fig. 6.4. From this batch the samples to be characterized were simply obtained by, gently, cutting the batch along one of the flakes with a scalpel. The resulting sample was then fixed on a Tantalum sample holder, inset in Fig. 6.4, using epoxy conducting glue and was subsequently dried at 150°C for $\sim 20\text{ min}$. Later on, the sample was cleaved, using a common scotch tape, at room temperature in a pressure better than $1 \times 10^{-8}\text{ mbar}$ and transferred immediately to the measurement chamber where the sample is quickly cooled down to 60 K . The transfer is carried out in less than 3 min , and was done at a pressure below $1 \times 10^{-9}\text{ mbar}$. The pressure in the analysis chamber was below $3 \times 10^{-10}\text{ mbar}$. The layered structure and the weak van der Waals bonding between the quintuple layers (Fig. 6.2) ensure the (111), mainly Se atoms, termination of the surface. Other high symmetry planes are not possible within this approach. The Rb atoms were evaporated from a commercial alkali metal dispenser

¹All crystals used here are chemically synthesized by J. L. Mi and B. B. Iversen, from the Center for Materials Crystallography, Department of Chemistry, Interdisciplinary Nanoscience Center, Aarhus University, Denmark.

with a 5 A evaporation current for different time intervals. In ARPES setup, the deposition was done in the preparation chamber while the sample kept at a nominal temperature of 190 K, while in core-level photoemission the substrate was kept at 300 K during Rb deposition. The same evaporation parameters in both setups are used and the Rb coverage was determined following the relative intensity of Rb and substrate core levels. ARPES measurements were carried out at the beam line SGM III at the synchrotron radiation source ASTRID, ISA, Aarhus University. The setup components have been detailed already in chapter two. Core level photoemission has been also measured at the SGM I beam line, ASTRID. The STM experiments were performed in an UHV low-temperature scanning tunneling microscope facility cooled by a Joule-Thomson cryostat. The bulk Bi_2Se_3 samples were cleaved in UHV at room temperature and immediately transferred into the cryogenic microscope. During cool down, Rb was deposited onto the substrates at $T < 200$ K. For annealing, the samples were transferred in UHV from the STM to a Boron Nitride heater with a thermo couple. STM topographs were acquired at 1.2 K in the constant current mode at a current I with a bias voltage V applied to the sample. The coverage of surface-adsorbed Rb was determined by counting the number of Rb atoms visible in STM topographs of a certain area and dividing by the number of surface Se unit cells within the same area. Since the measurements were done in three different chambers, there are uncertainties in both the annealing temperatures and the Rb coverage. We estimated a deviation in the temperature from one chamber to another to be up to 20 K. The coverage of Rb is accurately estimated in STM with, however, about 20 % uncertainty in ARPES and XPS experiments.

6.3 Results and Discussion²:

Figure 6.5 shows the energy vs. momentum photoemission intensity plots for the Cd-doped Bi_2Se_3 crystal and the stepwise deposition of Rb atoms. Initially, only the topological state (the V shaped feature) is observed with its Dirac point slightly below

²The author's contribution to this work is limited to the measurements and analysis of ARPES data on the clean and Rb exposed samples in collaboration with M. Bianchi, R. Hatch and Ph. Hofmann from Department of Physics and Astronomy, Interdisciplinary Nanoscience Center, Aarhus University. Oxygen exposure test, XPS and STM data were taken and analyzed by Aarhus group and their collaborators.

6. RESULTS AND DISCUSSION IV

the Fermi level (-0.09 eV), Fig. 6.5(a). The M-shaped states at ~ -0.3 eV and higher binding energy features represent the valence band of $\text{Ca-Bi}_2\text{Se}_3$. After subsequent deposition of Rb atoms at 190 K, the Dirac point shifts toward higher binding energy. For 5 sec Rb deposition the Dirac point binding energy was found to be at 0.505 eV (Fig. 6.5(b)) and slightly increased to 0.560 eV after additional 5 sec deposition (Fig. 6.5(c)).

Such downward shift, with its subsequent increase of Fermi wave vectors, is very common for alkali metal deposition on the surface state of topologically trivial noble metal surfaces. The most remarkable observation is, however, the formation of the Rashba spin-orbit split states together with a series of M-shaped states seen as a quantization of, respectively, the conduction and valence band, Fig. 6.5(b-c). One of the latter states is marked by the yellow dotted curves, as a guide for the eyes. They are also better seen in Fig. 6.6, where the full dispersion of the M-states can be clearly recognized. The Rb-adsorption-induced electronic states, was actually reported in previous works using a variety of different adsorbates, although different explanations of their physical origin were given.

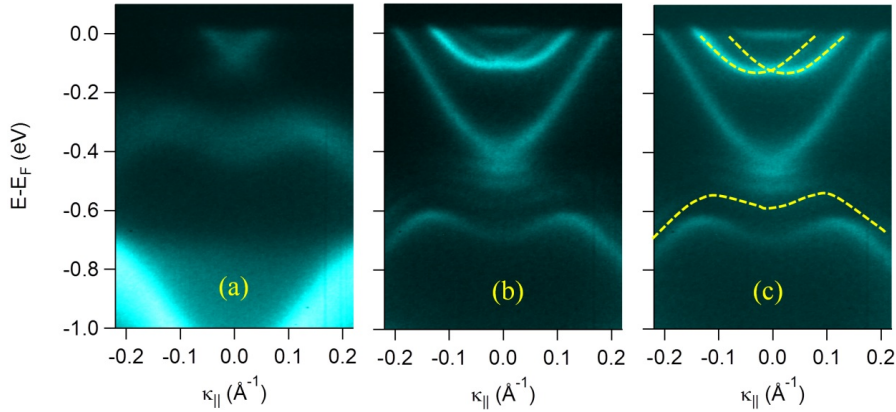


Figure 6.5: ARPES Data: Rb Deposition - ARPES photoemission intensity plot of the surface electronic structure of (a) clean Ca-doped Bi_2Se_3 and Rb-doped with (b) 5 sec and (c) 10 sec. Rb deposition was done at 190 K and the measuring temperature was 70 K. Measurements are performed using a photon energy of 16 eV. The yellow dotted lines in (c) mark two of the Rb-induced states close to the conduction and valence bands.

Surface states do not disperse with the momentum component perpendicular to the surface. In ARPES experiments they can be identified quite simply using photon energy

dependent measurements. Such a scan can then be used to test the dimensionality of these states.

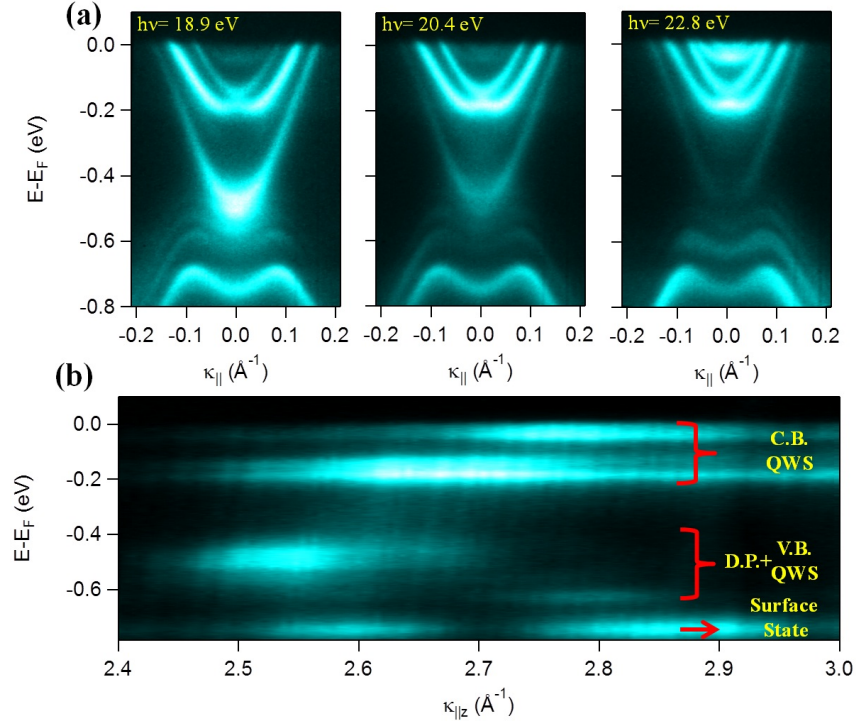


Figure 6.6: ARPES Data: Energy Dependent Plots - (a) ARPES photoemission intensity plot of the surface electronic structure of the 10 sec Rb-doped sample taken at three different photo energies. (b) The corresponding photon energy scan (expressed in terms of the component of the momentum perpendicular to the surface) of EDCs taken at normal emission. The photon energy was scanned from 14 eV to 32 eV in steps of 0.1 eV. The measuring temperature was 70 K.

Figure 6.6(a) shows the topological and the induced states on the stepwise (5+5) sec doped Rb sample taken at three different photo energies. The variation of the intensity in Fig. 6.6 is a cross section effect where different states are better seen for different photon energies. Assuming a free-electron final state and a crystal inner potential of 11.8 eV^[251], the perpendicular component of the momentum (k_z) is obtained for all photon energies. In Fig. 6.6(b) EDC spectra at normal emission as a function of k_z are displayed. Both the Rashba split state and the M-shaped states are not dispersing with k_z and are, therefore, classified as 2D surface/interface states. Due to their visual proximity to the conduction and valence bands, we shall call them quantum well states,

6. RESULTS AND DISCUSSION IV

i.e., “*C.B. QWS*” and “*V.B. QWS*”, respectively. The apparent doubling of each C.B. QWS in Fig. 6.6(b) is, actually, due to a slight deviation from the normal emission in our measurements, appearing like a slightly avoided cross of the spin-split states. The highest binding energy non-dispersing feature is classified as the surface state of Bi_2Se_3 . Throughout the text we will use the 2DEG (2D electron gas) and M-state referring to the C.B. QWS and V.B. QWS, respectively.

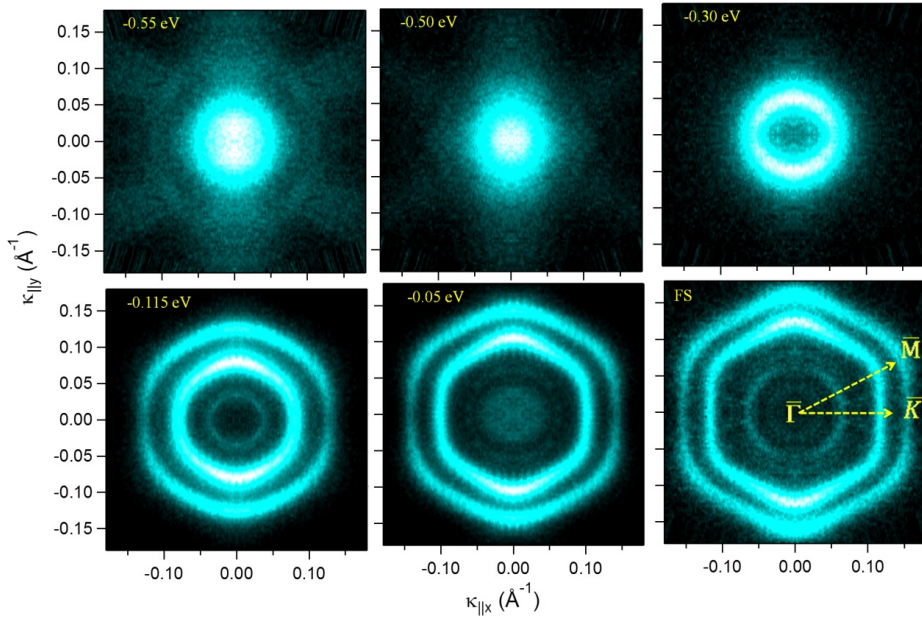


Figure 6.7: ARPES Data: FSMs - (a) Constant energy surfaces (CES) of the 10 sec doped Rb sample as measured by ARPES. The hexagonal warping of both the 2DEG and the topological state is clearly seen for CESs close to the Fermi level. Close to the Dirac point a circular contours are observed. The measuring temperature and the photon energy were, respectively, 70 K and 16 eV.

The dispersion plots in Fig. 6.5 and Fig. 6.6 were taken close to the $\overline{\Gamma K}$ direction of the surface Brillouin zone. In order to map out the dispersion along all other high symmetry directions, an angular scan was acquired for the (5+5) sec doped Rb sample. Figure 6.7 shows a series of constant energy surfaces (CESs) at different binding energies. The bright central intensity spot at the higher binding energy cuts is the topological state. The topological state has a circular CES in the proximity of the Dirac point and has a hexagonally shaped CES close to the Fermi level. The hexagonal shape of the FS is a natural consequence of the Fermi wavevectors anisotropy in $\overline{\Gamma M}$

and $\overline{\Gamma K}$ directions^[255] being $\sim 0.164 \text{ \AA}^{-1}$ and $\sim 0.151 \text{ \AA}^{-1}$, respectively, as seen in their corresponding MDCs in Fig. 6.8. The 2DEG states appear hexagonally shaped as well with, however, smaller Fermi wavevectors ($\Delta k=0.007 \text{ \AA}^{-1}$).

The hexagonal shaping of the latter reflects a different effective mass in $\overline{\Gamma M}$ and $\overline{\Gamma K}$, directions being $0.18 m_e$ and $0.16 m_e$, respectively. The FS encloses 5 contours which are assigned to the topological states and the two branches of each 2DEG states. The inner branches of both Rashba states are less bright than the outer ones and are, therefore, barely visible in the FS contours. They are, however, surely present as can be judged from the dispersion plots shown in Fig. 6.8. At the Fermi level the low binding energy 2DEG state is still showing a circular FS.

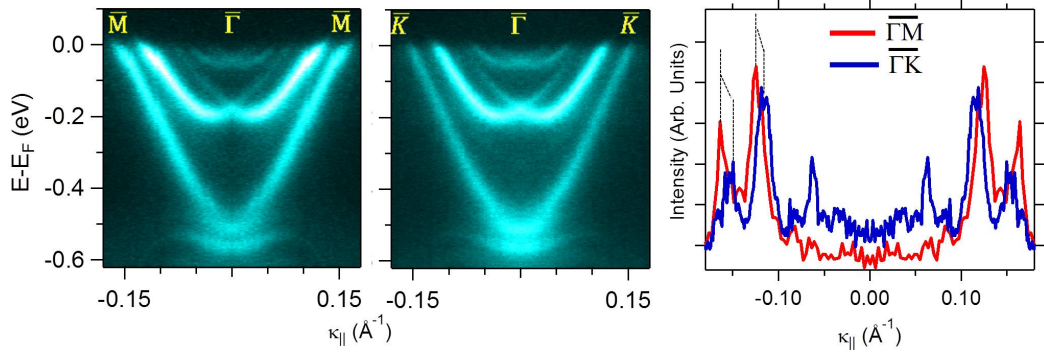


Figure 6.8: ARPES Data: Dispersion Plots - Photoemission intensity plot showing the spectral features dispersion along $\overline{\Gamma M}$ and $\overline{\Gamma K}$ directions for the 10 sec Rb doped crystal. The profiles to the right are MDCs at the Fermi level in these directions.

At this point we would like to review some literature about topological insulators exposed to different type of adsorbates. Similar to Rb deposition on Bi_2Se_3 , other adsorbate atoms, gases, and molecules were found to induce, quantitatively to some extent, the very same observations. A complete agreement on the physical origin of such new states is, however, missing. Gas adsorbates through time dependent measurements^[256] or direct dosing of CO^[257] gas was shown to induce the same effects and a “*band bending*” due to sticking of the adsorbates gases onto the “*surface*” has been proposed as their physical origin. The model reproduces all the spectral features, especially, both the hexagonal shaping of the states and the spin-orbit splitting. The same scenario has been proposed by another group with, however, differences in the sticking mechanism. They claim a “*surface chemical reaction*” between water^[258] adsorbates

6. RESULTS AND DISCUSSION IV

and surface Se atoms that induces the “*band bending*”. Atomic adsorbates, such as K^[259] (alkali metal), Ag^[260] (noble metal) and Fe^[261] (magnetic transition metal) have been also shown to induce the same effect. In case of Ag adsorbates, for example, the authors concluded that Ag atoms are “*intercalated*” into the van der Waals gaps of the crystal. As a consequence, series of trivial 2DEG states the number of which depends on the number of detached quintuple layers were observed^[260,261]. In-line with these observations a new interpretation scenario for the physical origin of the 2DEG and M states has been theoretically proposed^{3 [261]}. Instead of simulating the electronic structure of adsorbate atoms on the surface of such layered topological insulators, they rather simulate the effect of the “*van der Waals interlayer relaxation*”. The calculation reproduces all the spectral features reported in the case of Ag intercalation with, however, $\sim 36\%$ expansions in the interlayer spacing^[260]. Such high relaxation is not reported experimentally yet. In fact, a recent work on Cu^[262] atoms on top of Bi₂Se₃ has been also interpreted as intercalation-induced relaxation of the van der Waal gaps and the subsequent emergence of the new states with only 3 % expansion of the interlayer spacing, much less than the value reported by the theory. One last “*fundamental*” contradiction between different adsorbates experiments is the case of Fe^[263] deposition on Bi₂Se₃. Since the presence of time reversal invariant at the TRIMs is what protects the topological state in the first place, the Fe “*magnetic*” impurity was shown to open up an energy gap at the Dirac points agreeing with the theoretical predictions^[247,248]. It turns out that similar apparent Dirac-gaps are seen by non-magnetic adsorbates, such as CO and also the Rb deposition in this work, Fig. 6.8, raising unsolved question about the nature of such gaps.

A case example of these competing interpretations on the physical origin of the 2DEG and M-shaped states is schematically presented in Fig. 6.9. The plots are adapted from the models proposed for the surface CO^[257], as well as for the intercalated Ag^[260] induced band bending and relaxation of the van der Waals gaps, respectively. In the band bending proposal (a), an electrostatic potential near the surface can lead to a band bending of both the C.B and V.B (blue areas) and the subsequence confinement of QWSs (brown and green lines). The full electronic dispersion (see red box) is, therefore,

³Intercalation of atoms, such as Rb, Fe, etc, can be understood by diffusion through the many surface vacancies on Bi₂Se₃. Although gas intercalation does not seem obvious, it has been attributed to vertical diffusion through the same surface defects besides lateral sliding from step edges.

characterized by a single Dirac state (blue crossed lines), 2DEGs (C.B. QWSs), and M-states (V.B. QWSs). Quantitatively, in the case of CO adsorption^[257], a band bending of 450 meV was used in the model to reproduce the experimental data. Such high value allows the authors in Ref. [252]^[257], to similarly attribute the M-states to a band bending exceeding the width of the upper part of the valence band ((~ 200 meV)^[264].

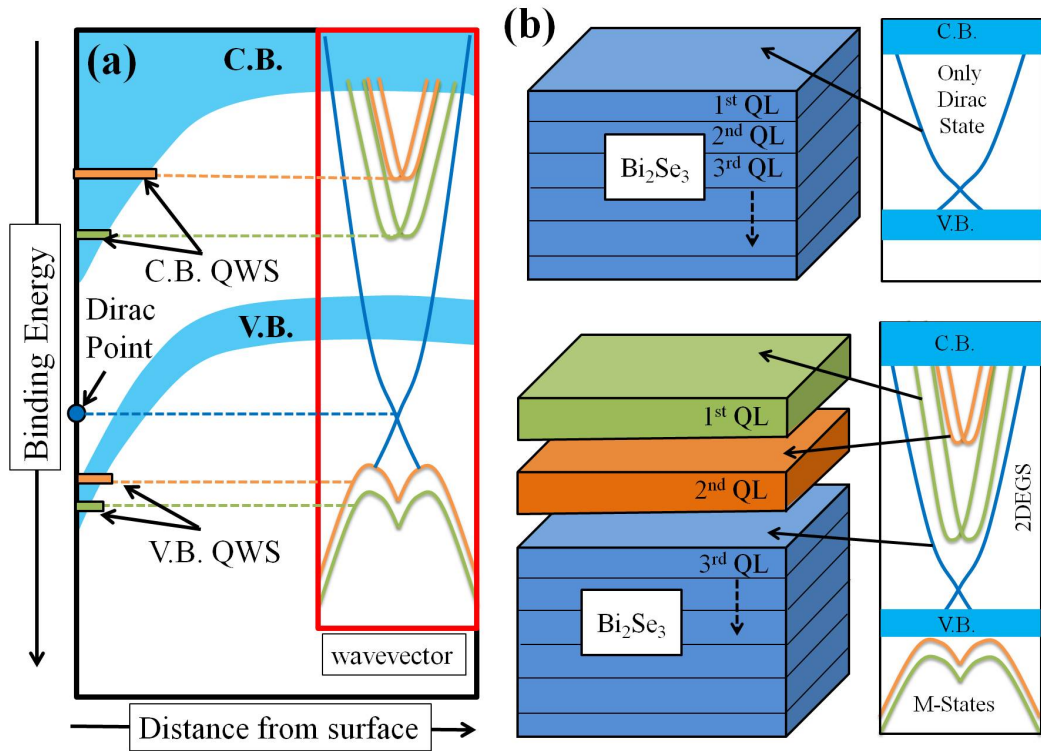


Figure 6.9: Band Bending vs. Van der Waals Interlayer Relaxation Scenarios

- (a) Schematic representation of the quantum confinement of the C.B. and V.B. states due to a band bending near the surface. The corresponding electronic surface structure is sketched inside the red box. Confined QWSs are marked by brown and green lines, whereas the Dirac state is marked by blue crossed lines. (b) Schematic drawing of the quintuple layered (QL) structure of Bi₂Se₃ (left) and the corresponding electronic surface structure (right). The top panel shows the ideal single Dirac state characteristic of the un-relaxed QL crystal, whereas the lower panel indicates the formation of pairs of 2DEGs and M-states after the relaxation of the first two QL.

In Fig. 6.9(b) the quintuple layered (QL) structure of Bi₂Se₃ crystal is sketched (left). The electronic dispersion (right) is characterized by a single Dirac state (blue

6. RESULTS AND DISCUSSION IV

lines) connecting the C.B and V.B (blue areas). For successive QLs relaxation (1st and 2nd QLs in the present case), a series of 2DEG and M-shaped states are seen (brown and green lines). Their number depends on the number of the relaxed QL layers, and the Dirac state is, accordingly, relocated below the last relaxed QL. In order to reproduce the experimental data, for Ag-intercalation case^[260], the authors used a significant expansion (typically 36 %) of the first and second quintuple layers. For further details regarding these two interpretation scenarios the reader is referred to the original publications^[257,260,261].

Back to our current experiment; a deposition of more Rb atoms (15 sec) results in broader spectra with marginally the same energetic positions for all features. Annealing to ~ 380 K only improves the quality of the spectral features. In fact, a single dose of Rb deposition of 10 sec, in a fresh $\text{Ca-Bi}_2\text{Se}_3$ crystal, shows poor quality spectra as compared to the stepwise (5+5) sec deposition, Fig. 6.10. A gradual annealing results in a sudden improvement of the features quality, close to 350 K, as seen in Fig. 6.10(c-d). This situation is different from the one shown in Fig. 6.5, where high quality features without annealing are seen for the same Rb amount. We exclude that such broaden features are due to different quality of the initial $\text{Ca-Bi}_2\text{Se}_3$ crystals as can be judged from both Fig. 6.5(a) and Fig. 6.10(a).

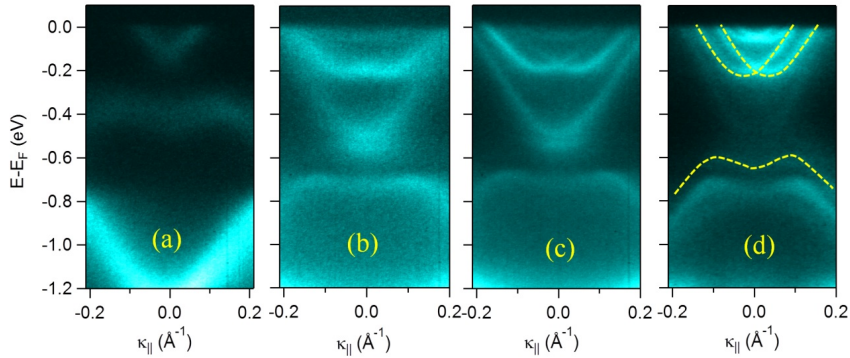


Figure 6.10: ARPES Data: Dispersion Plots - ARPES photoemission intensity plot of the surface electronic structure of (a) clean Ca-doped Bi_2Se_3 and (b) Rb-doped with 10 sec as one single dose (dosing at 190 K). (c) The same as in (b) but annealed to 350 K and cooled down to be measured at 70 K. The photon energy was 16 eV. (d) The same as in (c) but taken with photon energy of 22 eV to better visualize the induced states. The yellow dotted lines in (d) mark one 2DEG and M-state.

Here we must notice that, our LEED measurements only reveals the 1×1 spots of the bare Bi_2Se_3 crystal with no traces of any additional superstructure spots in all the cases. This will also exclude that the physical origin of the 2DEG, or M states to be due to superstructures, as reported for topologically trivial metallic surface alloys^[225,265]. One can anticipate that, the difference between the two different ways of deposition is due to a better ordering of Rb atoms in the stepwise dosing case. Annealing the sample may also result in an incorporation of Rb atoms into the crystal, re-evaporation of the excess Rb atoms, or higher ordering of the surface Rb atoms. The re-evaporation of Rb atoms is unlikely taking place since the annealing temperature is rather low. A chemical reactivity cannot also be completely excluded.

The previously mentioned conflicts in the literature, together with the annealing temperature effect in our present work raise the following questions: Does the Rb atom stick to the surface or it intercalates into the van der Waals gap? What is the physical origin of the new states in both cases? And how does the annealing temperature affects the surface and/or intercalated Rb atoms? In the following discussion we try to find appropriate answers to these questions.

The temperature-induced changes of Rb atoms on Bi_2Se_3 can be followed by monitoring the Bi $4f$, Rb $3d$ and Se $4d$ core levels. The bottom spectra in Fig. 6.11(a) shows the photoemission intensity in the appropriate binding energy regions prior to Rb adsorption. The Bi $4f$ and Se $3d$ core levels are each well described by two doublets^[266,267]; a very small minority component which can be ascribed to surface adatoms, clusters or bound impurities and a majority component ascribed to atoms in the bulk of Bi_2Se_3 . No surface core level shift for the outermost Se atoms is observed. The curve fit (black dotted lines) are superimposed on the data for both core levels (solid colored lines). The intensity ratio and separation is fixed following literature values. In each case, the position of the largest component has been highlighted by a black vertical line.

Once ~ 0.23 monolayers of Rb are adsorbed at room temperature, a clear Rb $3d$ core level is also observable. It can also be well described by two doublets with the expected separation and intensity ratio^[266,267]. The intensity of the low binding energy doublet (outlined in pink) is very weak. This component will subsequently be shown to arise from the intercalated Rb atoms and its presence immediately after adsorption suggests that a degree of intercalation occurs at room temperature. The

6. RESULTS AND DISCUSSION IV

adsorption of Rb immediately leads to a shift of the Bi and Se core level lines by 0.4 eV to higher binding energy. This is the expected behavior due to surface doping, consistent with a similar shift of the valence band features. Due to the electrostatic nature of the shift, both the Bi and Se core level lines change their position by the same amount. Except for this shift, the structure and composition of these core levels

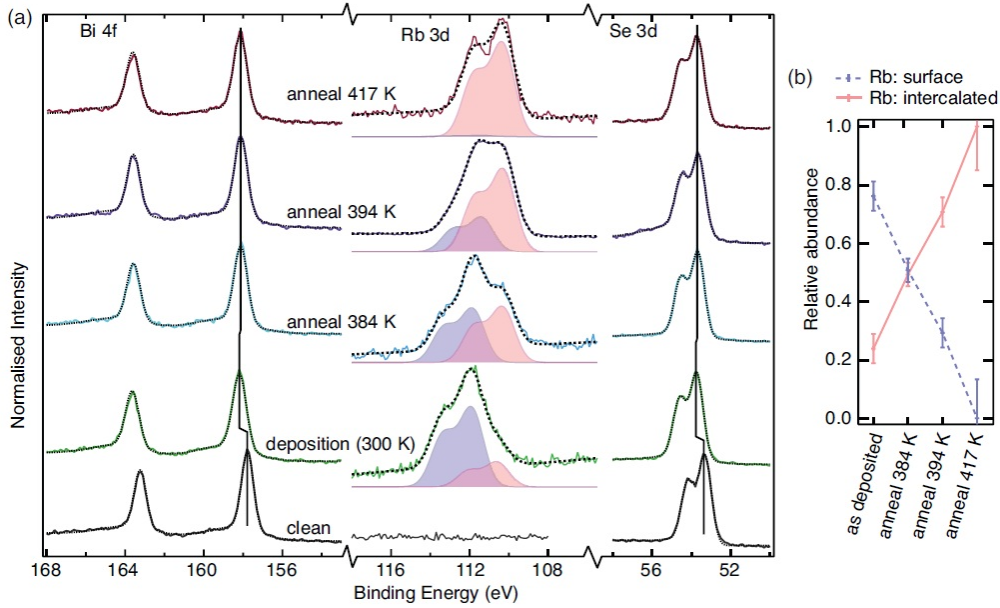


Figure 6.11: The Bi_2Se_3 Crystal - (a) Bi 4f, Se 3d and Rb 3d core levels (coloured lines) and fits (black dotted lines) of a clean surface, following deposition of 0.23 ML Rb and incremental annealing for 5 minutes at the given temperatures. The Rb 3d core levels can be fitted by two doublets that are assigned to on-surface (purple) and intercalated (pink) Rb atoms. Measurements are collected at room temperature using photon energy of 353 eV and have been normalized such that the principal components are of equal intensity. (b) The relative intensity of the surface and intercalated Rb components at selected stages of the experiment.

is essentially unchanged. Annealing the sample to increasingly higher temperatures leads to the following changes in the spectra: the low binding energy doublet in the Rb 3d peak strongly increases at the expense of the high binding energy doublet (surface contribution), Fig. 6.11(b). We interpret this as caused by the conversion of on-surface Rb atoms to Rb atoms intercalated below the surface, most likely in the van der Waals gaps between quintuple layers. After annealing to 417 K only the low binding energy

doublet is observed, suggesting that almost all Rb atoms are now found below the surface. The relative intensity of the Rb $3d$ core level with respect to Bi $4f$ and Se $3d$ is also decreasing during the annealing. This decrease is also consistent with Rb intercalation. A final small change during annealing is a small reversal of the initial doping: the Bi $4f$ and Se $3d$ peaks move slightly back to smaller binding energies, as seen by following the solid lines that mark the position of the highest peak.

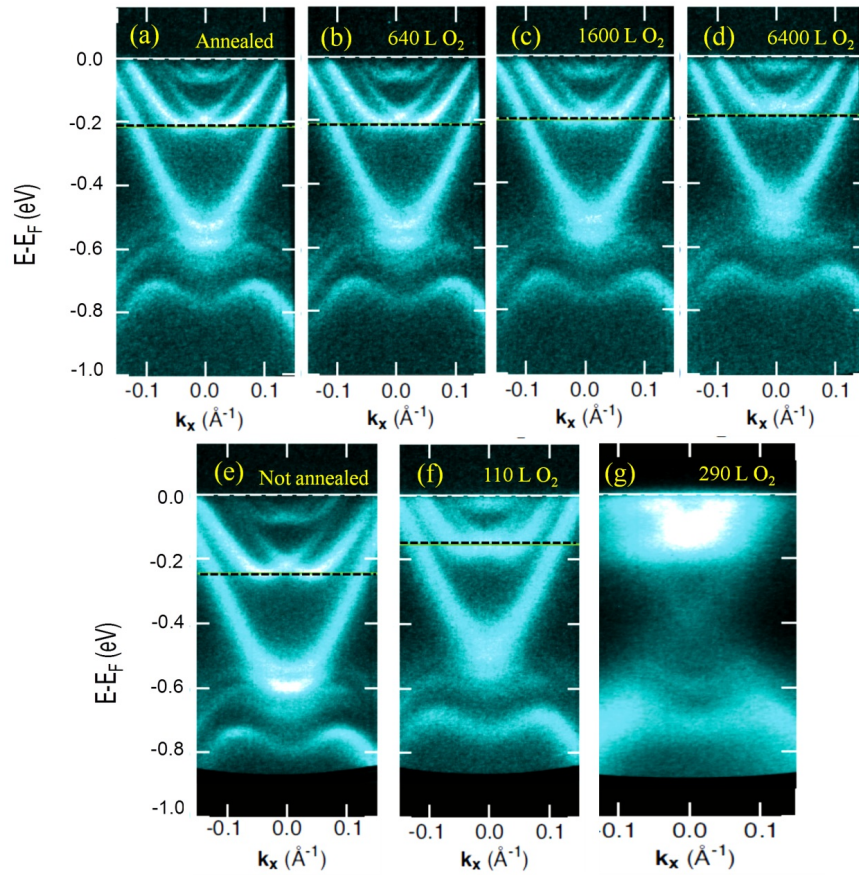


Figure 6.12: ARPES Data: Oxygen Exposure Test - ARPES measurements of Ca-doped Bi_2Se_3 (a) after Rb deposition at 190 K and annealing to 350 K and (b), (c) and (d) following exposure to 640 L, 1600 L and 6400 L of O_2 , respectively. (e) A similar sample after a similar deposition of Rb at 190 K, but without subsequent annealing and (f) and (g), the same not-annealed sample following exposure to 110 L and 290 L of O_2 respectively. Data are collected at 70 K using photon energy of 16 eV.

Although the effect of Rb intercalation is very pronounced in the core levels, it hardly affects the electronic structure in the valence and conduction bands. Both

6. RESULTS AND DISCUSSION IV

ARPES data for the as deposited Rb, Fig. 6.10(b) and the 350 K annealed samples, Fig. 6.10(c), looks the same (apart from the broader features in the former) suggesting that intercalation has almost no effect on the reported surface electronic structure as well as the doping induced downward shift for all spectral features. The intercalation of Rb atoms, however, is preferred compared to the surface adsorbed ones. In fact, the annealed Rb doped samples was shown to be, in contrast to the LT deposition, more robust when kept for quite long time in the main chamber at 60 K. This is further demonstrated by intentional exposure of both as-deposited and annealed samples to molecular oxygen. Following Rb deposition and annealing (in this case to 350 K), a surface doping (Dirac point is shifted to ~ -0.65 eV) is observed, but little changes following increasing O_2 exposure. After 6400 L of O_2 exposure, the doping is marginally reduced (Dirac point is found at ~ -0.60 eV), but neither the 2DEGs nor the topological surface state are significantly degraded, Fig. 6.12(a-d). Conversely, a similar experiment in which Rb is dosed at 190 K and not annealed reveals that the surface is quickly degraded following O_2 exposure; already after ~ 300 L, the conduction band quantum well states are barely discernible, Fig. 6.12(e-f). Therefore, the intercalation of Rb, interestingly, results in a very stable situation, something that is important for potential applications. The strong doping of the surface apparently leads to a saturation of the downward band bending so that the surface remains stable over long periods of time. Similar saturation effects have also been reported for K^[259] adsorption on Bi_2Se_3 at low temperature. In our case, however, it is not only the band bending that remains stable but the intercalation also leads to a chemical and thermal stability of the doped surface, simply because the reactive dopants are removed from direct contact with the environment. The above conclusion is, therefore, of obvious importance. For practical (environmental) applications, the stability of the intercalated atoms over long enough period of time is also required. Old studies on Bi_2Se_3 intercalated with hydrazine, for example, reported a time dependent de-intercalation^[268]. The rate of the de-intercalation was, however, much longer (60 days) compared to the simultaneous intercalation process. Whatever was the property of the intercalated Bi_2Se_3 involved in specific device, the de-intercalation rate has to be as slow as possible. We can speculate that this will be the lifetime limitation for working devices based on the stability of intercalated topological insulator. For most of the recently reported intercalated atoms on topological insulators, we are not aware of measurements for long enough aging to

allow observation of de-intercalation. A combined intercalation/de-intercalation agents (temperature, passivation, etc) might be the switch on/off gates for such devices.

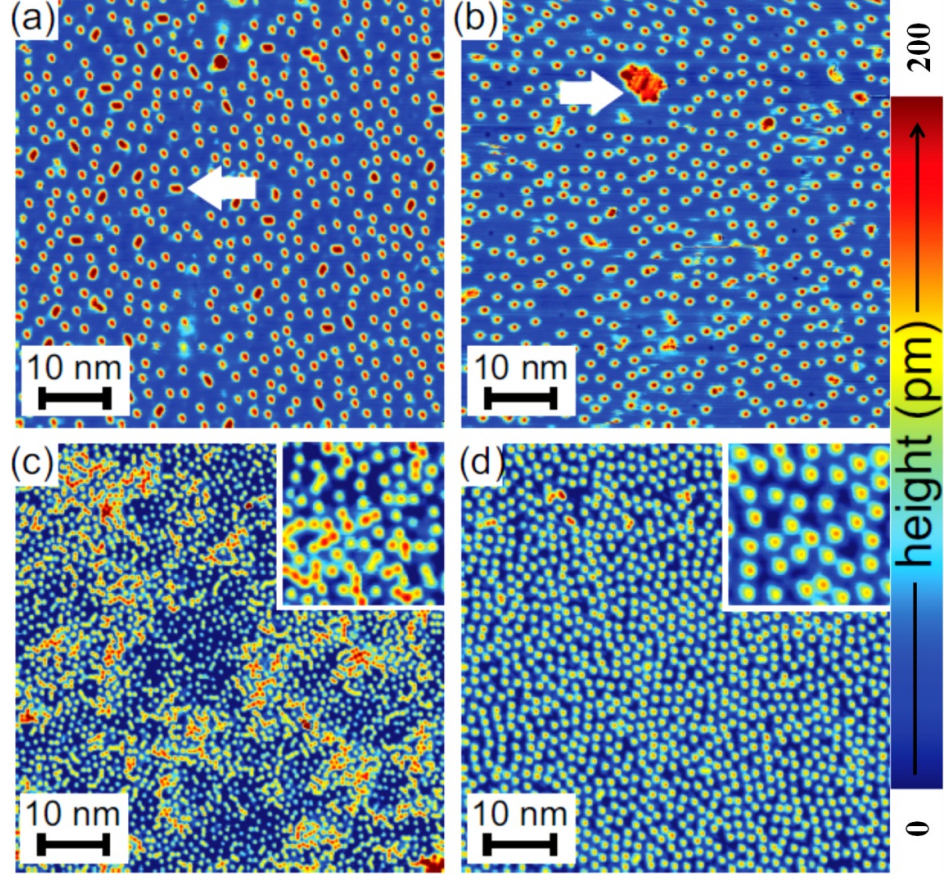


Figure 6.13: STM Topographs - (a,b) STM topographs of 0.025 ML Rb on Ca-doped Bi_2Se_3 before (a) and after (b) annealing at 400 K for 10 min. After annealing the on-surface Rb coverage is reduced by 20 % (b). Arrows: see text. (c-d) Corresponding data for an initial coverage of 0.12 ML Rb before (c) and after (d) annealing. After annealing the on surface Rb coverage is reduced by 60 % (d). The insets (10 nm \times 10 nm) show magnified views of the samples. (Tunneling parameters: $V = 1$ V, $I = 15$ pA, measurement temperature = 1.2 K.).

To further confirm the annealing induced intercalation of Rb atoms and its driving force we present a temperature and Rb coverage dependent STM measurement, shown in Fig. 6.13. Two different Rb coverages are investigated before and after annealing to 400 K for 10 min. The low/high Rb coverage (0.025 ML⁴/ 0.12 ML) is shown in Fig.

⁴The surface coverage of Rb was determined by the relative intensity of Rb and substrate core level

6. RESULTS AND DISCUSSION IV

6.13(a,c) for the as-deposited Rb and in Fig. **6.13**(b,d) for the 400 K annealed samples. In all samples the major features are single, well separated Rb atoms, which appear as circular protrusions with a height of ~ 150 pm. For the sample covered with 0.025 ML Rb a few dimers are visible before annealing (see arrow in (a)) and after annealing some clusters are formed most probably from residual gas adsorption (see arrow in (b)). In this low coverage region, the on-surface Rb atoms are reduced by only 20 % and the dimers have disappeared. The high Rb coverage, however, exhibit much stronger change in coverage and re-distribution of the on-surface Rb atoms upon annealing.

We found (before annealing) a distribution of well separated Rb atoms with an increase in the apparent height in areas of locally higher coverage, probably due to charge accumulation effect. After annealing, the coverage of the on-surface Rb atoms is strongly reduced to 0.05 ML (Fig. **6.13**(d)) indicating that 60 % of Rb atoms have diffused into the bulk. We exclude a re-evaporation of Rb atoms with annealing, since the core-level findings for similar Rb coverage confirmed fixed total (surface + intercalated) Rb atoms. With STM, we also notice that the distribution of the remaining on-surface Rb atoms is much more homogeneous after annealing. The enhanced tendency for intercalation at higher coverage, as well as the trend for a more uniform distribution of the Rb atoms after annealing, can both be ascribed to the strong Coulomb interaction between the Rb atoms that are highly ionic due to a charge transfer to the bulk. While we do not directly see that the disappearing Rb atoms are intercalated into the van der Waals gaps between the quintuple layers making up the Bi_2Se_3 structure, this appears very likely due to its weaker bonds compared to any other bonds through the entire structure. This also is in favor with the fact that intercalation processes were achieved during the bulk crystal growth or using electrochemical methods, and hence known for a long time.

So far we have shown that the “*surface*” Rb atoms and, therefore, the subsequent formation of band bending are the main physical origin of all the spectral features and changes; the “*intercalation*” only increases the stability of these features. Discarding the intercalation and the subsequent relaxation of van der Waals gaps as a source of such spectral feature formation is, however, not completely ensured. The reason is that, the as-deposited sample in our case has a tinny contribution from intercalated

lines. It is given in monolayers (ML), i.e. relative to the number of Se atoms in the first layer.

Rb atoms, as seen from Fig. 6.11. Since there is no criterion concerning the amount of intercalated adsorbates capable of relaxing the van der Waals gaps, such relaxation is possible.

Adsorbates	Dirac point (eV)	First 2DEG (eV)	ΔE (eV)	Ref.
Rest gases	0.51	0.19	0.32	[251] ^[256]
CO	0.56	0.20	0.36	[252] ^[257]
H ₂ O	0.58	0.24	0.34	[253] ^[258]
Rb1	0.56	0.20	0.36	Present ^[269]
K	0.68	0.32	0.36	[254] ^[259]
Ag	0.50	0.18	0.32	[255] ^[260]
Cu	0.48	0.17	0.31	[265] ^[270]
Fe	0.57	0.21	0.36	[257] ^[262]
Cs	0.70	0.33	0.37	[266] ^[271]
Gd	0.52	0.21	0.32	[266] ^[271]
Rb2	0.60	0.27	0.33	[266] ^[271]

Table 6.1: Survey on the 2DEG and M-States - Binding energy of the topological state's Dirac point and the first 2DEG state for different adsorbates on top of Bi₂Se₃ reported in literature. The energy different between the Dirac point and the 2DEG state is also included.

Next, we quantitatively compare our results on the Rb doped samples to other adsorbates reported in recent literatures. Table 6.1 summarizes the energetic position of the Dirac point (E_D) and the first 2DEG state (E_{2DEG}) for different adsorbates on Bi₂Se₃. The difference in energy (ΔE) between E_D and E_{2DEG} is also tabulated. We notice that, the band minima saturation for these features is slightly different. This can be due to different quality of the samples, different doping strength by different adsorbates, and some differences in the measurements temperature. We also note that, the tabulated values are estimated from the intensity plots in their original articles, if not declared in the text, which adds extra uncertainty to these values. What is remarkable, however, is that the energy different between the Dirac points and the first 2DEG states (ΔE), within the error limits, is independent on the adsorbates, neither the sample quality nor the measuring temperature, where a value of $\Delta E = (0.34 \pm 0.03)$ eV is estimated. This finding suggests that the observed modifications

6. RESULTS AND DISCUSSION IV

Experimental Observations	Band Bending		Relaxation	
	Likely	Unlikely	Likely	Unlikely
Rb atoms stay on the surface ^[269]	✓			✓
Atoms incorporate inside the bulk ^[260,261]	✓		✓	
Many adsorbates induce similar effect ^[256-262]	✓		✓	
Water induced surface chemical reaction ^[258]	✓			✓
M-states on Bi ₂ Te ₃ ^[272]		✓	✓	
No 2DEG or M states on TiBiSe ₂ ^[260]		✓	✓	
36 % expansion of van der Waals gaps ^[260]				✓
Gases induce similar effect ^[256,257]	✓		✓	

Table 6.2: Band Bending vs. van der Waals Relaxation - Summary of the experimental evidences discussed in the text and the current weakness and strength of the band bending and van der Waals relaxation scenarios.

of the near surface electronic structure are, mainly, decided by the Bi₂Se₃ crystal. For Bi₂Te₃ crystal, a different ΔE value (0.4 eV) was estimated after N₂ gas exposure of Bi_{2.6}Se_{0.4}^[272]. There, the Bi₂Te₃ was also found to show series of M-shaped states upon exposure to N₂ or air, in disagreement with the band bending scenario that restricts the M-states formation in Bi₂Se₃ to its special valence band structure^[257,272]. A recent study, in favor of the relaxation-induced such electronic changes, has compared the intercalated Ag atoms on Bi₂Se₃ to on-surface Ag atoms on top of TiBiSe₃ which has similar surface structure as Bi₂Se₃ but with, however, no van der Waals gaps^[260]. They observed the 2DEG and M-states only for Bi₂Se₃ where the Ag atoms are intercalated, the finding of which disagrees with our band bending interpretation. A summary of the weaknesses and strengths of both band bending and quintuple gap relaxation scenarios is presented in table 6.2.

6.4 Conclusions:

In summary, we have shown that deposition of Rb atoms on Bi₂Se₃ results on drastic changes on the near surface electronic structure. In particular, series of spin-orbit split 2DEG and M-states were found. The core-level photoemission study allowed us to propose a band bending induced by surface adsorbed Rb atoms as the main physical

origin of these new states. The same study for the annealed sample indicates that Rb atoms intercalate into the crystal with the same surface electronic structure obtained by the surface Rb. Although, our findings most likely point toward surface atoms inducing band bending, the relaxation of van der Waals layers proposed by other groups cannot be completely discarded. The intercalated Rb atoms were of particular importance due to the extreme stability of all the electronic features, even after progressive exposure to molecular oxygen, pointing toward environmental applications.

6. RESULTS AND DISCUSSION IV

7

Summery

The present work is focused on the dislocation network that spontaneously arises after room-temperature deposition of a single monolayer of Ag on the Cu(111) surface. For such system, the interaction between the surface state and the superstructure leads to a highly featured Fermi surface, namely a surface band structure with gaps at the Fermi energy and at high symmetry points (\bar{M} and \bar{K}).

We investigated the possibility of further tuning the 1 ML Ag surface state dispersion, by depositing Ag monolayer on three different substrates. These are, the “*alloyed*” Au/Cu(111), the “*vicinal*” Cu(111), and the “*magnetic*” Cu/Ni(111). The characteristic surface state in such cases were found to significantly change from the gaped surface state of the 1 ML Ag on top of “*clean*”, “*flat*”, and “*non-magnetic*” Cu(111).

* In Au/Cu(111) we observed the Shockley-type surface band shifting rigidly towards higher binding energies. The size of this shift could be tuned by both the Au coverage and the annealing temperature. We obtained a maximum of (~ 140 meV) downward shift for 0.67 ML Au annealed to 600 K. The size of the shift is unexpected from a simple Cu-to-Au surface state transition. Instead, it can be explained as due to the moiré corrugation of the alloyed interface, as determined by a phase accumulation model analysis. The surface state of the 1 ML Ag on top of such tunable Au/Cu alloy was found to shift accordingly towards higher binding energy, without significant broadening of its spectral features. Consequently, we were able to relocate the \bar{M} -point gap below the Fermi level, leading to a complete “*Lifshitz transition*”.

** In the step superlattice of a vicinal Cu(111) substrate [v-Cu(111)], we measured,

7. SUMMERY

firstly, the magnitude of the step potential using a curved crystal. We obtained a 1.2 eV.Å barrier strength, in contrast to the 0.6 eV.Å value of the highly “*transparent*” Ag step, obtained in both v-Ag(111) and 1 ML Ag/v-Cu(111). For 1 ML Ag/v-Cu(111) step and dislocation superlattices gaps were found to coexist and interplay in a complex way, giving rise to a textured Fermi surface that was well explained with a plane-wave band structure calculation.

*** In Cu films on Ni(111) we analyze surface states prior and after Ag capping. For Cu thicknesses > 3 ML, the gapped surface state characteristic for 1 ML Ag/Cu(111) is recovered. However, a likely “*spin-orbit-split-like*” surface state is observed, with a spin orbit coupling strength that varies with the Cu film thickness. Such unusual spin-orbit-split surface state is attributed to the atomic roughness of the Cu film when compressed to match the Ni lattice parameter. We also discussed an alternative explanation, where the hybridization between the surface/interface states and bulk bands could induce similar states.

In the last chapter of the thesis we briefly investigated the effect of Rubidium (Rb) deposition on the stability and electronic structure of a typical “*topological insulator*” crystal, namely Bi_2Se_3 . A number of 2D electron gas (2DEG) and M-shaped states were identified following the Rb deposition. Intercalating the Rb atoms by annealing was shown to render a extremely robust surface electronic structure, which survives after progressive exposure to oxygen.

Appendix A

Noble Metals and Surface States

In this appendix, some basic information about the bulk noble metals (Copper, Silver, and Gold) and the corresponding low-index surfaces will be given. The surfaces to be highlighted here are the (111) oriented surfaces. The crystallographic structure as well as the Brillouin zone for both the bulk and surfaces of the three noble metals will be given in section I. The bulk band structure as well as the shape of the Fermi surface of the three noble metals will be discussed in section II. Since the main concern of the thesis is the investigation of the surface states on nanostructured noble metal surfaces, an introduction to surface states, their origin, classification, etc, will be stated in section III. In particular, the dispersion of the Shockley surface states for the clean flat (111) noble metal surfaces as well as their Fermi surfaces will be included in section IV. The combined phase accumulation model and the two-band theory commonly used for surface and quantum well states calculations will be briefly discussed.

I. Crystallographic Structure of Noble Metals: Bulk and Surface

The noble metals Cu, Ag, and Au all have the face centered cubic (“*fcc*”) crystallographic structure. Figure A.1 shows the real space unit cell of an *fcc* lattice^[273]. The atomic arrangements on a different low-index *fcc* crystal surfaces, i.e. (100), (110), and (111) are also shown in Fig. A.1. The (111) surface of Cu undergoes a relaxation at the crystal plane (from 0 to 4 % relaxation), Ag does not undergoes any relaxation, and

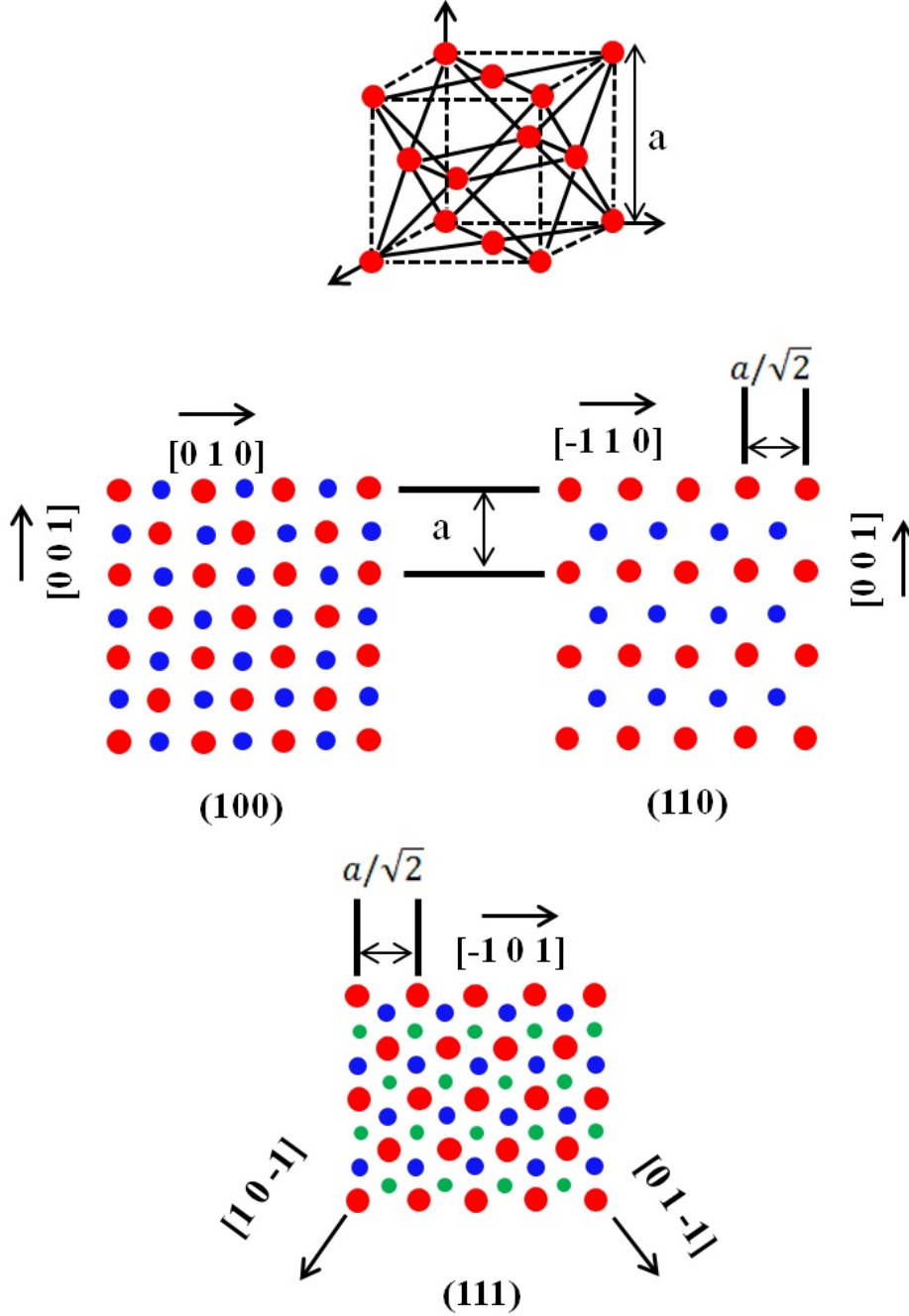


Figure A.1: Crystal Structure: *fcc* Lattice - The unit cell and the (100), (110), and (111) surfaces of an ideal *fcc* crystal. The red circles represent atoms in the surface layer, the blue circles are atoms in the second layer, and the green circles are atoms in the third layer. The nearest neighbor atoms in the unit cell are shown connected by solid lines. Adapted from Ref. [268]^[273].

the Au(111) surfaces undergoes a reconstruction^[274], commonly known as “*herringbone reconstruction*”^[142].

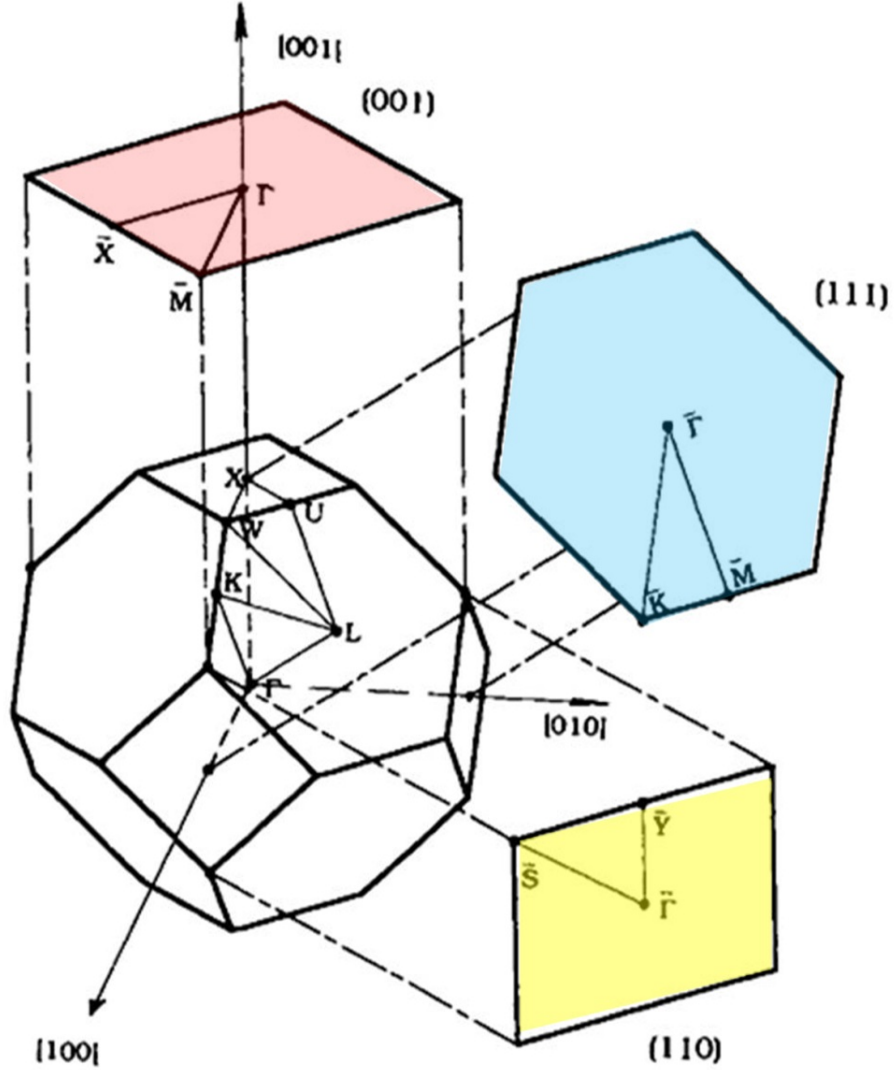


Figure A.2: Brillouin Zone: *fcc* Lattice - First Brillouin zones for the bulk, (100), (110), and (111) planes of *fcc* crystal. Adapted from Ref. [268]^[273].

In the present work we are only interested in the (111) oriented surfaces, and their lattice parameters are given in table A.1. The reciprocal space Brillouin zone (BZ) of bulk *fcc* crystals is known to be a body centered cubic (“*bcc*”)^[22–24] and is also shown in Fig. A.2. The symmetry points are indicated on the graph. The projected surface

A. NOBLE METALS AND SURFACE STATES

Brillouin zone (SBZ) for the three (100), (110), and (111) surfaces are included as well. The three high symmetry points for the (111) surfaces are also indicated in the graph, these are $\bar{\Gamma}$, \bar{M} , and \bar{K} points. The reciprocal space unit cell parameters are given in table A.1.

	a_o (Å)	d (Å)	$a_{1\times1}$ (Å)	$\bar{\Gamma}\bar{M}$ (Å ⁻¹)	$\bar{\Gamma}\bar{K}$ (Å ⁻¹)
		$\frac{a_o}{\sqrt{3}}$	$\frac{a_o}{\sqrt{2}}$	$\frac{2\pi}{\sqrt{3}}a_{1\times1}$	$\frac{4\pi}{3}a_{1\times1}$
Cu(111)	3.61	2.084	2.55	1.423	1.643
Ag(111)	4.09	2.361	2.89	1.255	1.449
Au(111)	4.08	2.355	2.88	1.259	1.454

Table A.1: Lattice Parameters: Noble Metals - Crystallographic parameters of the three (111) noble metal surfaces. a_o is the bulk lattice parameter, d the interlayer spacing, and $a_{1\times1}$ the surface lattice parameter. $\bar{\Gamma}\bar{M}$ and $\bar{\Gamma}\bar{K}$ are the momentums at the edge of the SBZ, as defined in Fig. A.2.

II. Fermi Surface and Band Structure of Bulk Noble Metals

The surface states on the (111) oriented noble metal surfaces, to be discussed in section III, are confined in the projected L -band gap of the bulk metal. There are many theoretical calculations^[70,275–282] for the bulk band structure of noble metals which show good enough agreements with the experimentally measured ones, especially for the case of Cu. These calculated band structures are shown in Fig. A.3 for Cu, Ag, and Au¹. The three noble metals do have, qualitatively, similar band structure close to the L -point. Therefore, the discussion here will be focused on copper and the generalization to the other noble metals is straightforward. The symmetry points of special interest for the *fcc* noble metals are: Γ (the center of the BZ), X (the midpoint of the diamond square of the BZ boundary), L (the center of the hexagonal BZ boundary), and K (the midpoint of the edges) as sketched in Fig. A.2.

Figure A.4(a) shows a closer view at the sp -inverted gap located at the L -point. All the three noble metals have the inverted gap character and, therefore, the occurrence of Shockley surface states inside such projected band gap, shown in Fig. A.4(b), is

¹The calculated band structures presented here are obtained using ELAN 1.0 Energy Level Analyzer software, developed by V. Joco.

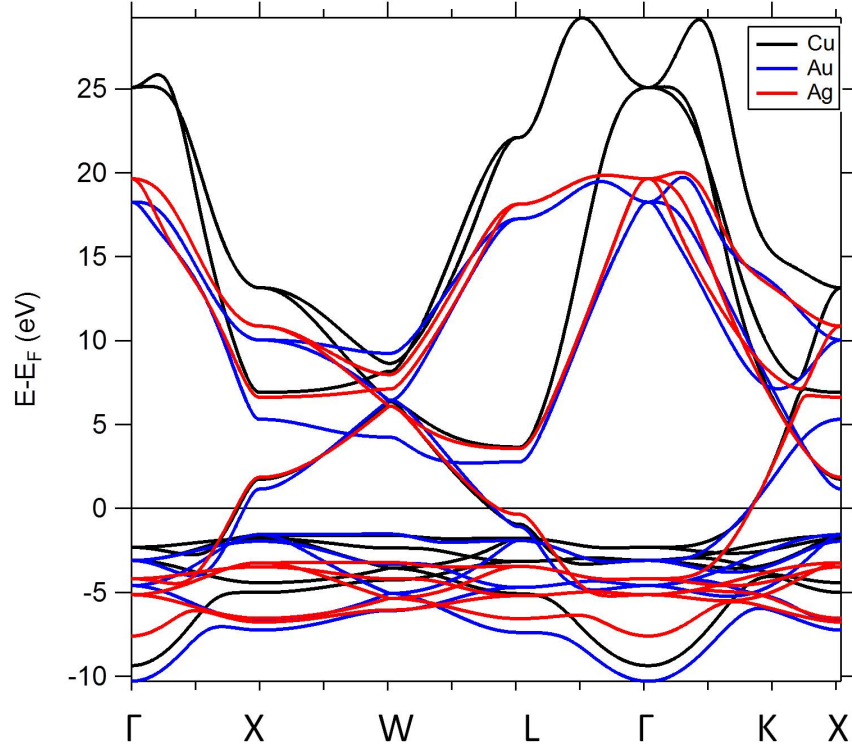


Figure A.3: Bulk Band Structure: Noble Metals - Calculated band structure of Cu (black), Au (blue), and Ag (red) along the various symmetry axes on the BZ.

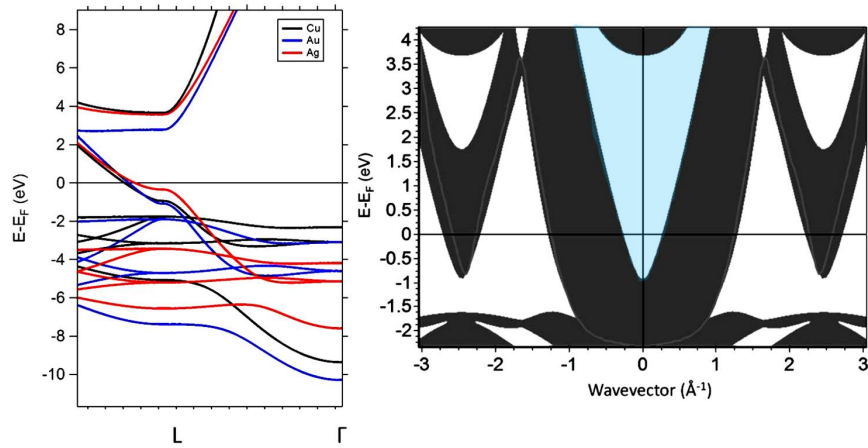


Figure A.4: Projected Bulk Gap: Cu(111) - (a) Zoom in the band structure shown in Fig. A.3., close to the *sp*-inverted gap at the *L*-point. (b) The projected bulk band gap of Cu on the (111) surface. The Shockley surface states as well as the image potential states, discussed in section III, are confined in the blue shaded area.

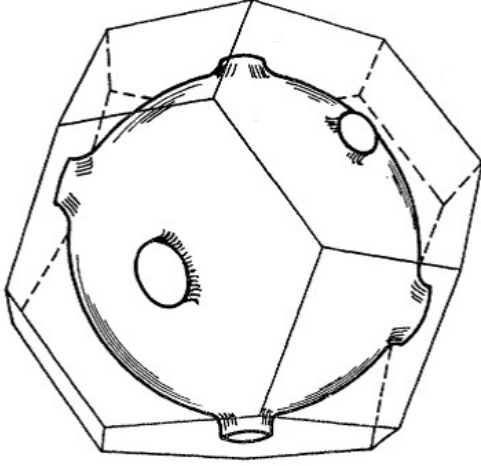


Figure A.5: Fermi Surface: Copper. A sketch of the Fermi surface of Cu. The polyhedron represents the BZ. Adapted from Ref. [270]^[275].

possible^[96]. Clearly seen, the sizes of the L -gaps are different for the three noble metals. More importantly, the energetic position of the lower edges of the L -gap ($L_{2'}$) is different, where it is close to the Fermi level for Ag than for Cu and Au. The d -bands for all the three noble metals are not so far below the Fermi energy. In case of Au and Cu they are degenerate and have, nearly, the same energy at the L -point, rendering it difficult to make an estimation of the Au or Cu coverage on top of their alternative substrates. The d -band of Ag, however, lies at different energy as compared to Au and Cu and, therefore, an estimation of the Ag coverage on top of these substrates is possible via the d -band analysis.

Within the free-electron model, the Fermi surface of an fcc structure and one conduction electron per atom, as for Cu, is a sphere with a volume equal to half the volume of the BZ and is, therefore, completely contained within the BZ without touching its surface. Different experimental observations, however, suggested that the Fermi surface is distorted from being a sphere and it is multiply-connected. The shape of such Fermi surface for Cu, is, therefore, significantly different from the free-electron Fermi surface, as shown in Fig. A.5. This shape was first established in the history of Fermiology by Pippard^[283] and it can be deduced from the band structure calculation shown in Fig. A.3. A Fermi level crossing takes place in three different momentum regions; between the L and W -point, between the Γ and X -point, and between the Γ and K -point. The crossing in the L - W direction indicates that each BZ are connected by a tube with a radius (neck) equal to the k -distance from the L to the Fermi level crossing in the direction towards W . The crossings in the Γ - X and Γ - K directions,

on the other hand, have a slight difference in the k -distance between these crossing and the Γ -point and thus represent two spheres with different radii (belly). Since all the mentioned features have the same origin (the sp -state) these features must be connected^[94]. Therefore, the final shape of the Fermi surface can be described as distorted spheres (the belly close to X and K -points) connected by tubes-like features (the neck at the L -point), as shown in Fig. A.5 and Fig. A.6.

The Fermi surfaces of Ag and Au are, in principle, similar to Cu with, however, different neck and belly values, as shown schematically in Fig. A.6, and quantitatively given in Ref. [279,280]^[284,285]. One sees that the distortion from the free-electron spherical Fermi surface (dotted lines) is much less in Ag as compared to Au and Cu.

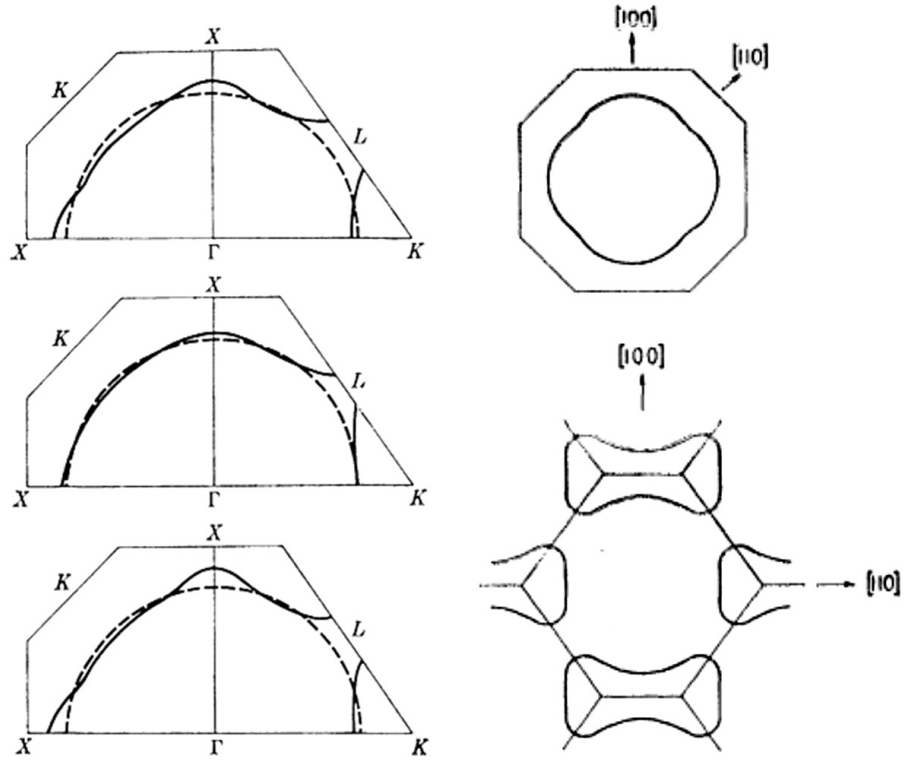


Figure A.6: Fermi Surface: All Noble Metals - (Left) Illustration of the relative distortions of the Fermi surfaces of (top) Cu, (middle) Ag, and (bottom) Au. Adapted from Ref. [70,281]^[70,286]. (Right) Top: (100) cross-section of the Fermi surface showing the belly; Bottom: (110) cross section showing the necks. Adapted from Ref. [270]^[275].

The differences between the three noble metals, especially at the L point, are

strongly reflected on the energetic position of their Shockley surface state of (111) oriented surfaces. This issue is explained in the following sections.

III. Electronic Structure of Surfaces: Surface States

The basic of electronic states theory in solid state physics is the Bloch theorem^[287] which takes advantage of the fact that atoms in a crystal are periodically located. In other words, the crystal potential has a translational invariance^[25]. This assumption can only exist in crystals of infinite size. The solution of Schrödinger equation for such periodic potential yields electronic states that are extended over the whole crystal. These are called “*bulk states*” and their energy dispersion relation is in the form of continuous energy bands separated by energy gaps in some regions in the momentum space^[66]. The gaps appear because of the splitting of the energy bands at the Brillouin zone boundaries and their size is about twice the magnitude of the second Fourier component of the crystal potential [3-6,25]^[22-24,76,142]. For surfaces- or generally finite systems- the translational invariance perpendicular to the surface is broken. The solution of Schrödinger equation in such cases results in new states, generally called “*surface states*” (and/or “*surface resonances*”) and their energies lie on the gaps of the bulk states^[26]. Those surface electronic states were first postulated in 1932 by Tamm^[27] who studied the problem of 1D semi-infinite potential well with a delta-function periodic potential^[288]. Later on, Shockley^[28] showed that the surface states found by Tamm were due to an incompleteness of the potential at the surface. Tamm and Shockley states are caused by a changed potential or by finiteness of the lattice, respectively. Another distinction is based on the sense that, Tamm states are tight-binding type surface state and should be localized while Shockley states are free electron type^[289]. In general, one can consider surface states as a 2D analogue of the shallow and deep defects levels in semiconductors. The surface states have properties which are quite different from their bulk counterpart and, moreover, due to their 2D nature they are also distinct from most other defects levels^[10]. Practically, and because of its confinement to the surface region, the existence of surface states were found to have a pronounced influence on the physical and chemical properties of surfaces. Such effects was first observed for semiconductor surfaces, where the existence

of surface states has been postulated to explain phenomena like the band bending effect, Schottky barrier formation, etc^[10]. On metal surfaces, however, and due to the more complicated nature of metallic bonding, the relationship between the electronic structure and other surface properties was not that obvious. Therefore, the connection between the presence of metallic surface states and the observed surface properties, such as dipole layer formation, dynamical properties, chemical reactivity, etc was one of the most important goals of surface physics.

The possible types of electronic states that may occur at the surface of a perfect crystal are summarized in Fig. A.7. The first obvious ones are the bulk states which are extended to the surface region and reflected back by the vacuum barrier. Such states have periodically varying amplitude through the crystal and match the free electron states in the vacuum. The second type are the surface states which only exist at the surface and have an exponentially decaying wavefunction both in the direction into the solid and the vacuum. These states are restricted to regions where no bulk states of the same symmetry and quantum numbers are allowed otherwise it will mix with the bulk states and becomes a surface resonance. Surface states, although confined on the surface regions they are periodic in the two dimensions parallel to the surface where the translational invariance is not broken. The third type is “*vacuum states*”, which cannot be matched in energy and momentum to a crystalline wavefunction in the interior, are present in the surface as evanescent states. These states contribute a large amount to the photoemission process and they are responsible for the usually observed background signal^[10]. A different type of surface states is what is called “*image potential states*”. Those can be understood by considering an electron in front of a metal surface. The screening properties of the metal can be described by a positive image charge inside the metal which has an attractive Coulomb interaction with the electron in front of the surface, Fig. A.8(a). Such potential can support unoccupied bound states with energies above the Fermi energy but below the vacuum energy, Fig. A.8(b). This means that image potential states can be populated but the electrons in these states cannot leave the solid^[76,77]. In the criterion developed by Echenique and Pendry^[29] based on the phase accumulation model, the image potential states are classified as a barrier induced states, where the Shockley and other surface states are classified as a crystal induced states.

A. NOBLE METALS AND SURFACE STATES

In the following, we discuss the use of Echnique and Pendry model and its impact to the surface and image potential state on the (111) oriented noble metal surfaces updated by V. Smith^[98]. We also show some experimental measure of them, by angle resolved photoemission (ARPES).

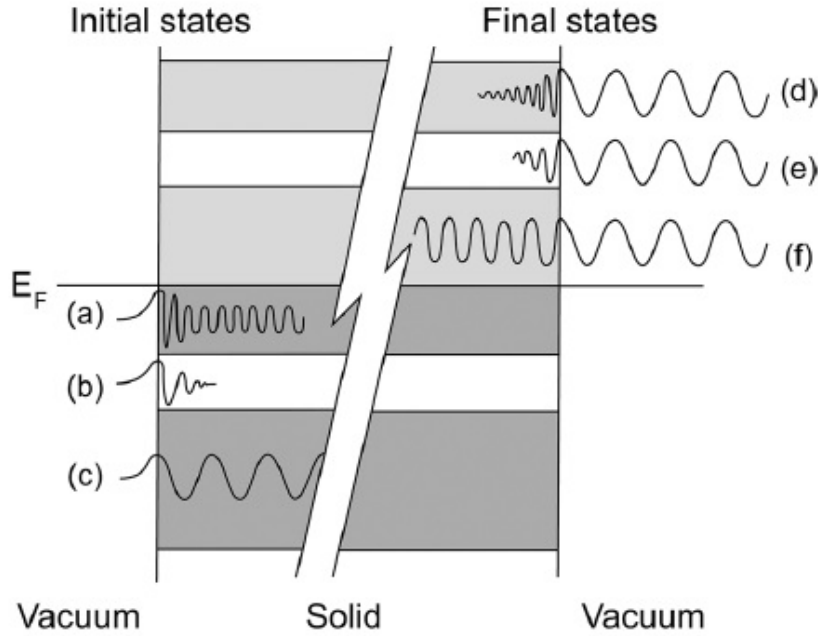


Figure A.7: Types of Surface States - Initial (left) and final (right) wavefunctions for the semi-infinite crystal. (a) Surface resonance; (b) Shockley surface state; (c) bulk Bloch state; (d) surface resonance above the Fermi level; (e) in-gap evanescent state; and (f) bulk Bloch state above the Fermi level. Taken from Ref. [77]^[77].

The criterion developed by Echenique and Pendry^[29] on the possible existence of surface and image states is based on the multiple reflection theory. The essence of this multiple-reflection approach is illustrated in Fig. A.9. The crystal potential is chosen to terminate at some plane, beyond which the potential will be a barrier like and must have an asymptotic image form. Due to the presence of the bulk gap, the electrons will be reflected at both the vacuum barrier ($r_B e^{i\phi_B}$) and the crystal gap ($r_C e^{i\phi_C}$). Therefore, bound surface states (crystal and/or barrier induced) occur when;

$$\phi_B + \phi_C = 2\pi n, \quad (\text{A.1})$$

where ϕ_C and ϕ_B are the crystal and barrier phase changes, respectively, and n is an

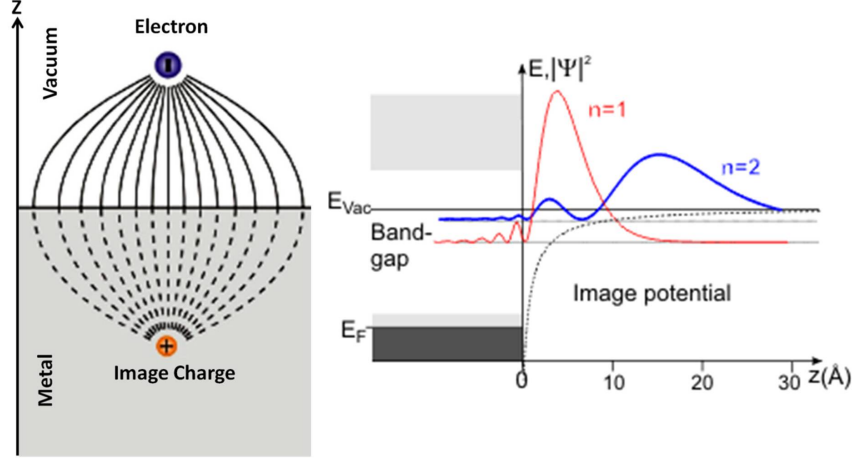


Figure A.8: Image Surface States - (a) Electric field potential energy diagram of an electron in front of a metal surface ($z=0$). (b) The potential well formed by band gap and the Coulomb tail leads to a series of discrete hydrogen-like electronic states that extend into the vacuum ($z>0$). The squares of the wave functions of the lowest three states are shown in (b) as well. Taken from Ref. [285]^[290].

integer number. Both ϕ_C and ϕ_B and their explicit energy dependence are, therefore, required to obtain the energy spectra of the induced states. Expressions for ϕ_B in the case of abrupt step- and image-potential barrier may be written, respectively, as;

$$\frac{\phi_B}{\pi} = \sqrt{\frac{3.4eV}{E_V - \varepsilon}} - 1, \quad (\text{A.2})$$

and,

$$\tan\left(\frac{\phi_B}{2}\right) = -\sqrt{\frac{E_V - E}{\varepsilon}}, \quad (\text{A.3})$$

where E_V is the vacuum energy and ε is the perpendicular energy and is given by $\varepsilon = [E - \frac{\hbar^2 k_{\parallel}^2}{2m}]$, where E is the electron energy measured from the bottom of the inner potential well, and k_{\parallel} is the parallel wavevector. If ϕ_C is considered as being constant, only the image states can be obtained. Over the energy range of a crystal gap, the variation of ϕ_C has to be taken into account. Within the frame work of nearly free electron model, an expression for the ϕ_C variation across the crystal gap can be obtained;

$$k \tan \frac{\phi_C}{2} = p \tan(pz_o + \delta) - q, \quad (\text{A.4})$$

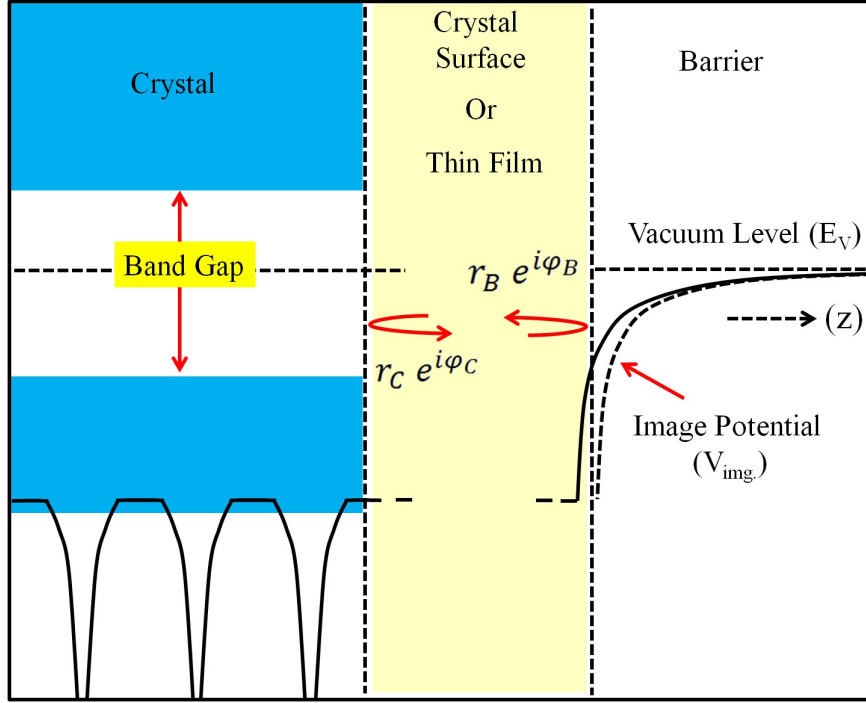


Figure A.9: Multiple Reflection Theory - (a) Schematic potential in the vicinity of a crystal surface. Barrier/Crystal induced surface states arise through multiple reflections between the terminating plane of the crystal and surface barrier. Modified from Ref. [98]^[98].

The definition of these parameters can be found in Ref. [98]^[98]. Equations (A.2) and (A.3) can now be substituted in (A.1) and the energetic position of the possible surface and image states can be obtained. The result for the phase shift for Cu(111) crystal at the $\bar{\Gamma}$ point is shown in Fig. A.10. The abrupt-step barrier and image potential are also compared. L_2' and L_1 denote, respectively, the lower and upper edges of the bulk projected gap. The value of ϕ_C varies from 0 to π at the lower and upper edges of the gap, respectively. For images states ($n \geq 1$), ϕ_C can be considered constant of a value π . The solution for $n=0$ is the surface state. In case of the image potential it has a binding energy of 0.3 eV, i.e. close to the experimentally reported values. For a step-like potential, its energetic position is completely above the Fermi level, beside that there is no image states are existing, where $n=1$ image state occurs for the choice of image potential instead. This finding is the reason why the surface and image states are classified, respectively, as crystal and image-potential induced surface

states.

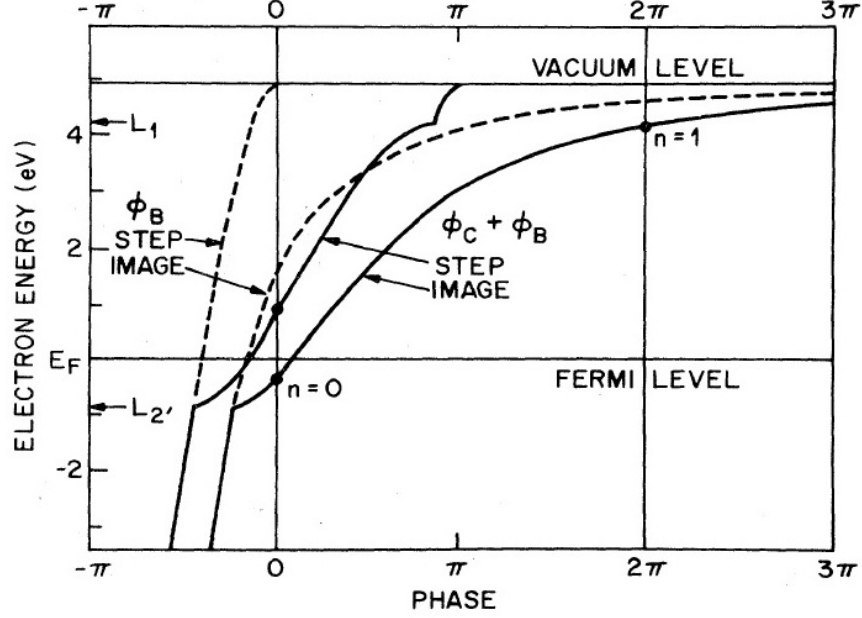


Figure A.10: Phase Accumulation Model: Cu(111) - Energy variation of the reflection phase changes ϕ_B and $\phi_B + \phi_C$ for the lower edge of the L -gap in Cu(111). Taken from Ref. [98]^[98].

Here we want to note that, the energetic position of $n=0$ (surface state) and $n \geq 1$ (image states) are close to the $L_{2'}$ and L_1 edges, respectively. Since the variation of ϕ_C is stronger close to the $L_{2'}$ edge, the surface state energetic position is believed to depend mostly on the lower edge of the bulk gap. The contrary applies for the image states. Temperature dependent measurements on (111) oriented surfaces of noble metals, shown in Fig. A.11, demonstrated the dependency of surface state band minima on the lower edge of the bulk gap.

Metallic overlayers on top of such noble metal substrate, under some conditions, result in the formation of quantum well states. These can, similarly, be described by the multiple reflection theory. Equation (A.1) in this case will read;

$$\phi_B + \phi_C + 2k_{\perp}d = 2\pi n, \quad (\text{A.5})$$

where k_{\perp} is the momentum perpendicular to the surface and d is the film thickness. ϕ_B and ϕ_C are now the phase shifts in the film-vacuum and film-substrate interfaces,

A. NOBLE METALS AND SURFACE STATES

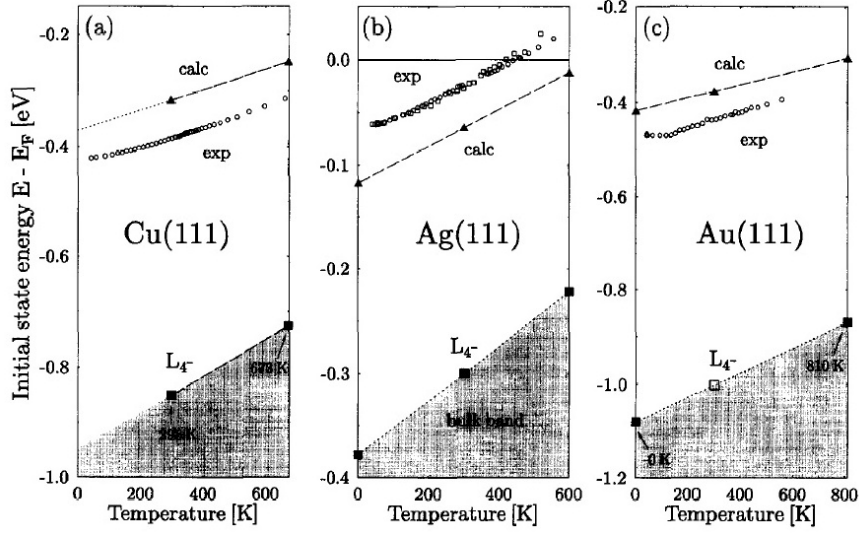


Figure A.11: Noble Metals Surface States: Temperature Dependent - Theoretical (calc) and experimental (exp) temperature dependence of surface state band minima from Cu(111), Ag(111) and Au(111) as well as the lower edge of the L -gap of the projected bulk band structure. Taken from Ref. [99]^[99].

respectively. The expression for ϕ_C , in case of sp -type band gap, can be empirically written as;

$$\phi_C = 2 \arcsin \sqrt{\frac{E - E_L}{E_U - E_L}}, \quad (\text{A.6})$$

where E_L and E_U are the energetic position of the lower and upper edges of the substrate gap, respectively. Using the two-band nearly-free electron model, the k_\perp can be obtained by solving the determinant^[96];

$$\begin{vmatrix} \frac{\hbar^2 k_\perp^2}{2m} - E & v_g \\ v_g & \frac{\hbar^2}{2m} (k_\perp - G)^2 - E \end{vmatrix} = 0 \quad (\text{A.7})$$

with the thin film reciprocal lattice vector (G), the respective Fourier-coefficient of the crystal potential (v_g) (width of the band gap is $2v_g$), the electron mass (m), and the Planck's constant divided by 2π . By solving the equations (A.2) (A.6), and (A.7) which satisfy Equ. (A.5), the perpendicular component of the momentum (i.e. the overlayer's bulk band structure along the symmetry line perpendicular to the surface) can be deduced for known film thicknesses and vice versa.

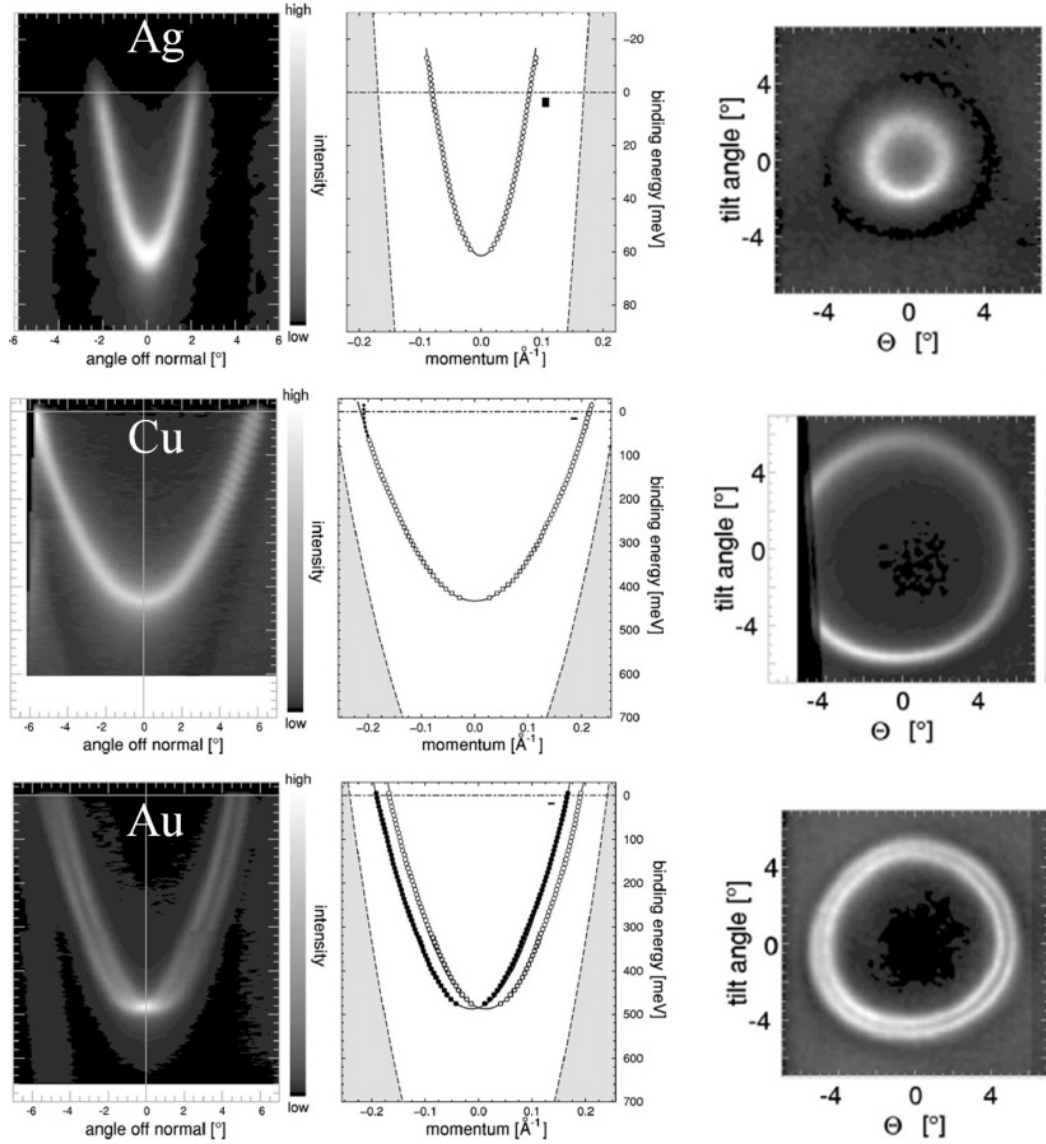


Figure A.12: Surface States Dispersion: Experimental Data - The dispersion of the Ag(111), Cu(111), and Au(111) surface states as measured by ARPES (left), the result of the momentum distribution curves fitting showing the dispersion as well as the gap of the projected band structure “the shaded area” (middle), and their Fermi surface map as measured by ARPES (right). The surface state and the Fermi surface of Au(111) exhibits clearly the spin-orbit splitting, where its two parabolas are centered at $\pm 0.013 \text{ \AA}^{-1}$. Taken from Ref. [100]^[100].

IV. Shockley Surface states of the (111) Noble Metal Oriented Surfaces

The first experimental evidence for a surface state on a metal surface was obtained by field emission studies of W(100)^[10]. In 1975, and using ARPES, a transition that conserves the parallel momentum from Cu(111) was claimed^[291]. The observation confirmed, for the first time, the presence of a Shockley-like surface state on the noble metal Cu(111). Later on, the existence of the surface states on the (111) surface of three noble metals have been experimentally confirmed^[221,291,292]. In Fig. A.12, we show one of the most accurate measurements on Shockley surface state of the three (111) oriented noble metal surfaces. The measurement was done at very low temperature and a high energy and angular resolution ARPES^[100]. The free-electron parabolic dispersion for the three noble metal surfaces is clearly seen in the photoemission intensity, the resultant fit from the momentum distribution curves, as well as the spherical shape of their Fermi surface, as shown, respectively, in the left, middle, and right panels of Fig. A.12. The surface states look as impeded in the gap of the projected bulk band structure, as discussed in section II and III. The energetic position of the surface states band minima (E_o), their effective mass (m_*), and the Fermi wavevectors (k_F) as extracted from such measurements are tabulated in table A.2. Clearly the Fermi surface volume, defined by the Fermi wavevector, is significantly different for the three noble metals. Moreover, the energetic position of the band minima is clearly different and scales with the energetic position of the lower edge of the L -gaps.

	E_o (meV)	m_* (m_e)	k_F (\AA^{-1})
Ag(111)	63 ± 1	0.397	0.080
Cu(111)	435 ± 1	0.412	0.215
Au(111)	487 ± 1	0.255	0.167/0.192

Table A.2: Dispersion Parameters: Noble Metal Surfaces - The parabolic dispersion fit results extracted from the photoemission intensity plots shown in Fig. A.12^[100].

Appendix B

Fermi Surface Distortion Correction

In this appendix¹, we give an illustrative example on the energy-momentum representation and the distortion correction of ARPES data taken with the Phoibos 150 analyzer at the Nanophysics Laboratory.

I. Sources of Distortion:

The sources of distortion in ARPES data can be related to the special design of the hemispherical analyzer (such as the shape of the entrance slit, the lens modes, etc) and/or mechanical deficiencies (such as the misalignment of the sample, the tilt of the manipulator, the misalignment of the CCD-camera, etc).

As for the special design of the Phoibos analyzers, the entrance slit can be straight or curved. Due to the spherical symmetry of the analyzer, a straight slit will be imaged onto a curved line at the detector. Since the detector is integrating the signals along one pixel row for each energy channel, this curvature gives a contribution to the energy broadening, which can only be neglected for relatively wide slits (> 1 mm). Throughout the present work, the entrance slit being used is a curved one. This allows for a reduced curvature of the iso-energy contours (lines of equal energy) on the CCD camera images, and therefore, an easy calibration of the energy axis on the channel plate image. In

¹This appendix has become possible due to the continuous efforts made by M. Matena, a post-doctor at the Nanophysics laboratory, through the initialization of ARPES setup.

B. FERMI SURFACE DISTORTION CORRECTION

this case, the iso-energy contours form lines which are parallel to one axis of the square CCD camera pixels array (hence, a Fermi edge would appear as straight line on the CCD camera image). The price one pays, however, to gain such free-distortion energy axis is other sources of distortion. On one hand, the iso-angle contours are not parallel to the two axes (the one of the energy and the perpendicular to it) of the CCD array. Actually, it is this deviation of the iso-angle contours from being lines perpendicular to the energy axis what referred as “*momentum distortion*” [293]. Due to such distortion, the intensity values occur at incorrect positions on the CCD camera. One therefore needs to find out a parameterized mapping function by which the intensity values can be moved to new positions so as to keep the energy-angle axes perpendicular to one another.

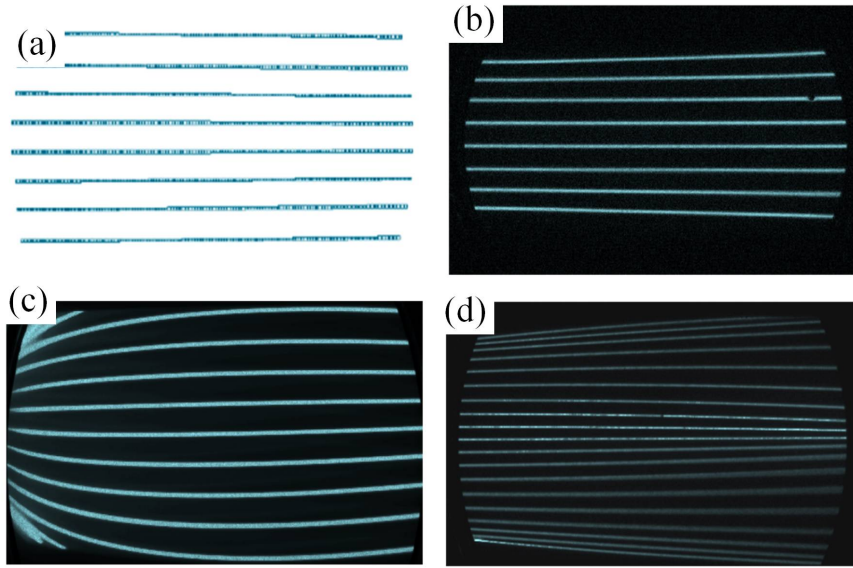


Figure B.1: Iso-Angle Contours: Different Lens Modes - A simulated line pattern from electrons emitted with discrete angles passing through a straight slit array. The CCD image with the lens only (a), and with the lens and the hemispherical analyzer for (b) LAD, (retarding ratio of 1), (c) LAD (retarding ratio of 2), and for (d) WAM (retarding ratio of 1). The yellow lines represent the iso-angle contours with the least distortion. Adapted from Ref. [289] [294].

Here we use the parameters and mapping functions provided by SPECS for different lens modes and retarding ratios in order to get rid of this distortion [294]. These parameters are, actually, used to be collected from a special kind of experiment, where

electrons emitted from a filament are passed through an equally spaced straight slit array and are imaged by the analyzer for different lens modes. These parameters and mapping function are continuously updated by SPECS.

The output of such experiment should be the same as the one shown in Fig. B.1 where the distortion of the iso-angle contour is clearly seen to be very much sensitive to the lens modes as well as the retarding ratio^[294].

Figure B.1(a) shows a simulation of the CCD image of the slit array with the lens only, where the array looks nearly distortion-free. The same images taken by the hemispherical analyzer in Low Angular Dispersion “*LAD*” mode with high (Fig. B.1(b)) and very low (Fig. B.1(c)) retarding ratios show distorted iso-angle contours. For *LAD* and high retarding ratios, such distortion can be easily corrected, even during the data acquisition, by linearly stretching/shrinking the image. This, in fact, allows the use of the swept mode for data acquisition. For very low retarding ratios, however, the distortion is far from being linear and therefore, could not be corrected in-line with the data acquisition. For Wide Angular Mode “*WAM*”, on the other hand, the distortion of the iso-angle contours is completely inhomogeneous, each part of the CCD image needing to be corrected differently. In order to correct such distortion for different lens mode using the algorithms written by SPECS, the position of the nearly distortion-free iso-angle contour, which corresponds to electron propagation along the optical axis (the yellow line), on the CCD image has to be known.

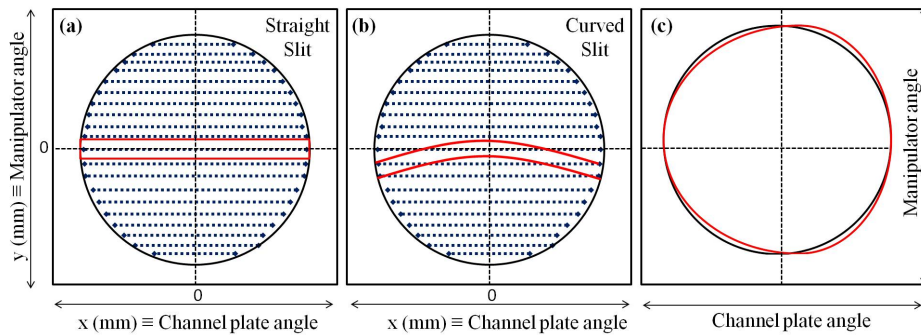


Figure B.2: Distortion due to a Curved Slit - Schematic drawing of a plane at straight (a) and curved (b) entrance slits. The dots represent electrons emitted from different angles from the sample. The manipulator and channel plate angles are related to y and x , respectively. Modified from Ref. [291]^[295]. In (c) the effect of imaging with a curved slit on a circular Fermi surface is drawn; where the egg-like shape (red) clearly deviates from the circular form (black).

B. FERMI SURFACE DISTORTION CORRECTION

On the other hand, the use of the curved-slit has another source of distortion which is illustrated in Fig II.2^[295,296]. One notice that the channel plate and the manipulator angles are only coupled for a curved slit, whereas they are completely independent for straight slits, Fig. B.2(a-b). It is only at normal emission configurations where, even with the curved slit, such distortion is negligible (see the overlap positions between the red and black circle in (c)). The overall effect, thus, induces an egg-like distortion to a circular Fermi surface (FS), as shown in Fig. B.2(c). We use this deviation of the surface state's FS to quantify the effect using the following equation:

$$\Delta x = \frac{y^2}{2R_S} \quad (\text{B.1})$$

where Δx is the deviation of the manipulator angular scale for every angle y on the channel plate and R_S is the radius of the curved slit.

At the end, and using a spherical FS, as the one of noble metal (111) oriented surfaces, one can further correct the transformed angular axis of the channel plate relying on the fact that the angular scale of the manipulator is correct. One can then obtains a factor, which is close to 1 in most of our cases, and uses it to re-scale the channel plate angular axis.

For ARPES setups free of mechanical deficiencies, the above mentioned effects are the main sources of the distortions, and getting rid of them will put the data in a perfect shape for further physical analysis.

Unfortunately, beside these intrinsic sources of distortions, our current ARPES setup still has some mechanical deficiencies, which are continuously minimized as much as possible. For example, the images acquired by the CCD camera, and due to its misalignment, are rotated by $\sim 1.4^\circ$. This, critically, requires the rotation of all the acquired raw images (pixel \times pixel) by this degree before going through any other transformation or distortion correction, specially the SPECS correction. Figure B.3 is an illustrative example showing the importance of such correction, especially for a high degree of camera misalignment. The left of each panel (a-d) shows a Fermi edge (the horizontal line) and the normal-emission line (NEL) (the vertical line) before applying the SPECS transformation.

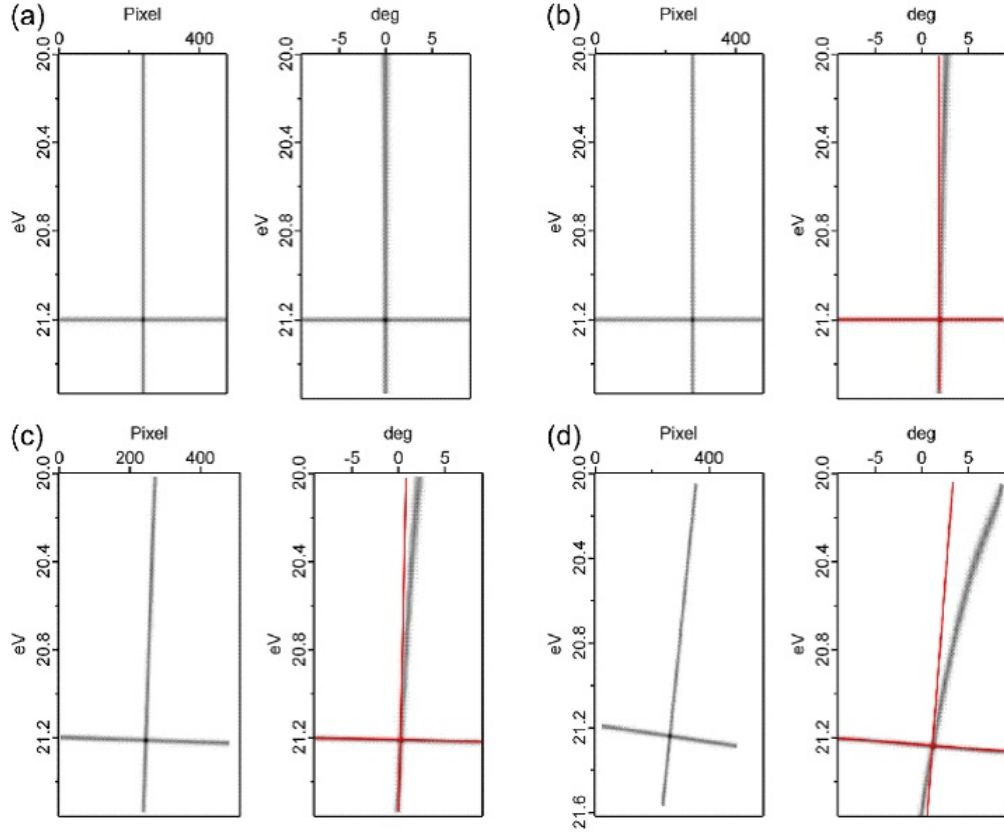


Figure B.3: SPECS Transformation Applied to Inclined Fermi Edge - Transformation to get straight iso-angular lines using the algorithm of SPECS. The images on the right show the transformation of the images shown on the left. The horizontal lines at 21.2 eV represent the Fermi edge. The vertical lines are chosen to be perpendicular to the Fermi edges and can be considered as “*normal emission lines*”. The horizontal red lines are superimposed to the transformed horizontal lines, with the vertical red lines lying perpendicular to them in order to illustrate deviations from a right angle. a) Everything is fine if the transformation is applied to a correctly aligned system. b) A small deviation is seen if the vertical line is shifted. c) A rotation of both lines by 2° . A distortion of the vertical axis can be seen. Moreover the angle between both lines deviates by 2° from a right angle. d) A rotation of both lines by 7° . The effects are now significantly enhanced.

B. FERMI SURFACE DISTORTION CORRECTION

The right panels show how those lines are affected after the SPECS transformation. The red lines are the NEL before the transformation and are superimposed on the transformed images to illustrate deviations from a right angle. One clearly sees that, applying the SPECS transformation to a non-horizontal Fermi edges, results in an additional distortion of the NEL and, therefore, the parabolic dispersion of a surface state will be tilted with respect to the Fermi edge. The more the Fermi edge is non-horizontal, the more the distortion of the NEL (Fig. B.3(b) to Fig. B.3(c), (see the figure caption)).

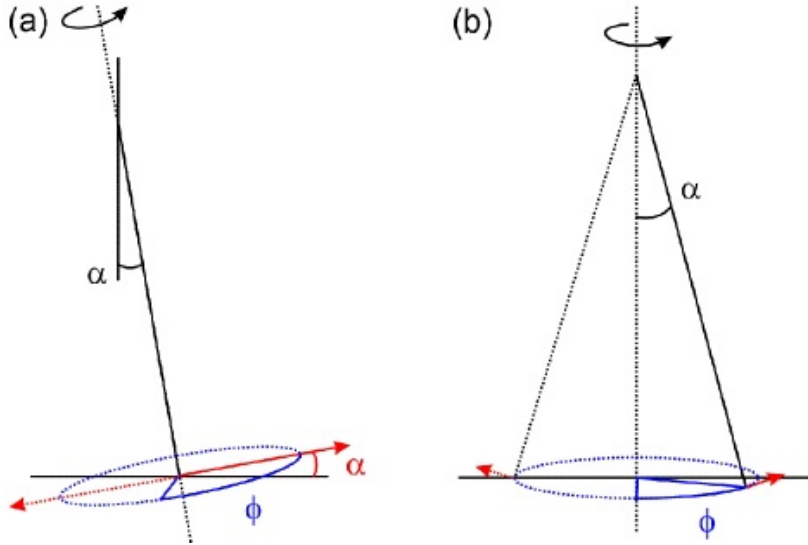


Figure B.4: Distortion due to a Manipulator Tilt - The slit of the analyzer is chosen to be vertical. a) Rotational axis of the manipulator tilted by (α) with respect to the slit of the analyzer. This tilt results in a maximum shift of normal-emission by (2α) after a rotation of $\varphi = 180^\circ$ (indicated by red arrows). In the angular axis of the channel plate the positions of normal-emission would change when rotating the manipulator. b) If the rotational axis is parallel to the slit and the manipulator axis is tilted by α the focus of beam and analyzer will move on the sample when the manipulator is rotated. Moreover, beam and analyzer will defocus.

The Second type of mechanical deficiencies we have is the rotational axis (The manipulator is not perpendicular to the analyzer lens axis). The result is that the tilt of the manipulator (a certain offset) varies with the rotational angle, and as a consequence, the NEL will move across the channel plate. A circular FS would, thus,

appear distorted as shown in Fig. B.4. We correct this effect using the following function:

$$\delta(\varphi) \simeq \tan(\alpha) \cos(\varphi) \quad (\text{B.2})$$

where δ is the deviation of the NE axis as a function of the tilt α and the rotational angle φ .

II. Distortion Correction: An Example

Here we give an illustrative example, showing how the various parameters needed for the energy-momentum transformation and distortion minimization, can be extracted from the ARPES raw data and using the menu shown in Fig. B.5. The sample to be studied here is the 1 ML Ag/Cu(111) surface measured in WAM with Hydrogen Lyman line (photon energy of 10.2 eV) and with pass energy of 7 eV, as tabulated in table B.1.

The ARPES raw data to be corrected here are a 3D data set taken at different manipulator angles (FSM), F05. Such data set is commonly used to construct constant energy surfaces including the Fermi surface. An image of the Fermi edge (F01-F02) is also taken to correct for the camera misalignment and/or energy calibration, Fig. B.6(a-b). The surface state of the 1 ML Ag/Cu(111) crystal is also taken at two different set energies (F03 and F04), Fig. B.6(b-c), and is used for accurate energy calibration and to check for the final correction of the data. Using these data files and the scripts called by the Manni menu, the transformation to energy-angle and the associated distortion correction will proceed as follow:

File Name	Scan Type	Lens Mode	Pass Energy (eV)	Set Energy (eV)
F01	Fermi Edge	WAM	7	-0.15
F02	Fermi Edge	WAM	7	0.0
F03	Surface State	WAM	7	-0.15
F04	Surface State	WAM	7	-0.30
F05	FSM Map	WAM	7	-0.15

Table B.1: ARPES Data: Calibration Files - The names and scanning parameters of the raw ARPES data used in the present example. All the measurements were done at 180 K.

B. FERMI SURFACE DISTORTION CORRECTION

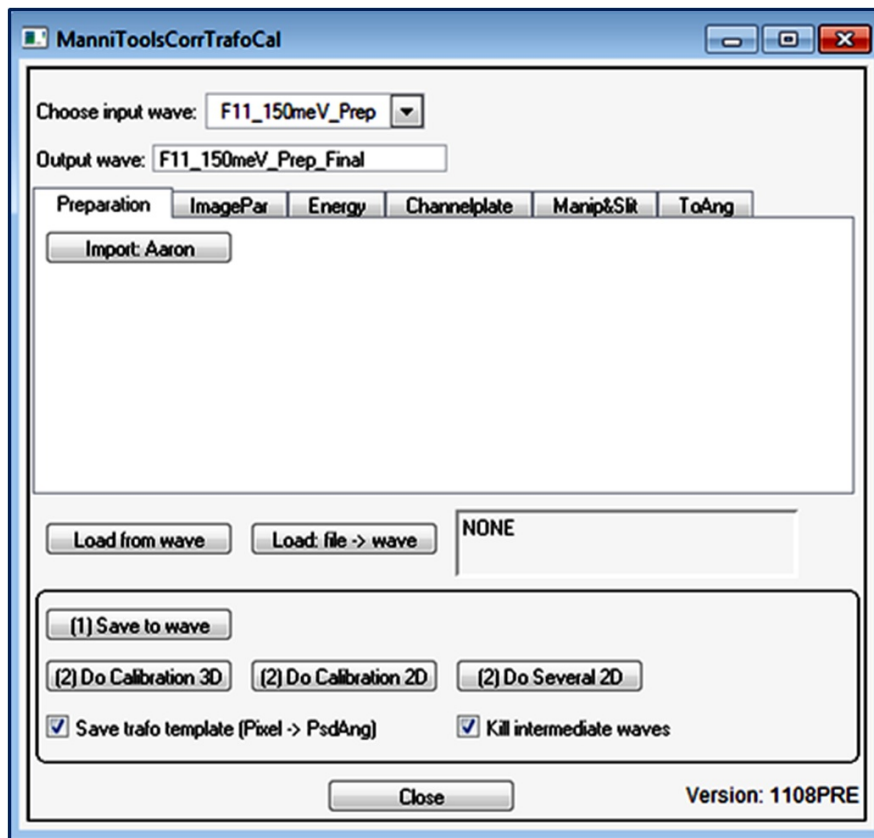


Figure B.5: Manni Tools: Main Panel - The Manni-panel used for performing a user friendly transformation and distortion correction as implemented by Manfred Matena.

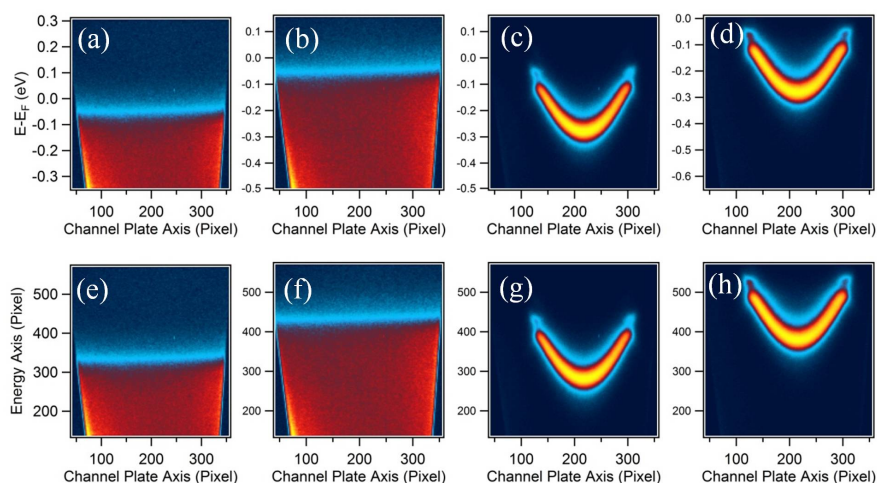


Figure B.6: ARPES Raw Data - The channel plate images for the acquired raw data (a-d) and the energy-to-pixel transformed ones (e-h), see table B.1

Images Preparation:

The images taken by Aaron’s software are represented with pixel units along the channel plate and in electron volt (eV) along the energy axis, as shown in Fig. B.6(a-d). Information concerning the set energy, the pass energy, the initial guess of energy calibration, the energy offset, the work function, and the photon energy for each image are stored and can be called through their spectrum IDs. These parameters can also be written manually into the “*ImagePra*” popup menu, shown in Fig. B.7. In case of 3D images, the third axis is not subject to corrections whether it was for the manipulator angles or any kind of lateral scan (such as a scan along a wedge or a curved crystal).

The screenshot displays the 'ImagePra' sub-menu, which is divided into two main sections. The top section is for energy-to-pixel conversion, featuring a 'Choose input wave' dropdown menu set to 'f00011_a', an 'Import: Aaron' button, an 'Output wave' text field containing 'f00011_a_INI', and a 'SpectrumID' text field containing '0'. Below these are input fields for 'Row Scale' (1), 'Row Offset' (0), 'Col Scale' (665), and 'Col Offset' (367). At the bottom of this section are two buttons: 'Import input wave' and 'Save as output wave'. The bottom section of the menu contains a tabbed interface with tabs for 'Preparation', 'ImagePar', 'Energy', 'Channelplate', 'Manip&Slit', and 'ToAng'. The 'Preparation' tab is currently selected, showing fields for 'E_bind (Image) (eV)' (-0.15), 'E_pass (eV)' (7), 'E_phot (eV)' (10.2) with a 'Choose' dropdown, and 'WF sample (eV)' (4.65) with another 'Choose' dropdown.

Figure B.7: Sub-Menu: Energy to Pixel Transformation - The menu used for energy-to-pixel conversion (top) and the stored parameters called by the spectrum ID.

Using the “*Import: Aaron*” button in Manni tools, the sub-menu shown in Fig. B.7 will pop up. Choosing the input wave and calling its scanning parameters by writing the spectrum ID, and by pressing the “*Import input wave*” button, the column and rows are converted into pixels and the new wave can be named and saved as a pixel by pixel image. This is seen for F01-F04 images, where the energy axis is re-converted into pixel, Fig. B.6(e-h).

B. FERMI SURFACE DISTORTION CORRECTION

CCD Camera Misalignment:

To account for this correction, one has to fit the Fermi edge images, shown in Fig. B.6(e-f), by a Fermi function for every pixel on the channel plate. The results of such fit are shown in Fig. B.8.

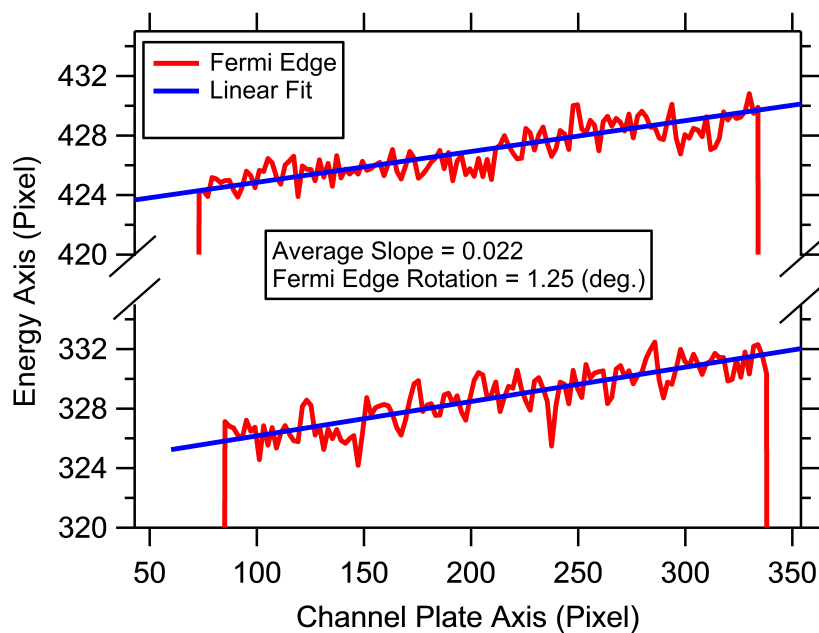


Figure B.8: Fermi Edge Fitting: Pixel Units - The energetic (pixel) position of the Fermi edge, taken at set energies of 0.0 eV (top) and -0.15 eV (bottom), as a function of the channel plate pixels.

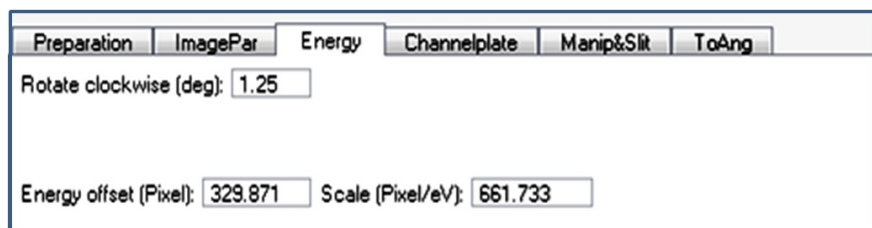


Figure B.9: Sub-Menu: Image Rotation and Energy Scaling - The menu used for image rotation, energy scaling, and setting the Fermi energy to 0 eV.

Fitting such non-horizontal Fermi edges with straight lines, the slopes of the lines are used to define the rotation angle of the camera. In our case, the average rotation angle was close to 1.25 deg. All images are then rotated by this angle using the “*energy*” popup

menu, shown in Fig. B.9. We note here that, each time a new parameter is inserted to the menu, one has to press the button “(1) Save to wave” shown in Fig. B.5. This stores all the parameters needed to perform the transformation and correction into a wave, to be called by pressing the “Do calibration XD” button. Depending on the dimensionality and the type of the images, different “Do calibration XD” buttons are used.

Energy Calibration

Now we wish to reconvert the energy axis into physical units (binding energy in eV) and to set the Fermi energy to zero. The two surface states taken at different set energy (F03-F04) are fitted by Gaussian for each pixel on the channel plate, Fig. B.10. The two parabolic dispersions are then fitted by a second order polynomial, and the pixels corresponding to normal emission (on the channel plate) and the minimum binding energy (on the energy axis) are obtained. These, respectively, are 223.23/ 382.71 and 222.76/ 283.45 for F03 and F04.

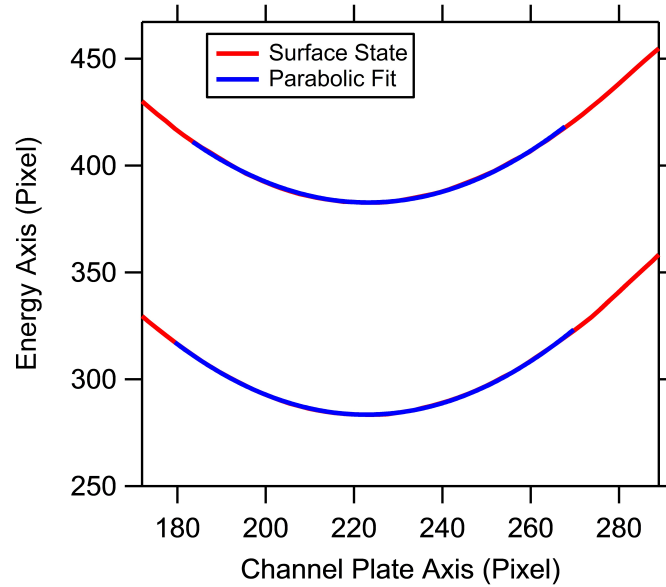


Figure B.10: Surface State Fitting: Pixel Units - (Red) Gaussian fitting of the EDCs of the two surface states (F03, F04) and (blue) parabolic fits for their energetic position as a function of the channel plate pixels.

Since the set energy different between F03 and F04 is 0.15 eV, the energy scaling is

B. FERMI SURFACE DISTORTION CORRECTION

given by $(382.71-283.45)/0.15 = 661.73$ Pixel/eV. This value is then written in “*Scale (Pixel/eV)*” button, Fig. B.9, the parameters are saved again and the calibration is applied to all images.

In order to set the Fermi energy to zero, we can then use the new Fermi edges (F01-F02) images and fit it for every pixel on the channel plate, Fig. B.11. The average energetic position of the, now, horizontal Fermi levels is found to be 0.498495 eV. The offset of the energy (in pixel) is then obtained by the multiplication of the Fermi energy and the energy scaling and is found to be 329.871. This value is then written in “*Energy offset (Pixel)*” button, Fig. B.9, the parameters are saved again and the calibration is applied to all images.

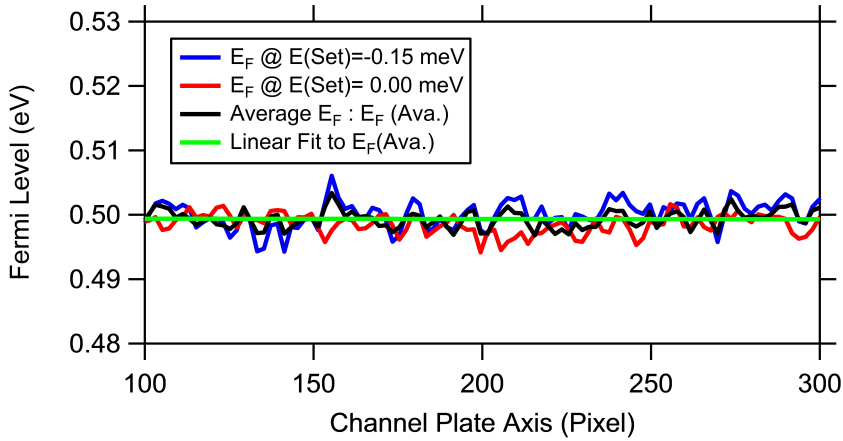


Figure B.11: Fermi Edge Fitting: eV Units - The energetic (pixel) position of the rotated Fermi edge, taken at set energies of 0.0 eV (red) and -0.15 eV (blue), as a function of the channel plate pixels. The green line is a linear fit to the average Fermi edge (black).

SPECS Transformation:

We use the algorithm and set of parameters provided by SPECS to correct for the curvature of the iso-angle contours. These parameters are lens mode dependent and they are all stored in a file named Phoibos150.calib2d within the subfolders of SPECS software. This file has to be loaded using the button “*channelplate*” in Manni tools and the subsequent popup menu shown in Fig. B.12. Once the file is loaded, all the parameters shown in Fig. B.12. are filled. The one that has to be manually corrected is the value of “*Center Angle (Pixel)*”. This is the line of the iso-angle contours that are

not distorted. One has to accurately choose this number so as the image is positioned correctly on the SPECS mesh as explained in Fig. B.1. This should be easily seen on the transformed image, since a slight deviation from the correct number significantly affects the distortion of the image. The pixel that gives less distortion in the present example was the pixel number 210. This value is then written in “*Center Angle (Pixel)*” button, Fig. B.12, the parameters are saved again and the calibration is applied to all images.

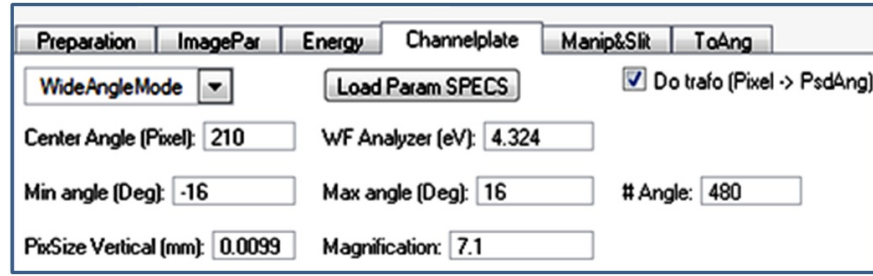


Figure B.12: Sub-Menu: SPECS Transformation - The menu used to apply the SPECS transformation.

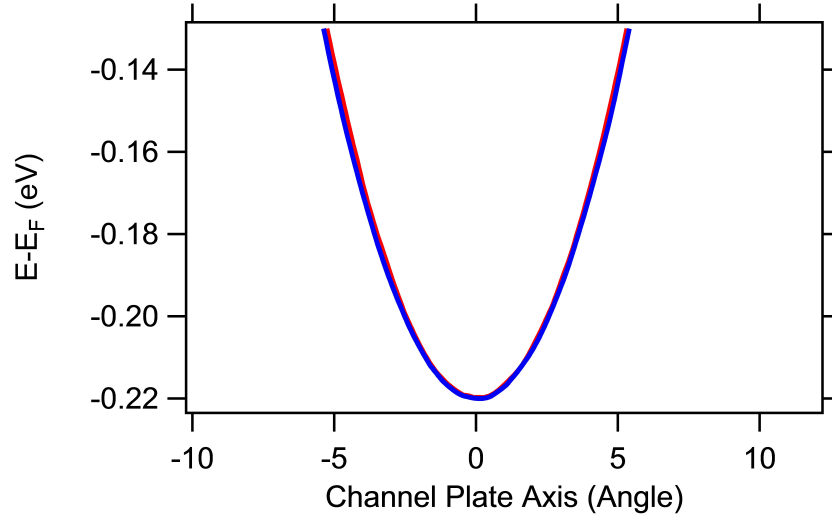


Figure B.13: Surface State Fitting: eV Units - Gaussian fitting of the EDCs of the two surface states F03 (red) and F04 (blue).

The output after all these corrections and transformations are images where the channel plate axis is now in degrees (angle) and the energy axis is in eV (binding energy), with the Fermi level set to zero. To check the quality of the transformation we again fit (using a Gaussian function) the transformed images F03 and F04 for each

B. FERMI SURFACE DISTORTION CORRECTION

pixel on the channel plate. The results of such fit are displayed on Fig. B.13, where a good overlap between the two surface states is seen in both the energy and angular axes.

Manipulator Tilt and Curved Slit Corrections:

In case of 2D images, such as F01-F04, the previous four steps of transformation and correction are enough to get physically transformed and corrected images. For Fermi surface 3D images, such as F05, the distortion results from the manipulator tilt, as discussed earlier, is still to be taken into account. This can be seen in Fig. B.14, where a constant energy surface (CES) at $E = -0.12$ eV is taken from F05 after the SPECS transformation.

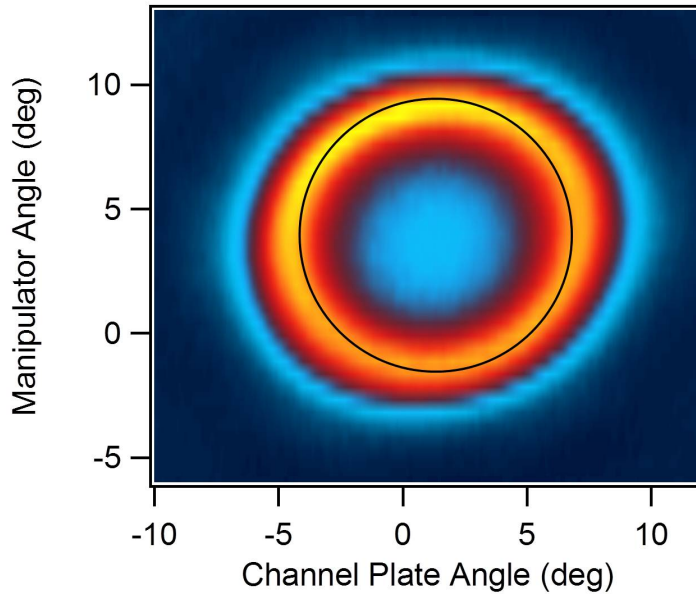


Figure B.14: Distorted CES: Degree (Angle) Units - A Constant Energy Surface (CES) taken at -0.12 eV (from the transformed data set F05) clearly shows the deviation from the circular shape (black circle).

The deviation from a circular (black circle) shape is clearly seen. The left and right side of this CES is fitted with a Gaussian peak for each manipulator angle and their average, shown in Fig. B.15, is then fitted with the function discussed earlier for the manipulator tilt correction. The results of such fit are: $\text{TanTilt} = 0.08869$ (Tilt=5.07), $\text{ManOffs} = 129.32$, $\text{NEOffs} = -4.1723$, $\text{PixToAng} = 1$ (fixed). We note that, the normal

emission on the channel plate changes slightly as a function of the manipulator angle. The fitting parameters are then written in the corresponding place in the popup menu of the “*ManipSlit*”, Fig. B.16. The whole parameters are saved again and the calibration is applied to image F05. The same CES is taken, after the manipulator tilt correction, and the left and right side of this CES is fitted with Gaussian peak for each manipulator angle and their difference, shown in Fig. B.17, is then fitted with the function discussed earlier for the curved slit correction. The results of such fit are: $\text{Rad} = 5.5305$, $\text{Slit (Radius)} = 358.28$ and $\text{PixToAng} = 0.56061$. The curved slit radius is then written in the corresponding place in the popup menu of the “*ManipSlit*”, Fig. B.16. The whole parameters are saved again and the calibration is applied to image F05.

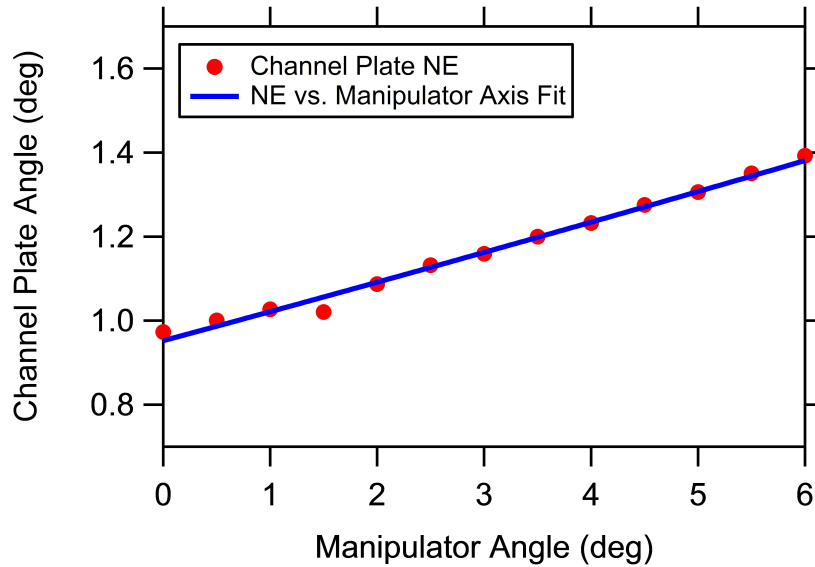


Figure B.15: Normal Emission vs. Manipulator Angle - The surface state normal emission (NE) as a function of the manipulator angle (red) and the corresponding fit using the manipulator tilt correction function (blue).

The CES at -0.12 eV after the previous corrections is shown in Fig. B.18. The CES is still not circular, but the distortions are minimized compared to the CES shown in Fig. B.14. The shape of the CES is nearly a perfect ellipse (blue) and a scaling factor of the channel plate is used to get rid of this deformation. In the present case the scaling factor, which is mainly dependent on the pass energy and lens mode, was found to be 0.88. The factor is then written in the corresponding place in the popup menu of the

B. FERMI SURFACE DISTORTION CORRECTION

Preparation	ImagePar	Energy	Channelplate	Manip&Slit	ToAng
MANIPULATOR					
		Tilt of manipulator (Deg): 5.06824			
		Offset - Angular axis of manipulator (Deg): 129.32			
		Offset - Normal emission channel plate (Deg): -4.1723			
		Normal emission manip axis (Deg): 3.75			
SLIT					
		Curved slit - Radius: 358.28		Curved slit - Smoothing: 1	

Figure B.16: Sub-Menu: Manipulator Tilt and Curved Slit - The menu used applying the manipulator tilt and the curved slit corrections.

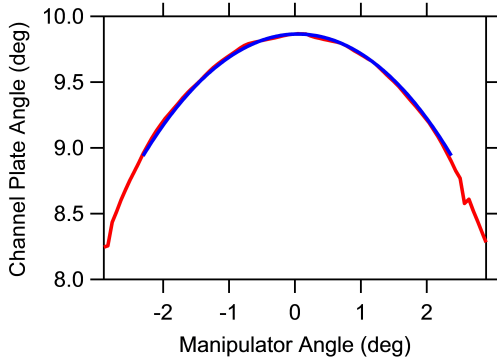


Figure B.17: Normal Emission vs. Manipulator Angle after Curved Slit Correction.

The surface state normal emission (NE) as a function of the manipulator angle (red) and the corresponding fit using the curved slit correction function (blue).

“ToAng”, Fig. B.19. The whole parameters are saved again and the final calibration is applied to all the images.

Figure B.20 shows the CES and the two surface states after this final correction and the distortion is clearly minimized in both cases. The transformation from angle to momentum (wave vector) is then performed in straight forward way using the momentum-angle equations explained in chapter two.

III. Data Visualization: Second Derivative Plots

Usually in ARPES data, the second derivative with respect to energy and/or momentum is performed in order to highlights features which are hardly visible in the raw images. This way can only be used for data visualization but not for quantitative analysis. In fact, the drawback for using the second derivative method is that, it gives a wrong estimation of the maxima (peaks positions) in the energy distribution curves (EDCs) or the momentum distribution curves (MDCs). An alternative and more re-

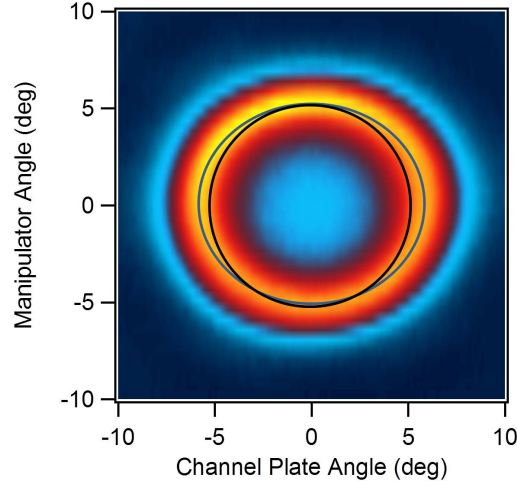


Figure B.18: Elliptically Distorted CES: Degree (Angle) Units - A CES taken at -0.12 eV (from the transformed data set F05) showing the pure elliptical (blue ellipse) deviation from the circular shape (black circle).



Figure B.19: Sub-Menu: Channel Plate Scaling - The menu used to scale the channel plate angles.

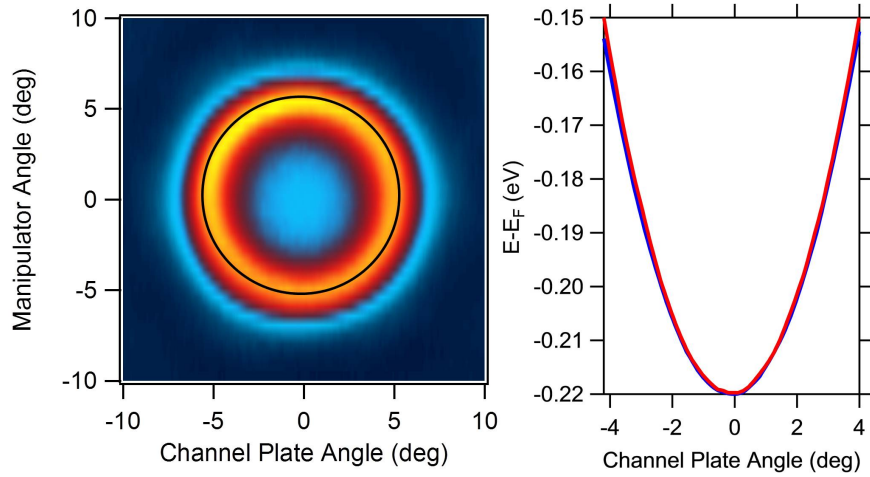


Figure B.20: Spherical CES: Final Result - (Left) The CES taken at -0.12 eV after the final energy-angle transformation and all intrinsic and extrinsic sources of distortion correction. (Right) Gaussian fitting of the EDCs of the two surface states F03 (red) and F04 (blue).

B. FERMI SURFACE DISTORTION CORRECTION

liable method for both visualization as well as tracing the correct energetic position in EDCs and MDCs is the 1D and 2D curvature method² [297]. In this method the curvature of the intensity plot function is expressed in terms of the first and the second derivatives with respect to the momentum and/or energy for 1D and/or 2D plots. The mathematical expression for the curvature also include one (two) free parameter(s) for 1D (2D) plots, which can be finely tuned to get the best visualization of the data, the sharpest representation, and the more reliable position of the maxima. Here we only write these mathematical expressions for 1D and 2D intensity plots and the reader is referred to Ref. [292] [297] for the mathematical derivation and further information. In 1D case, the curvature is given by

$$C(x) = \frac{f''(x)}{(C_0 + f'(x)^2)^{\frac{3}{2}}} \quad (\text{B.3})$$

where $f''(x)$ and $f'(x)$ are the second and first derivatives of with respect to x , which is energy (for EDC) or momentum (for MDC). The free parameter C_0 can be changed to obtain the best visualization and in the worst case, when C_0 goes to infinity, the curvature method will give the same results as the second derivative one. In the case of 2D image plot, the curvature is expressed as;

$$C(x, y) = \frac{[1 + C_x(\frac{\partial f}{\partial x})^2]C_y\frac{\partial^2 f}{\partial^2 y} - 2C_xC_y\frac{\partial f}{\partial x}\frac{\partial f}{\partial y}\frac{\partial^2 f}{\partial x\partial y}[1 + C_y(\frac{\partial f}{\partial x})^2]C_x\frac{\partial^2 f}{\partial^2 x}}{[1 + C_x(\frac{\partial f}{\partial x})^2 + C_y(\frac{\partial f}{\partial y})^2]^{\frac{3}{2}}} \quad (\text{B.4})$$

where x and y can be both k_x - k_y momenta (for the constant energy surfaces and FS) or energy and momentum (for the channel plate 2D image). The two free parameters can be then tuned to get the best visualization. We note, however, that for a better visualization the 2D curvature method requires a pre-interpolation of the 2D image, since the method works fine for square images where the number of columns and rows are equal. Figure B.21(a-c) shows an EDC (black) of the surface state of the 1 ML Ag/Cu(111) taken at wavevector of 1.1 nm^{-1} and 1.6 nm^{-1} , respectively. The corresponding EDCs after applying the second derivative (red) and the curvature method (blue) are shown as well. We notice that, the curvature method traces the peak position more correctly than the second derivative method. The deviation of the

²Thanks to Prof. Dr. Philip Hofmann-Department of Physics, Aarhus University, Denmark- for distributing and emailing the curvature method article around.

two methods in tracing the peak position becomes clear close to the Fermi level, where the curvature method can still provide a better estimation even above the Fermi level, Fig. B.21(c). When fitting close features in EDCs, a number of physical restrictions and fixed parameters (such as peak width, intensity, etc) are sometimes needed to extract reliable information. The curvature method can, thus, be used to give the exact position of the peaks, to be used later as a fixed parameter for the fitting program.

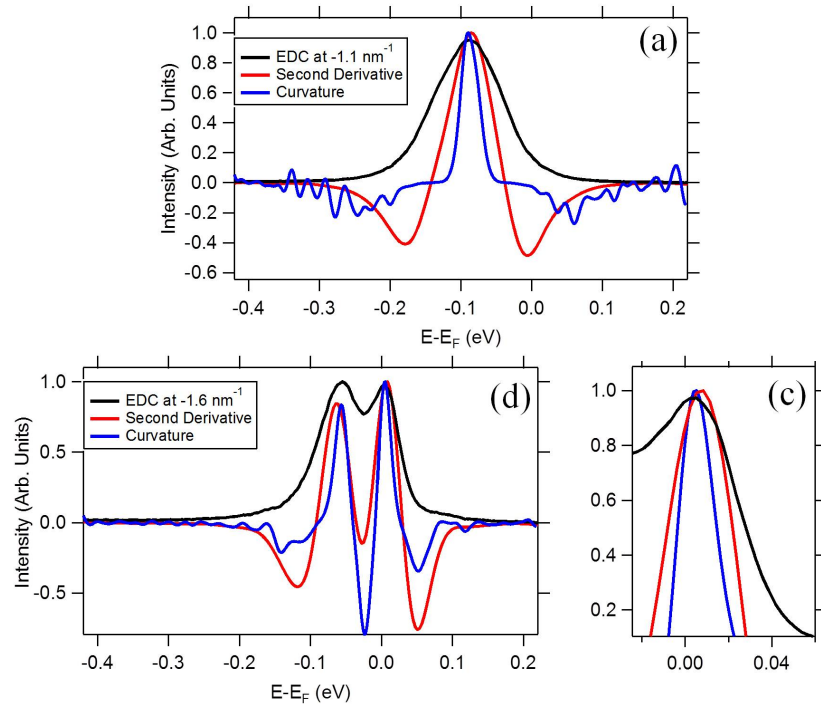


Figure B.21: Second Derivative vs. Curvature Method: EDCs Spectra - EDC (black) taken at wavevector of 1.1 nm^{-1} (a) and 1.6 nm^{-1} (b-c). The corresponding second derivative (red) and curvature method (blue) transformations are shown as well. (c) Represents a zoom in (green line) the peak above the Fermi level in (b).

It is also seen that, the curvature method yields much sharper EDCs as compared to second derivative. This allows a better visualization of features that, in some cases, are not well resolved using the common second derivative visualization. Figure B.22 show CES at +90 meV above the Fermi level after the application of the second derivative (left) and the 2D curvature method (right). These features are very weak and arise, in fact, due to other excitation line which gives another Fermi level slightly higher than the main one. The power of the curvature method in resolving such weak features is

B. FERMI SURFACE DISTORTION CORRECTION

clearly seen.

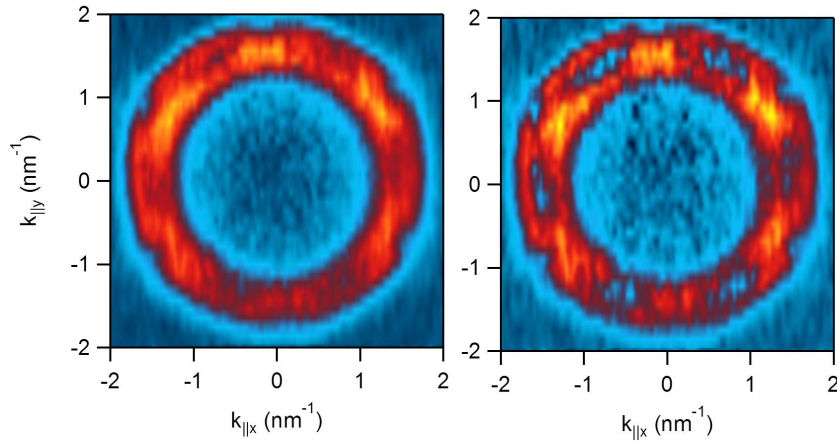


Figure B.22: Second Derivative vs. Curvature Method: CES Plots - CES at +90 meV above the Fermi level visualized using the second derivative (left) and the 2D curvature method (right). Since both methods give a different estimation of the peak position, the most resolved and featured CES in the second derivative case was found at slightly higher energy (+95 meV) as compared to the curvature method. Fine features are better seen with the curvature method.

Appendix C

Acronyms

UHV Ultra-High Vacuum	LAD Low Angular Dispersion
LEED Low Energy Electron Diffraction	WAM Wide Angular Mode
STM Scanning Tunneling Microscopy	CCD Charge Coupled Device
ARPES Angle Resolved Photoemission Spectroscopy	FS Fermi Surface
SPM Scanning Probe Microscopy	VLS-PGM Varied Line Space Plane Grating Monochromator
DOS Density of States	ISA Institute of Storage Ring
LDOS Local Density of States	SGM Spherical Grating Monochromator
VUV Vacuum Ultraviolet	MEG Medium Energy Grating
XPS X-ray Photoemission Spectroscopy	HEG Medium Energy Grating
UPS Ultraviolet Photoemission Spectroscopy	RT Room Temperature
ARUPS Angle Resolved Ultraviolet Photoemission Spectroscopy	LT Low Temperature
EDC Energy Distribution Curve	STS Scanning Tunneling Spectroscopy
CFS Constant Final State	MDC Momentum Distribution Curve
CIS Constant Initial State	QWS Quantum Well State
FWHM Full Width at Half Maximum	SBZ Surface Brillouin Zone
QMB Quartz Microbalance	CES Constant Energy Surface
SRC Synchrotron Radiation Center	PW Plane Wave
TMM Toroidal Mirror Monochromator	BEM Boundary Element Method
ETC Ellipsoidal Transfer Capillary	BZ Brillouin Zone
	KP Kronig-Penney
	TWD Terrace Width Distribution

C. ACRONYMS

FT Fourier Transform

QH Quantum Hall

TRIM Time Reversal Invariant Mo-
menta

C.B. QWS Conduction Band Quantum
Well State

V.B. QWS Valence Band Quantum Well

State

2DEG 2D Electron Gas

FCC Face Centered Cubic

BCC Body Centered Cubic

NEL Normal Emission Line

Bibliographic Research

- [1] R. P. FEYNMAN. **There's plenty of room at the bottom.** *Engineering and Science*, **23**[5]:22, 1960. [1](#)
- [2] M. A. VAN HOVE. **From surface science to nanotechnology.** *Catalysis Today*, **113**[34]:133, 2006. [1](#)
- [3] A. CHAMBERS, R. K. FITCH, AND B. S. HALLIDAY. *Basic Vacuum Technology*. Taylor & Francis, 2 edition, 1998. [1](#)
- [4] J. F. O'HANLON. *A User's Guide to Vacuum Technology*. Wiley-Interscience, 3 edition, 2003.
- [5] N. YOSHIMURA. *Vacuum Technology: Practice for Scientific Instruments*. Springer, 2008.
- [6] A. W. CZANDERNA, C. J. POWELL, AND T. E. MADEY. *Specimen Handling, Preparation, and Treatments in Surface Characterization*. Methods of Surface Characterization. Springer, 1999. [1](#)
- [7] H. J. GÜNTHERODT AND R. WIESENDANGER. *Scanning Tunneling Microscopy I: General Principles and Applications to Clean and Adsorbate-Covered Surfaces*. Scanning Tunneling Microscopy. Springer-Verlag, 1994. [2](#), [12](#), [13](#)
- [8] L. J. CLARKE. *Surface Crystallography: An Introduction to Low Energy Electron Diffraction*. A Wiley-interscience publication. Wiley, 1985.
- [9] S. HÜFNER. *Photoelectron Spectroscopy: Principles and Applications*. Springer Series in Solid-State Sciences. Springer, 1996. [19](#), [21](#)
- [10] S. D. KEVAN. *Angle-Resolved Photoemission: Theory and Current Applications*. Number v. 74 in Studies in Surface Science and Catalysis. Elsevier, 1992. [2](#), [19](#), [212](#), [213](#), [220](#)
- [11] M. T. SWIHART. **Vapor-phase synthesis of nanoparticles.** *Current Opinion in Colloid & Interface Science*, **8**[1]:127, 2003. [2](#)

BIBLIOGRAPHIC RESEARCH

- [12] B. L. CUSHING, V. L. KOLESNICHENKO, AND CH. J. O'CONNOR. **Recent advances in the liquid-phase syntheses of inorganic nanoparticles.** *Chemical Reviews*, **104**[9]:3893, 2004.
- [13] W. A. GODDARD, D.W. BRENNER, S. E. LYSHEVSKI, AND G. J. IAFRATE. *Handbook of Nanoscience, Engineering, and Technology*. The Electrical Engineering Handbook Series. Taylor & Francis, 2 edition, 2007.
- [14] M. D. VENTRA, S. EVOY, AND J. R. HEFLIN. *Introduction to Nanoscale Science and Technology*. Nanostructure Science and Technology. Springer, 2004.
- [15] R. KELSALL, I. W. HAMLEY, AND M. GEOGHEGAN. *Nanoscale Science and Technology*. Wiley, 2005. [2](#)
- [16] J. V. BARTH, G. COSTANTINI, AND K. KERN. **Engineering atomic and molecular nanostructures at surfaces.** *Nature*, **437**[7059]:671, 2005. [2](#)
- [17] T. ITO AND SH. OKAZAKI. **Pushing the limits of lithography.** *Nature*, **406**[6799]:1027, 2000. [2](#)
- [18] M. FUECHSLE, J. A. MIWA, S. MAHAPATRA, H. RYU, S. LEE, O. WARSCHKOW, L. C. L. HOLLENBERG, G. KLIMECK, AND M. Y. SIMMONS. **A single-atom transistor.** *Nature Nanotechnology*, **7**[4]:242, 2012. [2](#)
- [19] M. SCHUNACK. *Scanning Tunneling Microscopy Studies of Organic Molecules on Metal Surfaces*. M.sc thesis, University of Aarhus, Denmark, 2002. [2](#), [11](#), [12](#), [13](#)
- [20] D. M. EIGLER AND E. K. SCHWEIZER. **Positioning single atoms with a scanning tunnelling microscope.** *Nature*, **344**[6266]:524, 1990. [2](#)
- [21] J. Z. ZHANG, Z. WANG, J. LIU, S. CHEN, AND G. LIU. *Self-Assembled Nanostructures*. New York : Kluwer Academic/Plenum Publishers, 2004. [2](#)
- [22] C. KITTEL. *Introduction to Solid State Physics*. John Wiley & Sons, 2004. [3](#), [207](#), [212](#)
- [23] N. W. ASHCROFT AND N. D. MERMIN. *Solid State Physics*. Science: Physics. Saunders College, 1976.
- [24] PH. HOFMANN. *Solid State Physics: An Introduction*. Physics Textbook. John Wiley & Sons, 2008. [3](#), [207](#), [212](#)
- [25] S. Y. REN. *Electronic States in Crystals of Finite Size: Quantum confinement of Bloch waves*. Number n.º 212 in Springer Tracts in Modern Physics. Springer, 2005. [3](#), [212](#)
- [26] J. POLLMANN AND P. KRGER. *Electronic Structure*, **2** of *Handbook of Surface Science*. North-Holland, 2000. [3](#), [212](#)

- [27] I. E. TAMM. **On a possible type of electron binding at crystal surfaces.** *Z.Phys.*, **76**[11]:849, 1932. 3, 179, 212
- [28] W. B. SHOCKLEY. **On the surface states associated with a periodic potential.** *Phys. Rev.*, **56**:317, 1939. 47, 179, 212
- [29] P. M. ECHENIQUE AND J. B. PENDRY. **The existence and detection of Rydberg states at surfaces.** *Journal of Physics C: Solid State Physics*, **11**[10]:2065, 1978. 3, 213, 214
- [30] F. BECHSTEDT. *Principles of Surface Physics.* Advanced Texts in Physics. Springer, 2003. 3
- [31] H. LÜTH. *Solid Surfaces, Interfaces and Thin Films.* Graduate Texts in Physics. Springer, 2001. 3, 29, 79
- [32] R. H. FRIEND AND D. JEROME. **Periodic lattice distortions and charge density waves in one- and two-dimensional metals.** *Journal of Physics C: Solid State Physics*, **12**[8]:1441, 1979. 4
- [33] J. CHANG, E. BLACKBURN, A. T. HOLMES, N. B. CHRISTENSEN, J. LARSEN, J. MESOT, RUIXING LIANG, D. A. BONN, W. N. HARDY, A. WATENPHUL, ZIMMERMANN, E. M. FORGAN, AND S. M. HAYDEN. **Direct observation of competition between superconductivity and charge density wave order in $\text{YBa}_2\text{Cu}_3\text{O}_y$.** 2012.
- [34] R. E. THORNE. **Charge density-wave conductors.** *Physics Today*, **49**[5]:42, 1996.
- [35] S. BROWN AND G. GRUNER. **Charge and spin density waves.** *Scientific American*, **270**:50, 1994. 4
- [36] M. D. JOHANNES AND I. I. MAZIN. **Fermi surface nesting and the origin of charge density waves in metals.** *Phys. Rev. B*, **77**[16]:165135, 2008. 4
- [37] P. AEBI, TH. PILLO, H. BERGER, AND F. LÉVY. **On the search for Fermi surface nesting in quasi-2D materials.** *Journal of Electron Spectroscopy and Related Phenomena*, **117-118**:433, 2001.
- [38] M.-H. WHANGBO, E. CANADELL, P. FOURY, AND J.-P. POUGET. **Hidden Fermi surface nesting and charge density wave instability in low-dimensional metals.** *Science*, **252**[5002]:96, 1991. 4
- [39] M. GIESEN, G. SCHULZE ICKING-KONERT, AND H. IBACH. **Interlayer mass transport and quantum confinement of electronic states.** *Phys. Rev. Lett.*, **82**[15]:3101, 1999. 4

BIBLIOGRAPHIC RESEARCH

- [40] K. MORGENSTERN, K.-F. BRAUN, AND K.-H. RIEDER. **Surface-state depopulation on small Ag(111) terraces.** *Phys. Rev. Lett.*, **89**[22]:226801, 2002. [4](#)
- [41] A. MUGARZA AND J. E. ORTEGA. **Electronic states at vicinal surfaces.** *Journal of Physics: Condensed Matter*, **15**[47]:S3281, 2003. [4](#), [117](#), [118](#), [119](#)
- [42] S. ROUSSET, V. REPAIN, G. BAUDOT, Y. GARREAU, AND J. LECOEUR. **Self-ordering of Au(111) vicinal surfaces and application to nanostructure organized growth.** *Journal of Physics: Condensed Matter*, **15**[47]:S3363, 2003. [117](#), [118](#), [119](#), [124](#)
- [43] M. CORSO, F. SCHILLER, L. FERNÁNDEZ, J. CORDÓN, AND J. E. ORTEGA. **Electronic states in faceted Au(111) studied with curved crystal surfaces.** *Journal of Physics: Condensed Matter*, **21**[35]:353001, 2009. [30](#), [118](#), [122](#), [124](#), [128](#)
- [44] J. E. ORTEGA, M. CORSO, Z. M. ABD-EL FATTAH, E. A. GOIRI, AND F. SCHILLER. **Interplay between structure and electronic states in step arrays explored with curved surfaces.** *Phys. Rev. B*, **83**[8]:085411, 2011. [4](#), [30](#), [118](#), [119](#), [126](#), [128](#)
- [45] A. BENDOUNAN, H. CERCELLIER, Y. FAGOT-REVURAT, B. KIERREN, V. Y. YUROV, AND D. MALTERRE. **Confinement of Shockley states in ultra thin films of Ag on Cu(111).** *Thin Solid Films*, **428**[1-2]:119, 2003. [4](#), [81](#)
- [46] A. BENDOUNAN, H. CERCELLIER, B. KIERREN, Y. FAGOT-REVURAT, V. Y. YUROV, AND D. MALTERRE. **Monitoring the local atomic structure by surface states spectroscopy.** *EPL (Europhysics Letters)*, **64**[3]:392, 2003. [81](#)
- [47] A. BENDOUNAN, H. CERCELLIER, Y. FAGOT-REVURAT, B. KIERREN, V. Y. YUROV, AND D. MALTERRE. **Modification of Shockley states induced by surface reconstruction in epitaxial Ag films on Cu(111).** *Phys. Rev. B*, **67**[16]:165412, 2003. [4](#), [84](#)
- [48] J. VAN DEN BRINK. **Graphene: What lies between.** *Nat Mater*, **9**[4]:291, 2010. [4](#)
- [49] E. SUTTER, P. ALBRECHT, AND P. SUTTER. **Graphene growth on polycrystalline Ru thin films.** *Applied Physics Letters*, **95**[13]:133109, 2009. [4](#)
- [50] F. SCHILLER, J. CORDÓN, D. VYALIKH, A. RUBIO, AND J. E. ORTEGA. **Fermi gap stabilization of an incommensurate two-dimensional superstructure.** *Phys. Rev. Lett.*, **94**[1]:016103, 2005. [4](#), [48](#), [49](#), [81](#), [85](#), [87](#), [106](#)
- [51] F. SCHILLER, J. CORDÓN, D. VYALIKH, A. RUBIO, AND J. E. ORTEGA. **Schiller et al. Reply:.** *Phys. Rev. Lett.*, **96**[2]:029702, 2006. [48](#), [81](#)
- [52] A. BENDOUNAN, F. FORSTER, J. ZIROFF, F. SCHMITT, AND F. REINERT. **Influence of the reconstruction in Ag/Cu(111) on the surface electronic structure: Quantitative analysis of the induced band gap.** *Phys. Rev. B*, **72**[7]:075407, 2005. [81](#), [87](#)

-
- [53] D. MALTERRE, B. KIERREN, Y. FAGOT-REVURAT, C. DIDIOT, F. J. GARCÍA DE ABAJO, F. SCHILLER, J. CORDÓN, AND J. E. ORTEGA. **Symmetry breaking and gap opening in two-dimensional hexagonal lattices.** *New Journal of Physics*, **13**[1]:013026, 2011. [81](#), [91](#), [92](#), [140](#)
 - [54] F. J. GARCÍA DE ABAJO, J. CORDÓN, M. CORSO, F. SCHILLER, AND J. E. ORTEGA. **Lateral engineering of surface states - Towards surface-state nanoelectronics.** *Nanoscale*, **2**[5]:717, 2010. [4](#), [81](#), [85](#), [87](#), [91](#), [92](#), [95](#), [131](#), [136](#)
 - [55] R. BALOG, B. JORGENSEN, L. NILSSON, M. ANDERSEN, E. RIENKS, M. BIANCHI, M. FANETTI, E. LAEGSGAARD, A. BARALDI, S. LIZZIT, Z. SLJIVANCANIN, F. BESSENBACHER, B. HAMMER, TH. G. PEDERSEN, PH. HOFMANN, AND L. HORNEKAER. **Bandgap opening in graphene induced by patterned hydrogen adsorption.** *Nat Mater*, **9**[4]:315, 2010. [4](#), [81](#)
 - [56] C. ENDERLEIN, Y. S. KIM, A. BOSTWICK, E. ROTENBERG, AND K. HORN. **The formation of an energy gap in graphene on ruthenium by controlling the interface.** *New Journal of Physics*, **12**[3]:033014, 2010. [4](#)
 - [57] M. GRIONI, CH. R. AST, D. PACILÉ, M. PAPAGNO, H. BERGER, AND L. PERFETTI. **Photoemission as a probe of coexisting and conflicting periodicities in low-dimensional solids.** *New Journal of Physics*, **7**[1]:106, 2005. [4](#), [136](#)
 - [58] M. Z. HASAN AND C. L. KANE. **Colloquium : Topological insulators.** *Reviews of Modern Physics*, **82**[4]:3045, 2010. [5](#), [179](#), [180](#)
 - [59] I. GIAEVER. **Energy gap in superconductors measured by electron tunneling.** *Phys. Rev. Lett.*, **5**[4]:147, 1960. [11](#)
 - [60] I. GIAEVER. **Electron tunneling between two superconductors.** *Phys. Rev. Lett.*, **5**[10]:464, 1960. [11](#)
 - [61] G. BINNIG AND H. ROHRER. **Scanning tunneling microscopy.** *Helvetica Physica Acta*, **55**:726, 1982. [11](#)
 - [62] G. BINNIG, H. ROHRER, CH. GERBER, AND E. WEIBEL. **Tunneling through a controllable vacuum gap.** *Applied Physics Letters*, **40**[2]:178, 1982.
 - [63] G. BINNIG, H. ROHRER, CH. GERBER, AND E. WEIBEL. **Surface studies by scanning tunneling microscopy.** *Phys. Rev. Lett.*, **49**[1]:57, 1982. [11](#)
 - [64] C. BAI. *Scanning Tunneling Microscopy and Its Application.* Springer Series in Surface Sciences. Springer, 2000. [12](#), [13](#)
 - [65] R. M. TROMP, R. J. HAMERS, AND J. E. DEMUTH. **Atomic and electronic contributions to Si(111)-(7×7) scanning-tunneling-microscopy images.** *Phys. Rev. B*, **34**[2]:1388, 1986. [13](#), [14](#)

BIBLIOGRAPHIC RESEARCH

- [66] A. MUGARZA. *Electronic Structure of Low-Dimensional Systems Analyzed by Angle-Resolved Photoemission Spectroscopy*. Phd thesis, University of the Basque Country, Donostia, 2002. [13](#), [14](#), [16](#), [17](#), [212](#)
- [67] C. DAVISSON AND L. H. GERMER. **Diffraction of electrons by a crystal of Nickel**. *Phys. Rev.*, **30**[6]:705, 1927. [14](#)
- [68] F. JONA, J. A. STROZIER JR, AND W. S. YANG. **Low-energy electron diffraction for surface structure analysis**. *Reports on Progress in Physics*, **45**[5]:527, 1982. [15](#)
- [69] F.-J. M. ZU HERINGDORF AND M. H. VON HOEGEN. **Reciprocal space mapping by spot profile analyzing low energy electron diffraction**. *Review of Scientific Instruments*, **76**[8]:085102, 2005. [15](#)
- [70] A. P. CRACKNELL AND K. C. WONG. *The Fermi Surface: Its Concept, Determination, and Use in the Physics of Metals*. Monographs on the physics and chemistry of materials. Clarendon Press, 1973. [18](#), [208](#), [211](#)
- [71] H. HERTZ. **An effect of ultraviolet light on electrical discharge**. *Annalen der Physik*, **267**:983, 1887. [19](#)
- [72] A. EINSTEIN. **On a heuristic viewpoint concerning the production and transformation of light**. *Annalen der Physik*, **322**:132, 1905. [19](#)
- [73] F. REINERT AND S. HÜFNER. **Photoemission spectroscopy: From early days to recent applications**. *New Journal of Physics*, **7**[1]:97, 2005. [20](#), [21](#)
- [74] W. SCHATTKKE AND M. A. VAN HOVE. *Solid-State Photoemission and Related Methods: Theory and Experiment*. John Wiley & Sons, 2008. [20](#), [22](#)
- [75] S. HÜFNER, R. CLAESSEN, F. REINERT, TH. STRAUB, V. N. STROCOV, AND P. STEINER. **Photoemission spectroscopy in metals:: Band structure-Fermi surface: Spectral function**. *Journal of Electron Spectroscopy and Related Phenomena*, **100**[1-3]:191, 1999. [22](#), [24](#), [26](#)
- [76] PH. HOFMANN. *Lecture Notes on Surface Science*. Aarhus University, 2005. [22](#), [23](#), [24](#), [29](#), [212](#), [213](#)
- [77] A. DAMASCELLI. **Probing the electronic structure of complex systems by ARPES**. *Physica Scripta*, **2004**[T109]:61, 2004. [22](#), [26](#), [213](#), [214](#)
- [78] F. J. HIMPSEL. **Angle-resolved measurements of the photoemission of electrons in the study of solids**. *Advances in Physics*, **32**[1]:1, 1983. [23](#)
- [79] G. J. LAPEYRE, R. J. SMITH, J. KNAPP, AND J. ANDERSON. **Constant final energy and constant initial energy spectroscopy**. *J. Phys. Colloques*, **39**:134, 1978. [24](#)

- [80] D. W. LYNCH AND C. G. OLSON. *Photoemission Studies of High-Temperature Superconductors*. Cambridge Studies in Low Temperature Physics. Cambridge University Press, 2005. 25, 26, 41
- [81] G. J. LAPEYRE. **Development of synchrotron radiation photoemission from photoionization to electron holography**. *Nuclear Instruments and Methods in Physics Research Section A: Accelerators, Spectrometers, Detectors and Associated Equipment*, **347**[1-3]:17, 1994. 25
- [82] F. SCHILLER, M. CORSO, J. CORDÓN, F. J. GARCÍA DE ABAJO, AND J. E. ORTEGA. **Interplay between electronic states and structure during Au faceting**. *New Journal of Physics*, **10**[11]:113017, 2008. 30, 119
- [83] Z. M. ABD EL-FATTAH. *Scanning Tunneling Microscopy Studies of Organic Molecules on top of Noble Metal Surfaces*. M.sc thesis, University of the Basque Country, 2009. 30
- [84] I. HORCAS, R. FERNANDEZ, J. M. GOMEZ-RODRIGUEZ, J. COLCHERO, J. GOMEZ-HERRERO, AND A. M. BARO. **WSXM: A software for scanning probe microscopy and a tool for nanotechnology**. *Review of Scientific Instruments*, **78**[1]:013705, 2007. 32, 33, 50
- [85] G. BINNIG, H. ROHRER, CH. GERBER, AND E. WEIBEL. **7×7 reconstruction on Si(111) resolved in real Space**. *Phys. Rev. Lett.*, **50**[2]:120, 1983. 34
- [86] K. D. BROMMER, M. NEEDELS, B. LARSON, AND J. D. JOANNOPOULOS. **Ab initio theory of the Si(111)-(7×7) surface reconstruction: A challenge for massively parallel computation**. *Phys. Rev. Lett.*, **68**[9]:1355, 1992.
- [87] S. KODIYALAM, K. E. KHOR, N. C. BARTELT, E. D. WILLIAMS, AND S. D. SARMA. **Energetics of vicinal Si(111) steps using empirical potentials**. *Phys. Rev. B*, **51**[8]:5200, 1995. 34
- [88] H. Z. SAR-EL. **Cylindrical capacitor as an analyzer I. Nonrelativistic Part**. *Review of Scientific Instruments*, **38**[9]:1210, 1967. 37
- [89] A. DAMASCELLI, Z. HUSSAIN, AND Z.-X. SHEN. **Angle-resolved photoemission studies of the cuprate superconductors**. *Rev. Mod. Phys.*, **75**[2]:473, 2003. 38, 40
- [90] H. DAIMON AND SH. INO. **Improvement of the spherical mirror analyzer**. *Review of Scientific Instruments*, **61**[1]:57, 1990. 39
- [91] D. SAKAI, D. MIURA, A. MARUYAMA, T. ISHIKAWA, AND CH. OSHIMA. **Large solid-angle analyzer applied to angle-resolved ultraviolet photoelectron spectroscopy**. *Journal of Electron Spectroscopy and Related Phenomena*, **159**[1-3]:39, 2007.

BIBLIOGRAPHIC RESEARCH

- [92] L. GREGORATTI, A. BARINOV, E. BENFATTO, G. CAUTERO, C. FAVA, P. LACOVIG, D. LONZA, M. KISKINOVA, R. TOMMASINI, S. MAHL, AND W. HEICHLER. **48-Channel electron detector for photoemission spectroscopy and microscopy.** *Review of Scientific Instruments*, **75**[1]:64, 2004. 37, 39
- [93] M. SEVERSON, M. BISSEN, M.V. FISHER, G. ROGERS, R. REININGER, M. GREEN, D. EISERT, AND B. TREDINNICK. **New SRC APPLE II variable polarization beamline.** *Nuclear Instruments and Methods in Physics Research Section A: Accelerators, Spectrometers, Detectors and Associated Equipment*, **649**[1]:55, 2011. 41
- [94] M. B. NIELSEN. *Fermi Surface Mappings using Angle-Resolved Ultraviolet Photoemission Spectroscopy.* M.sc thesis, Department of Physics and Astronomy, University of Aarhus, 2003. 43, 211
- [95] S.V. HOFFMANN, CH. SØNDERGAARD, CH. SCHULTZ, Z. LI, AND PH. HOFMANN. **An undulator-based spherical grating monochromator beamline for angle-resolved photoemission spectroscopy.** *Nuclear Instruments and Methods in Physics Research Section A: Accelerators, Spectrometers, Detectors and Associated Equipment*, **523**[3]:441, 2004. 43
- [96] F. SCHILLER AND C. LAUBSCHAT. **Surface states at close-packed surfaces of simple metals.** *Phys. Rev. B*, **74**[8]:085109, 2006. 47, 65, 210, 218
- [97] S. D. KEVAN, N. G. STOFFEL, AND N. V. SMITH. **Surface states on low-Miller-index copper surfaces.** *Phys. Rev. B*, **31**[6]:3348, 1985. 47
- [98] N. V. SMITH. **Phase analysis of image states and surface states associated with nearly-free-electron band gaps.** *Phys. Rev. B*, **32**[6]:3549, 1985. 63, 65, 98, 214, 216, 217
- [99] R. PANIAGO, R. MATZDORF, G. MEISTER, AND A. GOLDMANN. **Temperature dependence of Shockley-type surface energy bands on Cu(111), Ag(111) and Au(111).** *Surface Science*, **336**[1-2]:113, 1995. 62, 87, 98, 218
- [100] F. REINERT, G. NICOLAY, S. SCHMIDT, D. EHM, AND S. HÜFNER. **Direct measurements of the L -gap surface states on the (111) face of noble metals by photoelectron spectroscopy.** *Phys. Rev. B*, **63**[11]:115415, 2001. 47, 49, 71, 150, 219, 220
- [101] M. MATENA, T. RIEHM, M. STÖHR, TH. A. JUNG, AND L. H. GADE. **Transforming surface coordination polymers into covalent surface polymers: Linked polycondensed aromatics through oligomerization of N-Heterocyclic carbene intermediates.** *Angewandte Chemie International Edition*, **47**[13]:2414, 2008. 47
- [102] L. LIMOT, E. PEHLKE, J. KRÖGER, AND R. BERNDT. **Surface-state localization at adatoms.** *Phys. Rev. Lett.*, **94**[3]:036805, 2005. 47

- [103] F. E. OLSSON, M. PERSSON, A. G. BORISOV, J.-P. GAUYACQ, J. LAGOUTE, AND S. FÖLSCH. **Localization of the Cu(111) surface state by single Cu adatoms.** *Phys. Rev. Lett.*, **93**[20]:206803, 2004. 47
- [104] CH.-M CHENG, K.-D TSUEI, CH.-T. TSAI, AND D.-A. LUH. **Precise determination of absolute coverage of thin films by layer-resolved surface states.** *Applied Physics Letters*, **92**[16]:163102, 2008. 48, 61
- [105] A. BENDOUNAN, Y. FAGOT-REVURAT, B. KIERREN, F. BERTRAN, V. Y. YUROV, AND D. MALTERRE. **Surface state in epitaxial Ag ultrathin films on Cu(111).** *Surface Science*, **496**[1-2]:L43, 2002. 48, 49, 61
- [106] A. BENDOUNAN, K. AÏT-MANSOUR, J. BRAUN, J. MINÁR, S. BORNEMANN, R. FASEL, O. GRÖNING, F. SIROTTI, AND H. EBERT. **Evolution of the Rashba spin-orbit-split Shockley state on Ag/Pt(111).** *Phys. Rev. B*, **83**[19]:195427, 2011. 48, 61, 63
- [107] L. MORESCHINI, A. BENDOUNAN, H. BENTMANN, M. ASSIG, K. KERN, F. REINERT, J. HENK, C. R. AST, AND M. GRIONI. **Influence of the substrate on the spin-orbit splitting in surface alloys on (111) noble-metal surfaces.** *Phys. Rev. B*, **80**[3]:035438, 2009.
- [108] CH. R. AST, J. HENK, A. ERNST, L. MORESCHINI, M. C. FALUB, D. PACILÉ, P. BRUNO, K. KERN, AND M. GRIONI. **Giant spin splitting through surface alloying.** *Phys. Rev. Lett.*, **98**[18]:186807, 2007. 48, 169
- [109] T. MILLER, A. SAMSAVAR, G. E. FRANKLIN, AND T. C. CHIANG. **Quantum-well states in a metallic system: Ag on Au(111).** *Phys. Rev. Lett.*, **61**[12]:1404, 1988. 48, 66
- [110] F. FORSTER. *Eigenschaften und Modifikation zweidimensionaler Elektronenzustände auf Edelmetallen (Properties and Modification of Two-Dimensional Electronic States in Precious Metals)*. Phd thesis, Julius-Maximilians-Universität Würzburg, 2007. 48
- [111] A. BENDOUNAN, F. FORSTER, F. REINERT, B. KIERREN, Y. FAGOT-REVURAT, AND D. MALTERRE. **Comment on “Fermi gap stabilization of an incommensurate two-dimensional superstructure”.** *Phys. Rev. Lett.*, **96**[2]:029701, 2006. 48, 81
- [112] C. CHAMBON, A. COATI, M. SAUVAGE-SIMKIN, Y. GARREAU, J. CREUZE, A. VERDINI, A. COSSARO, L. FLOREANO, AND A. MORGANTE. **Early stages of formation of the Ag-Ni(111) interface studied by grazing incidence x-ray diffraction and x-ray photoelectron diffraction.** *Phys. Rev. B*, **84**[16]:165446, 2011. 48, 149, 154
- [113] K. UMEZAWA, SH. NAKANISHI, AND W. M. GIBSON. **Growth modes depending on the growing temperature in heteroepitaxy: Au/Ni(111).** *Phys. Rev. B*, **57**[15]:8842, 1998.

BIBLIOGRAPHIC RESEARCH

- [114] A. B. PREOBRJENSKI, M. L. NG, A. S. VINOGRADOV, AND N. MÅRTENSSON. **Controlling graphene corrugation on lattice-mismatched substrates.** *Phys. Rev. B*, **78**[7]:073401, 2008. 48
- [115] S. M. FOILES, M. I. BASKES, AND M. S. DAW. **Embedded-atom-method functions for the fcc metals Cu, Ag, Au, Ni, Pd, Pt, and their alloys.** *Phys. Rev. B*, **33**[12]:7983, 1986. 48, 53
- [116] J. JIN-FENG, I. KEISUKE, H. YUKIO, Y. WEI-SHENG, AND SAKURAI TOSHIO. **Scanning tunneling microscopy measurements of the local work function around steps on the Au/Cu(111) surface(STM-local states).** *Science reports of the Research Institutes, Tohoku University. Ser. A, Physics, chemistry and metallurgy*, **44**[1]:105, 1997-03-28. 48
- [117] J. F. JIA, K. INOUE, Y. HASEGAWA, W. S. YANG, AND T. SAKURAI. **Variation of the local work function at steps on metal surfaces studied with STM.** *Phys. Rev. B*, **58**[3]:1193, 1998.
- [118] J. F. JIA, Y. HASEGAWA, K. INOUE, W. S. YANG, AND T. SAKURAI. **Steps on the Au/Cu(111) surface studied by local work function measurement with STM.** *Applied Physics A: Materials Science & Processing*, **66**:1125, 1998. 48
- [119] A. K. SANTRA AND C. N. R. RAO. **Surface alloy formation in Pd/Ag, Cu/Au and Ni/Au bimetallic overlayers.** *Applied Surface Science*, **84**[4]:347, 1995. 48
- [120] M. KUHN, A. BZOWSKI, T. K. SHAM, J. A. RODRIGUEZ, AND J. HRBEK. **Ru-promoted alloying of Au and Cu ultrathin films: Photoemission studies.** *Thin Solid Films*, **283**[1-2]:209, 1996. 48, 53, 55, 59, 69
- [121] R. XU, S. BAO, AND G. LIU. **An investigation of the ordered Au/Cu(111) surface: LEED, ARAES and ARUPS results.** *Surface Science*, **234**[3]:335, 1990. 48
- [122] R. D. MALDONADO AND A. I. OLIVA. **Morphology and electrical resistivity of AuCu nanofilm alloys.** *Surface Review and Letters*, **15**[06]:881, 2008. 48
- [123] W. WALLAUER AND TH. FAUSTER. **Growth of Ag, Au, and Co on Cu(111) studied by high-resolution spectroscopy of image states.** *Surface Science*, **331-333**, Part A:731, 1995. 48
- [124] J. E. MACUR AND R. W. VOOK. **Initial epitaxial growth of (111) Au/(111) Cu and (111) Cu/(111) Au.** *Thin Solid Films*, **66**[3]:371, 1980.
- [125] T. C. Q. NOAKES AND P. BAILEY. **A medium energy ion scattering study of metal-on-metal epitaxy and surfactant-mediated growth for the Au on Cu(111) system.** *Thin Solid Films*, **394**[1]:15–22, 2001. 48

- [126] J. CORDÓN. *Interaction of Surface Electronic States with Periodic Superstructures*. Phd thesis, University of Basque Country UPV/EHU, 2012. 49, 65, 84, 85, 87, 150, 152, 156
- [127] D. MALTERRE, B. KIERREN, Y. FAGOT-REVURAT, S. PONS, A. TEJEDA, C. DIDOT, H. CERCELLIER, AND A. BENDOUNAN. **ARPES and STS investigation of Shockley states in thin metallic films and periodic nanostructures**. *New Journal of Physics*, 9[10]:391, 2007. 49, 81, 91
- [128] M. CORSO, L. FERNÁNDEZ, F. SCHILLER, AND J. E. ORTEGA. **Au(111)-based nanotemplates by Gd alloying**. *ACS Nano*, 4[3]:1603, 2010. 55, 80
- [129] M. P. SEAH AND W. A. DENCH. **Quantitative electron spectroscopy of surfaces: A standard data base for electron inelastic mean free paths in solids**. *Surface and Interface Analysis*, 1[1]:2, 1979. 55
- [130] Z. M. ABD EL-FATTAH, M. MATENA, M. CORSO, F. J. GARCÍA DE ABAJO, F. SCHILLER, AND J. E. ORTEGA. **Lifshitz transition across the Ag/Cu(111) superlattice band gap tuned by interface doping**. *Phys. Rev. Lett.*, 107[6]:066803, 2011. 59
- [131] H. BENTMANN, A. BUCHTER, AND F. REINERT. **Interplay of electronic structure and atomic ordering on surfaces: Momentum-resolved measurements of Cs atoms adsorbed on a Ag(111) substrate**. *Phys. Rev. B*, 85[12]:121412, 2012. 62
- [132] F. FORSTER, S. HÜFNER, AND F. REINERT. **Rare gases on noble-metal surfaces: An angle-resolved photoemission study with high energy resolution**. *The Journal of Physical Chemistry B*, 108[38]:14692, 2004. 62
- [133] J. REPP, G. MEYER, AND K.-H. RIEDER. **Snell’s law for surface electrons: Refraction of an electron gas imaged in real space**. *Phys. Rev. Lett.*, 92[3]:036803, 2004. 62
- [134] K. SAWA, Y. AOKI, AND H. HIRAYAMA. **Dislocation-induced local modulation of the surface states of Ag(111) thin films on Si(111) 7×7 substrates**. *Phys. Rev. Lett.*, 104[1]:016806, 2010. 63
- [135] Y. YU, K. SAGISAKA, AND D. FUJITA. **Modification of surface electronic properties on alloy surfaces: Standing waves on a Cu-9 at. % Al(111) surface observed by STM**. *Phys. Rev. B*, 79[23]:235427, 2009. 63
- [136] M. A. MUELLER, A. SAMSAVAR, T. MILLER, AND T.-C. CHIANG. **Probing interfacial properties with Bloch electrons: Ag on Cu(111)**. *Phys. Rev. B*, 40[8]:5845, 1989. 65, 66, 172
- [137] T.-C. CHIANG. **Photoemission studies of quantum well states in thin films**. *Surface Science Reports*, 39[7-8]:181, 2000. 65, 110

BIBLIOGRAPHIC RESEARCH

- [138] TH. ANDREEV, I. BARKE, AND H. HÖVEL. **Adsorbed rare-gas layers on Au(111): Shift of the Shockley surface state studied with ultraviolet photoelectron spectroscopy and scanning tunneling spectroscopy.** *Phys. Rev. B*, **70**[20]:205426, 2004. 65
- [139] S. MATHIAS, M. WESSENDORF, S. PASSLACK, M. AESCHLIMANN, AND M. BAUER. **Morphological modifications of Ag/Cu(111) probed by photoemission spectroscopy of quantum well states and the Shockley surface state.** *Applied Physics A: Materials Science & Processing*, **82**[3]:439–445, 2006.
- [140] L. HUANG, X. G. GONG, E. GERGERT, F. FORSTER, A. BENDOUNAN, F. REINERT, AND Z. ZHANG. **Evolution of a symmetry gap and synergetic quantum well states in ultrathin Ag films on Au(111) substrates.** *EPL (Europhysics Letters)*, **78**[5]:57003, 2007. 172
- [141] E. OGANDO, N. ZABALA, E. V. CHULKOV, AND M. J. PUSKA. **Quantum well states, resonances and stability of metallic overlayers.** *Journal of Physics: Condensed Matter*, **20**[31]:315002, 2008. 66
- [142] J. V. BARTH, H. BRUNE, G. ERTL, AND R. J. BEHM. **Scanning tunneling microscopy observations on the reconstructed Au(111) surface: Atomic structure, long-range superstructure, rotational domains, and surface defects.** *Phys. Rev. B*, **42**[15]:9307, 1990. 72, 207, 212
- [143] I. MEUNIER, G. TRÉGLIA, J.-M. GAY, B. AUFRAY, AND B. LEGRAND. **Ag/Cu(111) structure revisited through an extended mechanism for stress relaxation.** *Phys. Rev. B*, **59**[16]:10910, 1999. 80, 89
- [144] I. MEUNIER, R. TÉTOT, G. TRÉGLIA, AND B. LEGRAND. **Thermal dependence of surface polymorphism: The Ag/Cu (111) case.** *Applied Surface Science*, **177**[4]:252, 2001.
- [145] E. BAUER. **Epitaxy of metals on metals.** *Applications of Surface Science*, **1112**[0]:479, 1982.
- [146] B. AUFRAY, M. GÖTHELID, J.-M. GAY, CH. MOTTET, E. LANDEMARK, G. FALKENBERG, L. LOTTERMOSER, L. SEEHOFER, AND R. L. JOHNSON. **An incommensurate reconstruction studied with scanning tunneling microscopy and Surface X-Ray Diffraction.** *Microsc. Microanal. Microstruct.*, **8**[3]:167, 1997. 80
- [147] J. HRBEK AND R.Q. HWANG. **Interaction of adsorbates on strained metallic layers.** *Current Opinion in Solid State and Materials Science*, **5**[1]:67, 2001. 80
- [148] K. AÏT-MANSOUR, M. TREIER, P. RUFFIEUX, M. BIERI, R. JAAFAR, P. GRÖNING, R. FASEL, AND O. GRÖNING. **Template-directed molecular nanostructures on the**

- Ag/Pt(111) dislocation network.** *The Journal of Physical Chemistry C*, **113**[19]:8407, 2009. 80
- [149] D.-A. LUH, K.-CH. LIU, CH.-M. CHENG, AND K.-D. TSUEI. **Characterizing the wetting of metallic thin films with angle-resolved photoelectron spectroscopy.** *Phys. Rev. B*, **82**[7]:075434, 2010. 81
- [150] M. WIESENMAYER, M. BAUER, S. MATHIAS, M. WESSENDORF, E. V. CHULKOV, V. M. SILKIN, A. G. BORISOV, J.-P. GAUYACQ, P. M. ECHENIQUE, AND M. AESCHLI-MANN. **Lifetime of an adsorbate excitation modified by a tunable two-dimensional substrate.** *Phys. Rev. B*, **78**[24]:245410, 2008. 87
- [151] M. C. HÅKANSSON AND L. S. O. JOHANSSON. **Photoemission study of low coverage potassium adsorption on the Si(111)1×1: As surface.** *Surface Science*, **342**[13]:293, 1995. 87
- [152] T. GREBER, T. J. KREUTZ, AND J. OSTERWALDER. **Photoemission above the Fermi level: The top of the minority d band in Nickel.** *Phys. Rev. Lett.*, **79**[22]:4465, 1997. 91
- [153] H. BRUNE, H. RÖDER, C. BORAGNO, AND K. KERN. **Strain relief at hexagonal-close-packed interfaces.** *Phys. Rev. B*, **49**[4]:2997, 1994. 91
- [154] W. L. LING, J. C. HAMILTON, K. THRMER, G. E. THAYER, J. DE LA FIGUERA, R. Q. HWANG, C. B. CARTER, N. C. BARTELT, AND K. F. MCCARTY. **Herringbone and triangular patterns of dislocations in Ag, Au, and AgAu alloy films on Ru(0001).** *Surface Science*, **600**[9]:1735, 2006. 91
- [155] V. MYROSHNYCHENKO, E. CARBÓ-ARGIBAY, I. PASTORIZA-SANTOS, J. PÉREZ-JUSTE, L. M. LIZ-MARZÁN, AND F. J. GARCÍA DE ABAJO. **Modeling the optical response of highly faceted metal nanoparticles with a fully 3D boundary element method.** *Advanced Materials*, **20**[22]:4288, 2008. 92
- [156] T. OHTA, A. BOSTWICK, TH. SEYLLER, K. HORN, AND E. ROTENBERG. **Controlling the electronic structure of bilayer graphene.** *Science*, **313**[5789]:951, 2006. 95
- [157] C. LIU, T. KONDO, R. M. FERNANDES, A. D. PALCZEWSKI, E. D. MUN, N. NI, A. N. THALER, A. BOSTWICK, E. ROTENBERG, J. SCHMALIAN, S. L. BUD'KO, P. C. CANFIELD, AND A. KAMINSKI. **Evidence for a Lifshitz transition in electron-doped iron arsenic superconductors at the onset of superconductivity.** *Nature Physics*, **6**[6]:419, 2010. 95
- [158] J. KLIEWER, R. BERNDT, E. V. CHULKOV, V. M. SILKIN, P. M. ECHENIQUE, AND S. CRAMPIN. **Dimensionality effects in the lifetime of surface states.** *Science*, **288**[5470]:1399, 2000. 95

BIBLIOGRAPHIC RESEARCH

- [159] D.-A. LUH, K.-CH. LIU, CH.-M. CHENG, AND K.-D. TSUEI. **Rapid deterioration of metallic surfaces induced by intense ultraviolet radiation.** *Phys. Rev. B*, **81**[3]:035427, 2010. 96, 103
- [160] P. M. ECHENIQUE, R. BERNDT, E. V. CHULKOV, TH. FAUSTER, A. GOLDMANN, AND U. HFER. **Decay of electronic excitations at metal surfaces.** *Surface Science Reports*, **52**[78]:219, 2004. 101
- [161] PH. HOFMANN, I. Y. SKLYADNEVA, E. D. L. RIENKS, AND E. V. CHULKOV. **Electron-phonon coupling at surfaces and interfaces.** *New Journal of Physics*, **11**[12]:125005, 2009.
- [162] R. MATZDORF. **Quasi-particle lifetimes on noble metal surfaces studied by ARPES and STM.** *Chemical Physics*, **251**[13]:151, 2000. 101
- [163] A. EIGUREN, B. HELLSING, F. REINERT, G. NICOLAY, E. V. CHULKOV, V. M. SILKIN, S. HÜFNER, AND P. M. ECHENIQUE. **Role of bulk and surface phonons in the decay of metal surface states.** *Phys. Rev. Lett.*, **88**[6]:066805, 2002. 101
- [164] M. F. JENSEN. *Many-body Interactions Investigated with Angle-Resolved Photoemission Spectroscopy*. Phd thesis, Interdisciplinary Nanoscience Center (iNANO), Institute for Storage Ring Facilities in Aarhus, Department of Physics and Astronomy, Aarhus University, 2009. 101, 102
- [165] C. WALDFRIED, D. N. MCILROY, J. ZHANG, P. A. DOWBEN, G. A. KATRICH, AND E. W. PLUMMER. **Determination of the surface Debye temperature of Mo(112) using valence band photoemission.** *Surface Science*, **363**[13]:296, 1996. 102, 103
- [166] S. MATHIAS, S. V. EREMEEV, E. V. CHULKOV, M. AESCHLIMANN, AND M. BAUER. **Quantum oscillations in coupled two-dimensional electron systems.** *Phys. Rev. Lett.*, **103**[2]:026802, 2009. 103, 105
- [167] R. L. SCHWOEBEL AND E. J. SHIPSEY. **Step motion on crystal surfaces.** *Journal of Applied Physics*, **37**[10]:3682, 1966. 118
- [168] G. EHRLICH AND F. G. HUDDA. **Atomic view of surface self-diffusion: Tungsten on Tungsten.** *The Journal of Chemical Physics*, **44**[3]:1039, 1966. 118
- [169] S. SPELLER, S. DEGROOTE, J. DEKOSTER, G. LANGOUCHE, J. E. ORTEGA, AND A. NÄRMANN. **Low-temperature deposition of Co on Cu(111): Effects on step etching.** *Surface Science*, **405**[23]:L542, 1998. 119
- [170] F. J. HIMPSEL, A. KIRAKOSIAN, J. N. CRAIN, J.-L. LIN, AND D. Y. PETROVYKH. **Self-assembly of one-dimensional nanostructures at silicon surfaces.** *Solid State Communications*, **117**[3]:149, 2001.

- [171] H. RAUSCHER, T. A. JUNG, J.-L. LIN, A. KIRAKOSIAN, F. J. HIMPSEL, U. ROHR, AND K. MULLEN. **One-dimensional confinement of organic molecules via selective adsorption on CaF1 versus CaF2.** *Chemical Physics Letters*, **303**[3]:363, 1999.
- [172] S. FÖLSCH, A. HELMS, S. ZÖPHEL, J. REPP, G. MEYER, AND K. H. RIEDER. **Self-Organized Patterning of an Insulator-on-Metal System by Surface Faceting and Selective Growth: NaCl/Cu(211).** *Phys. Rev. Lett.*, **84**[1]:123, 2000.
- [173] F. SCHILLER, M. RUIZ-OSÉS, J. E. ORTEGA, P. SEGOVIA, J. MARTINEZ-BLANCO, B. P. DOYLE, V. PEREZ-DIESTE, J. LOBO, N. NEEL, R. BERNDT, AND J. KROGER. **Electronic structure of C₆₀ on Au(887).** *The Journal of Chemical Physics*, **125**[14]:144719, 2006.
- [174] N. NÉEL, J. KRÖGER, AND R. BERNDT. **Highly periodic fullerene nanomesh.** *Advanced Materials*, **18**[2]:174, 2006.
- [175] W. XIAO, P. RUFFIEUX, K. AÏT-MANSOUR, O. GRÖNING, K. PALOTAS, W. A. HOFER, P. GRÖNING, AND R. FASEL. **Formation of a regular fullerene nanochain lattice.** *The Journal of Physical Chemistry B*, **110**[43]:21394, 2006.
- [176] V. REPAIN, G. BAUDOT, H. ELLMER, AND S. ROUSSET. **Ordered growth of cobalt nanostructures on a Au(111) vicinal surface: Nucleation mechanisms and temperature behavior.** *Materials Science and Engineering: B*, **96**[2]:178, 2002.
- [177] M. MATENA ET AL. *unpublished*.
- [178] A. R. BACHMANN, S. SPELLER, A. MUGARZA, AND J. E. ORTEGA. **Driving forces for Ag-induced periodic faceting of vicinal Cu(111).** *Surface Science*, **526**[12]:L143, 2003. 119
- [179] A. R. BACHMANN, A. MUGARZA, J. E. ORTEGA, AND S. SPELLER. **One-dimensional Ag-Cu superlattices on vicinal Cu(111).** *Phys. Rev. B*, **64**[15]:153409, 2001. 119
- [180] N. NÉEL, J. KROGER, AND R. BERNDT. **Fullerene nanowires on a vicinal gold surface.** *Applied Physics Letters*, **88**[16]:163101, 2006.
- [181] O. FRUCHART AND A. THIAVILLE. **Magnetism in reduced dimensions.** *Comptes Rendus Physique*, **6**[9]:921, 2005. 119
- [182] J. E. ORTEGA, S. SPELLER, A. R. BACHMANN, A. MASCARAQUE, E. G. MICHEL, A. NÄRMANN, A. MUGARZA, A. RUBIO, AND F. J. HIMPSEL. **Electron wave function at a vicinal surface: Switch from terrace to step modulation.** *Phys. Rev. Lett.*, **84**[26]:6110, 2000. 119, 124
- [183] F. BAUMBERGER, T. GREBER, AND J. OSTERWALDER. **Step-induced one-dimensional surface state on Cu(332).** *Phys. Rev. B*, **62**[23]:15431, 2000.

BIBLIOGRAPHIC RESEARCH

- [184] A. MUGARZA, A. MASCARAQUE, V. PÉREZ-DIESTE, V. REPAIN, S. ROUSSET, F. J. GARCÍA DE ABAJO, AND J. E. ORTEGA. **Electron confinement in surface states on a stepped gold surface revealed by angle-resolved photoemission.** *Phys. Rev. Lett.*, **87**[10]:107601, 2001.
- [185] F. BAUMBERGER, T. GREBER, AND J. OSTERWALDER. **Fermi surfaces of the two-dimensional surface states on vicinal Cu(111).** *Phys. Rev. B*, **64**[19]:195411, 2001.
- [186] A. MUGARZA, A. MASCARAQUE, V. REPAIN, S. ROUSSET, K. N. ALTMANN, F. J. HIMPSEL, YU. M. KOROTEEV, E. V. CHULKOV, F. J. GARCÍA DE ABAJO, AND J. E. ORTEGA. **Lateral quantum wells at vicinal Au(111) studied with angle-resolved photoemission.** *Phys. Rev. B*, **66**[24]:245419, 2002.
- [187] F. BAUMBERGER, M. HENGESBERGER, M. MUNTWILER, M. SHI, J. KREMPASKY, L. PATTHEY, J. OSTERWALDER, AND T. GREBER. **Localization of surface states in disordered step lattices.** *Phys. Rev. Lett.*, **92**[19]:196805, 2004.
- [188] J. E. ORTEGA, M. RUIZ-OSÉS, J. CORDÓN, A. MUGARZA, J. KUNTZE, AND F. SCHILLER. **One-dimensional versus two-dimensional electronic states in vicinal surfaces.** *New Journal of Physics*, **7**[1]:101, 2005.
- [189] J. E. ORTEGA, A. MUGARZA, V. PÉREZ-DIESTE, V. REPAIN, S. ROUSSET, AND A. MASCARAQUE. **Probing wave functions at step superlattices: Confined versus propagating electrons.** *Materials Science and Engineering: B*, **96**[2]:154, 2002. 119
- [190] F. BAUMBERGER, M. HENGESBERGER, M. MUNTWILER, M. SHI, J. KREMPASKY, L. PATTHEY, J. OSTERWALDER, AND T. GREBER. **Step-lattice-induced band-gap opening at the Fermi level.** *Phys. Rev. Lett.*, **92**[1]:016803, 2004. 119
- [191] J. E. ORTEGA AND F. J. GARCÍA DE ABAJO. **Surface patterning: Self-assembly works for superlattices.** *Nat Nanotechnol*, **2**[10]:601, 2007. 119
- [192] J. LOBO, E. G. MICHEL, A. R. BACHMANN, S. SPELLER, J. KUNTZE, AND J. E. ORTEGA. **Tuning the surface state dimensionality of Cu nanostripes.** *Phys. Rev. Lett.*, **93**[13]:137602, 2004. 120
- [193] J. E. ORTEGA, M. RUIZ-OSÉS, AND J. KUNTZE. **Finite size effects in surface states of stepped Cu nanostripes.** *Phys. Rev. B*, **72**[19]:195416, 2005. 120
- [194] F. SCHILLER, M. RUIZ-OSÉS, J. CORDÓN, AND J. E. ORTEGA. **Scattering of surface states at step edges in nanostripe arrays.** *Phys. Rev. Lett.*, **95**[6]:066805, 2005. 120
- [195] Z. M. ABD EL-FATTAH M. MATENA F. SCHILLER D. MOWBRAY J. E. ORTEGA, J. LOBO-CHECA AND A. RUBIO . **Transparency of Ag steps to surface electrons.** *unpublished.* 131, 132

- [196] N. ZAKI, K. KNOX, P. D. JOHNSON, J. FUJII, I. VOBORNIK, G. PANACCIONE, AND R. M. OSGOOD. **Surface states on vicinal Cu(775): STM and photoemission study.** *Phys. Rev. B*, **83**[20]:205420, 2011. 136
- [197] V. M. KARPAN, P. A. KHOMYAKOV, A. A. STARIKOV, G. GIOVANNETTI, M. ZWIERZYCKI, M. TALANANA, G. BROCKS, J. VAN DEN BRINK, AND P. J. KELLY. **Theoretical prediction of perfect spin filtering at interfaces between close-packed surfaces of Ni or Co and graphite or graphene.** *Phys. Rev. B*, **78**[19]:195419, 2008. 149
- [198] C. CHAMBON, J. CREUZE, A. COATI, M. SAUVAGE-SIMKIN, AND Y. GARREAU. **Tilted and nontilted Ag overlayer on a Ni(111) substrate: Structure and energetics.** *Phys. Rev. B*, **79**[12]:125412, 2009. 149, 154
- [199] K. AÏT-MANSOUR AND O. GRÖNING. **Comment on Ag organisation on Ni(111) surface [Surface Science 602 (2008) 2363].** *Surface Science*, **604**[910]:872, 2010. 149, 154
- [200] A. MEYER, J. I. FLEGE, R. E. RETTEW, S. D. SENANAYAKE, TH. SCHMIDT, F. M. ALAMGIR, AND J. FALTA. **Ultrathin silver films on Ni(111).** *Phys. Rev. B*, **82**[8]:085424, 2010. 149
- [201] G. HELD. **The interplay between geometry, electronic structure, and reactivity of Cu-Ni bimetallic (111) surfaces.** *Applied Physics A: Materials Science Processing*, **76**[5]:689, 2003. 149, 150
- [202] J. LOBO-CHECA, T. OKUDA, M. HENGESBERGER, L. PATTHEY, TH. GREBER, P. BLAHA, AND J. OSTERWALDER. **Hidden surface states on pristine and H-passivated Ni(111): Angle-resolved photoemission and density-functional calculations.** *Phys. Rev. B*, **77**[7]:075415, 2008. 149, 153
- [203] A. VARYKHALOV, M. R. SCHOLZ, TIMUR K. KIM, AND O. RADER. **Effect of noble-metal contacts on doping and band gap of graphene.** *Phys. Rev. B*, **82**[12]:121101, 2010. 149, 150
- [204] A. M. SHIKIN, G. V. PRUDNIKOVA, V. K. ADAMCHUK, F. MORESCO, AND K.-H. RIEDER. **Surface intercalation of gold underneath a graphite monolayer on Ni(111) studied by angle-resolved photoemission and high-resolution electron-energy-loss spectroscopy.** *Phys. Rev. B*, **62**[19]:13202, 2000. 150
- [205] Y. S. DEDKOV, A. M. SHIKIN, V. K. ADAMCHUK, S. L. MOLODTSOV, C. LAUBSCHAT, A. BAUER, AND G. KAINDL. **Intercalation of copper underneath a monolayer of graphite on Ni(111).** *Phys. Rev. B*, **64**[3]:035405, 2001.
- [206] A. STARODUBOV, M. MEDVETSKII, A. SHIKIN, AND V. ADAMCHUK. **Intercalation of silver atoms under a graphite monolayer on Ni(111).** *Physics of the Solid State*, **46**[7]:1340, 2004. 149

BIBLIOGRAPHIC RESEARCH

- [207] A. H. C. NETO, F. GUINEA, N. M. R. PERES, K. S. NOVOSELOV, AND A. K. GEIM. **The electronic properties of graphene.** *Rev. Mod. Phys.*, **81**[1]:109, 2009. 150
- [208] D. JARIWALA, A. SRIVASTAVA, AND P. AJAYAN. **Graphene synthesis and band gap opening.** *ArXiv e-prints*, 2011. 150
- [209] Y. S. DEDKOV, M. FONIN, U. RÜDIGER, AND C. LAUBSCHAT. **Rashba effect in the graphene/Ni(111) system.** *Phys. Rev. Lett.*, **100**[10]:107602, 2008. 150
- [210] A. VARYKHALOV, J. SÁNCHEZ-BARRIGA, A. M. SHIKIN, C. BISWAS, E. VESCOVO, A. RYBKIN, D. MARCHENKO, AND O. RADER. **Electronic and magnetic properties of quasifreestanding graphene on Ni.** *Phys. Rev. Lett.*, **101**[15]:157601, 2008. 150
- [211] E. BERTEL. **Symmetry of surface states.** *Phys. Rev. B*, **50**[7]:4925, 1994. 151, 152, 153, 173
- [212] J. BRAUN AND M. DONATH. **Contest between surface resonances and surface states at 3d ferromagnets.** *EPL (Europhysics Letters)*, **59**[4]:592, 2002. 152, 153
- [213] M. DONATH, F. PASSEK, AND V. DOSE. **Surface state contribution to the magnetic moment of Ni(111).** *Phys. Rev. Lett.*, **70**[18]:2802, 1993. 152, 153
- [214] F. J. HIMPSEL AND D. E. EASTMAN. **Observation of a Λ_1 -symmetry surface state on Ni(111).** *Phys. Rev. Lett.*, **41**[7]:507, 1978. 153
- [215] J. KUTZNER, R. PAUCKSCH, C. JABS, H. ZACHARIAS, AND J. BRAUN. **High-resolution photoelectron emission spectroscopy of surface states on Ni(111).** *Phys. Rev. B*, **56**[24]:16003, 1997. 153
- [216] W. AUWÄRTER. *One monolayer of hexagonal boron nitride on Ni(111): An atomically sharp interface.* Phd thesis, Universitat Zurich, 2003. 153
- [217] P. LAZIĆ, Ž. CRLJEN, AND R. BRAKO. **Localization and hybridization of the electronic states in thin films of Ag on V(100).** *Phys. Rev. B*, **71**[15]:155402, 2005. 160
- [218] V. M. TRONTL, P. PERVAN, AND M. MILUN. **Growth and electronic properties of ultra-thin Ag films on Ni(111).** *Surface Science*, **603**[1]:125, 2009. 160
- [219] I. PLETIKOSIĆ, V. M. TRONTL, M. MILUN, D. ŠOKČEVIĆ, R. BRAKO, AND P. PERVAN. **d-band quantum well states in Ag(111) monolayer films; Substrate-induced shifts.** *Journal of Physics: Condensed Matter*, **20**[35]:355004, 2008. 160
- [220] J. VOIGT, X. L. DING, R. FINK, G. KRAUSCH, B. LUCKSCHEITER, R. PLATZER, U. WÖHRMANN, AND G. SCHATZ. **Monolayer-resolved detection of magnetic hyperfine fields at Cu/Ni(111) interfaces.** *Phys. Rev. Lett.*, **66**[24]:3199, 1991. 165

- [221] S. LASHELL, B. A. MCDUGALL, AND E. JENSEN. **Spin splitting of an Au(111) surface state band observed with angle resolved photoelectron spectroscopy.** *Phys. Rev. Lett.*, **77**[16]:3419, 1996. 167, 169, 220
- [222] I. GIERZ. *Investigation of Two-Dimensional Electron Gases with Angular Resolved Photoemission Spectroscopy.* Phd thesis, FACULT SCIENCES DE BASE LABORATOIRE DE SCIENCE L'CHELLE NANOMETRIQUE, 2011. 167, 169
- [223] Y. A. BYCHKOV AND É. I. RASHBA. **Properties of a 2D electron gas with lifted spectral degeneracy.** *Soviet Journal of Experimental and Theoretical Physics Letters*, **39**:78, 1984. 168
- [224] H. CERCELLIER, Y. FAGOT-REVURAT, B. KIERREN, F. REINERT, D. POPOVIĆ, AND D. MALTERRE. **Spin-orbit splitting of the Shockley state in the Ag/Au(111) interface.** *Phys. Rev. B*, **70**[19]:193412, 2004. 169
- [225] CH. R. AST, D. PACILÉ, L. MORESCHINI, M. C. FALUB, M. PAPAGNO, K. KERN, M. GRIONI, J. HENK, A. ERNST, S. OStanIN, AND P. BRUNO. **Spin-orbit split two-dimensional electron gas with tunable Rashba and Fermi energy.** *Phys. Rev. B*, **77**[8]:081407, 2008. 169, 193
- [226] H. BENTMANN, F. FORSTER, G. BIHLMAYER, E. V. CHULKOV, L. MORESCHINI, M. GRIONI, AND F. REINERT. **Origin and manipulation of the Rashba splitting in surface alloys.** *EPL (Europhysics Letters)*, **87**[3]:37003, 2009. 169
- [227] G. BIHLMAYER, YU.M. KOROTEEV, P.M. ECHENIQUE, E.V. CHULKOV, AND S. BLGEL. **The Rashba-effect at metallic surfaces.** *Surface Science*, **600**[18]:3888, 2006. 169
- [228] J. H. DIL. **Spin and angle resolved photoemission on non-magnetic low-dimensional systems.** *Journal of Physics: Condensed Matter*, **21**[40]:403001, 2009. 169
- [229] K. SUGAWARA, T. SATO, S. SOUMA, T. TAKAHASHI, M. ARAI, AND T. SASAKI. **Fermi surface and anisotropic spin-orbit coupling of Sb(111) studied by angle-resolved photoemission spectroscopy.** *Phys. Rev. Lett.*, **96**[4]:046411, 2006. 169
- [230] Z. Y. LI, Z. Q. YANG, S. QIAO, J. HU, AND R. Q. WU. **Spinorbit splitting in graphene on metallic substrates.** *Journal of Physics: Condensed Matter*, **23**[22]:225502, 2011. 172
- [231] P. MORAS, D. WORTMANN, G. BIHLMAYER, L. FERRARI, G. ALEJANDRO, P. H. ZHOU, D. TOPWAL, P. M. SHEVERDYAEVA, S. BLÜGEL, AND C. CARBONE. **Probing the electronic transmission across a buried metal/metal interface.** *Phys. Rev. B*, **82**:155427, Oct 2010. 172

BIBLIOGRAPHIC RESEARCH

- [232] P. MORAS, P. M. SHEVERDYAEVA, C. CARBONE, D. TOPWAL, L. FERRARI, G. BIHLMAYER, S. OUAZI, S. RUSPONI, A. LEHNERT, AND H. BRUNE. **Electronic states of moiré modulated Cu films.** *Journal of Physics: Condensed Matter*, **24**[33]:335502, 2012. 172
- [233] D.A. PAPACONSTANTOPOULOS. *Handbook of the Band Structure of Elemental Solids*. Plenum Press, 1986. 173, 176
- [234] F. SCHILLER, R. KEYLING, E. V. CHULKOV, AND J. E. ORTEGA. **Surface state scattering at a buried interface.** *Phys. Rev. Lett.*, **95**:126402, Sep 2005. 174
- [235] A. VARYKHALOV, D. MARCHENKO, M. R. SCHOLZ, E. D. L. RIENKS, T. K. KIM, G. BIHLMAYER, J. SÁNCHEZ-BARRIGA, AND O. RADER. **Ir(111) Surface State with Giant Rashba Splitting Persists under Graphene in Air.** *Phys. Rev. Lett.*, **108**:066804, Feb 2012. 176
- [236] K. V. KLITZING, G. DORDA, AND M. PEPPER. **New method for high-accuracy determination of the fine-structure constant based on quantized Hall resistance.** *Phys. Rev. Lett.*, **45**[6]:494, 1980. 179
- [237] D. C. TSUI, H. L. STORMER, AND A. C. GOSSARD. **Two-dimensional magneto-transport in the extreme quantum limit.** *Phys. Rev. Lett.*, **48**[22]:1559, 1982. 179
- [238] B. A. BERNEVIG, T. L. HUGHES, AND SH.-CH. ZHANG. **Quantum spin Hall effect and topological phase transition in HgTe quantum wells.** *Science*, **314**[5806]:1757, 2006. 179
- [239] M. KÖNIG, S. WIEDMANN, CH. BRNE, A. ROTH, H. BUHMANN, L. W. MOLENKAMP, X.-L. QI, AND SH.-CH. ZHANG. **Quantum spin Hall insulator state in HgTe quantum wells.** *Science*, **318**[5851]:766, 2007. 179
- [240] R. B. LAUGHLIN. **Anomalous quantum Hall effect: An incompressible quantum fluid with fractionally charged excitations.** *Phys. Rev. Lett.*, **50**[18]:1395, 1983. 179
- [241] B. I. HALPERIN. **Quantized Hall conductance, current-carrying edge states, and the existence of extended states in a two-dimensional disordered potential.** *Phys. Rev. B*, **25**[4]:2185, 1982.
- [242] D. J. THOULESS, M. KOHMOTO, M. P. NIGHTINGALE, AND M. DEN NIJS. **Quantized Hall conductance in a two-dimensional periodic potential.** *Phys. Rev. Lett.*, **49**[6]:405, 1982.
- [243] F. D. M. HALDANE. **Model for a quantum Hall effect without Landau levels: Condensed-matter realization of the "parity anomaly".** *Phys. Rev. Lett.*, **61**[18]:2015, Oct 1988. 179

- [244] SH. MURAKAMI, N. NAGAOSA, AND SH.-CH. ZHANG. **Spin-Hall insulator**. *Phys. Rev. Lett.*, **93**[15]:156804, 2004.
- [245] C. L. KANE AND E. J. MELE. **Quantum spin Hall effect in graphene**. *Phys. Rev. Lett.*, **95**[22]:226801, 2005.
- [246] C. L. KANE AND E. J. MELE. **Z_2 topological order and the quantum spin Hall effect**. *Phys. Rev. Lett.*, **95**[14]:146802, 2005. 179
- [247] L. FU AND C. L. KANE. **Topological insulators with inversion symmetry**. *Phys. Rev. B*, **76**[4]:045302, 2007. 179, 190
- [248] L. FU, C. L. KANE, AND E. J. MELE. **Topological insulators in three dimensions**. *Phys. Rev. Lett.*, **98**[10]:106803, 2007. 179, 190
- [249] D. HSIEH, D. QIAN, L. WRAY, Y. XIA, Y. S. HOR, R. J. CAVA, AND M. Z. HASAN. **A topological Dirac insulator in a quantum spin Hall phase**. 452[7190]:970, 2008. 179
- [250] H. ZHANG, CH.-X. LIU, X.-L. QI, X. DAI, Z. FANG, AND SH.-CH. ZHANG. **Topological insulators in Bi_2Se_3 , Bi_2Te_3 and Sb_2Te_3 with a single Dirac cone on the surface**. *Nat Phys*, **5**[6]:438, 2009. 181, 182
- [251] Y. XIA, D. QIAN, D. HSIEH, L. WRAY, A. PAL, H. LIN, A. BANSIL, D. GRAUER, Y. S. HOR, R. J. CAVA, AND M. Z. HASAN. **Observation of a large-gap topological-insulator class with a single Dirac cone on the surface**. *Nature Physics*, **5**[6]:398, 2009. 181, 187
- [252] D. HSIEH, Y. XIA, D. QIAN, L. WRAY, J. H. DIL, F. MEIER, J. OSTERWALDER, L. PATTHEY, J. G. CHECKELSKY, N. P. ONG, A. V. FEDOROV, H. LIN, A. BANSIL, D. GRAUER, Y. S. HOR, R. J. CAVA, AND M. Z. HASAN. **A tunable topological insulator in the spin helical Dirac transport regime**. *Nature*, **460**[7259]:1101, 2009. 182, 183
- [253] L. FU AND C. L. KANE. **Superconducting proximity effect and Majorana fermions at the surface of a topological insulator**. *Phys. Rev. Lett.*, **100**[9]:096407, 2008. 183
- [254] D.M. ROWE. *CRC Handbook of Thermoelectrics*. Taylor & Francis, 1995. 184
- [255] L. FU. **Hexagonal warping effects in the surface states of the topological insulator Bi_2Te_3** . *Phys. Rev. Lett.*, **103**[26]:266801, 2009. 189
- [256] M. BIANCHI, D. GUAN, SH. BAO, J. MI, B. B. IVERSEN, PH. D.C. KING, AND PH. HOFMANN. **Coexistence of the topological state and a two-dimensional electron gas on the surface of Bi_2Se_3** . *Nat Commun*, **1**:128, 2010. 189, 199, 200

BIBLIOGRAPHIC RESEARCH

- [257] M. BIANCHI, R. C. HATCH, J. MI, B. B. IVERSEN, AND PH. HOFMANN. **Simultaneous quantization of bulk conduction and valence states through adsorption of nonmagnetic impurities on Bi_2Se_3 .** *Phys. Rev. Lett.*, **107**[8]:086802, 2011. [189](#), [190](#), [191](#), [192](#), [199](#), [200](#)
- [258] H. M. BENIA, CH. LIN, K. KERN, AND CH. R. AST. **Reactive chemical doping of the Bi_2Se_3 topological insulator.** *Phys. Rev. Lett.*, **107**[17]:177602, 2011. [189](#), [199](#), [200](#)
- [259] J.-J. ZHU, D.-X. YAO, SH.-CH. ZHANG, AND K. CHANG. **Electrically controllable surface magnetism on the surface of topological insulators.** *Phys. Rev. Lett.*, **106**[9]:097201, 2011. [190](#), [196](#), [199](#)
- [260] M. YE, S. V. EREMEEV, K. KURODA, M. NAKATAKE, S. KIM, Y. YAMADA, E. E. KRASOVSKII, E. V. CHULKOV, M. ARITA, H. MIYAHARA, T. MAEGAWA, K. OKAMOTO, K. MIYAMOTO, T. OKUDA, K. SHIMADA, H. NAMATAME, M. TANIGUCHI, Y. UEDA, AND A. KIMURA. **Relocation of the topological surface state of Bi_2Se_3 beneath the surface by Ag intercalation.** *ArXiv e-prints*, 2011. [190](#), [192](#), [199](#), [200](#)
- [261] S. V. EREMEEV, T. V. MENSCHIKOVA, M. G. VERGNIORY, AND E. V. CHULKOV. **New interpretation of the origin of 2DEG states at the surface of layered topological insulators.** *ArXiv e-prints*, 2011. [190](#), [192](#), [200](#)
- [262] L. A. WRAY, S.-Y. XU, Y. XIA, D. HSIEH, A. V. FEDOROV, Y. S. HOR, R. J. CAVA, A. BANSIL, H. LIN, AND M. Z. HASAN. **A topological insulator surface under strong Coulomb, magnetic and disorder perturbations.** *Nat Phys*, **7**[1]:32, 2011. [190](#), [199](#), [200](#)
- [263] Y. L. CHEN, J.-H. CHU, J. G. ANALYTIS, Z. K. LIU, K. IGARASHI, H.-H. KUO, X. L. QI, S. K. MO, R. G. MOORE, D. H. LU, M. HASHIMOTO, T. SASAGAWA, S. C. ZHANG, I. R. FISHER, Z. HUSSAIN, AND Z. X. SHEN. **Massive Dirac fermion on the surface of a magnetically doped topological insulator.** *Science*, **329**[5992]:659, 2010. [190](#)
- [264] S. V. EREMEEV, Y. M. KOROTEEV, AND E. V. CHULKOV. **Effect of the atomic composition of the surface on the electron surface states in topological insulators A_2B_3 .** *JETP Letters*, **91**[8]:387, 2010. [191](#)
- [265] G. BIHLMAYER, S. BLÜGEL, AND E. V. CHULKOV. **Enhanced Rashba spin-orbit splitting in Bi/Ag(111) and Pb/Ag(111) surface alloys from first principles.** *Phys. Rev. B*, **75**[19]:195414, 2007. [193](#)
- [266] J. C. FUGGLE AND N. MÅRTENSSON. **Core-level binding energies in metals.** *Journal of Electron Spectroscopy and Related Phenomena*, **21**[3]:275, 1980. [193](#)

- [267] National Institute of Standards and Technology, Gaithersburg. *NIST X-ray Photoelectron Spectroscopy Database*, version 3.5 edition, 2003. 193
- [268] A. KALAMPOKIS, E. HATZIKRANIOU, AND K. M. PARASKEVOPOULOS. **Study of the deintercalation process in Bi_2Se_3 single crystals treated with hydrazine.** *Materials Research Bulletin*, **33**[9]:1359, 1998. 196
- [269] M. BIANCHI, R. C. HATCH, Z. LI, PH. HOFMANN, F. SONG, J. I. MI, B. B. IVERSEN, Z. M. ABD EL-FATTAH, P. LÖPTIEN, L. ZHOU, A. A. KHAJETOORIANS, J. WIEBE, R. WIESENDANGER, AND J. W. WELLS. **Robust surface doping of Bi_2Se_3 by Rubidium intercalation.** *ACS Nano*, null[null]:null, 2012. 199, 200
- [270] Y. S. HOR, A. J. WILLIAMS, J. G. CHECKELSKY, P. ROUSHAN, J. SEO, Q. XU, H. W. ZANDBERGEN, A. YAZDANI, N. P. ONG, AND R. J. CAVA. **Superconductivity in $\text{Cu}_x\text{Bi}_2\text{Se}_3$ and its implications for pairing in the undoped topological insulator.** *Phys. Rev. Lett.*, **104**[5]:057001, 2010. 199
- [271] T. VALLA, Z.-H. PAN, D. GARDNER, Y. S. LEE, AND S. CHU. **Photoemission spectroscopy of magnetic and nonmagnetic impurities on the surface of the Bi_2Se_3 topological insulator.** *Phys. Rev. Lett.*, **108**[11]:117601, 2012. 199
- [272] CH. CHEN, SH. HE, H. WENG, W. ZHANG, L. ZHAO, H. LIU, X. JIA, D. MOU, SH. LIU, J. HE, Y. PENG, Y. FENG, Z. XIE, G. LIU, X. DONG, J. ZHANG, X. WANG, Q. PENG, Z. WANG, SH. ZHANG, F. YANG, CH. CHEN, Z. XU, X. DAI, Z. FANG, AND X. J. ZHOU. **Robustness of topological order and formation of quantum well states in topological insulators exposed to ambient environment.** *Proceedings of the National Academy of Sciences*, 2012. 200
- [273] W. N. UNERTL. *Physical Structure*. Number v. 1 in Handbook of Surface Science. Elsevier, 1996. 205, 206, 207
- [274] A. KIEJNA AND K. WOJCIECHOWSKI. *Metal Surface Electron Physics*. Elsevier, 1996. 207
- [275] B. SEGALL. **Fermi surface and energy bands of copper.** *Phys. Rev.*, **125**[1]:109, 1962. 208, 210, 211
- [276] G. A. BURDICK. **Energy band structure of Copper.** *Phys. Rev.*, **129**[1]:138, 1963.
- [277] W. F. KROLIKOWSKI AND W. E. SPICER. **Photoemission studies of the noble metals. I. Copper.** *Phys. Rev.*, **185**[3]:882, 1969.
- [278] S. KUPRATAKULN. **Relativistic electron band structure of Gold.** *Journal of Physics C: Solid State Physics*, **3**[2S]:S109, 1970.

BIBLIOGRAPHIC RESEARCH

- [279] N. E. CHRISTENSEN. **High-energy band structure of Gold.** *Phys. Rev. B*, **13**[6]:2698, 1976.
- [280] C. B. SOMMERS AND H. AMAR. **Relativistic band structure of Gold.** *Phys. Rev.*, **188**[3]:1117, 1969.
- [281] P. E. LEWIS AND P. M. LEE. **Band structure and electronic properties of Silver.** *Phys. Rev.*, **175**[3]:795, 1968.
- [282] R. E. HUMMEL. *Electronic Properties of Materials*. Springer, 2001. 208
- [283] A. B. PIPPARD. **An experimental determination of the Fermi surface in Copper.** *Philosophical Transactions of the Royal Society of London. Series A, Mathematical and Physical Sciences*, **250**[979]:325, 1957. 210
- [284] R. L. JACOBS. **The electronic structure of the noble metals I. The energy bands.** *Journal of Physics C: Solid State Physics*, **1**[5]:1296, 1968. 211
- [285] M. SPRINGFORD. *Electrons at the Fermi Surface*. Cambridge University Press, 2011. 211
- [286] D. J. ROAF. **The Fermi surfaces of Copper, Silver and Gold II. Calculation of the Fermi surfaces.** *Philosophical Transactions of the Royal Society of London. Series A, Mathematical and Physical Sciences*, **255**[1052]:135, 1962. 211
- [287] F. BLOCH. **Heisenberg and the early days of quantum mechanics.** *Physics Today*, **29**[12]:23, 1976. 212
- [288] R. DE L. KRONIG AND W. G. PENNEY. **Quantum mechanics of electrons in crystal lattices.** *Proceedings of the Royal Society of London. Series A*, **130**[814]:499, 1931. 212
- [289] H. IBACH. *Physics of Surfaces and Interfaces*. Springer, 2006. 212
- [290] U. HÖFER, I. L. SHUMAY, CH. REUß, U. THOMANN, W. WALLAUER, AND TH. FAUSTER. **Time-resolved coherent photoelectron spectroscopy of quantized electronic states on metal surfaces.** *Science*, **277**[5331]:1480, 1997. 215
- [291] P. O. GARTLAND AND B. J. SLAGSVOLD. **Transitions conserving parallel momentum in photoemission from the (111) face of Copper.** *Phys. Rev. B*, **12**[10]:4047, 1975. 220
- [292] P. HEIMANN, H. NEDDERMEYER, AND H. F. ROLOFF. **Ultraviolet photoemission for intrinsic surface states of the noble metals.** *Journal of Physics C: Solid State Physics*, **10**[1]:L17, 1977. 220
- [293] J. A. ROSEN. *Distortion Correction and Momentum Representation of Angle-Resolved Photoemission Data*. M.sc thesis, University of British Columbia, 2008. 222

- [294] SPECS. *Application of the Phoibos Angular Dispersion Mode*. 222, 223
- [295] C. ENDERLEIN. *Graphene and its Interaction with Different Substrates Studied by Angular-Resolved Photoemission Spectroscopy*. Phd thesis, Fritz-Haber Institut der Max Planck Gesellschaft, 2011. 223, 224
- [296] F. HADJARAB AND J. L. ERSKINE. **Image properties of the hemispherical analyzer applied to multichannel energy detection**. *Journal of Electron Spectroscopy and Related Phenomena*, 36[3]:227, 1985. 224
- [297] P. ZHANG, P. RICHARD, T. QIAN, Y.-M. XU, X. DAI, AND H. DING. **A precise method for visualizing dispersive features in image plots**. *Review of Scientific Instruments*, 82[4]:043712, 2011. 238